

Final Report
ONR GRANT / CONTRACT INFORMATION

Grant / Contract Title: Hybrid Asymptotic-Numerical Methods in Scattering
Performing Organization: Boston University
Principal Investigator: Dr. Paul E. Barbone
Contract Number: N00014-95-1-0719
PR Number: 97PR03860-00
ONR Scientific Officer: Dr. Luise Couchman

16990518095

DISTRIBUTION STATEMENT A
Approved for Public Release
Distribution Unlimited

REPORT DOCUMENTATION PAGE

Form Approved
OMB No. 0704-0188

Public reporting burden for this collection of information is estimated to average 1 hour per response, including the time for reviewing instructions, searching existing data sources, gathering and maintaining the data needed, and completing and reviewing the collection of information. Send comments regarding this burden estimate or any other aspect of this collection of information, including suggestions for reducing this burden, to Washington Headquarters Services, Directorate for Information Operations and Reports, 1215 Jefferson Davis Highway, Suite 1204, Arlington, VA 22202-4302, and to the Office of Management and Budget, Paperwork Reduction Project (0704-0188), Washington, DC 20503.

1. AGENCY USE ONLY (Leave blank)			2. REPORT DATE 5 May 1999		3. REPORT TYPE AND DATES COVERED Final Report		
4. TITLE AND SUBTITLE Hybrid asymptotic-numerical methods in scattering <i>(Large object)</i>			5. FUNDING NUMBERS No: N00014-95-1-0719 PR: 97PR03860-00				
6. AUTHOR(S) Paul E. Barbone							
7. PERFORMING ORGANIZATION NAME(S) AND ADDRESS(ES) Department of Aerospace and Mechanical Engineering Boston University 110 Cummington St. Boston, MA 02215			8. PERFORMING ORGANIZATION REPORT NUMBER AM-99-005				
9. SPONSORING/MONITORING AGENCY NAME(S) AND ADDRESS(ES) Office of Naval Research Ballston Tower One 800 North Quincy St. Arlington, VA 22217			10. SPONSORING/MONITORING AGENCY REPORT NUMBER AM-99-005				
11. SUPPLEMENTARY NOTES							
12a. DISTRIBUTION / AVAILABILITY STATEMENT Openly available as BU/AME Report No. AM-99-005			12b. DISTRIBUTION CODE				
13. ABSTRACT (Maximum 200 words) <p>We have developed and studied hybrid asymptotic-numerical methods to compute the acoustic field scattered by a large object. The asymptotic approximation is based on a short wavelength expansion of the scattered field in the form of uniformly valid geometrical theory of diffraction. These were combined with two numerical methods: finite elements and boundary spectral strip methods. The coupling to finite elements was achieved with the introduction of a new variational principle to couple two incompatible approximations. The boundary spectral strip method is a spectral approximation applied to a boundary integral formulation of the boundary value problem. With this method, we have successfully evaluated diffraction coefficients, surface wave excitation coefficients, and solved large scattering problems with several diffraction points! We have also studied the error introduced by joining the numerical and asymptotic approximations, and determined its properties and scalings.</p>							
14. SUBJECT TERMS Acoustics, scattering, computational acoustics, rays, GTD, finite elements, boundary elements, asymptotic approximations.				15. NUMBER OF PAGES 294			
				16. PRICE CODE			
17. SECURITY CLASSIFICATION OF REPORT Unclassified		18. SECURITY CLASSIFICATION OF THIS PAGE Unclassified		19. SECURITY CLASSIFICATION OF ABSTRACT Unclassified		20. LIMITATION OF ABSTRACT Unlimited	

Contents

1 Research Objectives	3
2 Technical Approach and Review of Accomplishments	3
3 Conclusions	4
4 Relevance to the Navy	4
A List of publications, reports and presentations	6
A.1 Refereed Papers (Life of grant)	6
A.2 Non-Refereed Papers/Reports (Life of grant)	6
A.3 Presentations (Life of grant)	7
A.3.1 Invited	7
A.3.2 Contributed presentations:	7
B List of Honors/Awards	8
C Reprinted papers and reports	8
C.1 Surface and creeping caves in hybrid asymptotic numerical method	9
C.2 Scattering from submerged objects by a hybrid asymptotic-boundary integral equation method	42
C.3 Scattering by a Hybrid Asymptotic/Finite Element Method	63
C.4 Galerkin Formulation and Singularity Subtraction for Spectral Solutions of Boundary Integral Equations	80
C.5 Diffraction from simple shapes by a hybrid asymptotic-numerical method	98
C.6 Dispersion Free Finite Element Methods for Helmholtz Equation	108
C.7 FEM, BEM, Spectral FEM or Spectral BEM?	111
C.8 Nearly H^1 Optimal Finite Element Method for the Helmholtz Equation	159
C.9 Acoustic Scattering Calculations by a Hybrid Asymptotic Numerical Method	172
C.10 Finite Element Formulations for Exterior Problems: Application to Hybrid Methods, Non-reflecting Boundary Conditions, and Infinite Elements	262
C.11 Approximate Diffraction Coefficients by the Method of Matched Asymptotic Expansions	277

1 Research Objectives

We have developed an efficient framework for scattering calculations that combines the geometrical flexibility of FEM or BEM with the efficiency of high-frequency asymptotic methods. This framework is based on the definition of an asymptotically equivalent boundary value problem (ABVP) that replaces the original one. We have been studying the properties of this formulation.

2 Technical Approach and Review of Accomplishments

Our hybrid method is related to the method of matched asymptotic expansions where, in the short wavelength limit, the scattered field contains two asymptotic regions. In the “outer” domain, we have a “global” asymptotic expansion which we assume to be given by a geometrical optics ray series (short wavelength expansion.) This expansion is valid almost everywhere in the domain. Where it is not valid, we supplement the outer expansion with an “inner” or “local” solution. This local solution is found using either the finite element method or boundary integral equation method, and is patched to the outer expansion along an artificial boundary. Thus, the FEM/BEM is applied to a collection of small regions (size $O(\lambda)$ = wavelength) in the vicinity of diffraction points.

The total solution of a given scattering problem is thus decomposed into an application of the geometrical theory of diffraction (or any other suitable asymptotic approximation), in conjunction with a numerical solution of a problem defined over the union of several small domains.

We chose to develop this approach over adopting any of several existing approaches for a number of reasons (see Barbone, *et al.*, 1997). The oldest hybrid approaches in scattering are based on single-layer potential integral equations and thus are prone to uniqueness problems at “forbidden frequencies.” Even so, these involve integrations of rapidly oscillating kernels over large domains. More recently, FEM has been used as a “preprocess” to evaluate scattering impedance matrices. These scattering impedances then get incorporated into a UTD or GTD solution.

Our approach, we feel, has several benefits over existing strategies. First, by incorporating the definition of an ABVP, we have separated the asymptotic from the numerical (discrete) approximation. Thus we can analyze and understand each one separately. Further, this step allows us to describe a hybrid asymptotic-numerical approach that is independent of whether we choose boundary integral equation methods or finite element methods. Finally, by defining the ABVP first on small domains (the size of a wavelength), we arrive at a numerical problem that is compact and easy to discretize. It contains no infinite nor even large integration domains. The domain sizes over which any integration must be performed scales with the size of the wavelength (for example, 2λ , not 1000λ .)

Having developed a strategy that can be combined with either FEM or boundary integral equations, we examined both. For FEM implementation, we developed a new variational principle that allowed us to couple the asymptotic field to the finite element representation (described in Harari, Barbone and Montgomery (1997).) For the boundary integral formulation, we have adapted the highly efficient Boundary Spectral-strip Method (BSM) (see Michael & Barbone (1997).) We demonstrated the feasibility of using either method on the problem of scattering from wedge geometries, and have extended both methods to allow modeling of surface waves (Michael & Barbone, 1999-2.)

Whether to fully develop the FEM or BSM formulation remained an open question. The

earlier analysis of Harari & Hughes showing FEM to be more computationally efficient than BEM does not apply to the Boundary Spectral-strip Method. Therefore, we undertook a new study of the relative computational efficiencies of the corresponding spectral methods. Indeed, we found that when using 8-th order elements, BEM is always more cost effective than FEM, unless static condensation is used. When static condensation is used, then FEM regains a cost advantage in 3D. Generally speaking, BSM is more efficient in 2D, while high-order FEM is more efficient in 3D. The results of this study are available in report form in the appendix (Michael & Barbone, 1997-2).

In terms of implementation strategies, in FEM we have developed an element-like data-structure and basis for the asymptotic field. This allows the hybrid method to be coupled with existing FEM codes. This implementation can also be adapted to accommodate other analytical representations of the radiating field.

During the last year, we have devoted much of our attention to studying the error that is associated with the hybrid formulation, and understanding how it depends on various problem parameters. The unique aspect of the hybrid method lies in the "accurately transmitting" boundary conditions. These are the conditions that join the numerical domain to the asymptotic domain. These must not only be non-reflecting, but they must admit incoming radiation from other regions, and accurately predict diffraction coefficients. This study is summarized in Michael & Barbone (1999-3).

The error analysis includes estimates in errors of the diffraction coefficients for single and multiple diffraction points, and focuses on scalings with various problem parameters including geometry, boundary conditions, and frequency. We found that the method can produce reliable results for a large range of problem parameters. Typically, the results are as good as the asymptotics used to represent the field. If the field is accurately represented, the diffraction coefficients will be accurately predicted. If the field is not accurately represented in the asymptotic description, the associated diffraction coefficients will not necessarily be accurately predicted.

3 Conclusions

We believe that the hybrid method is currently sufficiently mature that it is ready to be incorporated into a test code. Our recommendation for the continuation of this project would be to try to interface it to an existing ray code and tackle problems as they emerge. The most efficient interface for a ray code would be probably through the FEM implementation described in Barbone, *et al.* (1997). Surface/creeping waves, including the acoustic fields associated with shell bending and shear waves, need to be incorporated in a uniform manner as in the examples in Michael & Barbone (1999-2). The anticipated errors are as described in Michael & Barbone (1999-3), which should be mastered by anyone hoping to become a practitioner in the area.

4 Relevance to the Navy

Our research goal has been to develop and study a hybrid asymptotic-numerical method with application to the solution of the Helmholtz equation for large wavenumber. Our method is especially efficient at high wavenumber. For example, the standard FEM representation of a field scattered by an obstacle of dimension L requires $O(kL^3)$ finite element degrees of freedom. With our hybrid formulation, we require only $O(kL)$ degrees of freedom for the

same problem. At lower frequencies, our method reverts to a standard formulation which we know to be well suited there.

The ability to solve the Helmholtz equation efficiently for high frequencies would allow Navy designers to perform scattering and radiation calculations at frequencies not otherwise possible. The method could be used to provide the forward modeling step of an inverse scattering procedure, where high efficiency is especially important. Finally, the result of using the formulation itself is an expression for the radiated acoustic field in terms of traveling wave amplitudes. Repeated calculation in such terms will help engineers develop insight into various radiation and scattering mechanisms.

A List of publications, reports and presentations

A.1 Refereed Papers (Life of grant)

1. "Error analysis and numerical aspects of hybrid asymptotic numerical method in scattering," Ofer Michael and Paul E. Barbone, *J. Acoust. Soc. Am.*, to be submitted, 1999.
2. "Surface and creeping caves in hybrid asymptotic numerical method," Ofer Michael and Paul E. Barbone, *J. Acoust. Soc. Am.*, accepted, January 1999.
3. "Scattering from submerged objects by a hybrid asymptotic-boundary integral equation method," Paul E. Barbone and Ofer Michael, *Wave Motion*, Vol. 29, pp. 137-156, 1999.
4. "Scattering by a Hybrid Asymptotic/Finite Element Method," Paul E. Barbone, Joshua M. Montgomery, Ofer E. Michael and Isaac Harari, *Computer Methods in Applied Mechanics and Engineering*, Vol. 164, Nos. 1-2, pp. 141-156, October 1998.
5. "Galerkin Formulation and Singularity Subtraction for Spectral Solutions of Boundary Integral Equations," Ofer Michael & Paul E. Barbone, *International Journal for Numerical Methods in Engineering*, Vol. 41, pp. 95-111, 1998.
6. "Diffraction from simple shapes by a hybrid asymptotic-numerical method," Joshua M. Montgomery and Paul E. Barbone, *Journal of the Acoustical Society of America*, vol 104(4), pp. 1964-1972, October 1998.
7. "Finite Element Formulations for Exterior Problems: Application to Hybrid Methods, Non-reflecting Boundary Conditions, and Infinite Elements," Isaac Harari, Paul E. Barbone and Joshua M. Montgomery, *International Journal for Numerical Methods in Engineering*, Vol. 40, 1997, pp. 2791-2805.
8. "Approximate Diffraction Coefficients by the Method of Matched Asymptotic Expansions," Paul E. Barbone, *Wave Motion*, Vol. 22, pp. 1-16, 1995.

A.2 Non-Refereed Papers/Reports (Life of grant)

1. "Dispersion Free Finite Element Methods for Helmholtz Equation," Paul E. Barbone and Isaac Harari, *Proc. 16th International Congress on Acoustics and 135th Meeting Acoustical Society of America*, Vol. 1, pp. 199-200, Acoustical Society of America, 1998. P.K. Kuhl and L.A. Crum, eds.
2. "FEM, BEM, Spectral FEM or Spectral BEM?" Ofer Michael and Paul E. Barbone, Also as BU Dept. Aerospace & Mechanical Eng. Technical Report No. AM-97-028, October 1997.
3. "Nearly H^1 Optimal Finite Element Method for the Helmholtz Equation," Paul E. Barbone and Isaac Harari, BU Dept. Aerospace & Mechanical Eng. Technical Report No. AM-97-011, May 7, 1997.
4. Joshua M. Montgomery, *Acoustic Scattering Calculations by a Hybrid Asymptotic Numerical Method*. M.Sc. Thesis, Boston University, Dept. of Aerospace & Mechanical Eng., Boston, MA. 1997.

A.3 Presentations (Life of grant)

A.3.1 Invited

1. Paul E. Barbone, "Hybrid asymptotic-numerical methods in acoustic scattering," *EuroMech Colloquium 369: Fluid-Structure Interaction in Acoustics*, Pier Scheveningen, The Netherlands, Sept. 23–26, 1997.
2. Paul E. Barbone, Ofer Michael, Joshua M. Montgomery, and Isaac Harari, "Hybrid Asymptotic-Numerical Methods for Scattering Calculations," Special Seminar, Dept. of Aerospace & Mechanical Engineering, Boston University, March 4, 1997.

A.3.2 Contributed presentations:

1. Paul E. Barbone and Isaac Harari, "Dispersion-free finite-element methods for the Helmholtz equation," *135th Meeting of the Acoustical Society of America*, Seattle, WA, June 20–26, 1998.
2. Paul E. Barbone, Joshua M. Montgomery, Isaac Harari, "Surface Waves in a Hybrid Asymptotic-Numerical Method," Fourth U.S. National Congress on Computational Mechanics, San Francisco, CA, August 6–8, 1997.
3. Ofer E. Michael, Paul E. Barbone, "FEM, BEM, Spectral FEM or Spectral BEM?" Fourth U.S. National Congress on Computational Mechanics, San Francisco, CA, August 6–8, 1997.
4. Ofer Michael & Paul E. Barbone, "Efficient Spectral Galerkin Formulation with Exact Singularity Subtraction for BIE," *The 1997 Joint American Society of Mechanical Engineers (ASME) American Society of Civil Engineers (ASCE) Society of Engineering Science (SES) Summer Meeting, McNU'97*, Northwestern University, Evanston, Illinois, USA, June 29 - July 2, (1997).
5. Paul E. Barbone and Ofer E. Michael, "Scattering calculations by a hybrid GTD-boundary integral equation method," *133rd Meeting of the Acoustical Society of America*, State College, PA, June 15–20, 1997.
6. Paul E. Barbone, Ofer Michael, Joshua M. Montgomery, Isaac Harari, "Hybrid Asymptotic Numerical Methods for Scattering Calculations," ONR Structural Acoustics Review Meeting, Austin TX, 18 February 1997.
7. Joshua M. Montgomery & Paul E. Barbone, "Diffraction from simple shapes by a hybrid asymptotic-numerical method," *131st Meeting of the Acoustical Society of America*, Indianapolis, IN, May 13–17, 1996.
8. Paul E. Barbone and Isaac Harari, "Hybrid asymptotic-numerical method for evaluating diffraction coefficients," *130th Meeting of the Acoustical Society of America*, St. Louis, MO, November 1995.

B List of Honors/Awards

<u>Name of Person Receiving Award</u>	<u>Recipient's Institution</u>	<u>Name, Sponsor and Purpose of Award</u>
Paul E. Barbone	Boston University	1999 R. Bruce Lindsay Award Acoust. Soc. Am. [†]
Joshua M. Montgomery	Boston University	ASA Student Paper Competition ^{††}

[†] R. Bruce Lindsay Award: Award presented annually to a member of the ASA who is under 35 years of age and who, ... has contributed substantially, through published papers, to the advancement of theoretical and/or applied acoustics. March, 1999.

Award encomium cites "... *for developing novel theoretical and computational acoustics techniques.*"

^{††} Best Student Paper in Structural Acoustics and Vibration, Awarded by ASA Structural Acoustics and Vibration Technical Committee, May 1996.

C Reprinted papers and reports

This section contains reprints of papers and reports that resulted from the current project in reverse chronological order. The first paper listed in the publications section is excluded from this list since it is still in preparation. Upon completion and publication, it will be sent under separate cover to the program manager. A revised version of the paper that won the student paper award is presented in section C.5.

C.1 Surface and creeping waves in hybrid asymptotic numerical method

"Surface and creeping waves in hybrid asymptotic numerical method," Ofer Michael and Paul E. Barbone, **J. Acoust. Soc. Am.**, accepted, January 1999.

SURFACE AND CREEPING WAVES IN HYBRID ASYMPTOTIC-BOUNDARY INTEGRAL METHOD

Ofer Michael

Paul E. Barbone*

Department of Aerospace and Mechanical Engineering
Boston University, Boston, MA 02215

August 28, 1998

Keywords: Surface waves, Creeping waves, Boundary Integral Equation, GTD, Scattering, Acoustics, High frequency asymptotics.

PACS numbers: 43.20.Dk

Short title: Surface waves in hybrid method.

*Corresponding author, E-mail:barbone@waves.bu.edu, Phone: (617) 353-6063, Fax: (617) 353-5866.

Abstract

We describe a hybrid asymptotic/boundary integral equation method for the solution of scattering problems including surface waves and creeping waves. The hybrid method is based on short wavelength asymptotics coupled with a boundary integral equation formulation (boundary spectral strip). The method is described using non-uniform representations for both surface wave and creeping waves, and a uniform representation for surface waves. The method is illustrated and investigated through simple examples with analytical or semi-analytical solutions. These examples show that excitation amplitudes and diffraction coefficients can be reliably and accurately evaluated, and that multiple scattering effects can be systematically included. We demonstrate the importance of using uniform asymptotics and enforcing boundary conditions on the diffraction coefficients. We investigated different values of boundary impedance with single and multi-domains problems. The error in the diffraction coefficients is evaluated using both representations. Finally, we conclude with a large scale example which shows how the formulation leads naturally to an efficient and simple domain decomposition strategy.

1 Introduction

Computing the acoustic or electromagnetic field scattered by large obstacles remains a challenge. Traditional numerical methods (e.g. FEM or BEM) have meshing requirements which scale (at least naively) with the wavelength, λ . The size of the domain to be meshed, on the other hand, scales with the size of the obstacle, L . Thus, the computation cost can be prohibitively high when $\lambda/L \ll 1$.

Asymptotic methods, including GTD and UTD, are devised specifically to capture the limit of $\lambda/L \rightarrow 0$. In practical application, however, these are typically limited by the availability of diffraction coefficients.

Several hybrid asymptotic-numerical methods have been developed to try to overcome the limits of each approach. The first was introduced in 1975 by Burnside, *et al.* [4]. It is typical of several hybrid formulations developed since then, in that GTD inspired shape functions are used in an otherwise straightforward discretization of the original boundary value problem [4, 11, 15, 20, 22].

Wang [22] in 1991 was the first to introduce surface wave based shape functions in a hybrid method. These he included for two-dimensional scattering and scattering from bodies of revolution. Wang noted that integration of the GTD based shape functions in order to obtain the discretized equations was computationally expensive, and suggested that these integrals be evaluated asymptotically.

An alternative strain of hybrid methods that has developed is that in which the numerical part (FEM typically) is used as a “preprocess.” Jin and coworkers [21, 6, 8] describe some very recent work on combining FEM with a uniform theory of diffraction (UTD). These authors propose solving the canonical diffraction problem as a preprocess using FEM, and they describe how to build the result into a UTD formulation. Similar approaches are advocated in [19, 5, 18]. Calamia, Cocciali & Pelosi [5] make a point of adequately enforcing the radiation condition on the calculation of the inner solution in order to avoid uniqueness problems at interior eigenfrequencies.

We have recently presented a hybrid method that falls outside the two categories just described [17, 2, 3]. Our approach is conceptually related to the method of matched asymptotic expansions. The *outer* or *global* asymptotic expansion satisfies the equations of geometrical optics. The *inner* or *local* field must satisfy the full Helmholtz equation, but is defined on a problem with greatly simplified geometry. The inner solution is necessary to describe the field in the vicinity of those points where the outer expansion fails to be valid. Our hybrid approach depends on dividing the entire domain into an *outer* asymptotic region, and an *inner* numerical region. In the outer domain, we describe the field using the geometrical theory of diffraction [10]. In the inner region, we solve the full Helmholtz equations numerically. On the artificial boundary between the two domains we enforce continuity of the field and its normal derivative. Thus our hybrid approach could be described as patched expansions, in which the inner

expansion is found numerically.

Our method avoids many of the problems associated with other hybrid methods. Our formulation completely circumvents the problem of evaluating large, high oscillatory integrals, noted in [22]. Further, our formulation naturally provides for appropriate enforcement of the radiation condition through patching on the artificial boundary.

In this contribution, we describe the treatment of surface and creeping waves in the hybrid method. In section §2 we describe our hybrid method in general. In section §3 we apply the method to the problem of radiation from a line-source on an impedance plane. This problem is known to give rise to surface wave phenomena for certain values of the impedance. We compare uniform vs. non-uniform representations of the surface wave fields. We derive the appropriate boundary conditions on the diffraction coefficients, and show their importance in numerical examples. We end section §3 with an examination of the error associated with surface wave coupling between two numerical regions. We treat a second example in section §4: radiation from a line source on a hard cylindrical surface. This problem is known to give rise to creeping wave phenomena. We discuss the asymptotic representation, the numerical formulation, and demonstrate high accuracy in predicting the diffracted field and the creeping wave amplitude. Finally, we conclude with an example that combines features of our first two examples. We show how our formulation leads naturally to an efficient and simple domain decomposition strategy.

2 The hybrid asymptotic-numerical method

We briefly discuss here the concepts of the hybrid method. More details and additional background are available in [17, 2, 3]. Here we shall present an outline of our hybrid method in the context of the scalar wave equation

$$\Delta u + k^2 u = 0 \quad x \in \Omega. \quad (1)$$

Here u is the (complex) field relative to a time dependence of $e^{-i\omega t}$. $\Omega \subset R^d$ is the d -dimensional infinite domain exterior to the scatterer; i.e. $\Omega = R^d \setminus \bar{\mathcal{S}}$, where \mathcal{S} represents the scatterer. On the surface of the scatterer $\partial\mathcal{S}$, u satisfies a (linear) boundary condition:

$$u = \mathcal{B} \frac{\partial u}{\partial n} \quad x \in \partial\mathcal{S}. \quad (2)$$

Here, \mathcal{B} is an operator related to the impedance of the surface.

We shall consider scattering from this body due to an incident wave u_{inc} , and write the total field as:

$$u = u_{inc} + u_{scat} \quad (3)$$

$$\lim_{r \rightarrow \infty} r^{(d-1)/2} \left[\frac{\partial u_{scat}}{\partial r} - ik u_{scat} \right] = 0. \quad (4)$$

With u_{inc} specified, equations (1-4) completely determine the scattered field u_{scat} .

For simplicity, we shall discuss our hybrid method in the context of GTD and a boundary integral equation formulation. Other hybrid formulations (UTD, modal expansions, Floquet theory with FEM/BEM/MoM, etc.) are also possible with our formulation. We begin by assuming that we have a GTD representation of the scattered field:

$$u_{scat} \approx u^G(x) = \sum_{ray\ j} a_j(kR) A_j(x) \exp(ik\psi_j(x)). \quad (5)$$

In (5) we require that the phase functions ψ and the amplitude functions A , satisfy the eiconal and transport equations:

$$(\nabla\psi)^2 = 1 \quad (6)$$

$$2\nabla\psi \cdot \nabla A + \Delta\psi A = 0. \quad (7)$$

Such an expansion (5) typically results in an approximation which is asymptotic in kR (R is a length scale to be specified):

$$\lim_{kR \rightarrow \infty} u^G = u_{scat} \quad \text{almost everywhere in } \Omega. \quad (8)$$

Those points at which u^G , the geometrical field, is not asymptotic to the scattered field u_{scat} are called "diffraction points". Thus we define the diffraction points as:

$$X^D = \{x \mid \lim_{kR \rightarrow \infty} u_{scat} - u^G \neq 0\} \quad (9)$$

We note that since u^G is not asymptotic to u_{scat} at x^D , then for any *finite value* of kR , u^G will typically provide a very poor approximation to u_{scat} in a whole neighborhood of x^D . For that reason, we must consider local corrections to u^G valid in the vicinity of x^D in order to obtain a practically useful approximation for moderate values of kR . This is one purpose of the numerical aspect of the hybrid method.

A diffraction point can be classified as either *essential* or *inessential*. The local solution valid in the vicinity of an essential diffraction point provides some coefficient needed in the global expansion (i.e. a diffraction coefficient). Local solutions valid near inessential diffraction points do not. UTD can provide solutions that have only essential diffraction points. In practice, we use local solutions available in the literature to describe the field in the vicinity of inessential diffraction points.

Around each *contiguous* set of essential diffraction points, we define a diffraction region Ω^D such that:

$$\Omega^D = \left\{ x \mid \|x - x^D\| \leq (kR)^\alpha f \left(\frac{x - x^D}{\|x - x^D\|} \right) \right\} \quad (10)$$

Here, x^D is a diffraction point and R is a fixed distance, a parameter to be chosen by the analyst, which determines the size of the diffraction region. The accuracy of our hybrid method depends on $kR \gg 1$. We denote by Γ_R the boundary of each diffraction region.

Now we are in position to define an asymptotically equivalent boundary value problem. This problem is nothing more than a restriction of our original boundary value problem to the diffraction regions, with continuity enforced across the artificial boundary Γ_R . Thus we define

$$\Delta u^D + k^2 u^D = 0 \quad x \in \Omega^D \quad (11)$$

$$u^D = \mathcal{B}\partial_n u^D \quad x \in \partial\Omega^D \cap \partial\Omega \quad (12)$$

$$u^D = u_{inc} + u^A \quad x \in \Gamma_R \quad (13)$$

$$\partial_n u^D = \partial_n u_{inc} + \partial_n u^A \quad x \in \Gamma_R. \quad (14)$$

Here, u^A is our global asymptotic approximation. It could be obtained by GTD as indicated in equation (5), by UTD, or by GTD with local corrections near inessential diffraction points. Figure 1 illustrates the method. We wrap all the diffraction points by a numerical domain and patch the numerical solution to the asymptotic solution which is valid elsewhere.

The main solution stage of our hybrid method involves solving the asymptotically equivalent boundary value problem ABVP (11-14). This problem is defined on a union of domains, each of which is size $O(R) = O(\lambda)$. Thus each is easily discretized with few degrees of freedom. The coupling of one region to another is accomplished through the definition of u^A . We note that u^A has undetermined functions in its definition. Any discretization of the ABVP must allow for these functions to be evaluated, and enforce continuity on Γ_R (equations (13) and (14)). A formulation that accomplishes these goals in the context of the finite element method is described in [7, 17]. A formulation based on boundary integral equations is presented in [2].

3 Surface waves

We shall start with surface waves problems and demonstrate the method by solving the problem of a source over half a plane with an impedance boundary condition as shown in Figure 2. The problem is given by:

$$\Delta u + k^2 u = 0 \quad \text{in } \Omega \quad (15)$$

$$\partial_n u + k\beta u = f(x) \quad \text{on } y = 0 \quad (16)$$

$$u = \text{outgoing}. \quad (17)$$

We shall treat the case in which the support of $f(x)$ is smaller than a wavelength λ . We will define the arbitrary boundary Γ_R as a semi circle (as shown in Figure 2) providing $kR \gg 1$. The discretization takes place along the boundary of the domain which is bounded inside Γ_R . Note

that it is an interior problem and therefore uniqueness problems which might arise in boundary integral equation are not relevant here.

3.1 Global Solution: Non-Uniform Representation

The solution of the eiconal equation (6) in $y > 0$ is:

$$\psi_1 = r. \quad (18)$$

From (16) we find an additional solution which is:

$$\psi_2 = \sqrt{1 + \beta^2} |x| - \beta y. \quad (19)$$

Substituting these solutions into the transport equation (7) yields the non-uniform asymptotic solution u^{NU} :

$$u^A = u^{NU} = (kR)^{-1/2} D(\theta) \sqrt{\frac{R}{r}} e^{ikr} + A_{sw_L} F_{sw_L}^{NU}(\theta, r) + A_{sw_R} F_{sw_R}^{NU}(\theta, r) \quad kR \rightarrow \infty; r \neq 0; \theta \neq \pi/2. \quad (20)$$

Note that the first term represents a cylindrical wave while the last two represent two surface waves going in the $\pm x$ directions. A_{sw_L}, A_{sw_R} are the amplitudes of the two surface waves, while their corresponding functions are:

$$F_{sw_L}^{NU} = \mathcal{H}(\theta - \frac{\pi}{2}) e^{-ikr \cos(\theta + \theta_{sw})} \quad (21)$$

$$F_{sw_R}^{NU} = \mathcal{H}(\frac{\pi}{2} - \theta) e^{ikr \cos(\theta - \theta_{sw})}. \quad (22)$$

Here \mathcal{H} is the Heaviside step function and θ_{sw} is:

$$\theta_{sw} = i \left| \cosh^{-1} \sqrt{1 + \beta^2} \right| \quad (23)$$

3.1.1 Boundary condition

Equation (20) should satisfy the boundary condition given in equation (16). Asymptotic expansion of this boundary conditions shows that the leading term satisfies:

$$\left(i \frac{\partial \psi_1}{\partial y} + \beta \right) D(\theta) = 0 \quad \theta = 0, \pi. \quad (24)$$

3.2 Global Solution: Uniform Representation

The non-uniform representation is not valid along the line $\theta = \pi/2$. We shall use a boundary layer solution [1] to obtain a uniform representation. In this case the uniform scattered field u^U is:

$$u^A = u^U = D^U(\theta) \frac{e^{ikr}}{\sqrt{kr}} + A_{sw_L} F_{sw_L}^U(\theta, r) + A_{sw_R} F_{sw_R}^U(\theta, r) \quad kR \rightarrow \infty; r \neq 0 \quad (25)$$

while the uniform surface wave functions are defined as:

$$F_{sw_L}^U = \frac{1}{\sqrt{\pi}} e^{ikr - i\pi/4} F \left[(2kr)^{\frac{1}{2}} \sin \frac{1}{2}(\pi - \theta_{sw} - \theta) \right] \quad (26)$$

$$F_{sw_R}^U = \frac{1}{\sqrt{\pi}} e^{ikr - i\pi/4} F \left[(2kr)^{\frac{1}{2}} \sin \frac{1}{2}(\theta - \theta_{sw}) \right] \quad (27)$$

where:

$$F(z) = e^{-iz^2} \int_z^\infty e^{it^2} dt \quad (28)$$

3.2.1 Uniform boundary condition

We wish to derive a boundary condition that would yield a relation between the directivity and the surface wave amplitudes. We also want that this boundary condition would be suitable for a large range of impedance values β .

In this section we will develop such a boundary condition for a more general case with different impedance values at $\theta = 0, \pi$ noted by β_L and β_R , respectively. We will start with the right going surface wave. From eqs. (25,27) we can write the right going surface wave as:

$$u_{sw_R} = A_{sw_R} \frac{e^{-i\pi/4}}{\sqrt{\pi}} e^{ikr} F(z_R) \quad (29)$$

where

$$z_R = (2kr)^{\frac{1}{2}} \sin \frac{1}{2}(\theta - \theta_{sw_R}) = -i [k\sigma_R x + ik\beta_R y - kr]^{\frac{1}{2}}. \quad (30)$$

Here, $\sigma_R = \sqrt{1 + \beta_R^2}$ and $-\pi/2 \leq \arg(z_R) \leq 0$ for $y \geq 0$. Expanding $F(z_R)$ for large z_R [9] yields:

$$F(z_R) \sim \sqrt{\pi} e^{i\pi/4} e^{(ikx\sigma_R - k\beta_R y) - ikr} + \frac{i}{2z_R} + \mathcal{O}(z_R^{-3}). \quad (31)$$

The right going surface wave can then be written as:

$$u_{sw_R} = A_{sw_R} \left\{ e^{(ik\sigma_R x - k\beta_R y)} + \frac{e^{-i\pi/4}}{\sqrt{\pi}} \frac{e^{ikr}}{\sqrt{kr}} \left[-\frac{1}{2} d_R(\theta) \right] \right\} \quad (32)$$

where

$$d_R(\theta) = [\sigma_R \cos \theta + i\beta_R \sin \theta - 1]^{-1/2}. \quad (33)$$

Similarly, we obtain for the left going wave:

$$u_{sw_L} = A_{sw_L} \left\{ e^{(ik\sigma_L x - k\beta_L y)} + \frac{e^{-i\pi/4}}{\sqrt{\pi}} \frac{e^{ikr}}{\sqrt{kr}} \left[-\frac{1}{2} d_L(\theta) \right] \right\} \quad (34)$$

with

$$d_L(\theta) = [-\sigma_L \cos \theta + i\beta_L \sin \theta - 1]^{-1/2}. \quad (35)$$

After setting the directivity $D(\theta)$ at the surface at $\theta = 0, \pi$ to zero in accord with equation (24), we obtain the desired boundary condition.

$$D^U(0) - \frac{e^{-i\pi/4}}{2\sqrt{\pi}} \left[\frac{A_{sw_R}}{\sqrt{\sigma_R - 1}} + \frac{A_{sw_L}}{i\sqrt{\sigma_L + 1}} \right] = 0 \quad (36)$$

$$D^U(\pi) - \frac{e^{-i\pi/4}}{2\sqrt{\pi}} \left[\frac{A_{sw_R}}{i\sqrt{\sigma_R + 1}} + \frac{A_{sw_L}}{\sqrt{\sigma_L - 1}} \right] = 0. \quad (37)$$

3.3 Local solution

After we have defined the global solution, we can proceed and define the local problem. Based on equations (11-14) we can formulate the local problem:

$$\Delta u^D + k^2 u^D = 0 \quad x \in \Omega^D \quad (38)$$

$$\partial_n u^D + k\beta u^D = f(x) \quad x \in \partial\Omega^D \cap \partial\Omega \quad (39)$$

$$u^D = u^A \quad x \in \Gamma_R \quad (40)$$

$$\partial_n u^D = \partial_n u^A \quad x \in \Gamma_R. \quad (41)$$

Here, the asymptotic solution u^A is given by eq. (20) or eq. (25) for the non-uniform or the uniform representation, respectively.

To solve the inner problem, we use the boundary strip method [16]. By using BIE, we can obtain a relation between the scattered field and its normal derivative along the boundary. This can be written in discrete form as:

$$\mathbf{H}\mathbf{u} = \mathbf{G} \partial_n \mathbf{u} \quad \text{on } \partial\Omega^D \quad (42)$$

Here \mathbf{u} and $\partial_n \mathbf{u}$ are two column vectors of the nodal values (or coefficients of approximating series in the case of BSM) of the variables u and $\partial_n u$, respectively. \mathbf{H} and \mathbf{G} are the associated coefficient matrices evaluated by a weighted residual or collocation procedure. In the examples we shall show, we used a collocation procedure.

By dividing the boundary of the computational domain $\partial\Omega^D$ into the artificial boundary Γ_R and the rest of the boundary $\Gamma_{\bar{R}}$ we can rewrite the last equation (42) as:

$$[\mathbf{H}_{\Gamma_R}, \mathbf{H}_{\Gamma_{\bar{R}}}] \begin{Bmatrix} \mathbf{u}_{\Gamma_R} \\ \mathbf{u}_{\Gamma_{\bar{R}}} \end{Bmatrix} = [\mathbf{G}_{\Gamma_R}, \mathbf{G}_{\Gamma_{\bar{R}}}] \begin{Bmatrix} \partial_n \mathbf{u}_{\Gamma_R} \\ \partial_n \mathbf{u}_{\Gamma_{\bar{R}}} \end{Bmatrix} \quad (43)$$

In the case of impedance boundary condition on $\Gamma_{\bar{R}}$ both $\mathbf{u}_{\Gamma_{\bar{R}}}$ and $\partial_n \mathbf{u}_{\Gamma_{\bar{R}}}$ are unknown. In order to solve both vectors we use the impedance boundary condition eq. (16):

$$\partial_n \mathbf{u}_{\Gamma_{\bar{R}}} + k\beta \mathbf{u}_{\Gamma_{\bar{R}}} = f(\mathbf{x}), \quad \mathbf{x} \in \Gamma_{\bar{R}}. \quad (44)$$

Using equation (20) or (25), and its normal derivative together with eqs. (43,44) yields the following set of equations:

$$\begin{bmatrix} -\mathbf{M}_D & -\mathbf{F}_{sw_L} & -\mathbf{F}_{sw_R} & \mathbf{M}_U & 0 & 0 \\ -\mathbf{M}_{\partial_n D} & -\partial_n \mathbf{F}_{sw_L} & -\partial_n \mathbf{F}_{sw_R} & 0 & \mathbf{M}_{\partial_n U} & 0 \\ 0 & 0 & 0 & \mathbf{H}_{\Gamma_R} & -\mathbf{G}_{\Gamma_R} & \mathbf{H}_{\Gamma_{\bar{R}}} + k\beta \mathbf{G}_{\Gamma_{\bar{R}}} \end{bmatrix} \begin{Bmatrix} \mathbf{D} \\ \mathbf{A}_{sw_L} \\ \mathbf{A}_{sw_R} \\ \mathbf{u}_{\Gamma_R} \\ \partial_n \mathbf{u}_{\Gamma_R} \\ \mathbf{u}_{\Gamma_{\bar{R}}} \end{Bmatrix} = \begin{Bmatrix} 0 \\ 0 \\ \mathbf{G}_{\Gamma_{\bar{R}}} f(\mathbf{x}) \end{Bmatrix} \quad (45)$$

Note that if eq. (42) represents nodal values of \mathbf{u} and $\partial_n \mathbf{u}$ then the matrices $\mathbf{M}_U, \mathbf{M}_{\partial_n U}$ are unit matrices while the matrices \mathbf{M}_D and $\mathbf{M}_{\partial_n D}$ are unit matrices multiplied by the constants e^{ikR}/\sqrt{kR} and $(ik - 1/2R)e^{ikR}/\sqrt{kR}$, respectively.

3.4 Numerical results

To demonstrate the half-plane problem, we have chosen the radius of the numerical domain to be $R = 2\lambda$, the wave number as $k = \pi$, the impedance as $\beta = 1$ and the source is described by a Gaussian $f(\mathbf{x}) = \exp(-\frac{1}{2}\gamma x^2)$ where $\gamma = 10$. The problem was solved using the uniform and non-uniform representations and the results were compared to the analytical solution given in the appendix. Figure 3 depicts the results obtained for the values of the field \mathbf{u} along the surface of the half-plane. In this figure and in the following figures the dashed and full lines denote the imaginary and real part of the field, respectively, unless specified otherwise. It can be seen that both representations yield excellent agreement with the analytical results. However, if we examine the error obtained by the two representations as shown in Figure 4, we will see that the uniform representation generally gives better results.

In order to further investigate the error, we present in Figure 5 the error in the surface wave amplitudes as a function of the impedance. As expected, the results of the uniform representation gives much better results over a much wider range of impedance values.

We next investigate the error in the directivity. Figures 6a,b describe the amplitude of the directivity for impedance values of $\beta = 1, 0.1$ using both representations. It can be seen that for the value of $\beta = 1$, both representations yield very accurate results. For the value of $\beta = 0.1$, however, only the uniform representation gives acceptable results. We note here that though the directivity result from the non-uniform representation looks bad, the results of the field u matches the analytical results very well. This indicates that a “non-reflecting” boundary condition which gives good results for the interior field does not necessarily represent the problem correctly (i.e. diffraction coefficients can be wrong). We will extend the discussion of the error after introducing a multi-domain problem in the next section.

3.5 Multiple diffraction points: Domain coupling

We now consider problems with multiple diffraction points. For this discussion we consider the case in which each diffraction point is associated with three diffraction coefficients: two surface waves and a directivity. The field u can be written as the contribution from all diffraction points:

$$u^A = \sum_{n=1}^N \left\{ D_n(\theta_n) \frac{e^{ikr_n}}{\sqrt{kr_n}} + A_{sw_L}^n F_{sw_L}^n(\theta_n, r_n) + A_{sw_R}^n F_{sw_R}^n(\theta_n, r_n) \right\} \quad (46)$$

Here N is the total number of the essential diffraction points. Along each artificial boundary Γ_{R_n} we have to find the normal derivative of the field $\partial_n u$. Assuming that this boundary is defined by an arc with a radius R_n we can write (with implied summation over n):

$$\partial_n u^A |_{\Gamma_{R_j}} = \frac{\partial u}{\partial r_j} = \frac{\partial r_n}{\partial r_j} \frac{\partial u}{\partial r_n} + \frac{\partial \theta_n}{\partial r_j} \frac{\partial u}{\partial \theta_n}. \quad (47)$$

Thus,

$$\begin{aligned} \partial_n u^A |_{\Gamma_{R_j}} = \sum_{n=1}^N & \left\{ \left[\frac{\partial r_n}{\partial r_j} \left(ik - \frac{1}{2r_n} \right) D_n(\theta_n) + \frac{\partial \theta_n}{\partial r_j} D'_n(\theta_n) \right] \frac{e^{ikr_n}}{\sqrt{kr_n}} + \right. \\ & A_{sw_L}^n \left[\frac{\partial r_n}{\partial r_j} \frac{\partial F_{sw_L}^n(\theta_n, r_n)}{\partial r_n} + \frac{\partial \theta_n}{\partial r_j} \frac{\partial F_{sw_L}^n(\theta_n, r_n)}{\partial \theta_n} \right] + \\ & \left. A_{sw_R}^n \left[\frac{\partial r_n}{\partial r_j} \frac{\partial F_{sw_R}^n(\theta_n, r_n)}{\partial r_n} + \frac{\partial \theta_n}{\partial r_j} \frac{\partial F_{sw_R}^n(\theta_n, r_n)}{\partial \theta_n} \right] \right\}. \end{aligned} \quad (48)$$

The global set of equations would be composed from several sets of equations like eq. (45). Note that in the case of multi-domains the matrices M_D and $M_{\partial_n D}$ would not be just a unit matrix multiplied by a constant (as in the case of single domain) but they would include coupling terms as in eqs. (46,48) respectively.

3.6 Numerical results

We will demonstrate the multi-domain problem using an extension of the example given in section 3.4 for a single domain. Here we consider a second diffraction point a distance d from the first, as shown in Figure 7. This diffraction point might be due, say, to a sudden change in the impedance from one value to another. In order to highlight any error associate with coupling two numerical domains together, we choose the second diffraction point so that it has identically zero diffraction coefficients; i.e. we consider *zero* step in the impedance. In this case we expect the surface wave excited by the source to pass through the second computational domain, and result in zero diffraction from the second domain. We chose all the data to be the same as in the first example and the distance between the domains was set to $d = 100\lambda$. The result for the field u in the first domain looks very much like the single domain case which was shown in Figure 3 and therefore we choose not to present it again. The result of the field on the second domain is presented in Figure 8.

Figure 9 depicts the amplitude of the directivity of the second domain. It can be seen that the directivity is almost zero (about 0.1% of the maximal value of the directivity of the first domain). Figure 10 presents the error in the directivity in the second domain as a function of the distance between the domains. It can be seen very clearly that this error behaves like one over the distance, which agrees with our approximation order. However, if we will plot the error in the amplitude of the surface waves as function of the distance (Figure 11) we see that the error is not a function of the separation distance d .

4 Creeping waves

The second class of problems that we consider here is those that contain creeping waves. We will demonstrate the method through an investigation of a source on a cylinder. Figure 12 illustrates the problem. The coordinate system of the cylinder will be (r_c, θ_c) and its radius is R_c ; the coordinate system (r, θ) shall remain centered in the numerical domain. The governing equations are:

$$\Delta u + k^2 u = 0 \quad \text{in } \Omega \quad (49)$$

$$\partial_n u + k\beta u = f(\theta_c) \quad \text{on } r_c = R_c \quad (50)$$

$$u = \text{outgoing}. \quad (51)$$

Here the source function $f(\theta_c)$ is assumed to have support which is smaller than a wavelength.

In the next sections we will develop the non-uniform representation for the creeping waves problem. A *convenient*, fully uniform representation is at present unknown to the authors. We note, however, that the fully uniform representations can be found in the literature [12, 13, 14].

4.1 Global solution: Non-Uniform representation

The eiconal equation (6) for $r_c > R_c$ yields:

$$\psi_1 = r_c. \quad (52)$$

Equation (49) and the homogeneous form of the boundary condition (50) also admit non trivial solutions of the form:

$$u = A_\nu H_{k\nu}^{(1)}(kr_c) e^{ik\nu|\theta_c|} \quad (53)$$

Here ν satisfies the homogeneous form of (50):

$$\frac{\partial}{\partial r_c} [H_{k\nu}^{(1)}(kR_c)] + k\beta H_{k\nu}^{(1)}(kR_c) = 0 \quad (54)$$

Thus we find the asymptotic global solution:

$$u^A = u^{NU} = \begin{cases} (kR)^{-1/2} D(\theta) \sqrt{\frac{R}{r}} e^{ikr} & \theta_{co} < \theta < \pi - \theta_{co} \\ A_{cwL} F_{cwL}^{NU}(\theta, r) & \theta > \pi - \theta_{co} \\ A_{cwR} F_{cwR}^{NU}(\theta, r) & \theta < \theta_{co} \end{cases} \quad kR \rightarrow \infty; ; r \neq 0 \quad \theta \neq \pi/2. \quad (55)$$

Here θ_{co} is the cut-off angle shown in Figure 13. A_{cwL} and A_{cwR} are the creeping wave amplitudes and related functions are given by:

$$F_{cwL}^{NU} = H_{k\nu}^{(1)}(kr_c) e^{-ik\nu\theta_c} \quad (56)$$

$$F_{cwR}^{NU} = H_{k\nu}^{(1)}(kr_c) e^{ik\nu\theta_c} \quad (57)$$

Unlike the surface wave formulation where the cylindrical wave and the surface waves could both contribute to the field at one point (in both uniform or non-uniform formulations), the creeping waves and the cylindrical waves do not appear together in the non-uniform representation. The cylindrical wave will appear only in the region above the cut-off line (the horizontal line tangent to the point where the source is applied as shown in Figure 13). Below the cut off line on each side of it, a creeping wave exists starting at the cutoff line.

4.2 Local solution

The formulation of the local problem is nearly identical to that of the surface wave problem, eqs. (38-41). The set of equations that we form in the case of the creeping waves consists of the following: Along the whole computational boundary the BIE holds (eq. (42)). On the boundary $\Gamma_{\bar{R}}$ we will use a hard boundary condition:

$$\partial_n u = f(\theta_c) \quad \text{on } \Gamma_{\bar{R}} \quad (58)$$

The artificial boundary Γ_R is divided into three parts: the part above the cutoff line (denoted by Γ_{R_2}) and the two segments below the cutoff line (denoted by Γ_{R_1} and Γ_{R_3} for the left and right segments, respectively). From eqs. (40,41,55) we set the boundary condition on Γ_R to be the following:

$$\left. \begin{array}{l} u = D(\theta) \frac{e^{ikr}}{\sqrt{kr}} \\ \partial_n u = (ik - \frac{1}{2R}) D(\theta) \frac{e^{ikr}}{\sqrt{kr}} \end{array} \right\} \text{ on } \Gamma_{R_2} \quad (59)$$

$$\left. \begin{array}{l} u = A_{cw_L} F_{cw_L}^{NU}(\theta, R) \\ \partial_n u = A_{cw_L} \partial_n F_{cw_L}^{NU}(\theta, R) \end{array} \right\} \text{ on } \Gamma_{R_1} \quad (60)$$

$$\left. \begin{array}{l} u = A_{cw_R} F_{cw_R}^{NU}(\theta, R) \\ \partial_n u = A_{cw_R} \partial_n F_{cw_R}^{NU}(\theta, R) \end{array} \right\} \text{ on } \Gamma_{R_3}. \quad (61)$$

On the boundary Γ_{R_2} we use the same set of equations as in the surface wave case. On the boundaries Γ_{R_1} (and Γ_{R_3}) we have to fit the functions $F_{cw_L}^{NU}$ (or $F_{cw_R}^{NU}$) and their normal derivatives $\partial_n F_{cw_L}^{NU}$ (or $\partial_n F_{cw_R}^{NU}$) to the nodal values of u or $\partial_n u$. Since the field on Γ_{R_1} (or Γ_{R_3}) is described simply in terms of a single creeping wave solution, we have some flexibility in the way we enforce the continuity conditions (60) (or 61). We shall choose to enforce continuity of $\partial_n u$ at each of the collocation points on Γ_{R_1} (or Γ_{R_3}). That leaves us with just one equation to enforce continuity on u . This we enforce in a least squares sense. Thus, we are led to the following matrix equation:

$$\left[\begin{array}{cccc} -M_D & M_U & 0 & 0 \\ -M_{\partial_n D} & 0 & M_{\partial_n U} & 0 \\ 0 & H_{\Gamma_R} & -G_{\Gamma_R} & H_{\Gamma_{\bar{R}}} \end{array} \right] \times \left\{ \begin{array}{l} \{D \ A_{cw_R} \ A_{cw_L}\} \{u_{\Gamma_{R_1}} \ u_{\Gamma_{R_2}} \ u_{\Gamma_{R_3}}\} \{\partial_n u_{\Gamma_{R_1}} \ \partial_n u_{\Gamma_{R_2}} \ \partial_n u_{\Gamma_{R_3}}\} \{u_{\Gamma_{\bar{R}}}\} \end{array} \right\}^T = \left\{ \begin{array}{l} 0 \\ 0 \\ G_{\Gamma_{\bar{R}}} f(x) \end{array} \right\}. \quad (62)$$

Here

$$M_D = \left[\begin{array}{ccc} 0 & F_{cw_R}^T \cdot F_{cw_R} & 0 \\ M_{D_2} & 0 & 0 \\ 0 & 0 & F_{cw_L}^T \cdot F_{cw_L} \end{array} \right]; \quad M_U = \left[\begin{array}{ccc} F_{cw_R}^T M_{U_1} & 0 & 0 \\ 0 & M_{U_2} & 0 \\ 0 & 0 & F_{cw_L}^T M_{U_3} \end{array} \right] \quad (63)$$

$$M_{\partial_n D} = \left[\begin{array}{ccc} 0 & \partial_n F_{cw_R} & 0 \\ M_{\partial_n D_2} & 0 & 0 \\ 0 & 0 & \partial_n F_{cw_L} \end{array} \right]; \quad M_{\partial_n U} = \left[\begin{array}{ccc} M_{\partial_n U_1} & 0 & 0 \\ 0 & M_{\partial_n U_2} & 0 \\ 0 & 0 & M_{\partial_n U_3} \end{array} \right] \quad (64)$$

In the last set of equations we have used least squares on the functions F_{cw_L} and F_{cw_R} . It is also possible to use least squares on the normal derivatives. In this case the matrices would be:

$$\mathbf{M}_D = \begin{bmatrix} 0 & \mathbf{F}_{cw_R} & 0 \\ \mathbf{M}_{D_2} & 0 & 0 \\ 0 & 0 & \mathbf{F}_{cw_L} \end{bmatrix}; \quad \mathbf{M}_U = \begin{bmatrix} \mathbf{M}_{U_1} & 0 & 0 \\ 0 & \mathbf{M}_{U_2} & 0 \\ 0 & 0 & \mathbf{M}_{U_3} \end{bmatrix} \quad (65)$$

$$\mathbf{M}_{\partial_n D} = \begin{bmatrix} 0 & \partial_n \mathbf{F}_{cw_R}^T \cdot \partial_n \mathbf{F}_{cw_R} & 0 \\ \mathbf{M}_{\partial_n D_2} & 0 & 0 \\ 0 & 0 & \partial_n \mathbf{F}_{cw_L}^T \cdot \partial_n \mathbf{F}_{cw_L} \end{bmatrix}$$

$$\mathbf{M}_{\partial_n U} = \begin{bmatrix} \partial_n \mathbf{F}_{cw_R}^T \cdot \mathbf{M}_{\partial_n U_1} & 0 & 0 \\ 0 & \mathbf{M}_{\partial_n U_2} & 0 \\ 0 & 0 & \partial_n \mathbf{F}_{cw_L}^T \cdot \mathbf{M}_{\partial_n U_3} \end{bmatrix} \quad (66)$$

4.3 Numerical results

The first example is of a cylinder of a radius $R_c = \sqrt{29}\lambda \approx 5.39\lambda$ with a hard boundary condition. The radius of the numerical domain is $R = 2\lambda$ and the source is a Gaussian $f(\theta_c) = \exp(-\frac{1}{2}\gamma R_c^2 \cos^2 \theta_c)$ where $\gamma = 5$ and the wave number is $k = \pi$.

Figure 14a shows the result along the cylinder surface within the numerical domain. Since we find the amplitude of the creeping waves, we can also evaluate the field outside of the numerical domain along the cylinder surface, as shown in Figure 14b. We see that for both cases the analytical and numerical results agree well. We also see very good correlation between the numerical and the analytical results in the directivity, as shown in Figure 15.

We will not show here the derivation of multi-region coupling since it is very similar to the surface wave case. We will present however, an additional example related to coupling between domains. This problem involves an external creeping wave which propagates along the cylinder as shown in Figure 16. The results for the field u and for the directivity are presented in Figure 17a and 17b, respectively. Again a very good agreement is obtained in the u values while the directivity is almost zero (as we expected, since the wave should “pass” through the domain).

5 A Concluding Example

So far we have presented some simple examples with analytical solution in order to verify our method. We would like to conclude with a more complex problem which will demonstrate the potential of the method. Figure 18 defines that problem. We will consider a source over a 2D cylinder with circular ends. The length between the arcs centers is 40 wavelengths and the radius

of the arcs is 10 wavelengths. On the straight lines we use an impedance boundary condition with $\beta = 1$, while on the arcs we apply a hard surface boundary condition. On the intersections between the straight lines and the arcs we have a geometrical discontinuity and a boundary condition discontinuity. Therefore we expect to see diffraction from these points.

We solve this problem by defining four numerical domains around each diffraction point. The results for the directivity of each corner are presented in Figure 19.

6 Domain Decomposition

Because of the fact that there is no coupling between the cylindrical wave and the creeping waves in the non-uniform representation, we can use a very efficient domain decomposition technique to solve complex problems such as that defined in the last section.

We will decompose the problem in places where we have creeping waves. Figure 20 describes how we decompose the last problem. Along the arcs only creeping waves exist. We will solve the top problem first assuming that there is no influence from the bottom problem. Then after solving the amplitude of the creeping waves we would apply them as external waves (as we did before; see Figure 16) to the bottom problem. Thus we get new amplitudes for the creeping waves which we use as external input for the top problem. We repeat these procedure until convergence is achieved. Figure 21 shows the convergence obtained by this procedure. It can be seen that the convergence rate is exponential and that we achieve machine precision after only four iterations.

7 Remarks and Conclusions

In this work we have extended the applicability of the hybrid method to surface and creeping wave problems. We have presented a non-uniform and a uniform representation for surface wave problems and gave the non-uniform representation for creeping waves problems. We investigated the method through some simple test case problems and presented the behavior of the error for different impedance values. We have also presented a more complicated problem that might shed more light on the class of problems for which this method is suitable.

8 Appendix: a Gaussian source over an impedance surface

In this appendix we briefly present the solution for a Gaussian source over an impedance surface.

We wish to solve eqs. (15-17) with $f(x) = e^{-\frac{1}{2}\gamma x^2 - i\omega t}$ where γ is an arbitrary constant. Using

a Fourier transform in the x -direction leads us to the solution:

$$u(x, y) = \frac{1}{\sqrt{2\pi\gamma}} \int_{-\infty}^{\infty} \frac{e^{-\frac{1}{2}\frac{s^2}{\gamma} + i[sx + \sqrt{k^2 - s^2}y]}}{i\sqrt{k^2 - s^2} + k\beta} ds \quad (67)$$

The integrand has two poles at $s_0 = \pm k\sqrt{1 + \beta^2}$ which corresponds to the two surface waves. The contour in (67) is indented below any singularities on the right of the real axis, and above any singularities to the left. By the residue theorem, we find that the surface wave contribution is:

$$u_{sw}(x, y) = \frac{2\pi i}{\sqrt{1 + 1/\beta^2}} e^{[-\frac{1}{2}k^2(1+\beta^2)/\gamma - k\beta y] + ik\sqrt{1+\beta^2}|x|} \quad (68)$$

The far field can be evaluated using stationary phase:

$$u_d(r, \theta) = \frac{\sin \theta}{\sqrt{ikr\gamma}} \frac{1}{(i \sin \theta + \beta)} e^{-\frac{1}{2}k^2 \cos^2 \theta / \gamma + ikr} \quad r \rightarrow \infty, \quad \theta \neq 0, \pi \quad (69)$$

An alternative way to evaluate the integral (67) is numerically by using FFT. When doing so, however, one should first subtract the pole singularities and only then perform the FFT.

References

- [1] Paul E. Barbone. Approximate diffraction coefficients by the method of matched asymptotic expansions. *Wave Motion*, 22:1–16, 1995.
- [2] Paul E. Barbone and Ofer Michael. Scattering from submerged objects by a hybrid asymptotic-boundary integral equation method. *Wave Motion*, accepted, 1998.
- [3] Paul E. Barbone, Joshua M. Montgomery, Isaac Harari, and Ofer Michael. Scattering by a hybrid asymptotic/finite element method. *Comput. Methods in Appl. Mech. and Engrg.*, in press, 1998.
- [4] W.D. Burnside, C.L. Yu, and R.J. Marhefka. A technique to combine the geometrical theory of diffraction and the moment method. *IEEE Trans. Ant. and Prop.*, AP-23:551–558, 1975.
- [5] M. Calamia, R. Cocciali, G. Pelosi, and G. Manara. A hybrid FEM/UTD analysis of the scattering from a cavity-backed aperture in a face of a perfectly conducting wedge. *COMPEL, Int. J. Comput. Math. Electr. Eng.*, 13(A):229–235, 1994.
- [6] A.D. Greenwood, S.S. Ni, J.M. Jin, and S.W. Lee. Hybrid fem/sbr method to compute the radiation pattern from a microstrip patch antenna in a complex geometry. *Proceedings of the 1996 Antenna Applications Symposium*, vi:1–6, 1996.
- [7] Isaac Harari, Paul E. Barbone, and Joshua M. Montgomery. Finite element formulations for exterior problems: Application to hybrid methods, non-reflecting boundary conditions, and infinite elements. *Int. J. of Num. Meth. in Eng.*, 40:2791–2805, 1997.
- [8] J.M. Jin, S. Ni, and S.W. Lee. Robust hybrid technique for calculating scattering by large and complex targets. *Electronics Letters*, 30(25):2169–70, 1994.
- [9] D. S. Jones. *Acoustic and Electromagnetic Waves*. Oxford University Press, New York, 1986. Advanced text on wave propagation and problem solving.
- [10] Joseph B. Keller. Geometrical theory of diffraction. *J. Opt. Soc. America*, 52(2):160–130, 1962.
- [11] T.J. Kim and G.N. Thiele. A hybrid diffraction technique – general theory and applications. *IEEE Trans. Ant. and Prop.*, AP-30(5):888–897, 1982.
- [12] Robert M. Lewis, Norman Bleistein, and Donald Ludwig. Uniform asymptotic theory of creeping waves. *Comm. Pure and Appl. Math*, 20:295–328, 1967.
- [13] Donald Ludwig. Uniform asymptotic expansion of the field scattered by a convex object at high frequencies. *Comm. Pure and Appl. Math*, 20:103–138, 1967.

- [14] Donald Ludwig. Boundary layers in the field scattered by a convex object at high frequencies. *Comm. Pure and Appl. Math.*, 22:715–736, 1969.
- [15] L.N. Medgyesi-Mitschang and D.S. Wang. Hybrid methods for analysis of complex scatterers. *Proceedings of the IEEE*, 77(5):770–779, 1989.
- [16] O. Michael, J. Avrashi, and G. Rosenhouse. The boundary strip method in elastostatics and potential equations. *Int. J. for Num. Methods in Engng.*, 39:527–544, 1996.
- [17] Joshua M. Montgomery and Paul E. Barbone. Diffraction from simple shapes by a hybrid asymptotic-finite element method. *J. Acoust. Soc. Am.*, accepted, 1998.
- [18] G. Pelosi, A. Freni, and R. Coccioni. Hybrid technique for analysing scattering from periodic structures. *IEE Proceedings H*, 140(2):65–70, 1993.
- [19] B. Roturier, B. Souny, and H. Baudrand. Calculation of diffracted fields by hybrid finite-element/geometrical-theory-of-diffraction method. *JINA 94. Journees Internationales de Nice sur les Antennes Conferences (Proceedings of the International Symposium on Antennas)*, ix:237–40, 1994.
- [20] J.N. Sahalos and G.N. Thiele. On the application of the GTD-MM technique and its limitations. *IEEE Trans. Ant. and Prop.*, AP-29(5):780–786, 1981.
- [21] X.Q. Sheng and J.M. Jin. A hybrid FEM/SBR method to compute scattering by large bodies with small protruding scatterers. *Microwave and Optical Technology Letters*, 15(2):78–84, 1997.
- [22] D.S. Wang. Current-based hybrid analysis for surface-wave effects on large scatterers. *IEEE Trans. Ant. and Prop.*, 39(6):839–850, 1991.

Figure captions

Fig. 1 The hybrid method: The numerical domains are shown shaded.

Fig. 2 Surface wave on an infinite plane with an impedance boundary condition.

Fig. 3 Surface wave, one diffraction point: Results of the field u .

Fig. 4 Surface wave, one diffraction point: Error in the field results.

Fig. 5 Surface wave, one diffraction point: Error in the surface wave amplitudes.

Fig. 6 Surface wave, one diffraction point: Directivity results. (a) $\beta = 1$. (b) $\beta = 0.1$.

Fig. 7 Surface wave, two diffraction points: Problem definition.

Fig. 8 Surface wave, two diffraction points: Results of the field u on the second domain.

Fig. 9 Surface wave, two diffraction points: Results of the directivity of the second domain.

Fig. 10 Surface wave, two diffraction points: Error in the directivity of the second domain.

Fig. 11 Surface wave, two diffraction points: Error in the surface wave amplitudes.

Fig. 12 Creeping wave: A source over a cylinder.

Fig. 13 Creeping wave: Coordinate systems and cut-off line.

Fig. 14 Creeping wave: Results of the field u :

- (a) Results within the numerical domain ($r_c = R_c$; $\theta_{co} \leq \theta \leq 2\pi - \theta_{co}$).
- (b) Results outside the numerical domain ($r_c = R_c$; $\theta \leq \theta_{co}$).

Fig. 15 Creeping wave: Directivity results.

Fig. 16 Creeping wave, wave traveling through a domain: Problem definition.

Fig. 17 Creeping wave, wave traveling through a domain:

- (a) Field results.
- (b) Directivity results.

Fig. 18 A 2D cylinder with circular ends: Problem definition.

Fig. 19 A 2D cylinder with circular ends: Directivity results.

Fig. 20 Domain decomposition.

Fig. 21 Domain decomposition: convergence results.

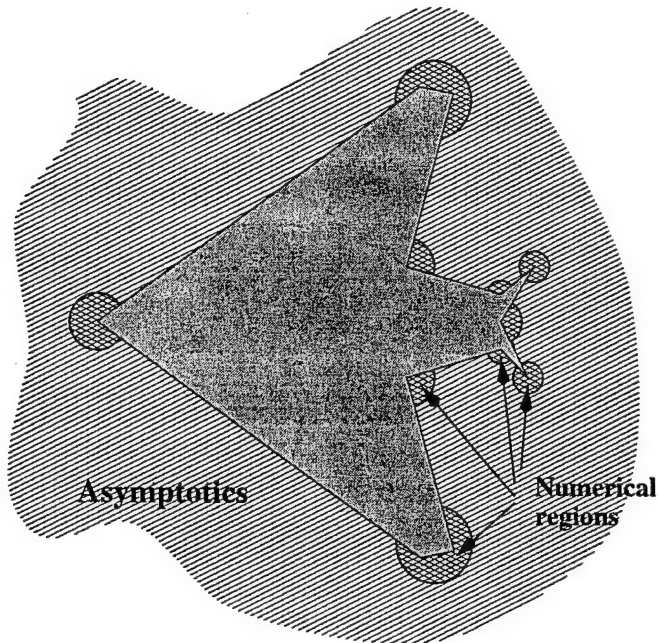


figure 1

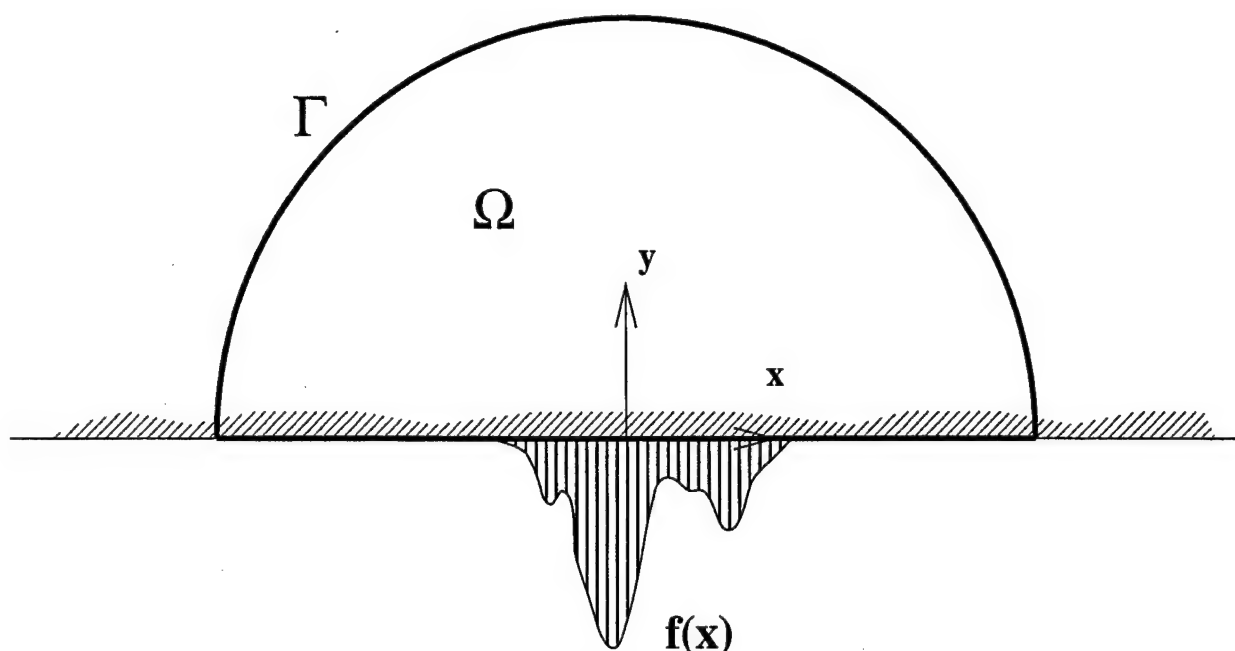


figure 2

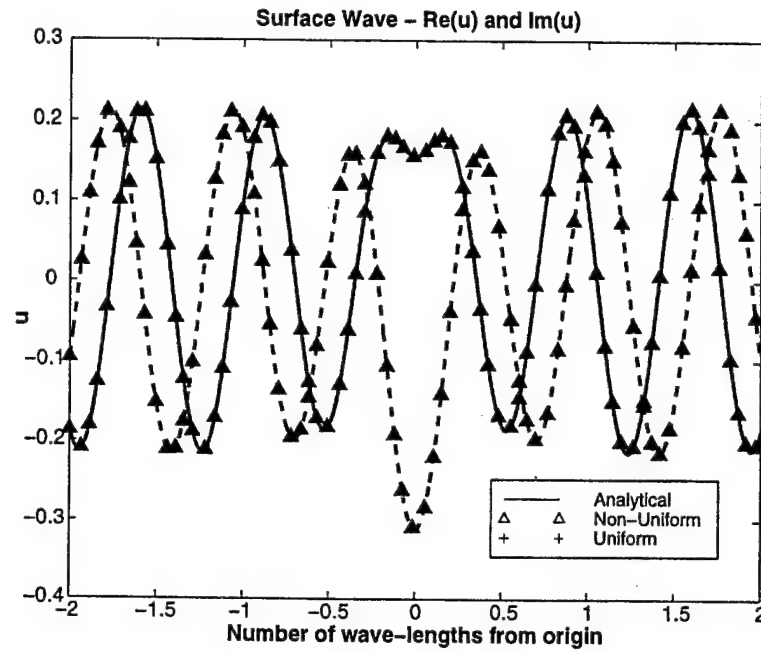


figure 3

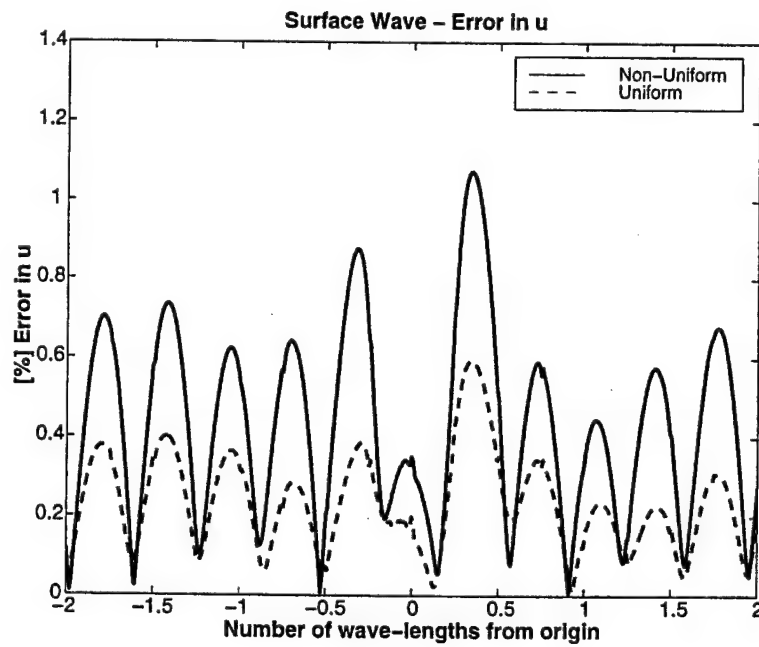


figure 4

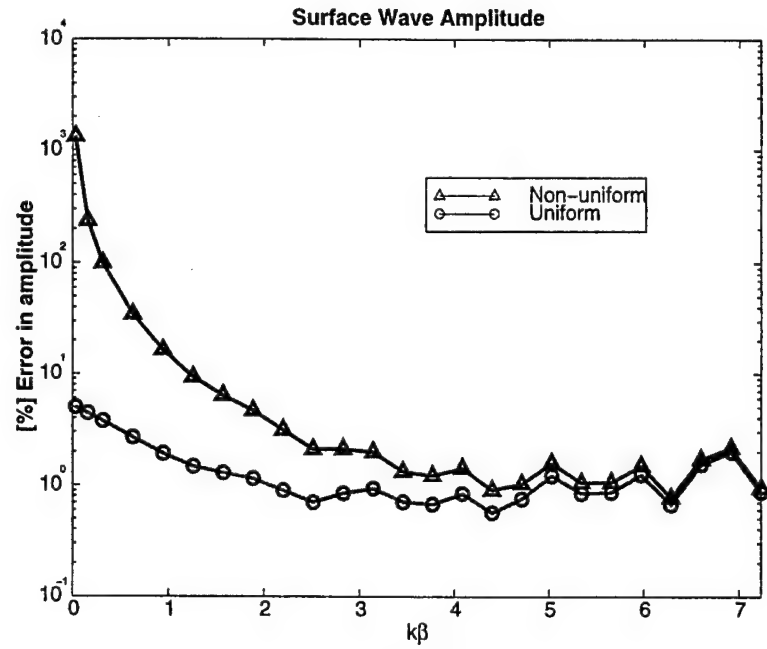


figure 5

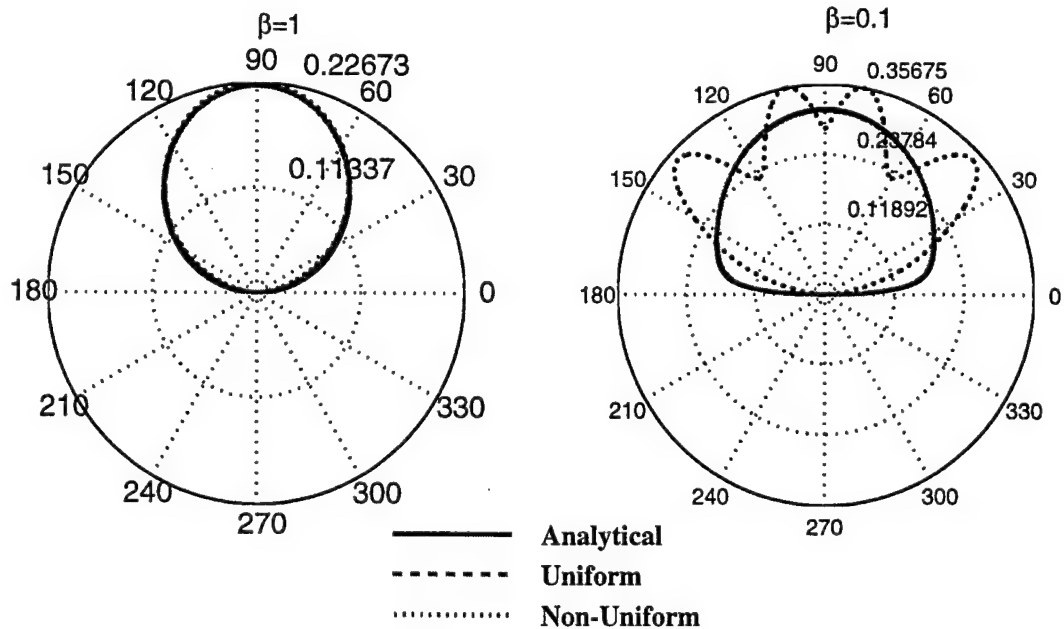
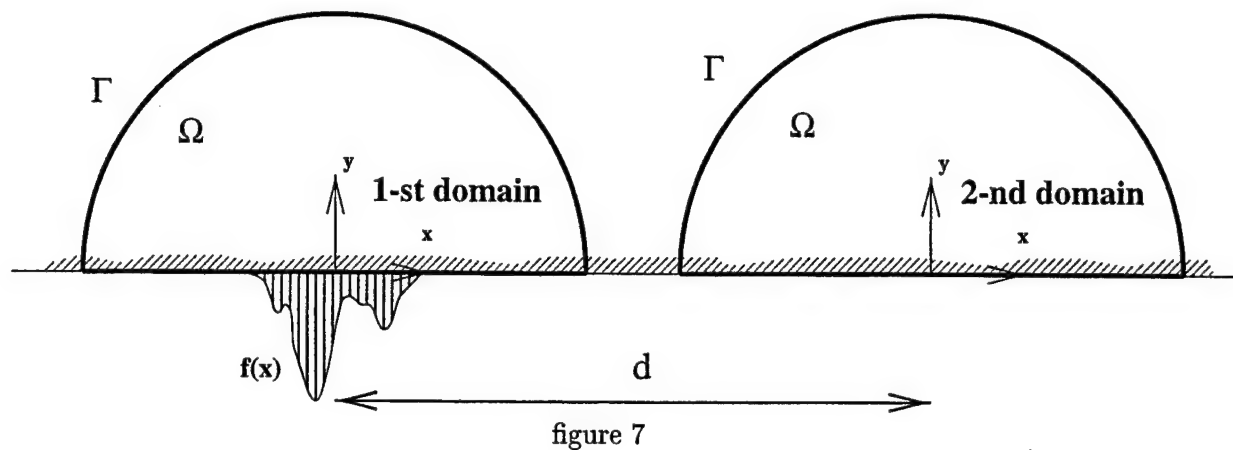


figure 6



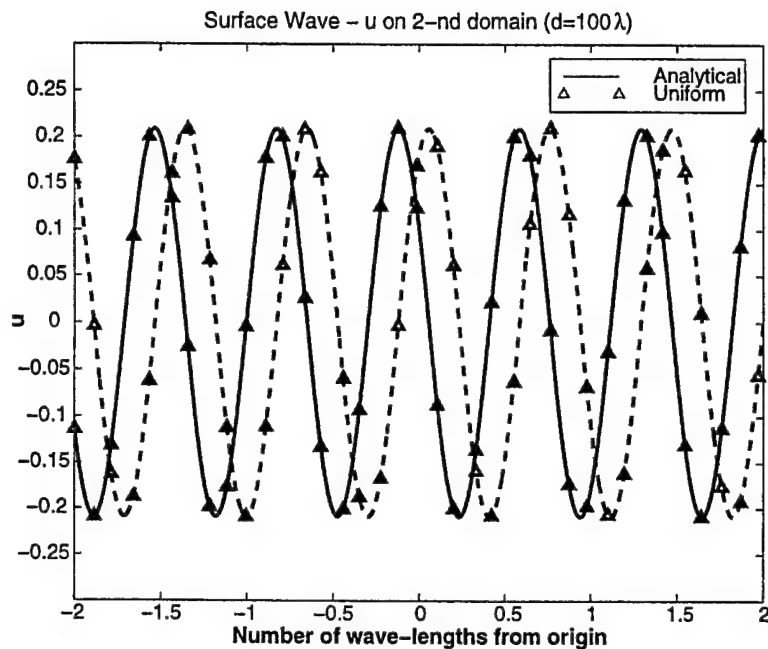


figure 8

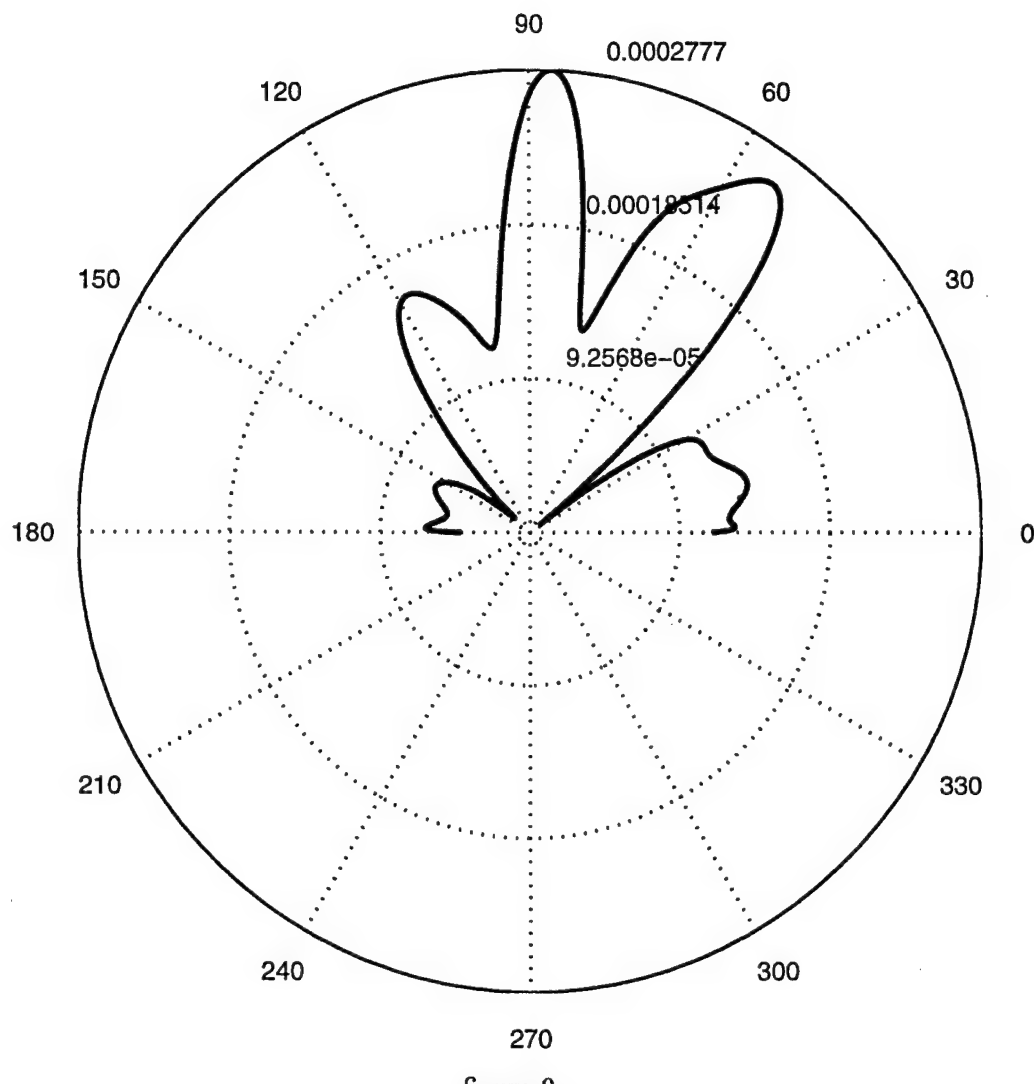


figure 9

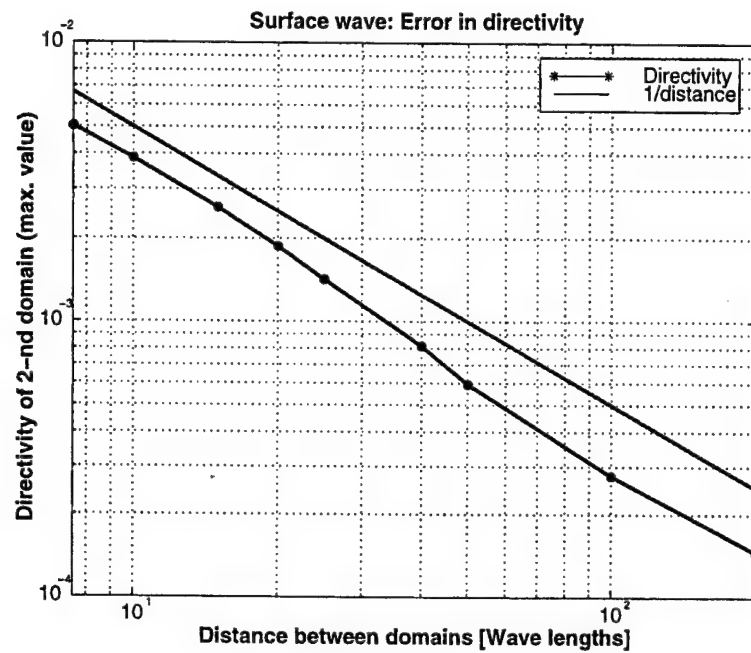


figure 10

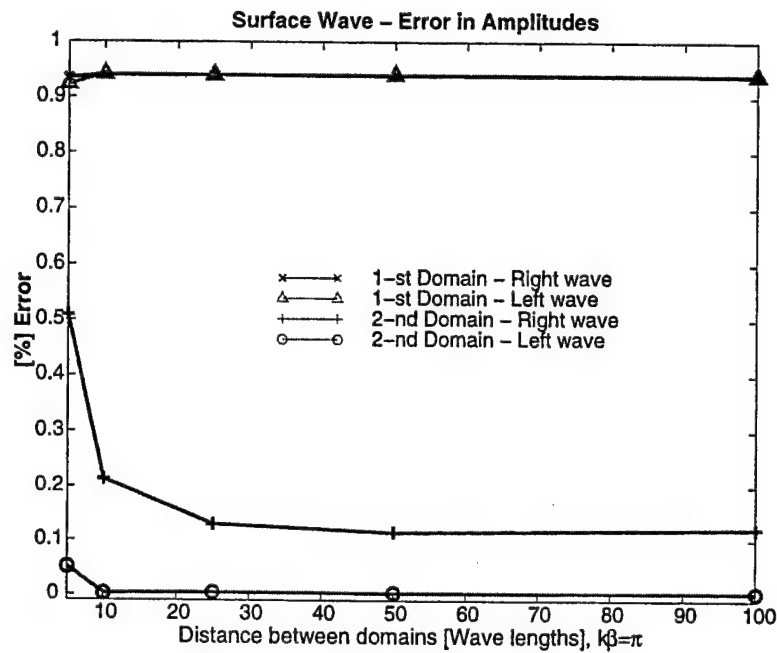


figure 11

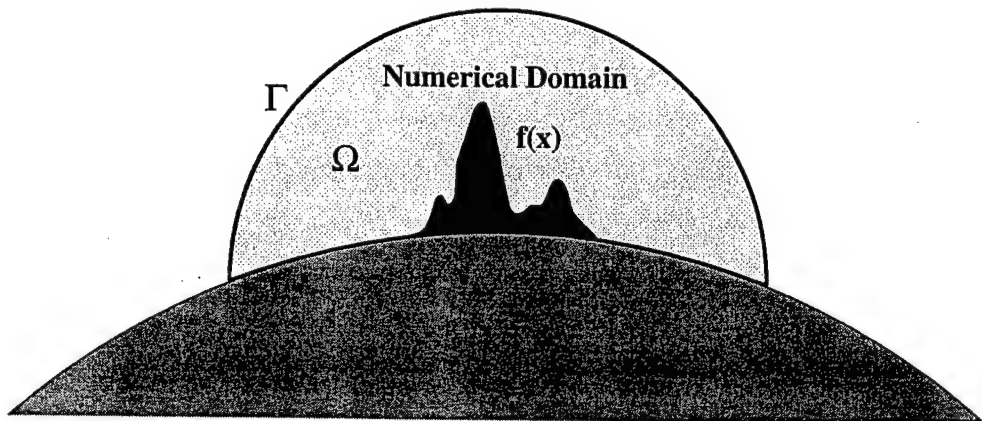


figure 12

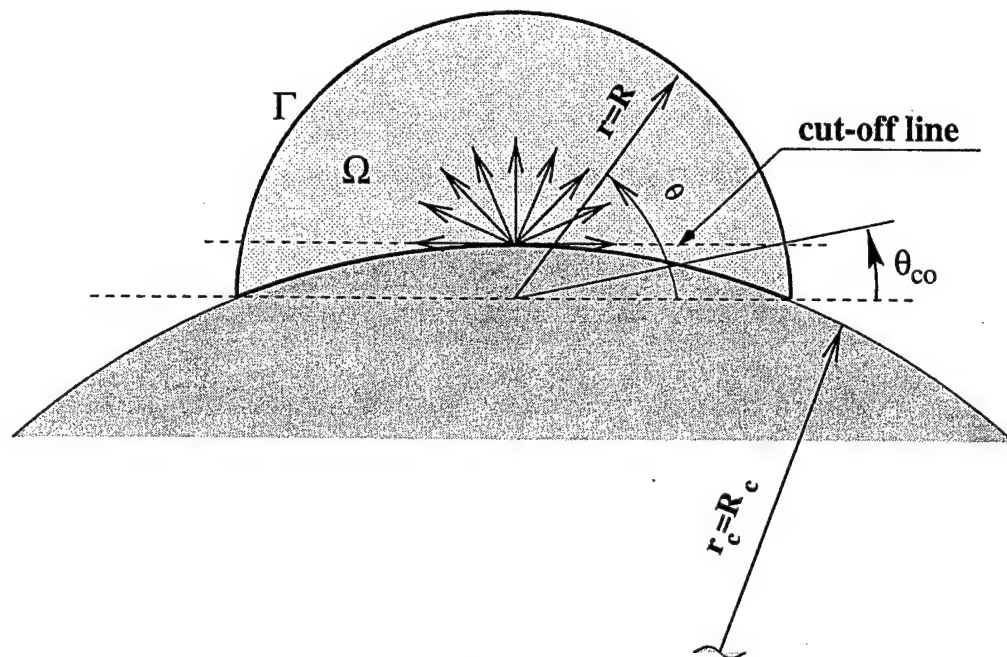


figure 13

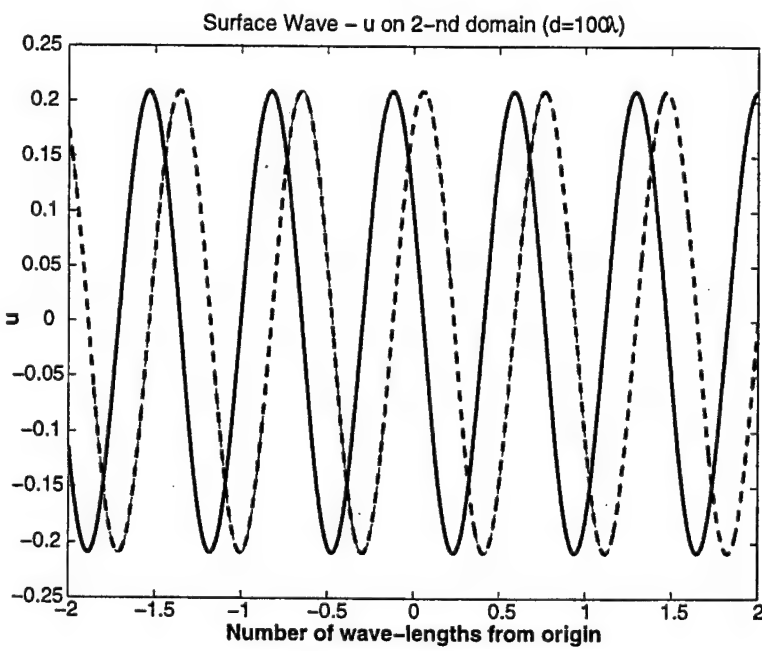


figure 14

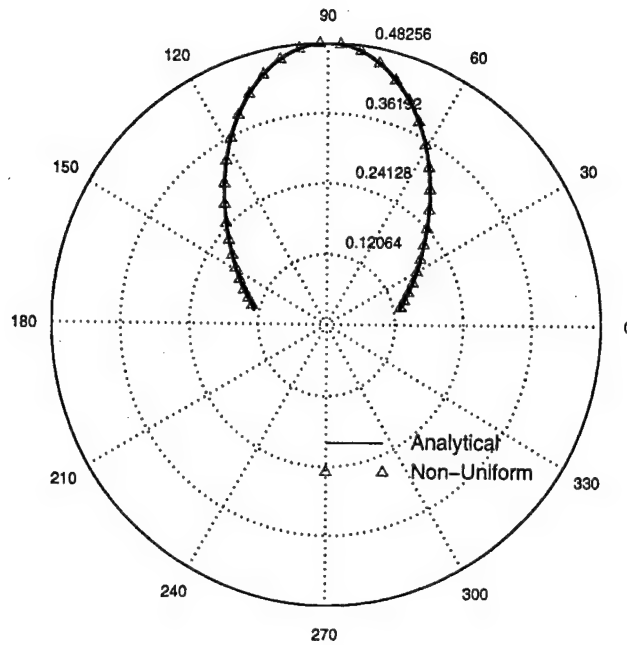


figure 15

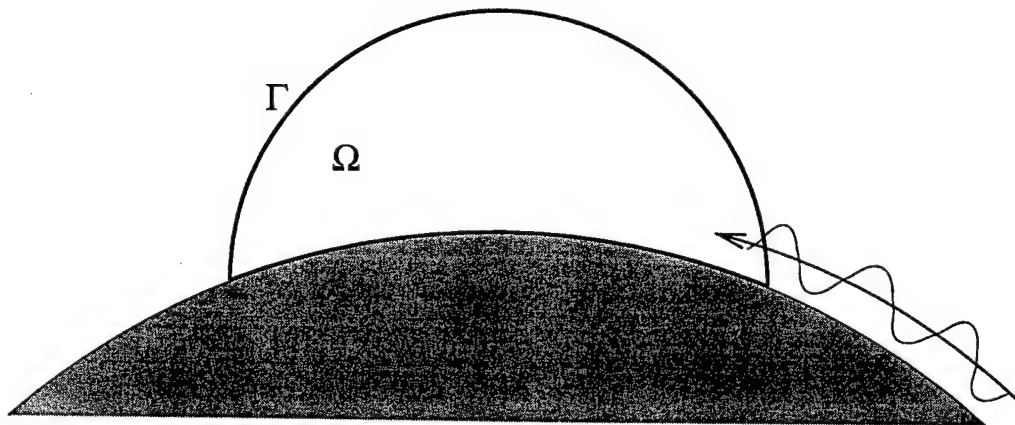


figure 16

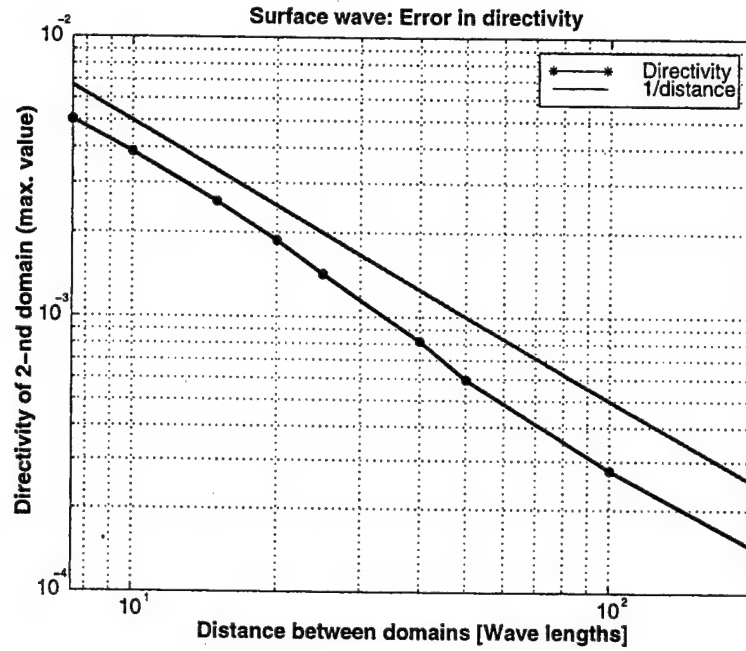


figure 17

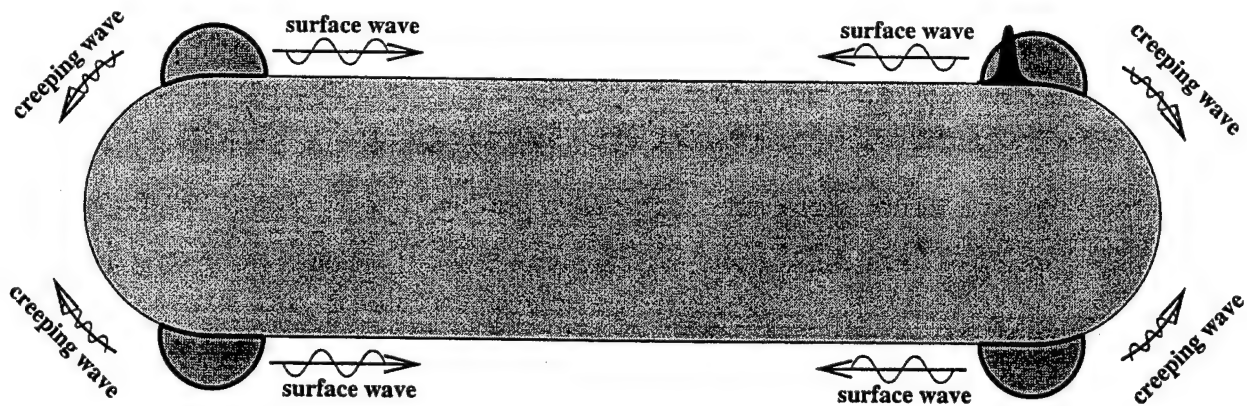


figure 18

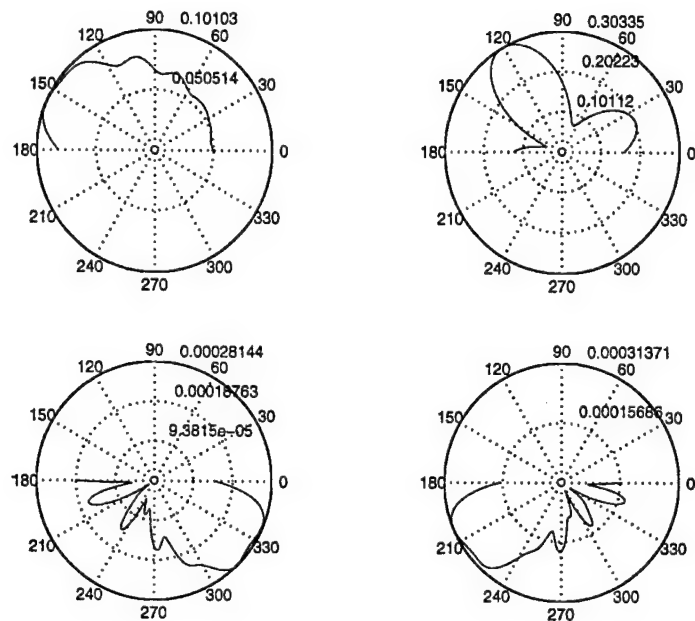
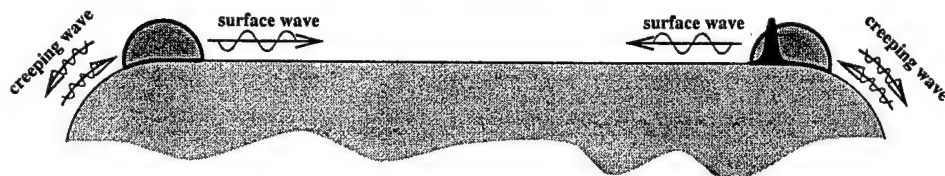


figure 19



Domain Decomposition

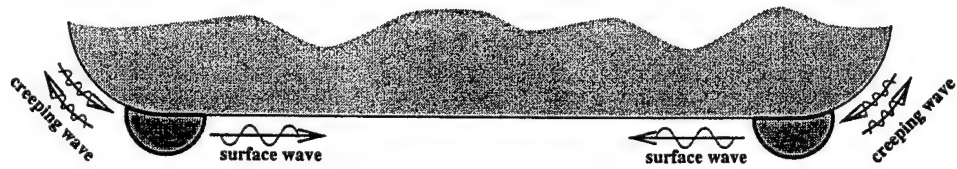


figure 20

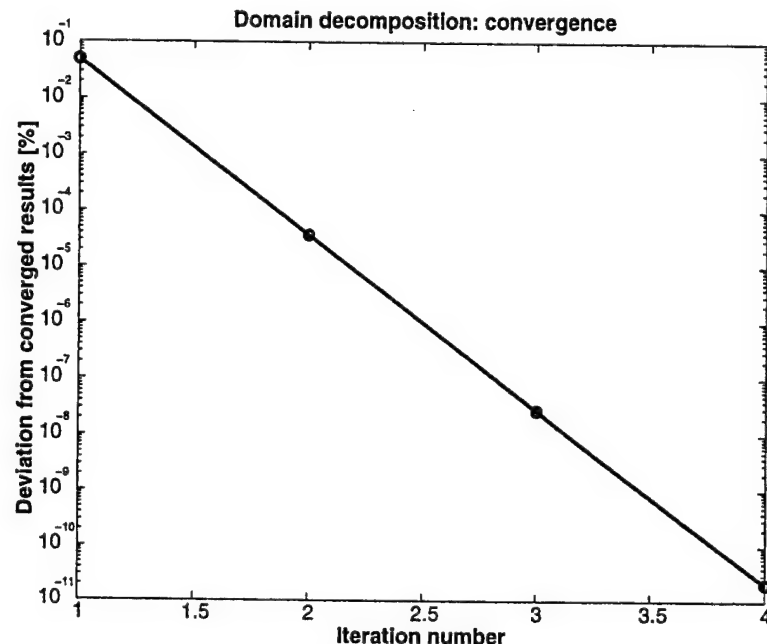


figure 21

C.2 Scattering from submerged objects by a hybrid asymptotic-boundary integral equation method

"Scattering from submerged objects by a hybrid asymptotic-boundary integral equation method,"
Paul E. Barbone and Ofer Michael, **Wave Motion**, Vol. 29, pp. 137–156, 1999.



ELSEVIER

Wave Motion 29 (1999) 137–156

WAVE
MOTION

Scattering from submerged objects by a hybrid asymptotic-boundary integral equation method

Paul E. Barbone *, Ofer Michael

Department of Aerospace and Mechanical Engineering, Boston University, Boston, MA 02215, USA

Received 14 November 1997; received in revised form 3 June 1998; accepted 9 June 1998

Abstract

We describe a method to compute the field scattered or radiated by acoustically large objects. The method combines the a high frequency asymptotic approximation with a boundary integral equation (BIE) method. The method is based on patching a short wavelength “outer expansion” to a BIE representation of the “inner solutions”. The inner solutions describe the field in the vicinity of sharp changes in geometry or boundary condition. We describe the formulation and solution of the inner problems using a boundary spectral strip method. The hybrid formulation consistently includes effects of infinite order multiple diffraction. The method is demonstrated by scattering from a wedge, from two small circular cylinders, and from a triangular shaped obstacle. © 1999 Elsevier Science B.V. All rights reserved.

1. Introduction

We consider the problem of computing the complex acoustic pressure field $p(x)e^{-i\omega t}$ scattered by large bodies. We shall be content with finding an approximation to $p(x)$ (the time harmonic factor shall be suppressed from hereon). We seek an approximation strategy that is capable (at least theoretically) of being refined arbitrarily so that we can get as accurate a solution as desired. A traditional numerical method that has this property is said to be convergent. Classical asymptotic approximations, on the other hand, are typically divergent. That is, they cannot be refined arbitrarily in a given application.

Here we describe a hybrid method for scattering which combines short-wavelength asymptotics with a boundary integral equation (BIE) method. In our hybrid approach, we attempt to draw on the benefits from both methods while eliminating their largest individual deficiencies. For example, an asymptotic approach can be computationally efficient for acoustically large scatterers; its applicability, however, is limited since diffraction coefficients are available for only relatively simple geometries. Boundary integral equations, on the other hand, can accommodate arbitrary geometries. Computational cost limits their applicability, however, to relatively small problems. Another issue facing simple single layer potential BIE methods in time-harmonic acoustic scattering is nonuniqueness. Our approach eliminates all nonuniqueness issues associated with simple BIE formulations for the Helmholtz equation.

* Corresponding author. E-mail: barbone@bu.edu

Our hybrid method is based on patching a short-wavelength asymptotic expansion of the scattered field to a BIE representation of the near field. That is, the “inner” or “canonical” solutions required for the short wavelength asymptotic expansion of the scattered field are found using a BIE method. The BIE is applied to a small *interior* region (size $\lambda = \text{wavelength}$) in the vicinity of a diffraction point. Inside that domain, the numerical solution can be refined to arbitrarily high accuracy. The patching condition to the “outer asymptotic approximation” takes place on an artificial boundary. The accuracy of the resulting boundary condition (on the numerical problem) depends on the (arbitrary choice of) the location of the artificial boundary. Thus, the “asymptotic approximation” can be refined arbitrarily by moving this boundary. The rate of “convergence” of the asymptotic approximation is determined by the order of the asymptotic approximation used in the “outer” domain.

This paper introduces our hybrid method (asymptotic-numerical) in the context of a BIE numerical formulation. Some earlier work in the area is summarized in the next section. Section 3 contains our problem formulation and describes our hybrid method. The first example application, diffraction from a wedge, is presented in Section 4. This example has been treated earlier in the context of the finite element method in [2,14]. Here we treat the problem using the boundary spectral strip method. We also include results that demonstrate the role of uniform asymptotics in defining the outer field. Following the wedge example in Section 4, we consider two more examples with interacting diffraction regions: scattering from two circular cylinders, and scattering from a triangular shaped obstacle.

2. Background

The first description of a hybrid GTD-integral equation approach is due to Burnside et al. [3]. His and other approaches since depend on a method of moments formulation of the overall problem. Shape functions based on a GTD ansatz (see Eq. (5)) are then substituted into the integral equation. (See [3,7,10,16,17].) This approach requires the evaluation of integrals over large domains of hypersingular kernels multiplying rapidly varying functions. Further, these formulations are based on integral equations that exhibit nonuniqueness at specific frequencies. For these reasons, we have rejected hybrid approaches based on these formulations.

Below we shall present a new hybrid GTD/BSM approach which combines GTD with BSM (boundary spectral strip method). The essential idea behind our method is to use a short wavelength asymptotic approximation wherever it provides an accurate representation of the field. In the neighborhoods of those points where it is not valid, we supplement the solution with a BIE representation. Thus, we divide the domain into two (not necessarily connected) regions: the asymptotic region and the numerical region.

In our formulation, we apply the BSM to *interior* domains, that are usually simply connected. Thus our formulation is free of any problems associated with nonuniqueness of the continuous BIE for *exterior* problems. The formulation naturally separates the asymptotic from numerical approximations, and can be refined systematically to obtain arbitrarily high accuracy. The formulation leads to a matrix system of equations in which the number of degrees of freedom scales as $N_{\text{dof}} = O((kL)^{d-2})$. Here, k is the wave number, L is the scatterer size, and d represents the dimensionality of the problem (i.e. 2 or 3.) Thus, the direct factorization costs scale as $\text{cost} = O((kL)^{3(d-2)})$. In two dimensions, the cost is asymptotically independent of frequency.

3. Formulation

The complex acoustic pressure satisfies the Helmholtz equation:

$$\Delta p + k^2 p = 0, \quad x \in \Omega. \quad (1)$$

$\Omega \subset \mathbb{R}^d$ is the d -dimensional infinite domain exterior to the scatterer; i.e. $\Omega = \mathbb{R}^d \setminus \bar{S}$, where S represents the scatterer. On the surface of the scatterer ∂S , p satisfies a (linear) boundary condition consistent with continuity of

traction and normal velocity:

$$B \frac{\partial p}{\partial n} + p = 0, \quad x \in \partial S. \quad (2)$$

Here, B is a (not necessarily local) operator related to the impedance of the surface.

The scattering excitation is due to an incident wave p_{inc} that identically satisfies (1) but not necessarily (2). This gives rise to the scattered wave p_{scat} . The scattered field satisfies

$$p = p_{\text{inc}} + p_{\text{scat}}, \quad (3)$$

$$\lim_{r \rightarrow \infty} r^{(d-1)/2} \left[\frac{\partial p_{\text{scat}}}{\partial r} - ik p_{\text{scat}} \right] = 0. \quad (4)$$

Eqs. (1)–(4) define a unique boundary value problem for the scattered pressure p_{scat} .

We are especially concerned with obtaining solutions at large kR . Here, R is a reference length which will be made specific later. We shall employ the geometrical theory of diffraction [6], or GTD, which has been devised especially to handle this limit. GTD can be thought of as an application of matched asymptotic expansions, in which the outer expansion is given by the ansatz

$$p_{\text{scat}} \approx p^G(x) = \sum_{\text{ray } j} a_j(kR) A_j(x) \exp(ik\psi_j(x)). \quad (5)$$

Such an expansion (5) typically results in an approximation which is asymptotic in kR :

$$\lim_{kR \rightarrow \infty} p^G \rightarrow p_{\text{scat}} \quad \text{almost everywhere in } \Omega. \quad (6)$$

To apply GTD, one must integrate the ray equations, integrate the phase along each ray, integrate the transport equations along each ray, etc. When a ray intersects the surface of the body, the wave can be reflected, transmitted, diffracted, etc., and corresponding reflected, transmitted, or diffracted rays are introduced accordingly [6]. Ray discretization requirements are determined by the geometry of the body (and the medium) and are therefore independent of k . Further, the ray and transport equations are independent of k . Thus the computational cost associated with computing the field scattered by a large body using GTD is independent of k .

At diffraction points (defined below), an inner or “canonical” problem must be solved and then asymptotically matched to the outer field. For matching purposes, such a solution is typically required in some analytical form. The availability of such solutions for complicated diffraction geometries practically limits the applicability of GTD to problems with simple discontinuities.

3.1. The hybrid asymptotic-numerical method

In most of the domain, we shall use the asymptotic approximation (5) based on $kR \gg 1$. In the rest of the domain, we shall use a BIE representation of the field. In this section, we first describe how we divide the domain into these asymptotic and numerical regions. This division depends on the concept of a diffraction point. Then we define an asymptotically equivalent boundary value problem on a union of “diffraction regions”. This is illustrated in Fig. 1. In this figure, we have noted “asymptotic regions” and “numerical regions”. (We use the terms “numerical regions” and “diffraction regions” interchangeably here). This example is treated in a later section, as are several other simpler examples. Those readers familiar with [2] may choose to skip ahead to Section 4.

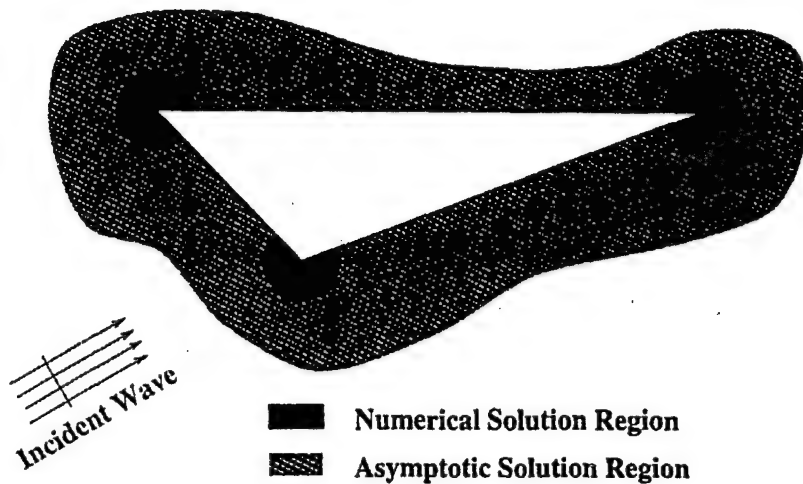


Fig. 1. An example scatterer. Shown in shades are the “numerical” and “asymptotic” regions. The field in the dark regions is found numerically and patched smoothly to an asymptotic expression, valid elsewhere.

3.1.1. Diffraction points

In order to obtain an approximation to p_{scat} , we proceed as follows. We first apply the principles of GTD to obtain a “global” asymptotic solution.¹ Some of the coefficients (diffraction coefficients in particular) in the outer expansion cannot be determined from the outer equations alone. These coefficients are associated with homogeneous solutions of the outer equations. Further, there is a set of points of zero measure at which expansion (5) is not asymptotic; i.e. that set of points where (6) is not valid. Thus we define the set of diffraction points \mathbf{X}^D to be

$$\mathbf{X}^D = \left\{ x \mid \lim_{kR \rightarrow \infty} p_{\text{scat}} - p^G \neq 0 \right\}. \quad (7)$$

We note that since p^G is not asymptotic to p_{scat} at x^D , then for any finite value of kR , p^G will typically provide a very poor approximation to p_{scat} in a whole neighborhood of x^D . For that reason, we must consider local corrections to p^G valid in the vicinity of x^D in order to obtain a practically useful approximation for moderate values of kR .

The diffraction points can be classified as either of two types. We shall refer to them as *essential diffraction points* and *inessential diffraction points*. The local solution valid in the neighborhood of an essential diffraction point is necessary to evaluate some undetermined functions (i.e. diffraction coefficients) in the homogeneous solutions of the outer equations. The local solution valid in the neighborhood of an inessential diffraction point on the other hand, yields no such global information. Typically, the locations of essential diffraction points do not depend on the properties of the incident field (such as its angle of incidence). They are purely geometric in origin and are typically associated with edges and vertices. The locations of inessential diffraction points, on the other hand, often change with the incident field parameters. Examples include shadow boundaries, foci and caustics. The distinction between essential and inessential diffraction points is hardly important except that we shall deal with the former numerically and with the latter analytically.

In order to obtain an approximate solution which is valid at the diffraction points, it is necessary to find an inner or local solution. This solution is then matched to the outer solution. The result is a set of approximations (local and global) that together have a range of validity that includes the entire domain. We again emphasize the importance of

¹ We shall alternatively use the terms “outer” and “global” to refer to quantities asymptotically valid in regions away from diffraction points. “Local” or “inner” regions are λ sized neighborhoods of diffraction points, where λ is the wavelength of sound in the fluid. Diffraction points are defined later in the text.

the local corrections when using the asymptotic approximations at any finite value of kR . For inessential diffraction points, local solutions are typically available in the literature. (see, e.g. [9].) For essential diffraction points, solutions are typically available for only simple shapes and boundary conditions. The hybrid method that we propose describes a way to obtain approximate solutions valid near essential diffraction points.

3.1.2. Diffraction regions

To do so, we introduce diffraction regions. Around each *contiguous* set of essential diffraction points, we define a diffraction region Ω^D such that

$$\Omega^D = \left\{ x \mid \|x - x^D\| \leq (kR)^\alpha f\left(\frac{x - x^D}{|x - x^D|}\right) \right\}. \quad (8)$$

Here, x^D is a diffraction point and R is a fixed distance, a parameter to be chosen by the analyst, which determines the size of the diffraction region. The function $f((x - x^D)/|x - x^D|)$ determines the shape of the diffraction region. The outer boundary of the diffraction region shall be denoted by Γ_R , indicating that its location depends on the choice of R . The value of α is chosen so that, as $kR \rightarrow \infty$, Γ_R is entirely contained in the domain of validity of the expansion (5) (e.g. typically the far-field of the diffraction point). The accuracy of our hybrid method depends on $kR \gg 1$.

3.2. Asymptotically equivalent boundary value problem

Now we are in a position to define an asymptotically equivalent boundary value problem. This problem is nothing more than a restriction of our original boundary value problem to the diffraction regions, with continuity enforced across the artificial boundary Γ_R . Thus we define

$$\Delta p^D + k^2 p^D = 0, \quad x \in \Omega^D, \quad (9)$$

$$B\partial_n p^D = -p^D, \quad x \in \partial\Omega^D \cap \partial\Omega, \quad (10)$$

$$p^D = p_{\text{inc}} + p^A, \quad x \in \Gamma_R, \quad (11)$$

$$\partial_n p^D = \partial_n p_{\text{inc}} + \partial_n p^A, \quad x \in \Gamma_R. \quad (12)$$

Here, p^A is our global asymptotic approximation. It could be obtained by GTD as indicated in Eq. (5), by the uniform theory of diffraction (e.g. [8]), or by GTD with local corrections for inessential diffraction points. We shall give examples using both corrected and uncorrected GTD below. Montgomery and Barbone [14] have shown in wedge geometries that patching p^D on $kR = \text{constant}$ as described in Eqs. (11) and (12) is asymptotically equivalent to matching.

Our hybrid GTD/BSM method is now simply stated. We have the “asymptotically equivalent” boundary value problem (9)–(12) defined on the small (size kR) *interior* domain Ω^D . We shall formulate and solve that boundary value problem using BSM. Any other numerical method might be adapted to solve this boundary value problem, too. Barbone and coworkers [2,14] demonstrate its solution using finite elements.

We shall now illustrate our method through simple examples. We shall first consider a simple wedge geometry. This will allow us to show examples of essential and inessential diffraction points, and show how to deal with each. Then we investigate the interaction between two essential diffraction points by considering the scattering from two small circular cavities. Finally, we discuss how to generalize the formulation to consider more complicated geometries. We demonstrate this by computing the field scattered by a large triangular scatterer.

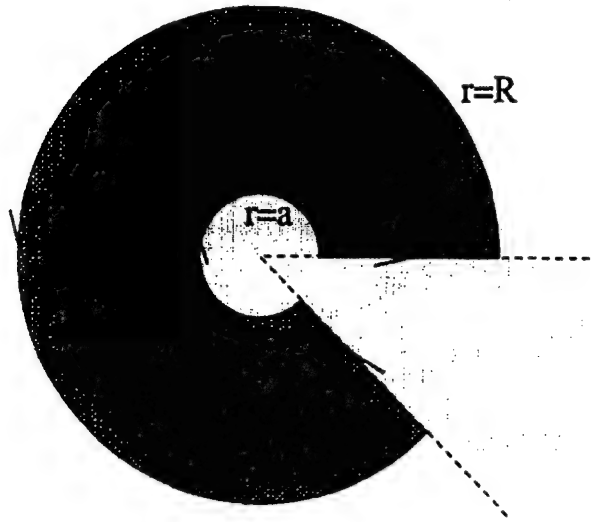


Fig. 2. A blunted wedge. Dark shaded area is the “diffraction region” or “numerical region”, the boundary of which is subsequently meshed. The “outer domain” corresponds to $r \geq R = 2\lambda$.

4. Application to a wedge

4.1. Formulation

Our first example is that of plane wave scattering from a soft blunted wedge. Since we have considered this example before in the context of FEM, we shall include only an outline of the asymptotic solution here. Readers interested in more detail should consult [2].

The problem of interest here is depicted in Fig. 2. We shall allow the end of the wedge to be truncated with some shape. Such geometrical detail is assumed to be the size of a wavelength or smaller. For definiteness, we consider the wedge blunted with a circle of radius $a = \lambda/2$. Since the wedge is soft, the boundary condition on the wedge surfaces is $p = 0$, or Eq. (2) with $B = 0$.

The incident plane wave is taken to be of the form

$$p_{\text{inc}} = e^{ik(x \cos \theta_i + y \sin \theta_i)} = e^{ikr \cos(\theta - \theta_i)}. \quad (13)$$

Here, θ_i is the angle of incidence and k is the wave number. Thus, p_{scat} satisfies (1)–(4) with $B = 0$ and p_{inc} given by (13).

4.2. The global solution

We apply the laws of GTD [6] to the wedge shown in Fig. 3. Thus we write the scattered field as a sum of two plane waves (shadow and reflected, denoted by p_{shd} and p_{ref} , respectively) and a diffracted cylindrical wave (p_{diff}) as indicated in Fig. 3:

$$p_{\text{scat}} \sim p^G = p_{\text{shd}} + p_{\text{ref}} + p_{\text{diff}}, \quad r \neq 0, \quad \theta \neq \theta_r, \theta_s. \quad (14)$$

We have chosen an incident angle for which there is both a reflected and a shadow wave. For other angles of incidence (i.e. $0 < \theta_i < 2\pi - \beta$), however, there could be two reflected waves. If (i.e. $\beta - \pi < \theta_i < \pi$) then there will be two shadow waves.

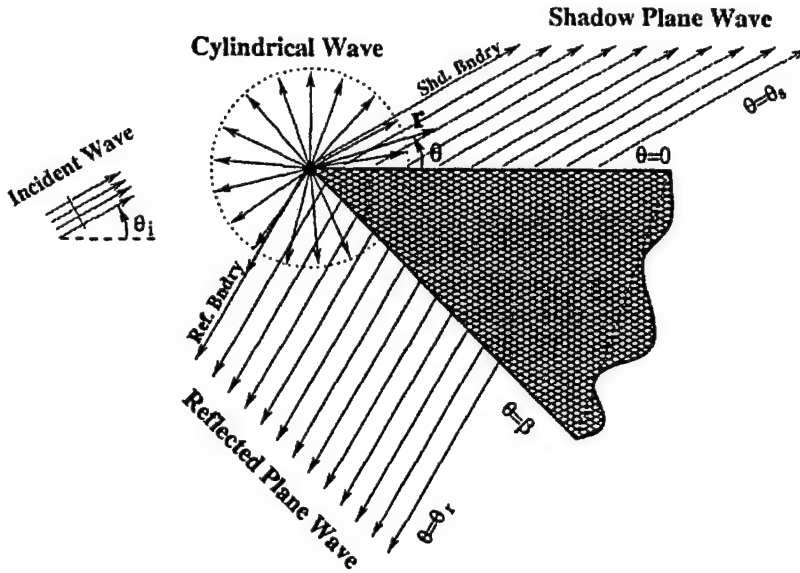


Fig. 3. The global reflected and diffracted waves from a wedge. Note that the geometrical details of the corner (α/λ in scale) are invisible from this “global” perspective.

The individual terms in (14) are given as follows:

$$\begin{aligned} p_{\text{shd}} &= -e^{ikr \cos(\theta - \theta_s)}, \quad 0 \leq \theta < \theta_s \\ p_{\text{ref}} &= -e^{ikr \cos(\theta - \theta_r)}, \quad \theta_r < \theta \leq \beta, \\ p_{\text{diff}} &= (kR)^{-1/2} D(\theta) \sqrt{\frac{R}{r}} e^{ikr} \quad 0 \leq \theta \leq \beta, \quad kr \rightarrow \infty. \end{aligned} \quad (15)$$

The reflected and shadow wave amplitudes are known from the boundary condition (2) on the wedge faces. The angles θ_s and θ_r are the angles in which the shadow-wave and the reflected-wave propagate, respectively, as shown in Fig. 3. The function $D(\theta)$, the diffraction coefficient for the edge, is considered unknown at this stage. We note that the plane waves expressions are defined only for certain values of the angle. Outside the ranges specified in (15) they are understood to be zero. Thus our expression for p^G has discontinuities at $\theta = \theta_s, \theta_r$.

4.3. Local solutions: diffraction points

We note that Eq. (14) is not valid at $r = 0$, nor at $\theta = \theta_r, \theta_s$. These define sets of “diffraction points”. The point $r = 0$ is classified as an essential diffraction point since the local solution there is required to evaluate $D(\theta)$. The boundary layer solutions around the angles $\theta = \theta_r, \theta_s$, on the other hand, merely provide local smoothness corrections, and are not associated with homogeneous solutions of the outer equations. Thus the set of points that make up the lines $\theta = \theta_r, \theta_s$ are classified as inessential diffraction points. We shall consider local solutions near the inessential diffraction points first.

4.3.1. Inessential diffraction points

An inner solution valid along the line $\theta = \theta_s$ represents a boundary layer solution. It can be found in many text books, either directly or indirectly (see, e.g. [4,5,15,18]). Here we simply state the result from one such choice:

$$p_{\text{shadow}}^{\text{uniform}} \equiv p_{\text{shd}}^u = -\frac{1}{\sqrt{\pi}} (F[(2kr)^{1/2} \sin 1/2(\theta - \theta_s)]) \exp \left\{ ikr - \frac{i\pi}{4} \right\}. \quad (16)$$

Here, $F(z)$ is defined as (note that we use the complex conjugate of that used by Jones [5]):

$$F(z) = e^{-iz^2} \int_z^\infty e^{it^2} dt. \quad (17)$$

We note that

$$p_s \sim p_{\text{shd}}^u + O(kR)^{-1/2} \quad \text{for } (kr)^{1/2} \sin \frac{1}{2}(\theta - \theta_s) \ll 1. \quad (18)$$

Thus, p_{shd}^u provides our asymptotic approximation to the scattered field that is valid in the vicinity of the shadow boundary. It has the advantage of some other representations in that it is an exact solution of Helmholtz equation. Similarly, we define p_{ref}^u for the reflection boundary region:

$$p_{\text{ref}}^u = \frac{1}{\sqrt{\pi}} \{F[(2kr)^{1/2} \sin \frac{1}{2}(\theta - \theta_r)]\} \exp \left\{ ikr - \frac{i\pi}{4} \right\}. \quad (19)$$

With p_{ref}^u and p_{shd}^u , we write an approximation to the scattered field valid at all angles:

$$p_{\text{scat}} \sim p^{\text{Asymp}} = p_{\text{ref}}^u + p_{\text{shd}}^u + p_{\text{diff}}^u \quad \forall \theta, r \neq 0, \quad (20)$$

$$p_{\text{diff}}^u = (kR)^{-1/2} D^u(\theta) \sqrt{\frac{R}{r}} e^{ikr}. \quad (21)$$

Eqs. (14) and (20) both provide asymptotic approximations to p_{scat} . They are both formally accurate to $O(kR)^{-1/2}$. The difference between them is that (20) is valid for all angles θ , while (14) is not valid at the two angles $\theta = \theta_r, \theta_s$. In the case of Eqs. (14) and (15), the function $D(\theta)$ is unknown and needs to be determined. In the case of (20) and (21), the as yet unknown function is $D^u(\theta)$.

4.3.2. The essential diffraction point

The point $r = 0$ we have classified as an essential diffraction point. We note that the approximation in (20) is formally valid everywhere except at $r = 0$. The “hybrid method” that we propose involves obtaining the solution in the vicinity of essential diffraction points numerically rather than analytically. Therefore, we shall formulate and solve numerically an “asymptotically equivalent boundary value problem” on a “diffraction region” which includes the neighborhood of $r = 0$.

We begin by defining our diffraction region:

$$\Omega^D = \{(r, \theta) \mid r \leq (kR)/k\}. \quad (22)$$

Thus, for fixed kR , the diffraction region shrinks as $k \rightarrow \infty$. On the other hand, for fixed k , the diffraction region grows as $kR \rightarrow \infty$.

We now wish to solve the problem described in Eqs. (9)–(12) with Ω^D as described in (22). This yields the following boundary value problem for $p^D = p_{\text{scat}}(x)|_{\Omega^D}$:

$$\Delta p^D + k^2 p^D = 0, \quad r < R, \quad 0 < \theta < \beta, \quad (23)$$

$$p^D = -p_{\text{inc}}, \quad \theta = 0, \quad \theta = \beta, \quad (24)$$

$$p^D = p^A \quad \text{on } r = R, \quad (25)$$

$$\partial_n p^D = \partial_n p^A \quad \text{on } r = R. \quad (26)$$

Here, p^A is given by either p^G in (15) or by p^{Asymp} in Eq. (20). The boundary condition in (25) and (26) would be over specified if p^A were known completely, since we cannot specify both p and its normal derivative on the same surface, in general. Since $D(\theta)$ is unspecified in p^A , however, conditions (25) and (26) are not over specified.

We now discuss the numerical solution of the boundary value problem (23)–(26).

4.4. Numerical solution for local problem

The method that we use for the numerical solution is the boundary spectral strip method (BSM). This numerical method is based on a boundary integral formulation and utilizes a spectral series basis rather than elements and nodes. The details of the method can be found in [11–13]. The model which is used for numerical solution is

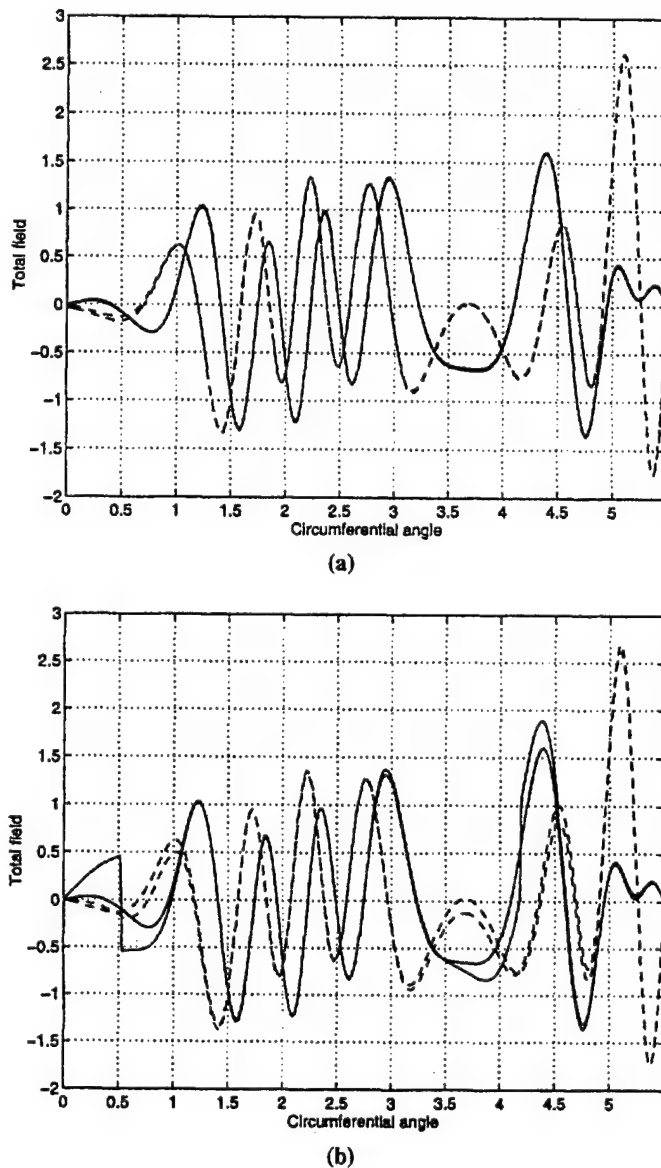


Fig. 4. The scattered field from the blunted wedge. Analytical and numerical results evaluated on the artificial boundary, Γ_R : (a) p^A given by p^{Asymp} ; (b) p^A given by p^G .

depicted in Fig. 2. It uses sixth-order polynomial strips; 10 for the outer boundary ($r = R$), 5 for the inner boundary ($r = a$), and two for each straight edge ($\theta = 0, \beta$). Note that the problem is formulated on a simply connected *inner* domain. Therefore there are no uniqueness problems as appear in the Helmholtz single layer potential BIE for exterior domains. The geometry is defined by $a = \lambda/2$ and $R = 2\lambda$, where λ is the wave length. The angle of the incident wave was chosen to be 30° as shown in Fig. 3.

We first consider the case of p^A given by p^{Asymp} . In this case, we get very good agreement between the numerical results and the analytical results (See Appendix A.) Fig. 4(a) shows this agreement for the real and the imaginary parts of the scattered field on Γ_R .

To demonstrate the importance of using uniformly valid asymptotics in p^A , we now consider p^A given by p^G in Eqs. (14) and (15). We recall that p^G has discontinuities along the shadow and reflected field boundaries, $\theta = \theta_s$, $\theta = \theta_r$. Fig. 4(b) shows a comparison of the results obtained by our hybrid method and the exact solution evaluated on Γ_R . We note that away from $\theta = \theta_r, \theta_s$, the results agree well with the exact solution. In large regions near the shadow and reflected field boundaries, however, we see that the presence of the discontinuities pollutes the quality of the hybrid solution. For large enough kR , the pollution would affect a very small portion of the full angular range. For practical values of kR like that used here, however, this range can be significant.

5. Interacting essential diffraction points

In this section we shall demonstrate our hybrid method on a problem with interacting diffraction points. For simplicity, we consider two-dimensional scattering from two small soft cylindrical cavities (with radius $a = O(\lambda)$) as shown in Fig. 5. The distance between their centers along the x -axis is $d \gg \lambda$. We shall consider the special case of symmetry about the x -axis.

5.1. The global asymptotic approximation

For the analysis of this problem, we introduce two polar coordinate systems, with the origins located at the centers of the two circles. Each point is located by either (r_1, θ_1) or (r_2, θ_2) . Therefore, the boundaries of the two circles

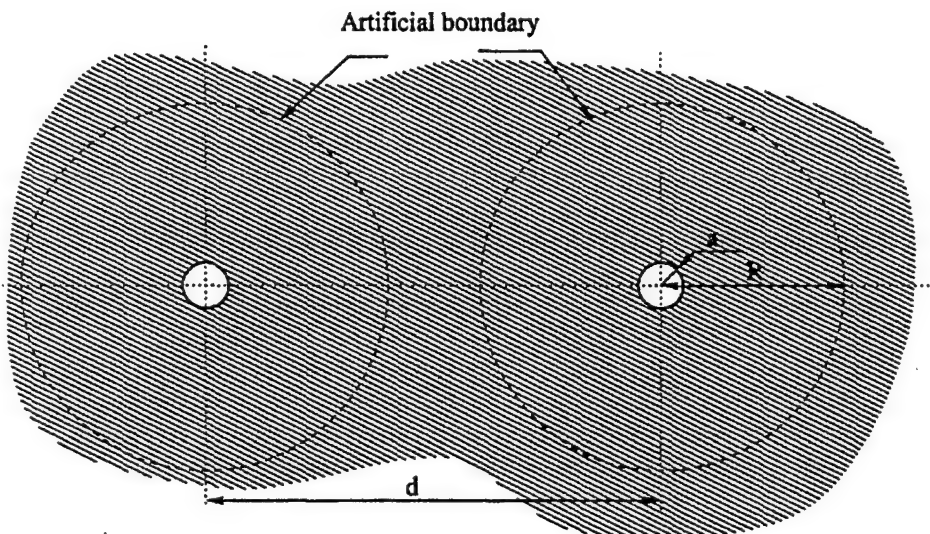


Fig. 5. Two pressure release cavities embedded in an infinite domain, problem definition.

are described by the equations:

$$\Gamma_1 = \{(r_1, \theta_1) | r_1 = a\}, \quad \Gamma_2 = \{(r_2, \theta_2) | r_2 = a\}. \quad (27)$$

In this case, we will write the exact solution and from it, extract the outer asymptotic expansion. In terms of the given coordinate system, the exact solution of (1)–(4) for the total field can be written as

$$p_{\text{tot}} = p_1 + p_2 + p_{\text{inc}} \quad \text{in } \Omega, \quad (28)$$

$$p_1 = \sum_{n=0}^{\infty} A_n H_n^{(1)}(kr_1) \cos(n\theta_1), \quad (29)$$

$$p_2 = \sum_{m=0}^{\infty} B_m H_m^{(1)}(kr_2) \cos(m\theta_2). \quad (30)$$

The coefficients A_n and B_m would in general be determined from the boundary conditions on the cylinders. We treat the cavities as soft, but allow forcing on the boundaries. Thus the boundary condition is (Eq. (2) with $B = 0$, and nonzero right-hand side):

$$p_{\text{tot}} = f_{1,2}(\theta_{1,2}) \quad \text{on } \Gamma_{1,2}. \quad (31)$$

We shall later compare our asymptotic approximation to a reference numerical solution. To obtain the reference solution, the sums in Eqs. (29) and (30) are truncated at large finite values. Eq. (31) is then enforced at various points and the coefficients A_n and B_m are determined by inverting the resulting matrix equation.

For $kr_j \gg 1$, or for $r_j > R$ and $kR \gg 1$, we can approximate p_1 and p_2 in (29) and (30) using the large argument expansion of the Hankel functions [1]:

$$\begin{aligned} p_1 &\sim \sum_{n=0}^{\infty} \sqrt{\frac{2}{\pi}} \exp(-i n \pi/2 - i \pi/4) A_n \cos(n\theta_1) \frac{1}{\sqrt{kr_1}} \exp ikr_1 \\ &\sim D_1(\theta_1) \frac{1}{\sqrt{kr_1}} \exp ikr_1, \quad k \rightarrow \infty, \quad r_1 \neq 0, \end{aligned} \quad (32)$$

$$\begin{aligned} p_2 &\sim \sum_{m=0}^{\infty} \sqrt{\frac{2}{\pi}} \exp(-i m \pi/2 - i \pi/4) B_m \cos(m\theta_2) \frac{1}{\sqrt{kr_2}} \exp ikr_2 \\ &\sim D_2(\theta_2) \frac{1}{\sqrt{kr_2}} \exp ikr_2, \quad k \rightarrow \infty, \quad r_2 \neq 0. \end{aligned} \quad (33)$$

Eq. (28) with expansions (32) and (33) is our outer asymptotic approximation of the field. This is the expression which is to be used as p^A in the asymptotically equivalent boundary value problem, (9)–(12). The limits on the validity of the expansions in (32) and (33) indicate that $r_1 = 0$ and $r_2 = 0$ are essential diffraction points. We note that the two functions $D_1(\theta_1)$ and $D_2(\theta_2)$ are as yet unknown.

5.2. The local solutions

We define the two diffraction regions as follows:

$$\Omega_1^D = \{(r_1, \theta_1) | a < r_1 < R\}, \quad (34)$$

$$\Omega_2^D = \{(r_2, \theta_2) | a < r_2 < R\}. \quad (35)$$

Here, we have chosen $R < d/2$. If we had chosen $R > d/2$, then a single boundary surrounding both the cylinders would be used. Examples like this will be treated separately in a forthcoming publication.

We now must solve the boundary value problem (9)–(12) on each of the diffraction regions Ω_1^D and Ω_2^D . To enforce Eq. (23), we write a boundary integral equation on the boundary of each diffraction region separately. This can be expressed in discrete operator form as

$$\mathbf{H}\mathbf{p} = \mathbf{G}\mathbf{v}. \quad (36)$$

Eq. (36) represents a (discretized) relation between the field p and its normal derivative $v = \partial p / \partial n$. \mathbf{H} and \mathbf{G} are two coefficient matrices, while \mathbf{p} and \mathbf{v} are two column vectors containing the coefficients of the series that approximate the functions p and v , respectively.

The boundaries of each diffraction region $\partial\Omega_m^D$ can be partitioned into Γ_{R_m} , the artificial boundary separating the diffraction and asymptotic regions, and $\Gamma_{\tilde{R}_m}$, the rest of the boundary of the diffraction region.

$$\partial\Omega_m^D = \Gamma_{R_m} \cup \Gamma_{\tilde{R}_m}. \quad (37)$$

We likewise partition Eq. (36) to write

$$[\mathbf{H}_{\Gamma_{R_m}}, \mathbf{H}_{\Gamma_{\tilde{R}_m}}] \begin{Bmatrix} \mathbf{p}_{\Gamma_{R_m}} \\ \mathbf{p}_{\Gamma_{\tilde{R}_m}} \end{Bmatrix} = [\mathbf{G}_{\Gamma_{R_m}}, \mathbf{G}_{\Gamma_{\tilde{R}_m}}] \begin{Bmatrix} \mathbf{v}_{\Gamma_{R_m}} \\ \mathbf{v}_{\Gamma_{\tilde{R}_m}} \end{Bmatrix}. \quad (38)$$

We note that Eq. (38) represents two independent, and so far uncoupled, equations. The value $m = 1$ corresponds to the discretized BIE for the region on the left, while the value $m = 2$ represents the discrete form of the BIE for the region on the right.

In order to enforce the continuity conditions (11) and (12), we seek expressions for $\partial_n p^A$ on Γ_{R_m} , $m = 1, 2$. In the asymptotic regions, the scattered field is given by $p_1 + p_2$, which, using (32) and (33), can be written as

$$p_{\text{scat}} \sim \sum_{m=1}^2 D_m(\theta_m) \frac{e^{ikr_m}}{\sqrt{kr_m}}. \quad (39)$$

Since Γ_R is a circle, the normal derivative is equal to the radial derivative. Thus we can write

$$v|_{\Gamma_{R_m}} = \left. \frac{\partial p}{\partial n} \right|_{\Gamma_{R_m}} = \left. \frac{\partial}{\partial r_m} \left\{ \sum_{n=1}^2 D_n(\theta_n) \frac{e^{ikr_n}}{\sqrt{kr_n}} \right\} \right|_{\Gamma_{R_m}}. \quad (40)$$

Applying the chain rule to (40) yields:

$$\frac{\partial p}{\partial r_m} = \sum_{n=1}^2 \left[\frac{\partial r_n}{\partial r_m} \left(ik - \frac{1}{2r_n} \right) D_n(\theta_n) + \frac{\partial \theta_n}{\partial r_m} D'_n(\theta_n) \right] \frac{e^{ikr_n}}{\sqrt{kr_n}}. \quad (41)$$

Here $D'_n(\theta_n)$ is the derivative of D_n with respect to θ_n . For the coordinate system employed here, we obtain the following relationships:

$$\frac{\partial r_n}{\partial r_m} = \cos(\theta_m - \theta_n), \quad \frac{\partial \theta_n}{\partial r_m} = \frac{1}{r_n} \sin(\theta_m - \theta_n). \quad (42)$$

At this stage, we have a choice of different ways to proceed. One way is to introduce interpolations of $D_n(\theta_n)$ into Eqs. (39)–(41), and substitute the result directly into (38). We chose the second option. That is to interpolate v and p on Γ_R separately from $D_n(\theta_n)$. Then enforce the continuity conditions (39) and (40) weakly. This affords two benefits. First, it allows added freedom in the choice of interpolation functions to be used in $D_n(\theta_n)$ and p . Second, it provides an obvious route to adapt our hybrid method to existing BEM codes.

Finally, using the relations between p , v and D given in Eqs. (39)–(41) together with Eq. (38) yields the following system of equations:

$$\begin{bmatrix} -M_{DP} & M_P & 0 & 0 \\ -M_{DV} & 0 & M_V & 0 \\ 0 & H_{\Gamma_R} & -G_{\Gamma_R} & -G_{\Gamma_{\bar{R}}} \end{bmatrix} \begin{Bmatrix} D \\ P_{\Gamma_R} \\ V_{\Gamma_R} \\ V_{\Gamma_{\bar{R}}} \end{Bmatrix} = \begin{Bmatrix} 0 \\ 0 \\ -H_{\Gamma_{\bar{R}}} p_{\Gamma_{\bar{R}}} \end{Bmatrix}. \quad (43)$$

Each of the vectors D , P_{Γ_R} , $P_{\Gamma_{\bar{R}}}$, V_{Γ_R} , $V_{\Gamma_{\bar{R}}}$ contain two sub-vectors of series coefficients representing the relevant variable on the two diffraction regions. The matrices M_{DP} and M_{DV} are evaluated using Eqs. (39) and (40), respectively.

We note that we make no special attempts to interpolate $D_n(\theta_n)$ smoothly. The interpolation assumes discontinuous shape functions, and continuity results from the solution of the equations themselves.

5.3. Numerical results

Here we let the two cavities have radius $a = 0.5 = \lambda/4$ at a distance $d = 10$. The wave number was chosen as $k = \pi$, and $R = 2$. The boundary conditions are $f_1 = \cos \theta_1 + \frac{1}{2} \cos 2\theta_1$ and $f_2 = 0$, with $p_{\text{inc}} = 0$. The boundary

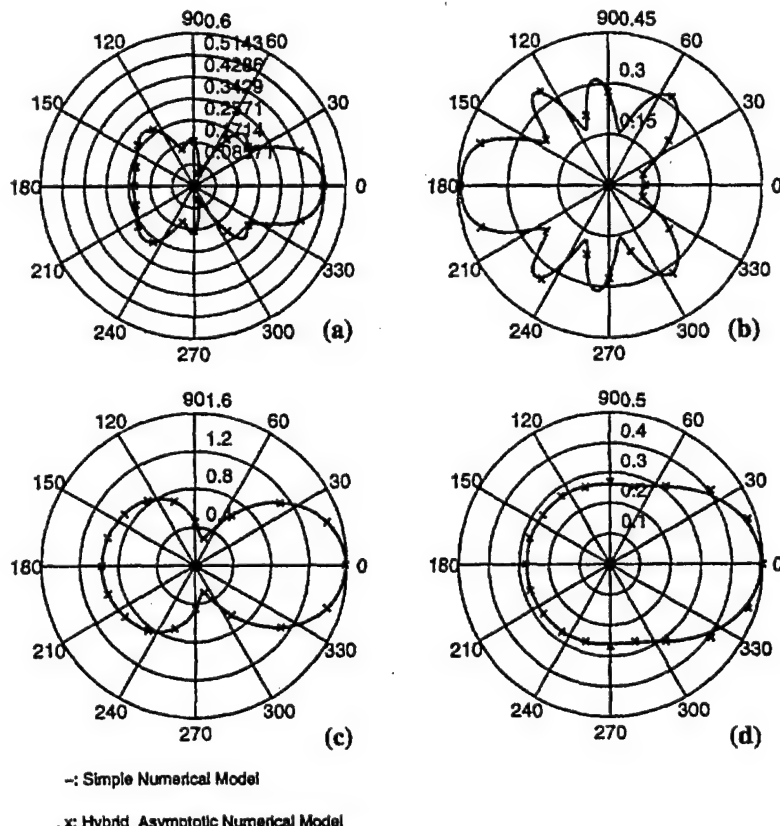


Fig. 6. Two cavities embedded in an infinite domain: (a) pressure field amplitude along the artificial boundary: right cavity; (b) pressure field amplitude along the artificial boundary: left cavity; (c) diffraction coefficients: right cavity; (d) diffraction coefficients: left cavity.

strip model used sixth-order polynomial strips. On each cavity, six strips were used to describe the boundary of the cavity and 20 strips on the artificial boundary.

We compare the results from the hybrid method to those obtained from a reference solution (described above). Fig. 6 shows a comparison of the amplitude of the scattered field and the directivity coefficients obtained from the reference solution and the hybrid asymptotic BSM solution. We see that there is a good agreement between the results of the two models. Other test cases showed similar agreement provided that the boundary data had sufficiently slow circumferential variation. For $f_1(\theta_1) = \cos n\theta_1$, good agreement was obtained for $n < 14$ when comparing the total pressure. When comparing the directivities, however, discrepancies in excess of 20% were apparent for $n = 3$. In general, comparisons of p_{tot} along an artificial boundary showed closer agreement than comparisons of $D_m(\theta)$.

Using higher-order asymptotics in the outer field improved accuracy of the directivities considerably. Increasing the order of accuracy in the outer field to $O(kR)^{-3/2}$ led to error in the directivities that was smaller than 5% for $n \leq 20$. Issues related to error estimation, numerical accuracy, and higher-order asymptotic approximation shall be addressed in detail in a forthcoming paper.

6. Scattering from a triangle

We shall now apply our method to a more challenging geometry: scattering from a triangle with blunted corners. The boundary condition on the surface of the triangle is $p_{\text{tot}} = 0$, and we consider a plane wave incident:

$$p_{\text{inc}} = e^{ikr_1 \cos(\theta_1 - \theta_i)} \quad (44)$$

For definiteness, we assume that the angle of incidence $0 \leq \theta_i \leq 3\pi/4$ measured with respect to corner 1. The corners of the triangle are blunted in a manner analogous to the wedge treated earlier. As with the examples described before, we begin with an expression for the global asymptotic approximation.

6.1. Global asymptotic approximation

The geometry of our triangular scatterer is described in Fig. 7. We choose three polar coordinate systems with origins located at the corners of the triangle. As with the wedge example, we obtain both plane wave contributions to the scattered field and diffracted cylindrical waves from each corner:

$$p_{\text{scat}} \sim p^G = p_{\text{diff}} + \sum_{n=1}^3 p_{pw(n)}, \quad r_n \neq 0, \quad \theta_n \neq 0, \beta_n, \quad \theta_n \neq \theta_n^{pw(j)}, \quad (45)$$

$$p_{pw1} = -e^{ikr_1 \cos(\theta_1 - \theta_1^{pw1})} = -e^{ikr_{12} \cos(\theta_1^{pw1})} e^{ikr_2 \cos(\theta_2 - \theta_2^{pw1})}, \quad 0 \leq \theta_1 < \theta_1^{pw1} \quad \text{and} \quad \theta_2^{pw1} < \theta_2 \leq \beta_2, \quad (46)$$

$$p_{pw2} = -e^{ikr_{12} \cos(\theta_1^{pw1})} e^{ikr_2 \cos(\theta_2 - \theta_2^{pw2})} = -e^{ikr_{13} \cos(\theta_1 - \theta_1 - \pi)} e^{ikr_3 \cos(\theta_3 - \theta_3^{pw2})}, \quad 0 \leq \theta_2 < \theta_2^{pw2} \quad \text{and} \quad \theta_3^{pw2} < \theta_3 \leq \beta_3, \quad (47)$$

$$p_{pw3} = -e^{ikr_1 \cos(\theta_1 - \theta_1^{pw3})} = -e^{ikr_{13} \cos(\theta_1^{pw3})} e^{ikr_3 \cos(\theta_3 - \theta_3^{pw3})}, \quad \theta_1^{pw3} < \theta_1 \leq \beta_1 \quad \text{and} \quad 0 \leq \theta_3 < \theta_3^{pw3}, \quad (48)$$

$$p_{\text{diff}} = (kR)^{-1/2} \sum_{m=1}^3 D_m(\theta_m) \sqrt{\frac{R}{r_m}} \exp ikr_m. \quad (49)$$

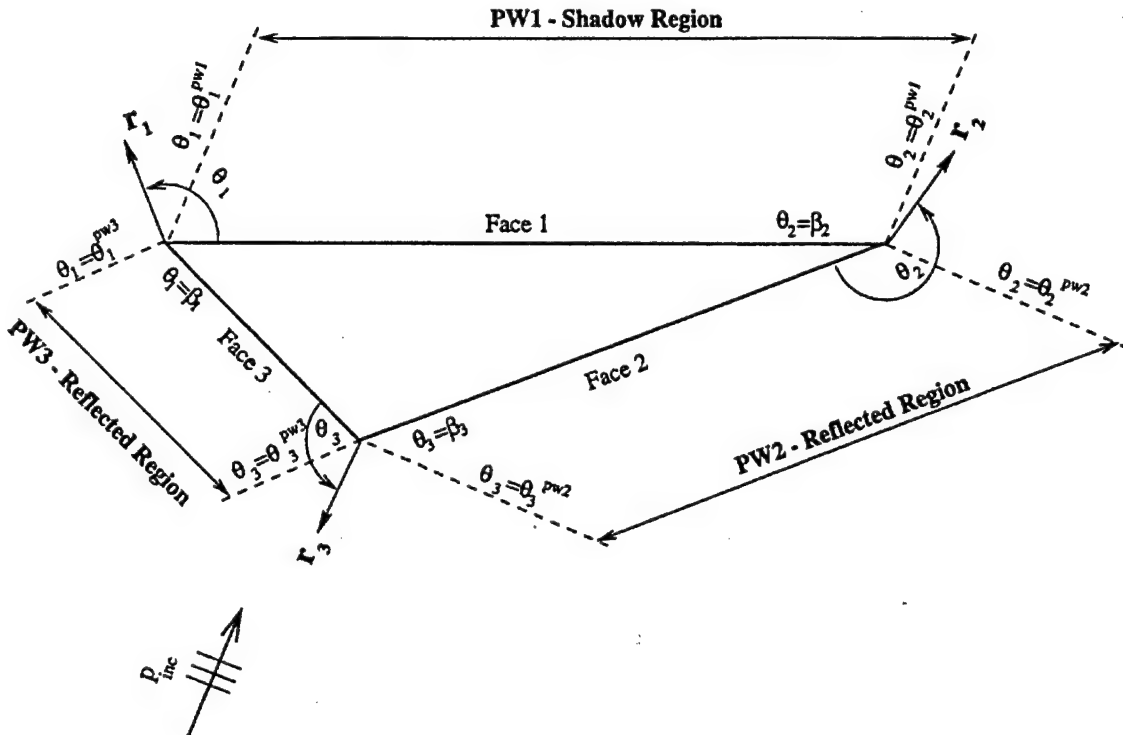


Fig. 7. Scattering from a triangle: problem definition.

Here, r_{ij} represents the distance between corners i and j , $\theta_i^{pw(j)}$ represents the angle of propagation of plane wave j as measured with respect to the θ_i origin. In regions of the domain where the value of $p_{pw(m)}$ is not explicitly specified in (46)–(48), it is understood to be zero.

Eqs. (45) and (49) show apparent discontinuities at the angles $\theta_n = 0, \beta_n$ (see Fig. 7). These we classify as inessential diffraction points since their local solutions yield no required information for the global field. Because of the soft boundary condition on the scatterer, we require that

$$D_n(\theta_n) = 0 \quad \text{on } \theta_n = 0, \beta_n. \quad (50)$$

Therefore, p^G is in fact continuous at these angles. The derivative of p^G , however, is discontinuous. For the purposes of describing our hybrid method, we shall not address these inessential diffraction points and shall witness their (small) effect on our solutions.

As with the wedge, the shadow and reflected field boundaries $\theta_n = \theta_n^{pw(j)}$ also represent inessential diffraction points. We deal with them in a manner similar to that described in Section 4.3. Thus we write

$$p_{\text{scat}} \sim p^{\text{Asymp}} = p_{\text{diff}}^u + \sum_{n=1}^3 p_{pw(n)}^n, \quad r_n \neq 0, \quad \theta_n \neq 0, \beta_n. \quad (51)$$

Here,

$$p_{\text{diff}}^u = (kR)^{-1/2} \sum_{m=1}^3 D_m^u(\theta_m) \sqrt{\frac{R}{r_m}} \exp ikr_m, \quad (52)$$

$$p_{pw1}^u = p_{pw1} + B(r_1, \theta_1 - \theta_1^{pw1}) + e^{ikr_{12} \cos \theta_1^{pw1}} B(r_2, \theta_2^{pw1} - \theta_2), \quad (53)$$

$$p_{pw2}^u = p_{pw2} + e^{ikr_{12} \cos \theta_1^{pw1}} [B(r_2, \theta_2 - \theta_2^{pw2}) + e^{-ikr_{23} \cos \theta_2^{pw2}} B(r_3, \theta_3^{pw2} - \theta_3)], \quad (54)$$

$$p_{pw3}^u = p_{pw3} + e^{ikr_{13} \cos \theta_3^{pw3}} [B(r_3, \theta_3 - \theta_3^{pw3}) + e^{-ikr_{13} \cos \theta_3^{pw3}} B(r_1, \theta_1^{pw3} - \theta_1)]. \quad (55)$$

In (51)–(55), we have introduced the plane wave boundary layer corrections defined by

$$B(r, \theta) = \frac{1}{\sqrt{\pi}} F[(2kr)^{1/2} \sin \frac{1}{2}\theta] e^{(ikr-i\pi/4)} - H(-\theta) e^{(ikr-i\pi/4)}. \quad (56)$$

The function $F(z)$ is defined in Eq. (17), while $H(x)$ is the Heaviside step function. $B(r, \theta)$ differs significantly from zero only in a region of angular thickness $O(kr)^{-1/2}$ around the line $\theta = 0$. It provides a uniformly valid additive correction along plane wave boundaries.

6.2. Local solutions for essential diffraction points

Here we have three interacting diffraction regions. The unknown functions in the outer field are the three “uniform” directivities $D_m^u(\theta)$, $m = 1, 2, 3$. The formulation of the local problems is nearly identical to that described in Section 5 for two regions, except that summation over regions must be extended to three.

Two configurations of the triangle were considered. In each case, the incident angle was 70° (as indicated in Fig. 7), the wavelength was $\lambda = 2$, and the radius of each circular blunt was $a = \lambda/2$. In the first configuration the height of the triangle was 8λ and in the second it was 50λ .

We have no reference solution for this problem. We know, however, that to a first approximation there is no mutual influence between the diffraction regions. For a corner in isolation, we have the exact solution to which our approximation was compared in Section 4. Fig. 8 shows the diffraction coefficients for each corner as compared to the case when there is no mutual influence between corners. We see that the influence is indeed small. Further, the effect of the nonuniformities at $\theta_n = 0, \beta_n$ is also apparently small.

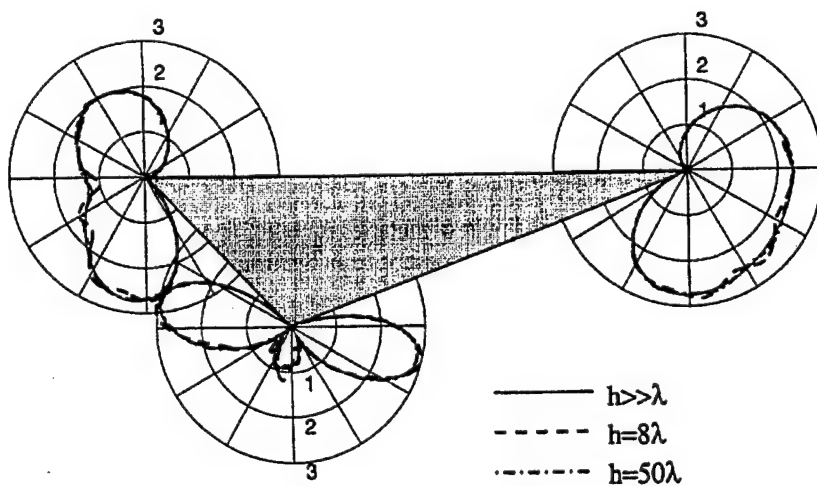


Fig. 8. Scattering from a triangle: diffraction coefficients of each corner for $h = 8\lambda, 50\lambda$.

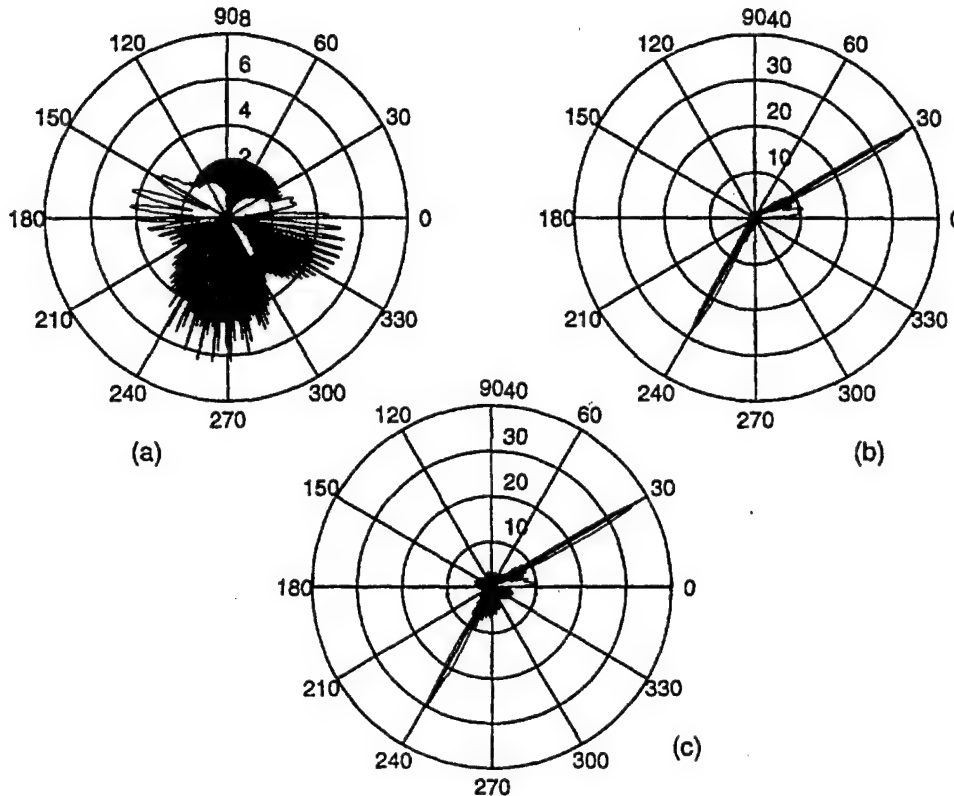


Fig. 9. Far field directivity for a triangle, $h = 8\lambda$: (a) contribution from cylindrical wave fields as expressed in Eq. (64). (b) Contribution from plane wave fields as expressed in Eqs. (61)–(63). (c) Combined contributions.

6.3. Far field directivity

In many domain based numerical methods, evaluating the far field can be difficult. In our method, the outer field is given semi-analytically (51) and so can be easily evaluated at arbitrarily large distances. Alternatively, the far field can be derived explicitly from (51) in terms of the quantities already evaluated. There is no integration required to evaluate the far field.

To derive an explicit expression for the far field, we begin by noting that as $r \equiv r_1 \rightarrow \infty$ with $\theta \equiv \theta_1$, we have

$$r_2 \sim r - r_{12} \cos \theta, \quad (57)$$

$$r_3 \sim r - r_{13} \cos(\theta - \beta_1), \quad (58)$$

$$\theta_2 \sim \theta + \beta_2 - \pi + (r_{12} \sin \theta)/r, \quad (59)$$

$$\theta_3 \sim \theta - \beta_1 + \pi + (r_{13} \sin(\theta - \beta_1))/r. \quad (60)$$

Eqs. (53)–(56) and the asymptotic expansion for $F(z)$ [5] can then be used to write

$$p_{pw1}^u \sim \frac{-e^{i\pi/4}}{2\sqrt{2\pi}} \frac{e^{ikr}}{\sqrt{kr}} \left[\frac{1 - \exp(ikr_{12}(\cos \theta_1^{pw1} - \cos \theta))}{\sin(\theta - \theta_1^{pw1})} \right], \quad r \rightarrow \infty, \quad (61)$$

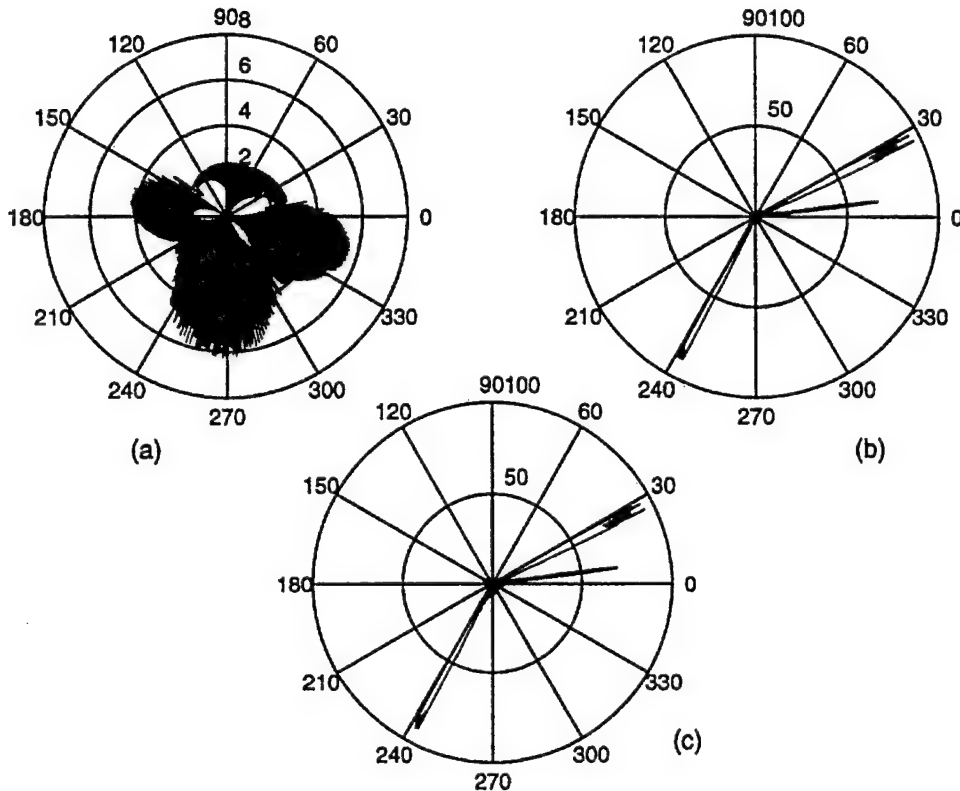


Fig. 10. Far field directivity for a triangle, $h = 50\lambda$: (a) Contribution from cylindrical wave fields as expressed in Eq. (64). (b) Contribution from plane wave fields as expressed in Eqs. (61)–(63). (c) Combined contributions.

$$P_{pw2}^u \sim \frac{-e^{i\pi/4}}{2\sqrt{2\pi}} e^{ikr_{12} \cos \theta_1^{pw1}} \frac{e^{ikr}}{\sqrt{kr}} \left[\frac{1 - \exp(ikr_{23}(\cos \theta_2^{pw2} + \cos(\theta + \beta_2)))}{\sin(\theta - \theta_1^{pw2})} \right], \quad (62)$$

$$P_{pw3}^u \sim \frac{-e^{i\pi/4}}{2\sqrt{2\pi}} e^{ikr_{13} \cos \theta_3^{pw3}} \frac{e^{ikr}}{\sqrt{kr}} \left[\frac{1 - \exp(-ikr_{13}(\cos \theta_3^{pw3} + \cos(\theta - \beta_1)))}{\sin(\theta - \theta_1^{pw3})} \right]. \quad (63)$$

Finally, we need only the far field form of P_{diff}^u . Using (57)–(60) in (52) yields

$$P_{diff}^u \sim (kR)^{-1/2} \sqrt{\frac{R}{r}} e^{ikr} [D_1^u(\theta) + e^{-ikr_{12} \cos \theta} D_2^u(\theta + \beta_2 - \pi) + e^{-ikr_{13} \cos(\theta - \beta_1)} D_3^u(\theta - \beta_1 + \pi)]. \quad (64)$$

Eqs. (61)–(64) yield the far field, directly in terms of $D_m^u(\theta)$ (Eq. (64)) or quantities that are already known (61)–(63).

Figs. 9 and 10 show the far field scattering pattern for the two triangle configurations studied. We note the large specular peaks (described by Eqs. (61)–(63)) and the highly oscillatory “fuzz”, which results from interference of the cylindrical waves as described in Eq. (64).

7. Remarks and conclusion

We have described and demonstrated a hybrid GTD/BSM technique for the calculation of high frequency scattered fields. Our method is based on patching the asymptotic outer expansions to BIE expressions of the near fields.

This is the first presentation of such a technique in which the inner field was described by a BIE. Further, we have demonstrated the application of the method to problems with multiple diffraction points, i.e. interacting computational regions.

In application to a wedge, we have shown the importance of using uniform asymptotic approximations to describe plane wave boundaries. Nonuniformities in the asymptotic expansion can pollute the hybrid solution in a large region of the computational domain.

In the application to scattering from circular cylinders, we demonstrated the hybrid technique when there are interacting numerical regions. In this case, we observed significant error (20%) in the directivities when $D'(\theta) = O(k)$. We conjecture that this error arises from the fact that $p_1|_{\Omega_2}$ (Eq. (32)) provides a poor approximation to a solution of Helmholtz equation over the whole of Ω_2 . (And vice versa for p_2 and Ω_1 .)

Our final application was to a triangularly shaped obstacle. It is easy to see that by changing the geometry of the tip truncations, and choosing a short enough wavelength, one could develop a problem that is impossible to solve by any means other than a hybrid asymptotic-numerical method. In this example, we also see one of the benefits of our hybrid formulation, which is a semi-analytical expression for the outer field. Thus we can easily evaluate the outer field at arbitrary locations in the asymptotic domain, and derive expressions for the far field directly in terms of the unknowns in the formulation.

Acknowledgements

The authors gratefully acknowledge the financial support of ONR.

Appendix A. Analytical solution for blunted wedge

In this appendix we present the analytical solution describing plane wave scattering from a soft wedge with a circularly blunted tip.

The boundary value problem that we wish to solve is:

$$\Delta p + k^2 p = 0, \quad (\text{A.1})$$

$$p = 0, \quad r = a, \quad \theta = 0, \beta, \quad (\text{A.2})$$

$$p_{\text{inc}} = e^{ikr \cos(\theta - \theta_0)}, \quad (\text{A.3})$$

$$p - p_{\text{inc}} = \text{outgoing}. \quad (\text{A.4})$$

The simplest starting point is to decompose p into two parts:

$$p = p_{\text{sharp}} + p_{\text{circ}}. \quad (\text{A.5})$$

Here, p_{sharp} is the total field (incident plus scattered field) with minimum singularity outside a sharp soft wedge illuminated by a plane wave. It is given by [5]:

$$p_{\text{sharp}} = \frac{4\pi}{\beta} \sum_{n=1}^{\infty} J_{v_n}(kr) e^{iv_n \pi/2} \sin v_n \theta_0 \sin v_n \theta. \quad (\text{A.6})$$

Eq. (A.6) satisfies Eqs. (A.1)–(A.4), except for the boundary condition on $r = a$.

We now use (A.5) and (A.6) to find that p_{circ} satisfies:

$$\Delta p_{\text{circ}} + k^2 p_{\text{circ}} = 0, \quad (\text{A.7})$$

$$p_{\text{circ}} = 0, \quad \theta = 0, \beta, \quad (\text{A.8})$$

$$p_{\text{circ}} = -p_{\text{sharp}}, \quad r = a, \quad (\text{A.9})$$

$$p_{\text{circ}} = \text{outgoing}. \quad (\text{A.10})$$

Thus, we determine p_{circ} by separation of variables and obtain

$$p_{\text{circ}} = -\frac{4\pi}{\beta} \sum_{n=1}^{\infty} \frac{J_{v_n}(ka)}{H_{v_n}^{(1)}(ka)} e^{iv_n \pi/2} \sin v_n \theta_0 \sin v_n \theta H_{v_n}^{(1)}(kr). \quad (\text{A.11})$$

References

- [1] M. Abramowitz, I.A. Stegun, *Handbook of Mathematical Functions*, Dover, New York, 1972.
- [2] P.E. Barbone, J.M. Montgomery, I. Harari, O. Michael, Scattering by a hybrid asymptotic/finite element method, *Comput. Methods in Appl. Mech. Eng.* (1998), in press.
- [3] W.D. Burnside, C.L. Yu, R.J. Marhefka, A technique to combine the geometrical theory of diffraction and the moment method, *IEEE Trans. Ant. Prop. AP-23* (1975) 551.
- [4] P.C. Clemmow, *The Plane Wave Spectrum Representation of Electromagnetic Fields*, Pergamon Press, Oxford, 1966.
- [5] D.S. Jones, *Acoustic and Electromagnetic Waves*, Oxford University Press, New York, 1986.
- [6] J.B. Keller, Geometrical theory of diffraction, *J. Opt. Soc. Am.* 52 (2) (1962) 160.
- [7] T.J. Kim, G.N. Thiele, A hybrid diffraction technique – general theory and applications, *IEEE Trans. Ant. Prop. AP-30* (5) (1982) 888.
- [8] R.G. Kouyoumjian, P.H. Pathak, A uniform geometrical theory of diffraction for an edge in a perfectly conducting surface, *Proc. IEEE* 62 (1974) 1448.
- [9] P. M. Marston, *Selected Papers on Geometrical Aspects of Scattering*, SPIE Optical Engineering Press, Bellingham, WA, 1994.
- [10] L.N. Medgyesi-Mitschang, D.S. Wang, Hybrid methods for analysis of complex scatterers, *Proc. IEEE* 77 (5) (1989) 770.
- [11] O. Michael, J. Avrashi, G. Rosenhouse, The boundary strip method in elastostatics and potential equations, *Int. J. Numer. Methods Eng.* 39 (1996) 527.
- [12] O. Michael, J. Avrashi, G. Rosenhouse, A new boundary spectral strip method for non-periodical geometrical entities based on analytical integrations, *Comput. Methods Appl. Mech. Eng.* 135 (1996) 327.
- [13] O. Michael, P.E. Barbone, Singularity subtraction and Galerkin formulation for spectral solutions of boundary integral equations, *Int. J. Numer. Methods Eng.* 41 (1998) 95.
- [14] J.M. Montgomery, J. Barbone, Diffraction from simple shapes by a hybrid asymptotic-finite element method, *J. Acoust. Soc. Am.* 104 (1998), to appear.
- [15] A.D. Pierce, *Acoustics: An Introduction to its physical principles and applications*, Acoustical Society of America, New York, 1989.
- [16] J.N. Sahalos, G.N. Thiele, On the application of the GTD-MM technique and its limitations, *IEEE Trans. Ant. Prop. AP-29* (5) (1981) 780.
- [17] D.S. Wang, Current-based hybrid analysis for surface-wave effects on large scatterers, *IEEE Trans. Ant. Prop.* 39 (6) (1991) 839.
- [18] E. Zauderer, *Partial Differential Equations of Applied Mathematics*, 2nd ed., Academic Press, New York, 1989.

C.3 Scattering by a Hybrid Asymptotic/Finite Element Method

"Scattering by a Hybrid Asymptotic/Finite Element Method," Paul E. Barbone, Joshua M. Montgomery, Ofer E. Michael and Isaac Harari, **Computer Methods in Applied Mechanics and Engineering**, Vol. 164, Nos. 1-2, pp. 141-156, October 1998.



ELSEVIER

Scattering by a hybrid asymptotic/finite element method

Paul E. Barbone^{a,*}, Joshua M. Montgomery^{a,†}, Ofer Michael^a, Isaac Harari^b

^aDepartment of Aerospace and Mechanical Engineering, Boston University, 110 Cummington Street, Boston, MA 02215, USA

^bDepartment of Solids, Materials and Structures, Tel Aviv University, 69978 Tel Aviv, Israel

Abstract

We describe a hybrid asymptotic/finite element method with application to the solution of the Helmholtz equation for large wavenumber. Thus, this method is suitable to compute the acoustic field radiated or scattered by acoustically large objects. The method is based on patching a short wavelength asymptotic expansion of the 'outer' field to an FEM interpolation of the 'inner' field. The patching takes place on an artificial boundary. Continuity of the field and its normal derivative across the artificial boundary is enforced weakly in a variational setting. The variational principle is described, as is an element-like implementation strategy. Two example applications are included: diffraction by a truncated wedge and radiation by a source on a wave bearing surface. © 1998 Elsevier Science S.A. All rights reserved.

1. Introduction

We describe a hybrid method for scattering which combines short-wavelength asymptotics with the finite element method (FEM). In our hybrid approach, we attempt to draw on the benefits from both methods while eliminating their largest individual deficiencies. For example, an asymptotic approach can be computationally efficient for acoustically large obstacles; its applicability, however, is limited, since diffraction coefficients are available for only relatively simple geometries. The finite element method, on the other hand, can accommodate arbitrary geometries and material properties. It is practically limited, however, to relatively low frequencies by its computational cost. A further complication of applying the finite element method to unbounded domains is the treatment of the radiation condition. In our formulation, the radiation boundary condition is satisfied by appropriately joining the finite element discretization with the asymptotic representation of the field.

The hybrid method presented here is related to the method of matched asymptotic expansions [8] where, in the short wavelength limit, the scattered field contains two asymptotic regions. In the 'outer' domain, we have a 'global' asymptotic expansion, which we assume to be given by a geometrical optics ray series (short wavelength expansion.) This expansion is valid almost everywhere in the domain. Where it is not valid, we supplement the outer expansion with an 'inner' or 'local' solution. This local solution is found using the finite element method, and is patched to the outer expansion along an artificial boundary. Thus, the FEM is applied to a collection of small regions (size $O(\lambda)$ = wavelength) in the vicinity of diffraction points. See Fig. 1.

The total solution of a given scattering problem is thus decomposed into an application of the geometrical theory of diffraction (GTD) or any other suitable asymptotic approximation, in conjunction with a finite element solution of a problem defined over the union of several small domains.

This paper combines and extends incremental contributions described previously into a unified framework, and makes precise several notions upon which our earlier work [1,23] was based. In some respects, it is the FEM counterpart to Barbone and Michael [3], which describes a hybrid GTD/BIE method and applies it to several examples. In [1], Montgomery and Barbone described a hybrid GTD/FEM method to evaluate

* Corresponding author.

† Current affiliation: Noise and Acoustics Division, The Boeing Company, Seattle, WA 98124, USA.

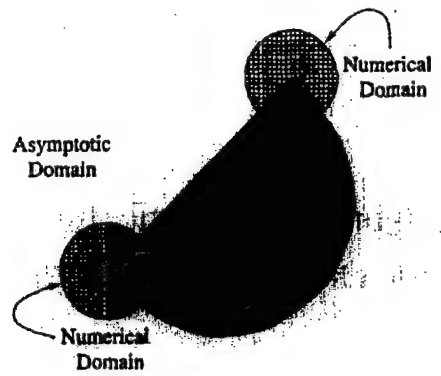


Fig. 1. Example scatterer. Almost everywhere outside the scatterer, a global asymptotic expansion in the form of a ray series is valid. We use this representation of the field in the 'asymptotic domain'. At each of the two corners in the scatterer, however, the ray-based asymptotic representation of the field is invalid. Near these corners, therefore, we represent the solution on a finite element mesh. The union of these two 'diffraction regions' is our 'numerical region'.

diffraction coefficients. The applicability of their implementation was limited to cylindrical waves in the outer field only. This was slightly generalized in [23].

In this paper, we define 'essential and inessential diffraction points' for the first time, and make precise the concept of a 'diffraction region'. This is the region within which we represent the solution on a finite element basis. We also describe an element-based data structure which allows our method to be incorporated into existing FEM codes. This strategy can accommodate any analytical representation of the outer field. We demonstrate this fact with the first reported example of our hybrid method that incorporates surface waves.

The paper is composed of the following sections. Section 2 describes the background of hybrid asymptotic-numerical methods in scattering. This is followed in Section 3 by a description of our hybrid method. This is presented in a manner which is independent of the numerical method chosen. Readers familiar with [3] in which our hybrid GTD/BIE method is described may elect to skip directly to Section 4, where a variational formulation suitable for finite element implementation is described. Section 5 describes an element-like data structure that simplifies FEM programming, and can easily accommodate any analytical representation of the outer field. Finally, two example applications are presented in Sections 6 and 7. The first of these represents scattering from a wedge, while the second applies to radiation from an impedance plane and includes trapped surface waves.

2. Background

We consider the problem of computing the complex acoustic pressure field scattered by large obstacles. In particular, we are interested in finding an efficient method to solve the Helmholtz equation for large wave number k :

$$\Delta u + k^2 u = 0 \quad x \in \Omega. \quad (1)$$

Here, u is the (complex) acoustic pressure perturbation or velocity potential relative to a time dependence of $e^{-i\omega t}$. $\Omega \subset R^d$ is the d -dimensional infinite domain exterior to the obstacle; i.e. $\Omega = R^d \setminus \bar{\mathcal{O}}$, where \mathcal{O} represents the obstacle. On the surface of the obstacle $\partial\mathcal{O}$, u satisfies a (linear) boundary condition consistent with continuity of traction and normal velocity. Though we later describe an example treating an impedance boundary condition, for simplicity of this presentation we shall employ the Dirichlet boundary condition:

$$u = 0 \quad x \in \partial\mathcal{O}. \quad (2)$$

The scattering excitation is due to an incident wave u_{inc} that identically satisfies (1) but not necessarily (2). This gives rise then to the scattered wave u_{scat} . The scattered field satisfies

$$u = u_{\text{inc}} + u_{\text{scat}} \quad (3)$$

$$\lim_{r \rightarrow \infty} r^{(d-1)/2} \left[\frac{\partial u_{\text{scat}}}{\partial r} - ik u_{\text{scat}} \right] = 0 \quad (4)$$

Eq. (1)–(4) define a unique boundary value problem for the scattered pressure u_{scat} .

2.1. Traditional numerical approaches

Many methods exist already to find approximate solutions of the above boundary value problem. Finite element methods are, perhaps, the most popular. A naive estimate of the cost of solving such a problem with FEM can be obtained by considering the discretization requirements to scale with the wavenumber (i.e. $kh = \text{constant}$; h is the element size).² For a three-dimensional body \mathcal{O} with typical dimension L , this requirement translates into $N_{\text{dof}} = O((kL)^3)$. Here, N_{dof} is the number of degrees of freedom in the discrete equations. Considering the banded structure of the finite element matrix, direct inversion cost scales as $\text{Cost} = O((kL)^7)$.

Another popular strategy for finding an approximate solution to the boundary value problem (1)–(4) is to apply boundary integral equation (BIE) techniques. These form the basis of the ‘Surface Variational Principle’ which is described in [26]. More traditionally, the BIE gives rise to Boundary Element Methods, Method of Moments, or the more recently described Boundary Strip Method. We shall neglect discussing formulation costs and uniqueness issues, and focus only on discretization requirements. Meshing the two-dimensional surface of a three-dimensional body according to $kh = \text{constant}$ yields a scaling that grows as $N_{\text{dof}} = O((kL)^2)$. The cost associated with the direct factorization of the resulting full, nonsymmetric matrix grows as $\text{Cost} = O((kL)^6)$.

The result of applying finite element or boundary element methods is an approximate solution $u_{\text{scat}}^h \approx u_{\text{scat}}$. The method is said to ‘converge’ if

$$\lim_{kh \rightarrow 0} u_{\text{scat}}^h \rightarrow u_{\text{scat}} \quad (5)$$

Of course, in any particular application, h is finite. Eq. (5) indicates that the numerical solution is an asymptotic approximation of the exact solution, evaluated at a finite value of the asymptotic parameter h . One important feature of numerical methods is that the user has control over the value of the asymptotic parameter. That is, the possibility usually exists of obtaining a better approximate solution by decreasing h .

We conclude this discussion by noting that both FEM and BEM costs grow rapidly at large kL . Further, the result of using either method is an asymptotic approximation of the exact solution which the user can refine as required. The relative cost at very large values of N_{dof} as presented here should not be taken too literally. For very large systems of equations, for example, iterative solvers would typically be employed. Therefore, our scalings based on direct inversion would be inapplicable. For more detailed cost considerations of the two methods, see Harari and Hughes [11] and Michael and Barbone [22].

2.2. Traditional asymptotic approaches

Since we are especially concerned with obtaining solutions at large kL , we briefly discuss asymptotic methods devised to capture this limit. The method with which we shall work here is the Geometrical Theory of Diffraction, or GTD [17]. GTD can be thought of as an application of matched asymptotic expansions, in which the outer expansion is given by the ansatz

$$u_{\text{scat}} \approx u^G(x) = \sum_{\text{ray } j} a_j(kl) A_j(x) \exp(ik\psi_j(x)). \quad (6)$$

²This estimate ignores ‘pollution’ effects arising from numerical dispersion.

In the first approximation, the *phase* functions ψ and *amplitude* functions $A(x)$ satisfy the following eiconal and transport equations:

$$(\nabla\psi)^2 - 1 = 0 \quad (7)$$

$$2\nabla\psi \cdot \nabla A + \Delta\psi A = 0. \quad (8)$$

Such an expansion (6) typically results in an approximation which is asymptotic in kL :

$$\lim_{kL \rightarrow \infty} u^G \rightarrow u_{\text{scat}} \quad \text{almost everywhere in } \Omega. \quad (9)$$

We note the similarity between (5) and (9). We also note a very important distinction. In (5), the analyst has control over the asymptotic parameter h , whereas in (9) the analyst is typically interested in the field at a fixed value of kL . Therefore, the possibility of obtaining a better approximation by raising kL does not exist. There is the possibility of increasing the rate of ‘convergence’ by using a higher order approximation. This typically improves the accuracy at a fixed kL . By the nature of a (non-convergent) asymptotic expansion, however, it is impossible to obtain arbitrarily high accuracy for a fixed value of kL .

To apply GTD, one must integrate the ray equations, integrate the phase along each ray, integrate the transport equations along each ray, etc. When a ray intersects the surface of the body, the wave can be reflected, transmitted, diffracted, etc. and corresponding reflected, transmitted, or diffracted rays are introduced accordingly. Ray discretization requirements are determined by the geometry of the body (and the medium) and are therefore independent of k . Further, the ray and transport equations are independent of k . Thus the computational cost associated with computing the field scattered by a large body using GTD is independent of k .

At diffraction points (defined below), an inner or ‘canonical’ problem must be solved and then asymptotically matched to the outer field. For matching purposes, such a solution is typically required in some analytical form. The availability of such solutions for complicated diffraction geometries practically limits the applicability of GTD to problems with simple discontinuities.

2.3. Hybrid asymptotic-numerical approaches

The first description of a hybrid GTD-integral equation approach is due to Burnside [4]. His and other approaches since depend on a method of moments formulation of the overall problem. Shape functions based on the ansatz (6) are then substituted into the integral equation (see [4,29,18,21,31]). These methods all rely on a single global integral equation representation of the field. Thus, they require the integration of rapidly oscillating and hyper-singular functions over large domains. Therefore, we have rejected hybrid approaches based on these formulations.

Jin and coworkers [30,10,15] describe some very recent work on combining FEM with a uniform theory of diffraction (UTD). These authors propose solving the canonical diffraction problem as a preprocess using FEM, and they describe how to build the result into a UTD formulation. Similar approaches are advocated in [28,5,24]. Calamia et al. [5] make a point of adequately enforcing the radiation condition on the calculation of the inner solution in order to avoid uniqueness problems at interior eigenfrequencies.

Ross et al. [27] describe combining the FEM with a modal expansion for the analysis of a jet engine inlet. Again, the FEM computation and inversion is done as a first step in the analysis in order to obtain an approximate scattering matrix for the engine inlet. Calculations combining FEM with analytical expansions in Floquet wave bases are presented in [7,24].

In all the hybrid FEM analyses just described, the FEM problem is formulated and solved independently of the total scattering problem. One might think of this as a simple extension of the original GTD framework. The difference is that the solutions of the ‘canonical’ problems here are found numerically for every incident field and then stored.

Givoli and Keller [9] have proposed DtN maps as a general method of computation in truncated domains. They require an exact solution of the field equations in some portion of the domain in order to construct the DtN map. Effectively, in what follows, one may think of our approach as a way to construct the DtN map using any approximation to the field.

3. The hybrid asymptotic-numerical method

Here, we consider acoustic scattering from a large obstacle; i.e. one that satisfies $kL \gg 1$. In most of the domain, we shall use an asymptotic approximation based on this inequality. In the rest of the domain, we shall use an FEM representation of the field. In this section, we first describe how we divide the domain into these asymptotic and numerical regions. This division depends on the concept of a diffraction point. Then, we define an asymptotically equivalent boundary value problem on a union of ‘diffraction regions.’ We discuss the numerical solution of this boundary value problem through several examples in the following sections.

3.1. Diffraction points

In order to obtain an approximation to u_{scat} , we proceed as follows. We first apply the principles of GTD to obtain a ‘global’ asymptotic solution.³ Some of the coefficients (diffraction coefficients in particular) in the outer expansion cannot be determined from the outer equations alone. Further, there is a set of points of zero measure at which the expansion (6) is not asymptotic; i.e. that set of points where (9) is not valid. Thus we define the set of diffraction points X^D to be

$$X^D = \left\{ x \mid \lim_{kL \rightarrow \infty} u_{\text{scat}} - u^G \neq 0 \right\} \quad (10)$$

We note that since u^G is not asymptotic to u_{scat} at x^D , then for any *finite value* of kL , u^G will typically provide a very poor approximation to u_{scat} in a whole neighborhood of x^D . For that reason, we must consider local corrections to u^G valid in the vicinity of x^D in order to obtain a practically useful approximation for moderate values of kL .

The diffraction points can be classified as either of two types. We shall refer to them as *essential diffraction points* and *inessential diffraction points*. The local solution valid in the neighborhood of an essential diffraction point determines the coefficients of the homogeneous solutions of the global equations. The local solution valid in the neighborhood of an inessential diffraction point, on the other hand, yields no information about the global solution. Typically, the locations of essential diffraction points do not depend on the properties of the incident field (such as its angle of incidence.) They are purely geometric in origin and are typically associated with edges and vertices. The locations of inessential diffraction points, on the other hand, often change with the incident field parameters. Examples include shadow boundaries, foci and caustics. The distinction between essential and inessential diffraction points is hardly important except that we shall deal with the former numerically and with the latter analytically.

In order to obtain an approximate solution which is valid at the diffraction points, it is necessary to find an inner or local solution. This solution is then matched to the outer solution. The result is a set of approximations (local and global) that together have a range of validity that includes the entire domain. We again emphasize the importance of the local corrections when using the asymptotic approximations at any finite value of kL . For inessential diffraction points, local solutions are typically available in the literature (cf. [20]). For essential diffraction points, solutions are typically available for only simple shapes and boundary conditions. The hybrid method that we propose describes a way to obtain approximate solutions valid near essential diffraction points.

3.2. Diffraction regions

To do so, we introduce diffraction regions. Around each *contiguous* set of essential diffraction points, we define a diffraction region Ω^D such that:

³ We shall alternatively use the terms ‘outer’ and ‘global’ to refer to quantities asymptotically valid in regions away from diffraction points. ‘Local’ or ‘inner’ regions are λ^a sized neighborhoods of diffraction points, where λ is the wavelength of sound in the fluid. Diffraction points are defined later in the text.

$$\Omega^D = \left\{ x \mid k|x - x^D| \leq (kR)^\alpha f \left(\frac{x - x^D}{|x - x^D|} \right) \right\} \quad (11)$$

Here, x^D is a diffraction point and R is a fixed distance, a parameter to be chosen by the analyst, which determines the size of the diffraction region. The shape of the diffraction region is determined by the choice of $f(x - x^D/|x - x^D|)$. The accuracy of our hybrid method depends on $kR \gg 1$. We denote by Γ_R the boundary of each diffraction region. The parameter α is chosen so that Γ_R lies in the ‘overlap’ domain between the inner and outer regions. That is, it lies in the domain where both inner and outer expansions are valid.

3.3. Asymptotically equivalent boundary value problem

Now, we are in position to define an asymptotically equivalent boundary value problem. This problem is nothing more than a restriction of our original boundary value problem to the diffraction regions, with continuity enforced across the artificial boundary Γ_R . Thus, we define

$$\Delta u^D + k^2 u^D = 0 \quad x \in \Omega^D \quad (12)$$

$$u^D = -u_{\text{inc}} \quad x \in \partial\Omega^D \cap \partial\Omega \quad (13)$$

$$u^D = u^{\text{Asymp}} \quad x \in \Gamma_R \quad (14)$$

$$\partial_n u^D = \partial_n u^{\text{Asymp}} \quad x \in \Gamma_R. \quad (15)$$

Here, u^{Asymp} is our global asymptotic approximation. It could be obtained by GTD as indicated in Eq. (6), by the Uniform Theory of Diffraction [19], or by GTD with local corrections for inessential diffraction points. We shall give examples using both corrected and uncorrected GTD below. Montgomery and Barbone [1] have shown in wedge geometries that patching u^D on $kR = \text{constant}$ as described in Eqs. (14) and (15) is asymptotically equivalent to matching.

Our hybrid GTD/FEM method is now simply stated. We have the ‘asymptotically equivalent’ boundary value problem (12)–(15) defined on the small (size kR) *interior* domain Ω^D . We shall formulate and solve that boundary value problem using FEM. Other numerical methods might be adapted to solve this boundary value problem, too. Barbone and Michael [3] demonstrate its solution using the boundary spectral strip method.

4. Variational formulation

We shall now describe a variational formulation suitable to solve the ABVP described above using the finite element method. The formulation was derived in [12].

The variational form of the boundary-value problem is stated in terms of sets of trial solutions, \mathcal{S}^i and \mathcal{S}^o for u^i and u^o , respectively. Here, we define

$$\mathcal{S}^i = \{u^i | u^i \in H^1(\Omega^D), \quad u^i = -u_{\text{inc}} \in \partial\Omega \cap \partial\Omega^D, \quad u^i = 0 \text{ in } \Omega^A\}. \quad (16)$$

The space \mathcal{S}^o is

$$\begin{aligned} \mathcal{S}^o = & \{u^o | \Delta u^o + k^2 u^o = 0 \in \Omega^A, \quad u^o \text{ is outgoing}, \\ & u^o = -u_{\text{inc}} \in \partial\Omega \cap \partial\Omega^A, \quad u^o = 0 \text{ in } \Omega^D\}. \end{aligned} \quad (17)$$

We introduce a functional $\Pi(u^i, u^o)$, defined as

$$\Pi(u^i, u^o) = \frac{1}{2} a(u^i, u^i) + \left(\partial_n u^o, u^i - \frac{1}{2} u^o \right)_{\Gamma_R} \quad (18)$$

$$a(w, u) = \int_{\Omega^D} (\nabla w \cdot \nabla u - wk^2 u) d\Omega \quad (19)$$

$$(w, u)_{\Gamma_R} = \int_{\Gamma_R} w u \, d\Gamma \quad (20)$$

$a(\cdot, \cdot)$ and $(\cdot, \cdot)_{\Gamma_R}$ are symmetric bilinear forms which are *not* inner products. We seek $u^i \in \mathcal{S}^i$ and $u^o \in \mathcal{S}^o$ that render Π stationary. This leads the following equations that hold for all $w^i \in \mathcal{V}^i$ and all $w^o \in \mathcal{V}^o$:

$$\begin{aligned} a(w^i, u^i) + (w^i, \partial_n u^o)_{\Gamma_R} &= 0 \\ (\partial_n w^o, u^i)_{\Gamma_R} - (\partial_n w^o, u^o)_{\Gamma_R} &= 0 \end{aligned} \quad (21)$$

The sets of variations \mathcal{V}^i and \mathcal{V}^o are the counterparts of \mathcal{S}^i and \mathcal{S}^o , respectively, satisfying homogeneous boundary conditions on the surface of the obstacle.

The Euler–Lagrange equations resulting from Eq. (21) include (12)–(15), the strong form of our boundary value problem on Ω^D . The weak form (21) requires integration only over the (small) diffraction regions, Ω^D , and the artificial boundary Γ_R . Further, the formulation is symmetric, and accommodates different interpolations in Ω^D and Ω^A , respectively. Continuity between the inner and outer fields is enforced weakly in the second of Eqs. (21). This equation also allows us to evaluate any unknown coefficients in the global expansion u^o .

5. Implementation: element formulation

The weak form (21) has non-standard terms in it that fall outside the typical finite element framework. In this section, we describe an element-type data structure that allows the above formulation to be readily implemented in an existing finite element code. The finite element code must be supplemented by a subroutine or function that can evaluate $u^o(x)$.

We begin by replacing \mathcal{S}^i and \mathcal{S}^o by finite dimensional approximations. In particular, we approximate u^o and w^o as

$$u^o \approx u^{Asymp} \approx u_h^A = \sum_{\alpha=1}^{N_{dof}^A} M_\alpha(x) b_\alpha + U(x), \quad (22)$$

$$w^o \approx w^{Asymp} \approx w_h^A = \sum_{\alpha=1}^{N_{dof}^A} M_\alpha(x) \gamma_\alpha. \quad (23)$$

Here, the coefficients b_α are unknown and γ_α are arbitrary weighting coefficients. The functions $M_\alpha(x) \in \mathcal{V}^o$ form the basis of our outer representation and are determined by a GTD analysis. The function $U(x) \in \mathcal{S}^o$ is known, and results from the inhomogeneous boundary data on $\partial\mathcal{O} \cap \partial\Omega^A$. We note that $M_\alpha(x)$ and $U(x)$ have non-compact support in general.

We divide Γ_R into a collection of nonoverlapping elements:

$$\Gamma_R = \bigcup_{e=1, N_{Bd_elem}} \Gamma_{el}^e \quad \Gamma_{el}^a \cap \Gamma_{el}^b = \emptyset \quad \{a \neq b\}. \quad (24)$$

Within each element, Γ_{el}^e , we approximate u^i by

$$u^i|_{\Gamma_{el}^e} \approx u_h^i|_{\Gamma_{el}^e} = \sum_{A=1}^{N_{dof}^{FEM}} N_A(x) d_A. \quad (25)$$

We now construct an ‘element’ that has $N_{dof}^{FEM} + N_{dof}^A$ total degrees of freedom as depicted in Fig. 2. The N_{dof}^A degrees of freedom are shared by *all the elements on Γ_R* , and represent all of the unknowns in u_h^A . The N_{dof}^{FEM} represent the nodal values of u_h^i at the finite element nodes in Γ_{el}^e .

With these definitions, we can introduce a complex symmetric ‘element stiffness’ matrix that has the form:

$$\mathbf{K}^e = \begin{bmatrix} 0 & K^{12} \\ K^{21} & K^{22} \end{bmatrix} = (N_{dof}^{FEM} + N_{dof}^A) \times (N_{dof}^{FEM} + N_{dof}^A) \quad (26)$$

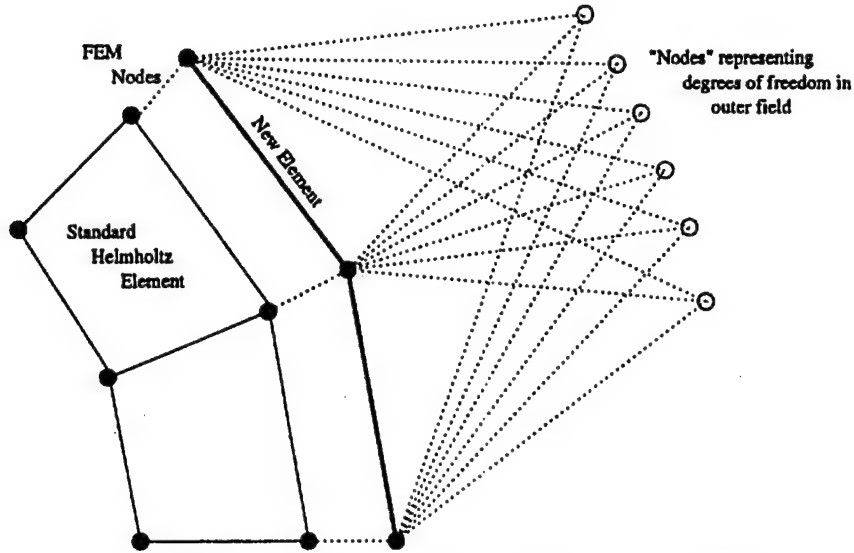


Fig. 2. Element Structure: The boundary elements contain N_{dof}^A generalized degrees of freedom associated with the outer asymptotic approximation. These generalized degrees of freedom are coupled to two standard finite element nodes in each boundary element. The two standard FEM nodes are shared between the boundary element and the standard element, indicated by a dotted line in the figure.

The terms in the individual blocks are given by:

$$K_{A\alpha}^{12} = \int_{\Gamma_{\text{el}}^e} N_A \frac{\partial M_\alpha}{\partial n_0} d\Gamma \quad (27)$$

$$K_{\alpha A}^{21} = K_{A\alpha}^{12} = \int_{\Gamma_{\text{el}}^e} N_A \frac{\partial M_\alpha}{\partial n_0} d\Gamma \quad (28)$$

$$K_{\alpha\beta}^{22} = K_{\beta\alpha}^{22} = - \int_{\Gamma_{\text{el}}^e} \frac{\partial M_\alpha}{\partial n_0} M_\beta d\Gamma \quad (29)$$

Similarly, the function $U(x)$ gives rise to an element force vector, given by

$$\mathbf{f}^e = \begin{Bmatrix} f^1 \\ f^2 \end{Bmatrix} = (N_{\text{dof}}^{\text{FEM}} + N_{\text{dof}}^A) \times 1 \quad (30)$$

$$f_A^1 = - \int_{\Gamma_{\text{el}}^e} N_A \frac{\partial U}{\partial n_0} d\Gamma \quad A = 1, \dots, N_{\text{dof}}^{\text{FEM}} \quad (31)$$

$$f_A^2 = - \int_{\Gamma_{\text{el}}^e} \frac{\partial U}{\partial n_0} U(x) d\Gamma \quad \alpha = 1, \dots, N_{\text{dof}}^A \quad (32)$$

The element can be treated geometrically using the standard isoparametric concept based on the FEM nodes alone. The integrals indicated in Eqs. (27)–(29) and (31)–(32) can be evaluated using low order Gaussian quadrature (based on the order of the finite element interpolations functions, N_A , when the inner field is sufficiently resolved.) To form the element stiffness, a function or subroutine must be available to evaluate M_α and $U(x)$ at the element Gauss points.

We shall now illustrate our method through simple examples. We shall first consider a simple wedge geometry. This will allow us to show examples of essential and inessential diffraction points, and show how to deal with each. Then we shall investigate radiation by a source on an impedance plane. In this latter example, the outer field has both radiated cylindrical waves and surface waves.

6. Application to a wedge

Our first example is diffraction from an infinite blunted wedge. This example was also treated in [1,3]. Montgomery and Barbone [1] required the solution for the corresponding sharp wedge, while Barbone and Michael [3] described the solution using a boundary integral formulation.

6.1. Formulation

Here, we consider scattering of a plane wave by a soft blunted wedge. The problem is depicted in Fig. 3. We shall allow the end of the wedge to be truncated with some shape. Such geometrical detail is assumed to be the size of a wavelength or smaller. For definiteness, we consider the wedge truncated with a circle of diameter $2a = \lambda$. Since the wedge is soft, the boundary condition on the wedge surfaces is $u = 0$.

The incident plane wave is taken to be of the form

$$u_{\text{inc}} = e^{ik(x \cos \theta_i + y \sin \theta_i)} = e^{ikr \cos(\theta - \theta_i)}. \quad (33)$$

Here, θ_i is the angle of incidence and k is the wave number. Thus, u_{scat} satisfies (1)–(4) with u_{inc} given by (33).

6.2. The global solution

To find a global approximation to the solution, we begin with a GTD ansatz in terms of R , a chosen reference length:

$$u_{\text{scat}} \sim [A_0(x) + (kR)^{-1} A_1(x) + \dots] e^{ik\psi_1(x)} + (kR)^{-1/2} [B_0(x) + (kR)^{-1} B_1(x) + \dots] e^{ik\psi_2(x)}. \quad (34)$$

The factor of $(kR)^{-1/2}$ in the second term on the right-hand side of (34) is inserted for scaling purposes. We apply the laws of GTD [17] to the wedge shown in Fig. 4. Thus, we write the scattered field as a sum of two plane waves and a diffracted cylindrical wave as indicated in the Fig. 4:

$$u_{\text{scat}} \sim u^G = u_{\text{shadow}} + u_{\text{reflected}} + u_{\text{diffracted}} \quad r \neq 0; \theta \neq \theta_r, \theta_i. \quad (35)$$

Here, the first two terms are associated with the A_0 solution in (34), while $u_{\text{diffracted}}$ is associated with the B_0 term in (34). We shall neglect A_1 , B_1 and all higher order terms. We have chosen an incident angle for which there is both a reflected and a shadow wave. For angles of incidence $0 < \theta_i < 2\pi - \beta$, however, there would be two reflected waves. If $\beta - \pi < \theta_i < \pi$ then there will be two shadow waves.

The individual terms in (35) are given as follows:

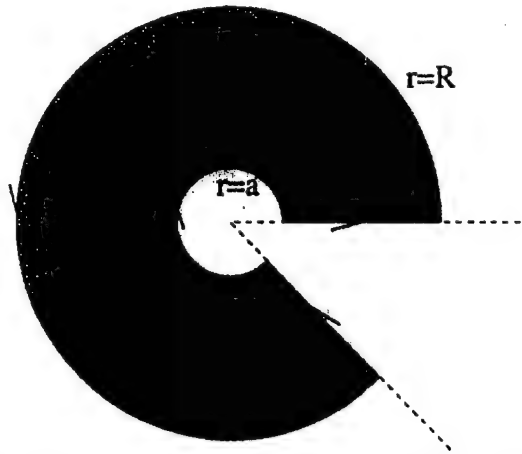


Fig. 3. A blunted wedge. Dark shaded area is the 'diffraction region,' which is subsequently meshed. The 'outer domain' corresponds to $r > R$, and r_a is the curve $r = R$.

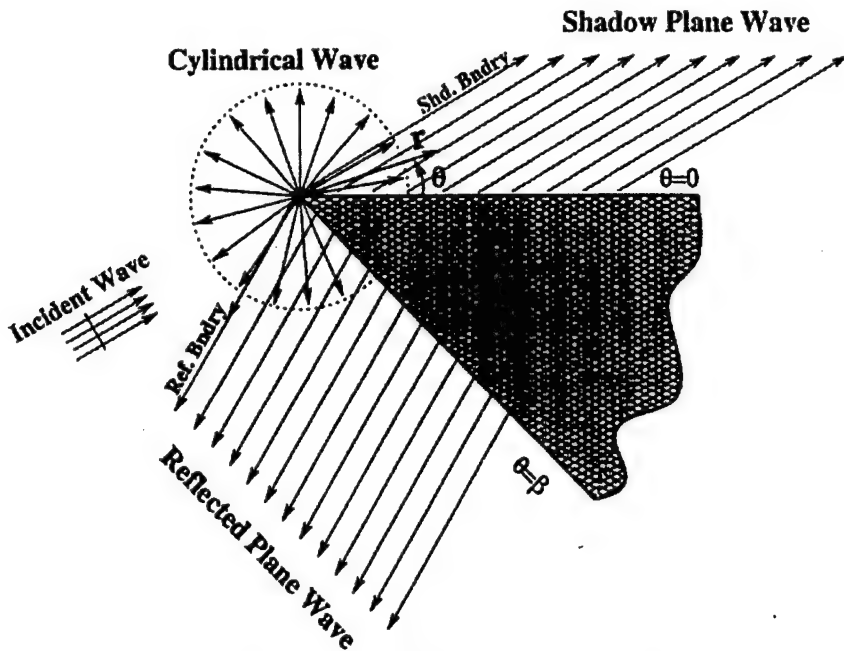


Fig. 4. The reflected and diffracted waves from a wedge.

$$\begin{cases} u_{\text{shadow}} = -e^{ikr \cos(\theta - \theta_s)} & 0 \leq \theta < \theta_s \\ u_{\text{reflected}} = -e^{ikr \cos(\theta - \theta_r)} & \theta_r < \theta \leq \beta \\ u_{\text{diffracted}} = (kR)^{-1/2} D(\theta) \sqrt{\frac{R}{r}} e^{ikr} & 0 \leq \theta \leq \beta \\ & kr \rightarrow \infty \end{cases} \quad (36)$$

The reflected and shadow wave amplitudes have been determined by enforcing the boundary condition (2) on the wedge faces to leading order in kR . The r dependence in $u_{\text{diffracted}}$ is determined by the transport equation for B_0 . The function $D(\theta)$, the diffraction coefficient for the edge, is unknown at this stage, and depends on the precise form of the truncation.

We note that the plane wave expressions in (36) are defined only for certain values of the angle. Outside the ranges specified in (36) they are understood to be zero. Thus, our expression for u^G has discontinuities at $\theta = \theta_s$, θ_r .

6.3. Local solutions

We note that Eq. (35) is not valid at $r = 0$, nor at $\theta = \theta_r$, θ_s . These define sets of ‘diffraction points.’ The point $r = 0$ is classified as an essential diffraction point since its location is independent of the incident field parameters. The angles $\theta = \theta_r$, θ_s , on the other hand, clearly do depend on the incident field parameters. The set of points that makeup the lines $\theta = \theta_r$, θ_s are classified as inessential diffraction points. We shall consider local solutions near the inessential diffraction points first.

6.3.1. Reflection and shadow boundaries

The inner solution valid along the line $\theta = \theta_s$ represents a boundary layer solution. It can be found in many text books, either directly or indirectly (see for example [32,6,16,25]). The boundary layer solution is required to satisfy the parabolic wave equation in the direction of propagation ($\theta = \theta_s$). The matching conditions require the boundary layer solution to tend to zero outside the shadow region and to reproduce the shadow wave in the shadow region.

There is no unique solution to the boundary layer equations. Many different representations are possible, including one that is an exact solution of the Helmholtz equation. (Recall that this is not required by the

asymptotic analysis.) We choose this representation for our boundary layer solution. It is expressed as

$$u_{\text{shadow}}^{\text{uniform}} = -\frac{1}{\sqrt{\pi}} \left\{ F \left[(2kr)^{1/2} \sin \frac{1}{2}(\theta - \theta_s) \right] \right\} \exp \left\{ ikr - \frac{i\pi}{4} \right\}. \quad (37)$$

Here, $F(z)$ is defined as (note that we use the complex conjugate of that used by Jones [16]):

$$F(z) = e^{-iz^2} \int_z^\infty e^{it^2} dt. \quad (38)$$

We note that

$$u_s \sim u_{\text{shadow}}^{\text{uniform}} + O(kR)^{-1/2} \quad \text{for } (kr)^{1/2} \sin \frac{1}{2}(\theta - \theta_s) \ll 1. \quad (39)$$

Thus, $u_{\text{shadow}}^{\text{uniform}}$ provides our asymptotic approximation to the scattered field that is valid in the vicinity of the shadow boundary. Similarly, we define $u_{\text{reflected}}^{\text{uniform}}$ for the reflection boundary region:

$$u_{\text{reflected}}^{\text{uniform}} = -\frac{1}{\sqrt{\pi}} \left\{ F \left[(2kr)^{1/2} \sin \frac{1}{2}(\theta_r - \theta) \right] \right\} \exp \left\{ ikr - \frac{i\pi}{4} \right\}. \quad (40)$$

The function $F(z)$ has the property that $F(-z) = \sqrt{\pi} e^{-iz^2+i\pi/4} - F(z)$ [16]. Further, when $z \gg 1$, $-\pi/2 < \arg(z) < \pi$, $F(z)$ can be approximated by the expansion [16]

$$F(z) \sim i/2z + 1/4z^3 + O(z^{-5}). \quad (41)$$

Combining the two features of $F(z)$ shows that

$$u_{\text{shadow}}^{\text{uniform}} \sim u_{\text{shadow}} \quad \text{for } (kr)^{1/2} \sin \frac{1}{2}(\theta - \theta_s) \gg 1, \quad (42)$$

$$u_{\text{reflected}}^{\text{uniform}} \sim u_{\text{reflected}} \quad \text{for } (kr)^{1/2} \sin \frac{1}{2}(\theta_r - \theta) \gg 1. \quad (43)$$

Thus, we see that $u_{\text{reflected}}^{\text{uniform}}$ and $u_{\text{shadow}}^{\text{uniform}}$ reproduce u_{shadow} and $u_{\text{reflected}}$ in the outer regions. Therefore, we conclude that $u_{\text{reflected}}^{\text{uniform}}$ and $u_{\text{shadow}}^{\text{uniform}}$ provide approximations to the scattered field valid at all angles. This allows us to write

$$u_{\text{scat}} \sim u^{\text{Asymp}} = u_{\text{reflected}}^{\text{uniform}} + u_{\text{shadow}}^{\text{uniform}} + u_{\text{diffracted}}^{\text{uniform}} \quad \forall \theta; r \neq 0. \quad (44)$$

$$u_{\text{diffracted}}^{\text{uniform}} = (kR)^{-1/2} D''(\theta) \sqrt{\frac{R}{r}} e^{ikr}. \quad (45)$$

Eqs. (35) and (44) both provide asymptotic approximations to u_{scat} . They are both formally accurate to $O(kR)^{-1/2}$. The difference between them is that (44) is valid for all angles θ , while (35) is not valid at the two angles $\theta = \theta_r, \theta_s$. In the case of Eqs. (35) and (36), the function $D(\theta)$ is unknown and needs to be determined. In the case of (44) and (45), the as yet unknown function is $D''(\theta)$.

6.3.2. The essential diffraction point

The point $r = 0$ we have classified as an essential diffraction point. We note that the approximation in (44) is formally valid everywhere but at $r = 0$. The ‘hybrid method’ that we propose involves obtaining the solution in the vicinity of essential diffraction points using the finite element formulation described in the previous section.

We begin by defining our diffraction region:

$$\Omega^D = \{(r, \theta) | r \leq (kR)/k\} \quad (46)$$

Thus, for fixed kR , the diffraction region shrinks as $k \rightarrow \infty$. On the other hand, for fixed k , the diffraction region grows as $kR \rightarrow \infty$.

We now wish to solve the problem described in equations (12)–(15) with Ω^D as described in (46). This yields the following boundary value problem for $u^D = u_{\text{scat}}(x)|_{\Omega^D}$:

$$\Delta u^D + k^2 u^D = 0 \quad r \leq R; 0 \leq \theta < \beta, \quad (47)$$

$$u^D = -u_{\text{inc}} \quad \theta = 0; \theta = \beta, \quad (48)$$

$$u^D = u^{\text{Asymp}} \quad \text{on } r = R, \quad (49)$$

$$\partial_n u^D = \partial_n u^{\text{Asymp}} \quad \text{on } r = R. \quad (50)$$

Here, u^{Asymp} is given by Eq. (44). The boundary condition in (49) and (50) would be over specified if u^{Asymp} were known completely, since we cannot specify both u and its normal derivative on the same surface, in general. Since $D(\theta)$ is unknown in u^{Asymp} , however, the conditions (49) and (50) are not over specified.

6.4. Numerical solution for local problem

We use the numerical formulation and implementation described in the previous section to solve (47)–(50). In this case, $U(x)$ (cf. Eqs. (22) and (44)) is given by

$$U(x) = u_{\text{reflected}}^{\text{uniform}} + u_{\text{shadow}}^{\text{uniform}}. \quad (51)$$

The unknown portion of u^{Asymp} is $u_{\text{diffracted}}^{\text{uniform}}$, which is interpolated with the same finite element interpolation as the interior field:

$$\begin{aligned} u_{\text{diffracted}}^{\text{uniform}} &= (kR)^{-1/2} D(u)(\theta) \sqrt{\frac{R}{r}} e^{ikr} \\ &\approx (kR)^{-1/2} \sqrt{\frac{R}{r}} e^{ik(r-R)} \sum_{\alpha=1}^{N_{\text{dof}}} b_\alpha N_\alpha(x)|_{x=(R \cos \theta, R \sin \theta)}. \end{aligned} \quad (52)$$

Here, $N_\alpha(x)$ are the finite element shape functions for the interior domain, restricted to the boundary Γ_R as functions of the arc length γ . The finite elements chosen were bilinear quadrilateral Helmholtz elements, implemented in Dlearn [14].

The interpolation in (52) violates the condition that u^0 be smooth, since the $N_\alpha(x)$ are C^0 . Nevertheless, this condition was ignored with apparently negligible effects on the results. To account appropriately for jumps in derivatives in u^0 , one must modify the variational formulation as in [13].

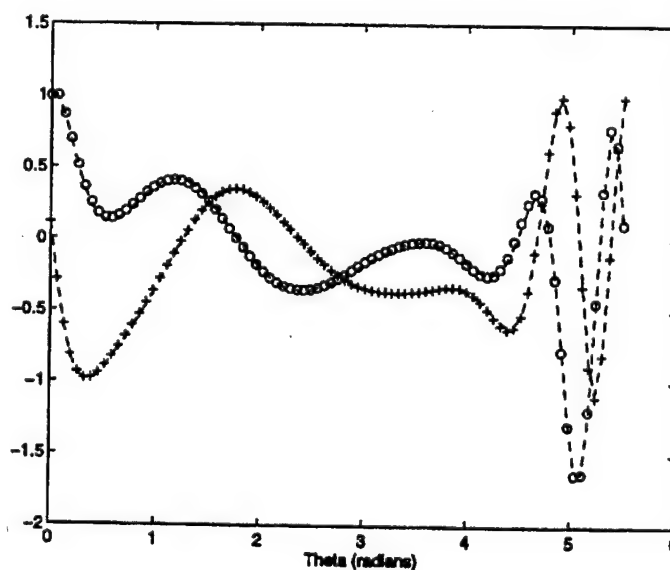


Fig. 5. FEM results for blunted wedge: real and imaginary parts of analytical solution in comparison to hybrid asymptotic-numerical solution.

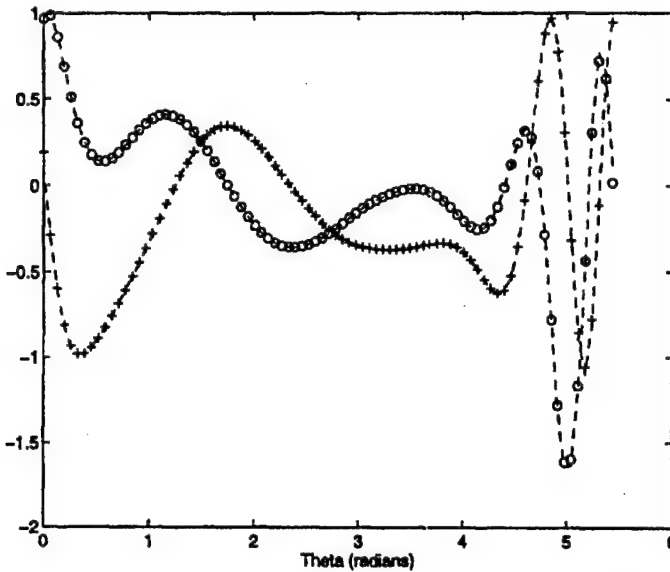


Fig. 6. Comparison of computed inner and outer fields on Γ_R : real and imaginary parts.

6.4.1. Results

We first compare the analytical solution to our computed solution on Γ_R , as shown in Fig. 5. For this example, the radius of the artificial boundary is chosen to be at $R = 2\lambda$, and the angle of incidence is 30° . The exact analytical solution can be found in the appendix of [3]. The finite element solution was obtained with a very fine discretization (more than 20 elements/wavelength) in order to minimize discretization error and highlight the deficiencies of the hybrid asymptotic/FEM boundary condition.

Since the formulation enforces continuity between the inner and outer fields weakly, we expect that discontinuity between the two fields may appear. Therefore we next compare the numerically evaluated u^i and u^o on Γ_R . The outer field u^o is evaluated by adding the contributions from $u_{\text{diffracted}}^{\text{uniform}}$ (52) and $U(x)$ (51). This comparison is shown in Fig. 6 and we again note very good agreement between the two curves.

The next example shows that comparable results can be obtained even in the presence of more complicated forms of the outer field.

7. Application: Source on impedance plane

In this section we shall demonstrate our hybrid method on a problem with surface wave phenomena. The simplest geometry that exhibits such phenomena is a source placed near an impedance half-plane.

7.1. Formulation and global asymptotic approximation

We wish to solve the following:

$$\Delta u + k^2 u = 0 \quad (53)$$

$$\frac{\partial u}{\partial y} + k\beta u = f(x) \quad \text{on } y = 0 \quad (54)$$

$$u = \text{outgoing} \quad (55)$$

We shall assume that the support of $f(x)$ is much smaller than λ in size, and is symmetric around the origin.

The solution of the eiconal equation (7) in $y > 0$ with initial data at $r = 0$ gives rise to the solution:

$$\psi_1 = r. \quad (56)$$

Further, on $y = 0$, we find a solution that satisfies (54) and (55) for $\beta > 0$ of the form

$$\psi_2 = |x|(1 + \beta^2)^{1/2} - \beta y. \quad (57)$$

Substituting these into (8) yields the following expression for u^{Asymp} :

$$u \sim u^{\text{Asymp}} = (kR)^{-1/2} D(\theta) \sqrt{R/r} \exp\{ikr\} + A \exp\{ik(1 + \beta^2)^{1/2}|x| - k\beta y\} \quad \text{for } kR \rightarrow \infty; r \neq 0, \theta \neq \pi/2. \quad (58)$$

Here, A is a constant, and is the amplitude of a radiated surface wave. In order for u^{Asymp} to satisfy the boundary condition (54) to leading order, we must require $D(0) = D(\pi) = 0$.

7.2. Local solution

We note that the expression (58) has a slope discontinuity along $x = 0$, and is not valid at $r = 0$. Further, (58) has a Stokes' line on $\theta = 0$ and an anti-Stokes line on $\csc \theta_A := (1 + \beta^2)^{1/2}$, which prevent the expansion (as is) to be very accurate below θ_A , and invalid for $\beta = 0$ (see [2]).

We shall consider $\beta = 1$, and note that in this case the magnitude of the discontinuity at $\theta = \pi/2$ is small and we shall ignore it. Further, β is sufficiently far from zero that we need not be concerned with the Stokes line. For smaller values of β , however, an expansion uniformly valid in β would be required for high accuracy.

Thus ignoring all the ‘inessential’ diffraction points, we concern ourselves only with the essential diffraction point $r = 0$. We again use the formulation described earlier, but suitably modified for impedance boundary conditions. In this case, $U(x) \equiv 0$, and u^{Asymp} is approximated as

$$u^{\text{Asymp}} \approx u_h^A = \sum_{\alpha=1}^{20} b_\alpha \sin((2\alpha - 1)\theta) \exp ikr/\sqrt{kr} + A \exp\{ik(1 + \beta^2)^{1/2}|x| - k\beta y\}. \quad (59)$$

We note that the problem is symmetric about $\theta = \pi/2$, and so only half the domain is discretized. The expression (59) satisfies the boundary conditions $D(0) = 0$ and $D'(\pi/2) = 0$.

7.3. Numerical results

We apply a force at the corner node of our domain and compare the results to the analytical solution of (53)–(56) with $f(x) = \delta(x)$. Again, $R = 2\lambda$ and the resolution is sufficiently high to make discretization error negligible.

The exact and computed directivities are shown in Fig 7. These show good agreement for angles above 45° , and a slight divergence for angles below 45° . This divergence represents about 2% of the total solution at these angles. The error of the magnitude of the surface wave is less than 2%. We suppose these errors to be reducible in several ways. First, a uniformly valid (in β) approximation can be used for u^{Asymp} . Second, a higher-order approximation (in (kR)) can be used in u^{Asymp} . Finally, a larger value of R can be used. In any case, at a distance of only two wavelengths, the error in far field quantities is of the order of a few percent.

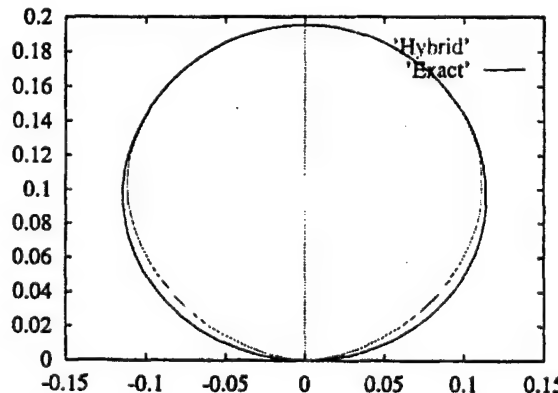


Fig. 7. Polar plots of directivities for line source on an impedance plane computed numerically and analytically.

8. Remarks and conclusion

We have presented a hybrid GTD/FEM approach for acoustic scattering and radiation calculations which combines the benefits of GTD with those of FEM. The essential idea behind our method is to use a short wavelength asymptotic approximation wherever it provides an accurate representation of the field. In the neighborhoods of those points where it is not valid, we supplement the solution with a FEM representation, and patch the two representations together on an artificial boundary. Thus, we divide the domain into two (not necessarily connected) regions: the asymptotic region and the numerical region.

The formulation presented naturally separates the asymptotic from numerical approximations, and can be refined systematically to obtain arbitrarily high accuracy. The formulation leads to a matrix system of equations in which the number of degrees of freedom $N_{\text{dof}} = O((kL)^{d-2})$. Thus, the direct factorization costs scale as $\text{Cost} = O((kL)^{3(d-2)})$. In two dimensions, the cost is asymptotically independent frequency.

We presented a variational formulation that allows us to couple the inner and outer fields. To ease implementation in existing FEM codes, we have developed and describe an element-like formulation that provides an element-type data structure to evaluate the coupling terms necessary. The formulation naturally incorporates various types of far field expressions, including surface waves, and can be readily adapted to other analytical representations of the field.

Finally, we have demonstrated the method for application to both diffraction and radiation problems. An analysis of the asymptotic error incurred in our hybrid formulation is forthcoming in a future contribution by the authors.

Acknowledgements

The authors are grateful to Prof. Dan Givoli who graciously made available to us his Helmholtz finite element routines. This work has been financially supported by the Office of Naval Research.

References

- [1] J.M. Montgomery and P.E. Barbone, Diffraction from simple shapes by a hybrid asymptotic-finite element method, *J. Acoust. Soc. Am.* (1997), under consideration.
- [2] P.E. Barbone, Approximate diffraction coefficients by the method of matched asymptotic expansions, *Wave Motion*, 22 (1995) 1–16.
- [3] P.E. Barbone and O. Michael, Scattering from submerged objects by a hybrid asymptotic-boundary integral equation method, BU Dept. of Aerospace and Mechanical Engineering Report No. AM-97-029, October 1997.
- [4] W.D. Burnside, C.L. Yu and R.J. Marhefka, A technique to combine the geometrical theory of diffraction and the moment method, *IEEE Trans. Ant. and Prop.*, AP-23 (1975) 551–558.
- [5] M. Calamia, R. Cocciali, G. Pelosi and G. Manara, A hybrid FEM/UTD analysis of the scattering from a cavity-backed aperture in a face of a perfectly conducting wedge, *COMPEL, Int. J. Comput. Math. Electr. Electron. Engrg.* 13(A) (1994) 229–235.
- [6] P.C. Clemmow, *The Plane Wave Spectrum Representation of Electromagnetic Fields*, (Pergamon, 1966).
- [7] S. Cui and D. Fang, A hybrid method for scattering by finite periodic structures, *Chinese J. Electron.* 6(2) (1997) 90–93.
- [8] M. Van Dyke, *Perturbation Methods in Fluid Mechanics* (Parabolic Press, Stanford, annotated edition, 1975).
- [9] D. Givoli and J.B. Keller, A finite element method for large domains, *Comput. Methods Appl. Mech. Engrg.* 76 (1989) 41–66.
- [10] A.D. Greenwood, S.S. Ni, J.M. Jin and S.W. Lee, Hybrid fem/sbr method to compute the radiation pattern from a microstrip patch antenna in a complex geometry, *Proc. 1996 Antenna Applications Symposium*, vi:1–6, 1996.
- [11] I. Harari and T.J.R. Hughes, A cost comparison of boundary element and finite element methods for problems of time-harmonic acoustics, *Comput. Methods Appl. Mech. Engrg.* 97 (1992) 77–102.
- [12] I. Harari, P.E. Barbone and J.M. Montgomery, Finite element formulations for exterior problems: Application to hybrid methods, non-reflecting boundary conditions, and infinite elements, *Int. J. Num. Methods Engrg.* 40 (1997) 2791–2805.
- [13] I. Harari, P.E. Barbone, M. Slavutin and R. Shalom, Boundary infinite elements for the Helmholtz equation in exterior domains, *Int. J. Num. Meth. Engrg.* (1997) accepted.
- [14] T.J.R. Hughes, *The Finite Element Method* (Prentice Hall, Englewood Cliffs NJ, 1987). DLearn appears in appendix. Helmholtz element as used was added by D. Givoli.
- [15] J.M. Jin, S. Ni and S.W. Lee, Robust hybrid technique for calculating scattering by large and complex targets, *Electron. Lett.* 30(25) (1994) 2169–2170.
- [16] D.S. Jones, *Acoustic and Electromagnetic Waves* (Oxford University Press, New York, 1986).
- [17] J.B. Keller, Geometrical theory of diffraction, *J. Opt. Soc. Am.* 52(2) (1962) 160–130.

- [18] T.J. Kim and G.N. Thiele, A hybrid diffraction technique-general theory and applications, *IEEE Trans. Ant. Prop. AP-30(5)* (1982) 888–897.
- [19] R.G. Kouyoumjian and P.H. Pathak, A uniform geometrical theory of diffraction for an edge in a perfectly conducting surface, *Proc. IEEE 62* (1974) 1448–1461.
- [20] P.M. Marston, Selected papers on Geometrical Aspects of Scattering (SPIE Optical Engineering Press, Bellingham WA, 1994).
- [21] L.N. Medgyesi-Mitschang and D.S. Wang, Hybrid methods for analysis of complex scatterers, *Proc. IEEE 77(5)* (1989) 770–779.
- [22] O. Michael and P.E. Barbone, FEM, BEM, spectral FEM or spectral BEM? A cost comparison, BU Dept. of Aerospace and Mechanical Engineering Report No. AM-97-028, August 1997.
- [23] J.M. Montgomery, Acoustic scattering calculations by a hybrid asymptotic numerical method, M.Sc. Thesis, Department of Aerospace and Mechanical Engineering, Boston University, 1996.
- [24] G. Pelosi, A. Freni and R. Coccioni, Hybrid technique for analysing scattering from periodic structures, *IEE Proc. H 140(2)* (1993) 65–70.
- [25] A.D. Pierce, *Acoustics: An Introduction to its Physical Principles and Applications*. (Acoustical Society of America, New York, 1989).
- [26] A.D. Pierce, Variational formulations in acoustic radiation and scattering, *Phys. Acoustics XXII* (1993) 195–371.
- [27] D.C. Ross, J.L. Volakis and H.T. Anastassiou, Hybrid finite element-modal analysis of jet engine inlet scattering, Conference Proceedings. 10th Annual Review of Progress in Applied Computational Electromagnetics, xv: (1994) 300–307.
- [28] B. Roturier, B. Souny and H. Baudrand, Calculation of diffracted fields by hybrid finite-element/geometrical-theory-of-diffraction method, JINA 94. Journees Internationales de Nice sur les Antennes Conferences (Proceedings of the International Symposium on Antennas), ix (1994) 237–240.
- [29] J.N. Sahalos and G.N. Thiele, On the application of the GTD-MM technique and its limitations, *IEEE Trans. Ant. Prop. AP-29(5)* (1981) 780–786.
- [30] X.Q. Sheng and J.M. Jin, A hybrid FEM/SBR method to compute scattering by large bodies with small protruding scatterers, *Microwave and Optical Technology Letters, 15(2)* (1997) 78–84.
- [31] D.S. Wang, Current-based hybrid analysis for surface-wave effects on large scatterers, *IEEE Trans. Ant. Prop. 39(6)* (1991) 839–850.
- [32] E. Zauderer, *Partial Differential Equations of Applied Mathematics*, 2nd edition (Academic Press, New York, 1989).

C.4 Galerkin Formulation and Singularity Subtraction for Spectral Solutions of Boundary Integral Equations

“Galerkin Formulation and Singularity Subtraction for Spectral Solutions of Boundary Integral Equations,” Ofer Michael & Paul E. Barbone, **International Journal for Numerical Methods in Engineering**, Vol. 41, pp. 95–111, 1998.

GALERKIN FORMULATION AND SINGULARITY SUBTRACTION FOR SPECTRAL SOLUTIONS OF BOUNDARY INTEGRAL EQUATIONS

OFER MICHAEL* AND PAUL E. BARBONE

Department of Aerospace and Mechanical Engineering, Boston University 110 Cummington Street, Boston, MA 02215, U.S.A.

ABSTRACT

A new spectral Galerkin formulation is presented for the solution of boundary integral equations. The formulation is carried out with an exact singularity subtraction procedure based on analytical integrations, which provides a fast and precise way to evaluate the coefficient matrices. The new Galerkin formulation is based on the exact geometry of the problem boundaries and leads to a non-element method that is completely free of mesh generation. The numerical behaviour of the method is very similar to the collocation method; for Dirichlet problems, however, it leads to a symmetric coefficient matrix and therefore requires half the solution time of the collocation method. © 1998 John Wiley & Sons, Ltd.

Int. J. Numer. Meth. Engng., 41; 95-111 (1998)

KEY WORDS: boundary integral equation; BEM; BSM; Galerkin; singularity subtraction

1. INTRODUCTION

Spectral methods are well established in the finite element method¹ (FEM). These methods are used because of their exponential convergence² properties. Spectral methods are employed in FEM in two ways. In the more conventional implementations, high-order polynomials are used as the shape functions of the elements.³ An alternative, however, is to use a spectral series in one or two directions while the remaining directions are discretized using traditional FEM interpolations.^{4,5} The second approach is sometimes called the 'finite strip' method or the 'spectral strip' method. One of the disadvantages of using spectral methods in FEM is the fact that the bandwidth of the matrices increases with the order of interpolation, thus increasing the solution time. Typically, however, the overall time that is required to solve a given problem for a given precision by spectral FEM is still less than the time required by using regular FEM.³

Another common numerical method is the boundary element method (BEM) which is based on the boundary integral equation (BIE) formulation. In this method, the problem is formulated in terms of fields on the boundaries only, which leads to a reduction in the number of degrees of freedom required for solution as compared to FEM. On the other hand, unlike the banded matrices of the FEM, the BEM matrices are fully populated. Therefore, it usually takes more time

*Correspondence to: Ofer Michael, Department of Aerospace and Mechanical Engineering, Boston University, 110 Cummington Street, Boston, MA 02215, U.S.A.

Contract grant sponsor: ONR

to solve the BEM equations. Comparisons between BEM and FEM can be found in many text books^{7,6} and papers.^{8,9}

Because of the fact that the BEM matrices are highly populated *a priori*, then no bandwidth penalty is incurred by utilizing a spectral method. Thus, we get the convergence benefits of spectral methods without the computational cost disadvantages that characterize spectral methods in FEM.

Shaw¹⁰ suggested the usage of eigenfunctions as shape functions in BEM. Another spectral method for solution of BIE was proposed by Michael *et al.*,¹¹ named the Boundary Spectral strip Method (BSM). In this method, the dependent variables in the BIE are expanded in a spectral series. Two spectral approximations were suggested. The first one was a Fourier series approximation¹¹ which performs well for continuous boundaries. The second approximation was based on a high-order polynomial series and is more suitable for non-continuous geometries.¹² In References 11 and 12, the BSM was shown to be both more precise and efficient than standard BEM.

One of the problems of BSM, BEM or the BIE, in general, is that generating the coefficient matrices requires the integration of singular kernels. This integration can be computationally expensive and is prone to numerical error.¹³ This is in fact one of the main reasons that the Galerkin formulation is not typically used in the BIE method, since it requires an additional integration which can be very computationally expensive. This is especially true in elastostatics where the second integration would also involve a singularity.

There are some advantages to using the Galerkin formulation. These include consistency of convergence and a unique structure of the coefficient matrices. In the FEM, the Galerkin formulation leads (for self-adjoint operators) to a symmetric coefficient matrix which for many problems is positive definite.¹⁴

In this paper we present a procedure for singularity subtraction which is well suited to the spectral method. It is based on the analytical integrations given in References 11 and 12. We combine the singularity subtraction procedure with a fast transformation from collocation to Galerkin matrices. This yields a highly efficient spectral Galerkin formulation for the BIE. The new formulation shows improved numerical performance, such as partially symmetric coefficient matrices, reduction of the matrix population, and exponential convergence. The modified Galerkin formulation seems to be more accurate than the regular collocation-based BSM formulation which was already proven to be more accurate and efficient as compared to the BEM.^{11,12} Another very important advantage to the new formulation is the fact that it is completely free of mesh generation and there is no need for any grid definition.

Some analytical integration formulas, on which our singularity subtraction procedure is based, will be given for the Laplace and elastostatics equations, corresponding to both straight line and circle geometries.

2. GALERKIN FORMULATION FOR BOUNDARY SPECTRAL STRIP

Consider a domain Ω with a piecewise smooth boundary Γ on which the BIE is satisfied:

$$c(\mathbf{x}_1)u(\mathbf{x}_1) + \int_{\Gamma} p^*(\mathbf{x}_1, \mathbf{x}_2)u(\mathbf{x}_2)d\Gamma = \int_{\Gamma} u^*(\mathbf{x}_1, \mathbf{x}_2)p(\mathbf{x}_2)d\Gamma \quad (1)$$

Here, u and p are the primary and secondary variables, and u^* , p^* are their kernels, respectively. c is a constant in the case of scalar equations such as Laplace or Helmholtz equation or a matrix of constants in the case of vector equations such as elastostatics or elastodynamics. Note that the point \mathbf{x}_2 is on the boundary Γ , while the point \mathbf{x}_1 is the collocation point (the point where we apply the Dirac delta function).

We split the boundary Γ into 'strips', according to its shape, where each strip is a smooth part of the boundary. The strips can be closed (e.g. circle, ellipse, closed smooth spline, etc.) or open strips (e.g. line, open spline, etc.). The boundary Γ is the union of all the strips:

$$\Gamma = \bigcup_{ns=1}^{NS} \bar{\Gamma}_{ns} \quad (2)$$

where $\bar{\Gamma}_{ns}$ is the part of the boundary defined by the ns th strip, and NS is the total number of strips which compose the boundary. We require further that $\bar{\Gamma}_{ns} \cap \bar{\Gamma}_{ms} = \emptyset$, $ns \neq ms$. Using the last definition for Γ we can rewrite the BIE as

$$c(\mathbf{x}_1)u(\mathbf{x}_1) + \sum_{ns=1}^{NS} \int_{\Gamma_{ns}} p^*(\mathbf{x}_1, \mathbf{x}_2)u(\mathbf{x}_2) d\Gamma_{ns} = \sum_{ns=1}^{NS} \int_{\Gamma_{ns}} u^*(\mathbf{x}_1, \mathbf{x}_2)p(\mathbf{x}_2) d\Gamma_{ns} \quad (3)$$

Equation (3) is the strip formulation. In order to get a spectral strip formulation we expand u and p on each strip by means of a spectral series:

$$u(\mathbf{x}) = \sum_n u_n f_n(\mathbf{x}); \quad p(\mathbf{x}) = \sum_m p_m g_m(\mathbf{x}) \quad \text{for } \mathbf{x} \in \Gamma_{ns} \quad (4)$$

where f_n and g_m are the spectral basis functions which are used for the approximation. u_n and p_m are the coefficients of these spectral series. Note that the spectral basis functions f_n and g_m need not be the same. For simplicity of formulation we shall take f_n and g_n to be the same spectral series on the same strip. We will also approximate u and p on the ns strip, with the same order of approximation NA_{ns} . Thus for the ns strip the variables u , p can be written as:

$$u(\mathbf{x}) = \sum_{n=v}^{NA_{ns}} u_n f_n(\mathbf{x}), \quad p(\mathbf{x}) = \sum_{n=v}^{NA_{ns}} p_n f_n(\mathbf{x}) \quad \text{for } \mathbf{x} \in \Gamma_{ns} \quad (5)$$

The integer parameter v is defined according to the series; for polynomial series, for example, $v = 0$ while for a full Fourier series $v = -NA_{ns}$. Substituting equation (5) into equation (3) yields the boundary spectral strip formulation based on collocation:^{11,12}

$$\sum_{ns=1}^{NS} \sum_{n=v}^{NA_{ns}} u_n \left\{ c(\mathbf{x}_1) f_n(\mathbf{x}_1) + \int_{\Gamma_{ns}} p^*(\mathbf{x}_1, \mathbf{x}_2) f_n(\mathbf{x}_2) d\Gamma_{ns} \right\} = \sum_{ns=1}^{NS} \sum_{n=v}^{NA_{ns}} p_n \left\{ \int_{\Gamma_{ns}} u^*(\mathbf{x}_1, \mathbf{x}_2) f_n(\mathbf{x}_2) d\Gamma_{ns} \right\} \quad (6)$$

For the Galerkin formulation, we multiply equation (3) by an arbitrary weight function $w(\mathbf{x}_1)$ and integrate over the boundary once more. This gives:

$$\begin{aligned} & \sum_{ms=1}^{NS} \left\{ \int_{\Gamma_{ms}} w(\mathbf{x}_1) c(\mathbf{x}_1) u(\mathbf{x}_1) d\Gamma_{ms} + \int_{\Gamma_{ms}} \sum_{ns=1}^{NS} \int_{\Gamma_{ns}} w(\mathbf{x}_1) p^*(\mathbf{x}_1, \mathbf{x}_2) u(\mathbf{x}_2) d\Gamma_{ns} d\Gamma_{ms} \right\} \\ &= \sum_{ms=1}^{NS} \left\{ \int_{\Gamma_{ms}} \sum_{ns=1}^{NS} \int_{\Gamma_{ns}} w(\mathbf{x}_1) u^*(\mathbf{x}_1, \mathbf{x}_2) p(\mathbf{x}_2) d\Gamma_{ns} d\Gamma_{ms} \right\} \end{aligned} \quad (7)$$

Choosing the approximation functions and the weight functions to be of the same form as equation (5) and substituting them into equation (7) yields:

$$\begin{aligned} \sum_{ms=1}^{NS} \sum_{m=v}^{NA_m} w_m \left\{ \sum_{ns=1}^{NS} \sum_{n=v}^{NA_n} u_n \left[\int_{\Gamma_{ms}} c(\mathbf{x}_1) f_m(\mathbf{x}_1) f_n(\mathbf{x}_1) d\Gamma_{ms} + \int_{\Gamma_{ms}} \int_{\Gamma_{ns}} p^*(\mathbf{x}_1, \mathbf{x}_2) f_m(\mathbf{x}_1) f_n(\mathbf{x}_2) d\Gamma_{ns} d\Gamma_{ms} \right] \right\} \\ = \sum_{ms=1}^{NS} \sum_{m=v}^{NA_m} w_m \left\{ \sum_{ns=1}^{NS} \sum_{n=v}^{NA_n} p_n \left[\int_{\Gamma_{ms}} \int_{\Gamma_{ns}} u^*(\mathbf{x}_1, \mathbf{x}_2) f_m(\mathbf{x}_1) f_n(\mathbf{x}_2) d\Gamma_{ns} d\Gamma_{ms} \right] \right\} \end{aligned} \quad (8)$$

Since w is an arbitrary function, then for each w_n , the terms inside the curly brackets on the left-hand side and on the right-hand side of equation (8) must be equal. Thus, each coefficient w_n will generate one equation. Hence, the total number of equations will be $\sum_{ms=1}^{NS} (NA_{ms} - v + 1)$, which is the number of unknown coefficients. This yields a set of equations of the form:

$$\mathbf{H}\mathbf{U} = \mathbf{G}\mathbf{P} \quad (9)$$

where \mathbf{U} and \mathbf{P} are two column vectors which contain the coefficients of the series that describe the variables u and p , respectively, on each strip. The matrices \mathbf{H} and \mathbf{G} are block matrices with $NS \times NS$ block matrices:

$$\mathbf{H} = \begin{bmatrix} \hat{\mathbf{H}}_{1,1} & \cdots & \hat{\mathbf{H}}_{1,NS} \\ \vdots & \ddots & \vdots \\ \hat{\mathbf{H}}_{NS,1} & \cdots & \hat{\mathbf{H}}_{NS,NS} \end{bmatrix}, \quad \mathbf{G} = \begin{bmatrix} \hat{\mathbf{G}}_{1,1} & \cdots & \hat{\mathbf{G}}_{1,NS} \\ \vdots & \ddots & \vdots \\ \hat{\mathbf{G}}_{NS,1} & \cdots & \hat{\mathbf{G}}_{NS,NS} \end{bmatrix} \quad (10)$$

The sub-matrices $\hat{\mathbf{H}}_{ms,ns}$, $\hat{\mathbf{G}}_{ms,ns}$ are rectangular matrices of the form:

$$\hat{\mathbf{H}}_{ms,ns} = \begin{bmatrix} h_{1,1} & \cdots & h_{1,NA_m} \\ \vdots & & \vdots \\ h_{NA_m,1} & \cdots & h_{NA_m,NA_m} \end{bmatrix}, \quad \hat{\mathbf{G}}_{ms,ns} = \begin{bmatrix} g_{1,1} & \cdots & g_{1,NA_m} \\ \vdots & & \vdots \\ g_{NA_m,1} & \cdots & g_{NA_m,NA_m} \end{bmatrix} \quad (11)$$

Finally, the sub-sub-matrices h_{mn} , g_{mn} are defined as

$$\begin{aligned} h_{mn} &= \int_{\Gamma_{ms}} c(\mathbf{x}_1) f_m(\mathbf{x}_1) f_n(\mathbf{x}_1) d\Gamma_{ms} + \int_{\Gamma_{ms}} \int_{\Gamma_{ns}} p^*(\mathbf{x}_1, \mathbf{x}_2) f_m(\mathbf{x}_1) f_n(\mathbf{x}_2) d\Gamma_{ns} d\Gamma_{ms} \\ g_{mn} &= \int_{\Gamma_{ms}} \int_{\Gamma_{ns}} u^*(\mathbf{x}_1, \mathbf{x}_2) f_m(\mathbf{x}_1) f_n(\mathbf{x}_2) d\Gamma_{ns} d\Gamma_{ms} \end{aligned} \quad (12)$$

Note that in the case of vector equations h_{mn} and g_{mn} are also matrices since c , u^* and p^* would be matrices as well.

From equation (12) we observe a few interesting characteristics of the matrices \mathbf{H} and \mathbf{G} . Since the kernel $u^*(\mathbf{x}_1, \mathbf{x}_2)$ is symmetric then the matrix \mathbf{G} is fully symmetric. Therefore, for Dirichlet problems, we see that this formulation leads to a symmetric coefficient matrix.

The first term in the h_{mn} is also fully symmetric, and its contribution to the matrices $\hat{\mathbf{H}}_{ms,ns}$ is zero in the case where $ms \neq ns$ (since $c = 0$ or a zero matrix in the case of vector equations). Furthermore, if we choose f_n to be an orthogonal series then the contribution of this term to the $\hat{\mathbf{H}}_{ms,ns}$ matrices would be diagonal.

We describe here two manners of spectral approximation: the first is a Fourier series which is suitable for closed continuous geometries; the second approximation uses high-order

polynomials and is more suitable for open non-continuous geometries. For Fourier series, the integrations to be performed in the collocation formulation are:

$$\oint_{\Gamma_m} e^{im\theta_m} u^*(x_1, x_2) d\Gamma_{ns}, \quad \oint_{\Gamma_m} e^{in\theta_m} p^*(x_1, x_2) d\Gamma_{ns} \quad (13)$$

In the Galerkin formulation, we need:

$$\begin{aligned} & \oint_{\Gamma_m} e^{im\theta_m} \oint_{\Gamma_m} e^{in\theta_m} u^*(x_1, x_2) d\Gamma_{ns} d\Gamma_{ms}, \quad \oint_{\Gamma_m} c(x_1) e^{im\theta_m} e^{in\theta_m} d\Gamma_{ms} \\ & \oint_{\Gamma_m} e^{im\theta_m} \oint_{\Gamma_m} e^{in\theta_m} p^*(x_1, x_2) d\Gamma_{ns} d\Gamma_{ms} \end{aligned} \quad (14)$$

Here, θ_{ns} is the circumferential angle which is measured along the ns strip. In the case of collocation in the polynomial approximation, we must evaluate the integrals:

$$\int_{\Gamma_m} (\eta_{ns})^n u^*(x_1, x_2) d\Gamma_{ns}, \quad \int_{\Gamma_m} (\eta_{ns})^n p^*(x_1, x_2) d\Gamma_{ns} \quad (15)$$

While for Galerkin, we require

$$\begin{aligned} & \int_{\Gamma_m} (\eta_{ms})^m \int_{\Gamma_m} (\eta_{ns})^n u^*(x_1, x_2) d\Gamma_{ns} d\Gamma_{ms}, \quad \int_{\Gamma_m} c(x_1) (\eta_{ms})^m (\eta_{ns})^n d\Gamma_{ms} \\ & \int_{\Gamma_m} (\eta_{ms})^m \int_{\Gamma_m} (\eta_{ns})^n p^*(x_1, x_2) d\Gamma_{ns} d\Gamma_{ms} \end{aligned} \quad (16)$$

Here, η_{ns} is a non-dimensional length co-ordinate which is measured along the boundary of the ns strip.

The integrations indicated in equation (13) can be evaluated analytically for a circular geometry both for the case where the collocation point lies on the strip (the singular case) or for the case where it lies off the strip. For the Laplace and elastostatics kernels, these integrals are known in closed form.¹¹ For the elastodynamics kernels, they are available in a series form.¹⁵ The integrations indicated in equation (15) can also be evaluated analytically for straight-line geometries: in closed form for the Laplace and elastostatics kernels,¹² and in a series form for elastodynamics.¹⁶ In the special cases of a straight-line or a circle geometry, the integrals in equations (14) and (16) can be also formed analytically for the Laplace's equation and for elastostatics. The analytical results for these integrals for the singular case where $ms = ns$, are given in the appendix.

In the case of geometries that are different from the above, the integrals must be evaluated numerically, both for collocation and Galerkin. One of the problems in evaluating these integrals numerically is that their integrands are singular. In the case of elastostatics or elastodynamics integrating the singularity can be almost prohibitively expensive. In the next section we will present a procedure for subtracting the singularities of the kernels by using a procedure which is based on the analytical results for a circle and for the line geometry.

3. SINGULARITY SUBTRACTION: LAPLACE AND ELASTOSTATICS

3.1. Continuous geometries

Consider an arbitrary closed smooth curve as shown in Figure 1. If we collocate along the boundary Γ at the point where $\theta = \theta_0$, then the kernels are singular at this point. Let us denote the primary and secondary kernels by $\tilde{u}^*(\theta, \theta_0)$ and $\tilde{p}^*(\theta, \theta_0)$, respectively. We also define the kernels $\bar{u}^*(\theta, \theta_0)$ and $\bar{p}^*(\theta, \theta_0)$ which are the corresponding kernels of a circular geometry, (with radius to be determined). (see Figure 1). The integrals to be evaluated are of the form:

$$\oint_{\Gamma} e^{in\theta} \tilde{u}^*(\theta, \theta_0) d\Gamma, \quad \oint_{\Gamma} e^{in\theta} \tilde{p}^*(\theta, \theta_0) d\Gamma \quad (17)$$

We will present the singularity subtraction procedure only for the primary variable kernel $\tilde{u}^*(\theta, \theta_0)$, since that for $\tilde{p}^*(\theta, \theta_0)$ is identical. Changing the integration variable in equation (17) to θ and adding and subtracting the function $e^{in\theta} \bar{u}^*(\theta, \theta_0) d\Gamma/d\theta(\theta_0)$ from the integrand yields:

$$\oint_{\Gamma} e^{in\theta} \tilde{u}^*(\theta, \theta_0) d\Gamma = \int_0^{2\pi} e^{in\theta} \left[\tilde{u}^*(\theta, \theta_0) \frac{d\Gamma}{d\theta} - \bar{u}^*(\theta, \theta_0) \frac{d\Gamma}{d\theta}(\theta_0) \right] d\theta + \frac{d\Gamma}{d\theta}(\theta_0) \int_0^{2\pi} e^{in\theta} \bar{u}^*(\theta, \theta_0) d\theta \quad (18)$$

Note that we choose the radius of the circle to be $d\Gamma/d\theta(\theta_0)$ as shown in Figure 1. The integral in equation (18) now contains two integrals. The first one has a non-singular integrand and it can be evaluated efficiently and accurately based on its special form, as we will describe later. The second integral has a singular integrand. We evaluate it analytically based on the closed form results of these integrals given in Reference 11. Figure 2 depicts the subtracted integrand $[\tilde{u}^*(\theta, \theta_0) d\Gamma/d\theta - \bar{u}^*(\theta, \theta_0) d\Gamma/d\theta(\theta_0)]$ compared to the original integrand $\tilde{u}^*(\theta, \theta_0) d\Gamma/d\theta$ for the Laplace kernel on an elliptical boundary.

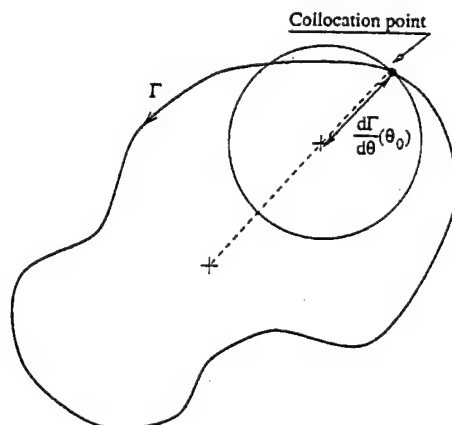


Figure 1. Singularity subtraction from a closed geometry

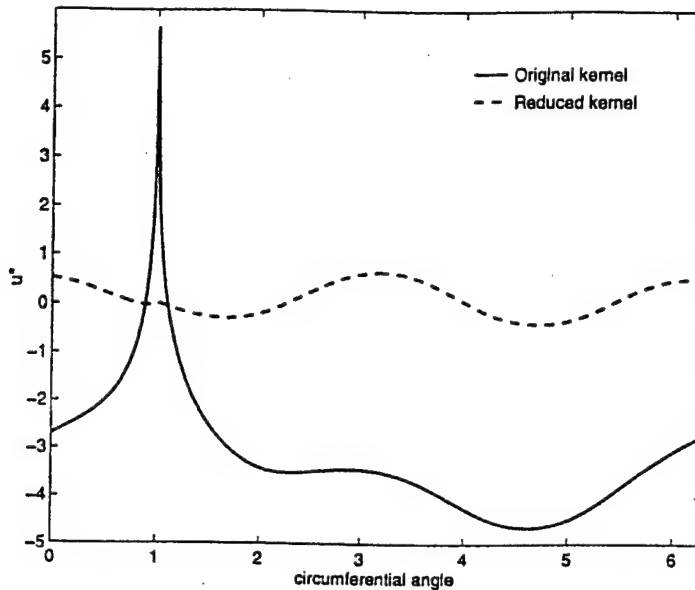


Figure 2. The subtracted integrand $[\tilde{u}^*(\theta, \theta_0) d\Gamma/d\theta - \tilde{u}^*(\theta, \theta_0) d\Gamma/d\theta(\theta_0)]$ compared to the original integrand $\tilde{u}^*(\theta, \theta_0) d\Gamma/d\theta$ (equation (18)) of Laplace equation, for a geometry of an ellipse with semi-major axes of 8 and 10 along the x - and y -axis, respectively, for a collocation point at $\theta = 1$

3.1.1. Evaluation of the reduced integrals. The reduced integrals with non-singular integrands can be evaluated using any integration rule such as Simpson or Gauss quadrature. However, when it comes to evaluation of high harmonics, these integrands vary rapidly and the evaluation of these integrals can be problematic and time consuming. In order to overcome this difficulty we suggest exploiting the special characteristics of these integrals.

The integral that has to be evaluated has the form of $\int_0^{2\pi} e^{in\theta} f(\theta) d\theta$. The function $f(\theta)$ which stands for the reduced singularity kernel, is smooth and periodic (e.g. see Figure 2). This integral is precisely the Fourier transform of $f(\theta)$. By using the fast Fourier transform (FFT) algorithm¹⁸ to evaluate the required integrals, we reduce the integration time for a given precision in a remarkable way as compared to other integration rules.

3.2. Non-continuous geometries

In the case of non-continuous geometries, the strips are open rather than closed. Here we define the geometry of the boundary Γ using a non-dimensional variable η which is the normalized length along the straight line connecting the start and end point of the strip as shown in Figure 3. Note that $\eta = 0$ and $\eta = 1$ at the start and end points of the strip, respectively.

For a given collocation point at $\eta = \eta_0$, the kernels in (15) will be denoted by $\tilde{u}^*(\eta, \eta_0)$, $\tilde{p}^*(\eta, \eta_0)$. The integrals that must be evaluated have the form:

$$\int_{\Gamma} \eta^n \tilde{u}^*(\eta, \eta_0) d\Gamma, \quad \int_{\Gamma} \eta^n \tilde{p}^*(\eta, \eta_0) d\Gamma \quad (19)$$

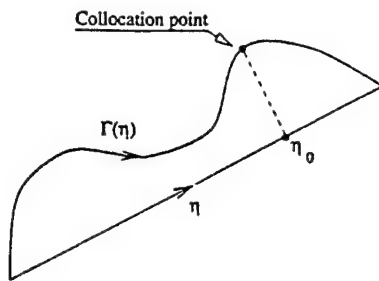


Figure 3. Singularity subtraction from an open curved geometry

We note here that the regular polynomial basis functions are suitable only for 'regular problems', i.e. problems without singularities at the corners (e.g. a convex corner in a finite domain). For non-regular problems, singular shape functions are necessary to capture the behaviour in interior corners. We limit our discussion below to regular problems.

Analogous to the procedure for the continuous geometries, we define $\tilde{u}^*(\eta, \eta_0)$ and $\tilde{p}^*(\eta, \eta_0)$ to be the kernels along a straight line with a singularity point at $\eta = \eta_0$. Changing integration variable to η and adding and subtracting the function $\eta^n \tilde{u}^*(\eta, \eta_0) d\Gamma/d\eta(\eta_0)$ from the integrand yields:

$$\int_{\Gamma} \eta^n \tilde{u}^*(\eta, \eta_0) d\Gamma = \int_0^1 \eta^n \left[\tilde{u}^*(\eta, \eta_0) \frac{d\Gamma}{d\eta} - \tilde{u}^*(\eta, \eta_0) \frac{d\Gamma}{d\eta}(\eta_0) \right] d\eta + \frac{d\Gamma}{d\eta}(\eta_0) \int_0^1 \eta^n \tilde{u}^*(\eta, \eta_0) d\eta \quad (20)$$

Once again we get two integrals. One has a non-singular integrand, while the other can be evaluated in closed form.¹²

A continuity condition between neighbouring strips might be imposed in a manner similar to that described in Reference 12, however, it is not necessary.

3.3. Singularity subtraction: Helmholtz and elastodynamics

One of the most problematic kernels to integrate is the hyper-singular elastodynamics kernel. The most convenient way to treat this kernel is to subtract from it the elastostatics kernel, leaving a non-singular kernel remaining.¹⁷ Rather than subtracting the elastostatics kernel for the same geometry, however, we propose subtracting the elastostatics kernel corresponding to the geometry of a circle or a straight line. This way, though we will still have to numerically evaluate the integrals over the subtracted kernel, the singular subtracted part of the integration is known analytically.

The same procedure can be applied to the Helmholtz equation. We subtract from the Helmholtz equation kernels for a curved geometry, the Laplace equation kernels for a circle or a straight line.

This procedure is applicable not just for BSM, since it can be used also in BEM using the polynomial approximation.

4. TRANSFORMING MATRICES FROM COLLOCATION TO GALERKIN

When we use Fourier series as the spectral series for the approximation, the coefficients matrices \mathbf{H} and \mathbf{G} can be transformed from collocation matrices to Galerkin matrices in a very rapid way using FFT.

In the collocation method the sub-sub-matrices have the form

$$\begin{aligned} h_{mn}^C &= c(x_1) e^{im\theta_m} + \int_{\Gamma_n} p^*(x_1, x_2) e^{im\theta_m} d\Gamma_{ns} \\ g_{mn}^C &= \int_{\Gamma_m} u^*(x_1, x_2) e^{im\theta_m} d\Gamma_{ns} \end{aligned} \quad (21)$$

In Galerkin they have the form

$$\begin{aligned} h_{mn}^G &= \int_{\Gamma_m} c(x_1) e^{i(m+n)\theta_m} d\Gamma_{ms} + \int_{\Gamma_m} \int_{\Gamma_n} p^*(x_1, x_2) e^{i(m\theta_m + n\theta_n)} d\Gamma_{ns} d\Gamma_{ms} \\ g_{mn}^G &= \int_{\Gamma_m} \int_{\Gamma_n} u^*(x_1, x_2) e^{i(m\theta_m + n\theta_n)} d\Gamma_{ns} d\Gamma_{ms} \end{aligned} \quad (22)$$

The superscripts C and G stand for collocation and Galerkin, respectively. Note that in the case of collocation each row in the global matrices \mathbf{H}^C and \mathbf{G}^C is due to a different collocation point. We choose to collocate along the boundary in even increments of the circumferential angle θ (which is the simplest and most convenient way to collocate). We then use these collocation points in the FFT algorithm to transform equation (21) to (22). To do this we simply multiply each row in the matrices $\hat{\mathbf{H}}^C$ and $\hat{\mathbf{G}}^C$ by the value of $d\Gamma/d\theta$ at the corresponding collocation point and then perform a FFT on each column of these matrices:

$$\hat{\mathbf{H}}_{ms,ns}^G = \text{FFT}_{ns} \left\{ \hat{\mathbf{H}}_{ms,ns}^C \cdot \frac{d\Gamma}{d\theta}(\theta_{ms}) \right\}, \quad \hat{\mathbf{G}}_{ms,ns}^G = \text{FFT}_{ns} \left\{ \hat{\mathbf{G}}_{ms,ns}^C \cdot \frac{d\Gamma}{d\theta}(\theta_{ms}) \right\} \quad (23)$$

the operator FFT_{ns} means that we form the FFT of the ns column.

In the case where we want to refine the values of the matrices \mathbf{H}^G , \mathbf{G}^G we can collocate at the mid-point between each two previous collocation points and repeat the procedure leading to equation (23). If we do so we can use the Richardson extrapolation¹⁹ for a further refinement.

The case of polynomial basis functions is more complicated and less effective than the Fourier basis. Nevertheless, we can transform the matrices from collocation to Galerkin quite easily. In this case we collocate in even increments of the parameter η . To obtain Galerkin matrices, we then multiply each line in the matrices $\hat{\mathbf{G}}^C$, $\hat{\mathbf{H}}^C$ by $\eta_0^n d\Gamma/d\eta(\eta_0)$ and integrate the columns by summation with relevant weights, e.g. using Simpson's integration or any other convenient integration rule which uses even spaces. This will give us the n th row in the Galerkin matrices $\hat{\mathbf{H}}^G$, $\hat{\mathbf{G}}^G$. Using an evenly spaced integration rule in η has an advantage if refinement is needed. To refine, we collocate only at mid-points of the previous collocation points, and utilize the previous values. Note that in this case we can also apply the Richardson extrapolation for a further refinement.

There is a difficulty in using this transformation for elastostatics and for elastodynamics since the values of the integral over the $p^*(\eta, \eta_0)$ kernel are singular for the collocation points at the edges. (See, for example, Reference 12, Appendix A, equation A.1). We know, however, that the

singularity at such points is logarithmic. Thus it can be subtracted using a procedure similar to that presented in this paper. Another possibility is using Gauss quadrature rule which would overcome the difficulty of singularity. Collocating at the Gauss points, however, prevents us from using previous function evaluations when refining our solution space.

5. NUMERICAL RESULTS

The collocation BSM was already compared to the BEM^{11,12} and BSM seems to be more efficient and accurate in most cases. Therefore, in this section we will focus on the comparison between the collocation BSM and the Galerkin BSM.

Three potential problems (Laplace equation) are investigated herein. The first problem involves an elliptical domain with an eccentric circular cavity as shown in Figure 4. The boundary conditions for this problem were taken as $u = 0$ and $u = 10$ on the outer and inner boundaries, respectively. The problem was modelled using two strips with a Fourier series approximation, and it was solved by BSM using both the collocation and Galerkin formulations. The converged results for $\partial u / \partial n$ along the boundaries are shown in Figure 5. It can be seen as expected that the solution contains high gradients in the region where the cavity boundary and the outer boundary are close. We define an overall average percentage error of the variable v along the boundary as

$$\text{Overall error [\%]} = 100 \times \frac{\int_{\Gamma} |v_{\text{exc}} - v_{\text{num}}| d\Gamma}{\max |v_{\text{exc}}| L_{\Gamma}} \quad (24)$$

Here L_{Γ} is the length of the integration path, v_{exc} is either the analytical solution (if available) or the converged numerical solution, and v_{num} is the numerical result. Figure 6 depicts the overall average percentage error for collocation and for Galerkin BSM as functions of the number of harmonics used for the approximation on each strip. Both formulations show an exponential

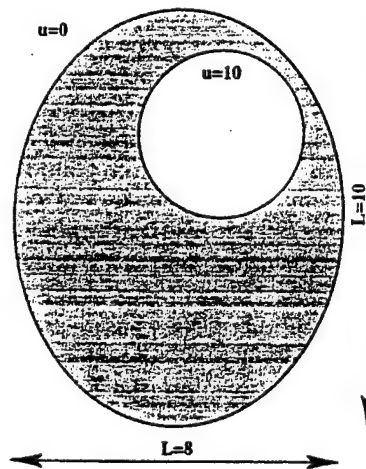


Figure 4. Elliptical domain with an eccentric circular cavity: geometry and boundary conditions

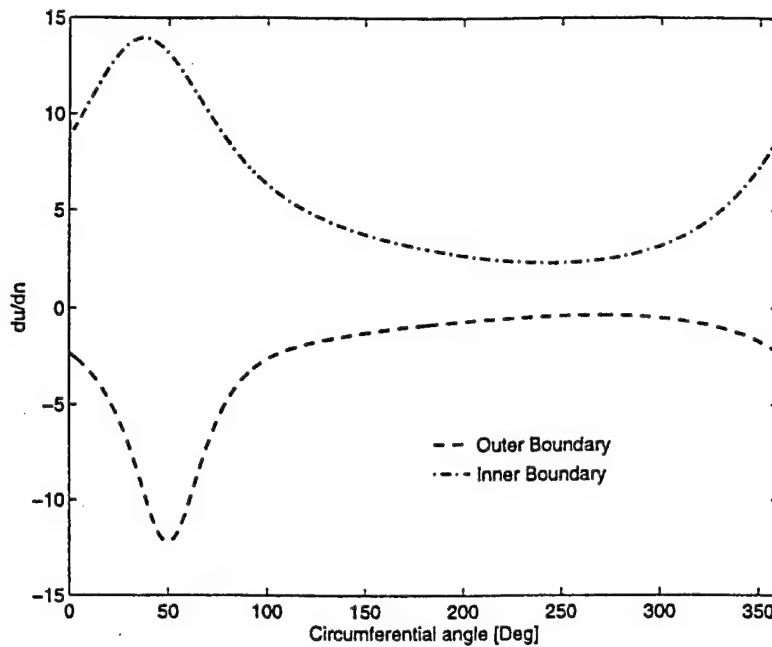


Figure 5. Elliptical domain with an eccentric circular cavity: $\partial u / \partial n$ distribution along the boundaries

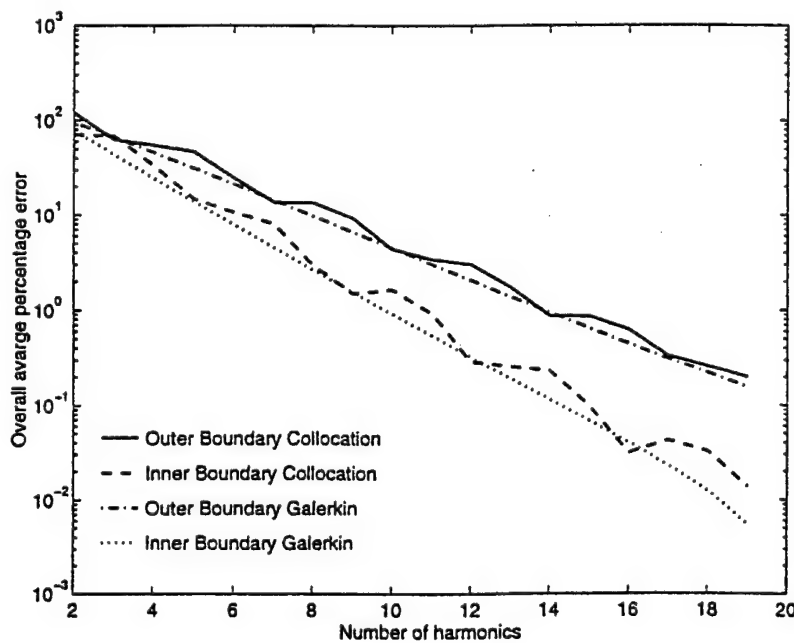


Figure 6. Elliptical domain with an eccentric circular cavity: overall error along the boundaries for collocation and for Galerkin BSM

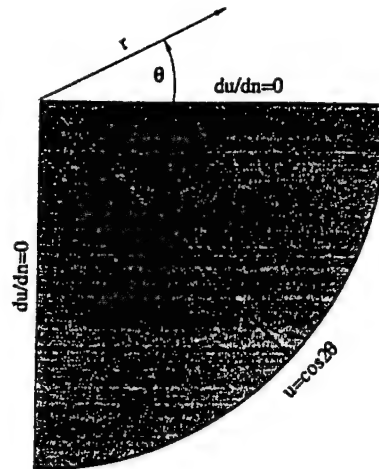


Figure 7. Quarter of a circle domain: geometry and boundary conditions

convergence rate. Furthermore, both formulations yield numerical results with an accuracy that is better than BEM for the same number of DOF. It can be seen that the Galerkin formulation is more consistent than collocation and that its convergence rate is almost purely exponential. The results of the Galerkin formulation are at least as accurate and often more accurate than the collocation formulation.

The second problem, which is described in Figure 7, is on a quarter-circle domain. The boundary conditions $\partial u / \partial n = 0$ are applied on the straight edges, while $u = \cos 2\theta$ on the curved edge. The analytical solution for this problem is $u = (r/R)^2$ on the straight edges and $\partial u / \partial n = 2 \cos 2\theta / R$ on the arc. Three strips are used to model the problem, two for the straight edges and one for the arc. The exact analytical solution is achieved when a polynomial approximation is used along the straight lines and a spectral half cosine approximation of the form $\sum \cos(n\theta/2)$ is used on the arc. However, in order to check the convergence of the polynomial approximation we used high order polynomials along all three strips. Figure 8 presents the overall percentage error as function of the order of polynomial which is used for the approximation on the arc strip, for collocation, for Galerkin and for an 'equivalent' (i.e. same number of DOF) BEM model of quadratic elements. As in the case of the harmonic approximation, the polynomial approximation yields exponential convergence for both spectral formulations. The Galerkin formulation seems to be more consistent than collocation in this problem as well.

Since the solution on the arc is an even function we expect that the odd polynomial orders will not contribute to the solution. We obtain this behaviour exactly in the Galerkin formulation (the steps), but not in the collocation formulation.

There is divergence in the collocation results when a polynomial order is higher than 15, and in the Galerkin formulation when it is higher than 10. Numerical experimentation shows that this divergence is due to accuracy of the numerical integration. The Galerkin formulation diverges first since it involves a double integration and therefore accumulates more error. We note, however, that ill conditioning for high order polynomials (15 to 20 and more) will appear even

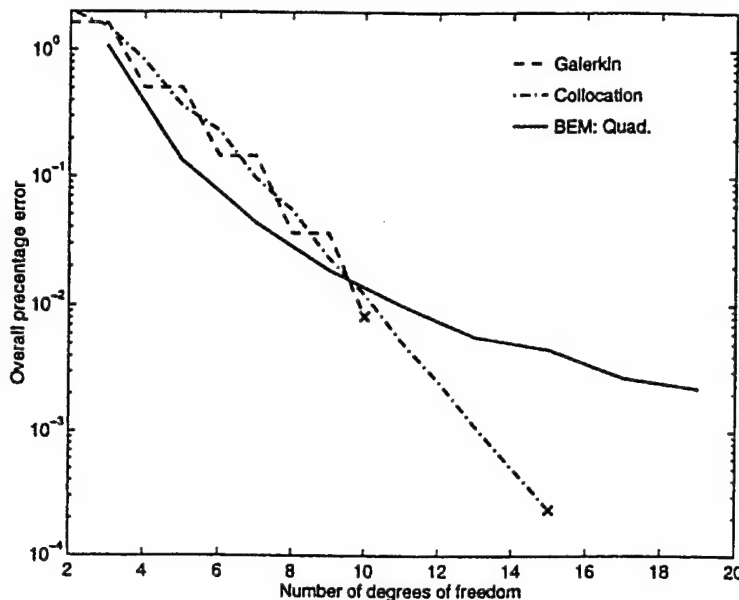


Figure 8. Quarter of a circle domain: overall percentage error versus number of degrees of freedom along the arc, for collocation and Galerkin BSM and for BEM quadratic elements

when using exact analytical integration.¹² We found the computational effort involved in integrating more accurately to be impractical. Therefore, without improved integration procedures, the polynomial Galerkin BSM is limited to $p10$. We emphasize that we found that no such limitation using Fourier series.

The third problem is of a curved cavity in an infinite domain as shown in Figure 9. The boundary conditions for this problem are $u_\infty - u = \text{Constant}$. The problem was modelled using only one strip with a Fourier series approximation. The results for $\partial u / \partial n$ along the boundary are depicted in Figure 9 for 2, 4 and 16 harmonics. For this problem the results of the collocation and the Galerkin results were almost identical, with only a small advantage to the Galerkin formulation.

Although the difference between the collocation and the Galerkin formulation in this problem is minor, this problem demonstrates the merits of the BSM, in general, and the Galerkin BSM in particular. Excellent results were achieved using only 4 harmonics (9 DOF). Equivalent results clearly would demand a much denser grid and thus a larger problem size if other BIE methods were used.

6. SUMMARY AND COMMENTS

In this paper we presented and considered a Galerkin formulation for spectral solutions of the boundary integral equation. To simplify and improve its implementation, we developed a procedure for exact singularity subtraction based some known analytical integrations. To our knowledge, this is the first regularization technique for spectral boundary integral methods.²¹ Further, we note that the subtracted integral functions are continuous. We presented a new Galerkin

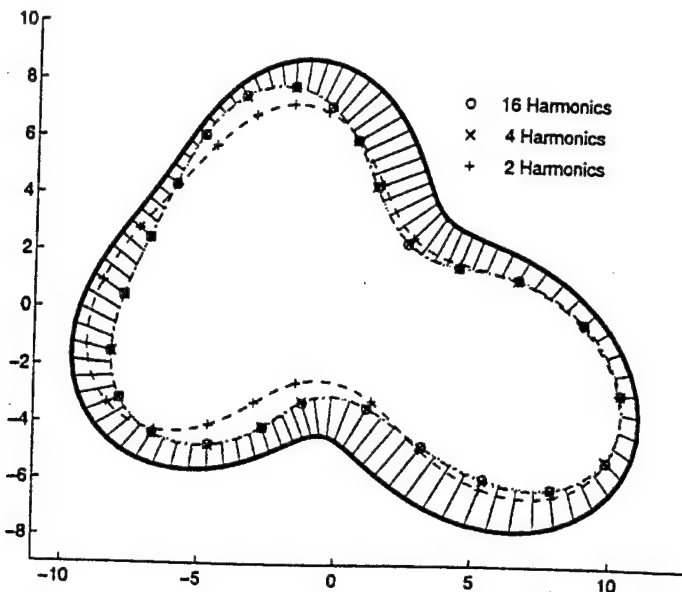


Figure 9. A curved cavity in an infinite domain: Geometry, boundary conditions and $\partial u / \partial n$ distribution for 4, 8 and 16 harmonics approximation

formulation for the boundary strip method, and showed a way to obtain the Galerkin BSM matrices directly from the collocation matrices by using a simple transformation rule (FFT in the case of harmonics or a summation with weights in the case of polynomials).

The new Galerkin BSM formulation shows some unique numerical properties and advantages that are not available in other BIE solution methods. The Galerkin BSM is completely free of mesh generation, and apart from the definition of the strips (as might be done anyway by any CAD system) there is no further requirement for a mesh. Another important advantage related to mesh generation is the fact that unlike the BEM, both collocation and Galerkin BSM solve the problem in the original geometry and there is no geometry distortion.

Both collocation and Galerkin BSM show exponential convergence rates. Generally, the Galerkin BSM seems to be more consistent and numerically stable for Fourier basis functions and low order polynomials. When using polynomial base functions, however, the Galerkin BSM becomes unstable at a $p \approx 10$.

Another advantage of the BSM is that the approximation coefficients are uncoupled. Thus, in order to increase the approximation order, we simply add to the old matrices, rows and columns that correspond to the added approximation coefficients.

Furthermore, we developed some analytical integrations for the Laplace and elastostatics kernels which can be used to improve numerical accuracy and efficiency. The integrations for the straight line geometry can be used also in a Galerkin formulation of a linear BEM. Using these integrals we can construct the integrals for required linear BEM shape functions.

Finally, comparing between Galerkin and collocation BSM, we conclude the following: Galerkin and collocation perform almost the same. Galerkin is completely meshless. The pre-processing time (i.e. the time to generate the coefficient matrices) is only modestly higher in

Galerkin since the Galerkin matrices can be obtained from a straightforward transformation of the collocation matrices. Further, for Dirichlet problems, the Galerkin coefficient matrix is symmetric and therefore would require about half of the time to solve the resulting system of equations as compared to the full unsymmetric coefficient matrix of collocation.²⁰

APPENDIX

Analytical integrations

In this appendix the analytical results for the integrals of equation (14) and (16) for Laplace's equation and for elastostatics are presented.

The kernel for the 2D Laplace equation is

$$u^*(\mathbf{x}_1, \mathbf{x}_2) = \frac{1}{2\pi} \ln\left(\frac{1}{r}\right), \quad p^*(\mathbf{x}_1, \mathbf{x}_2) = \frac{\partial u^*(\mathbf{x}_1, \mathbf{x}_2)}{\partial n} = -\frac{1}{2\pi r} \frac{\partial r}{\partial n} \quad (25)$$

Here r is the distance between the points $\mathbf{x}_1, \mathbf{x}_2$. Using the integrations in Reference 11 we have the following integrals along a circular path of radius R :

$$\begin{aligned} \oint_{\Gamma} e^{im\theta} \left[\oint_{\Gamma} e^{in\theta} u^* d\Gamma \right] d\Gamma &= \pi R^2 \begin{cases} -\ln R, & m = n = 0 \\ 1/n, & m = -n \quad |m| \geq 1 \\ 0, & \text{otherwise} \end{cases} \\ \oint_{\Gamma} e^{im\theta} \left[\oint_{\Gamma} e^{in\theta} p^* d\Gamma \right] d\Gamma &= \pi R \begin{cases} 1, & m = -n \quad |m| \geq 0 \\ 0, & \text{otherwise} \end{cases} \end{aligned} \quad (26)$$

For a straight line, we derive the integrals of equation (16) based on:¹²

$$\begin{aligned} \int_{\Gamma} \eta^m \left[\int_{\Gamma} \eta^n u^* d\Gamma \right] d\Gamma &= \frac{L^2}{2\pi(n+1)} \left\{ \frac{\ln(1/L)}{m+1} - \sum_{k=0}^{n+m+1} \binom{n+m+1}{k} \frac{(-1)^k}{(k+1)^2} \right. \\ &\quad \left. + \frac{1}{(n+m+2)^2} + \sum_{k=0}^m \binom{m}{k} \frac{(-1)^k}{(k+1)^2} + \sum_{k=1}^{n+1} \frac{1}{(n-k+2)(m+k)} \right\} \\ \int_{\Gamma} \eta^m \left[\int_{\Gamma} \eta^n p^* d\Gamma \right] d\Gamma &= 0 \end{aligned} \quad (27)$$

where L is the total length of the line strip.

The 2D elastostatics kernel is given by

$$\begin{aligned} u_{lk}^*(\mathbf{x}_1, \mathbf{x}_2) &= \frac{1}{8\pi\mu(1-\nu)} \left[(3-4\nu) \ln\left(\frac{1}{r}\right) \delta_{lk} + r_{,l} r_{,k} \right] \\ p_{lk}^*(\mathbf{x}_1, \mathbf{x}_2) &= -\frac{1}{4\pi r(1-\nu)} \left\{ \frac{\partial r}{\partial n} (1-2\nu) (\delta_{lk} + n_l r_{,k} - n_k r_{,l}) + 2 \frac{\partial r}{\partial n} r_{,k} r_{,l} \right\} \end{aligned} \quad (28)$$

Here, ν is Poisson's ratio and μ is the shear modulus. The elastostatics related harmonics integrals are:

$$\oint_{\Gamma} e^{im\theta} \left[\oint_{\Gamma} e^{in\theta} u^* d\Gamma \right] d\Gamma = \frac{\pi R^2}{4\mu(1-\nu)} \begin{cases} [1 - 2(3 - 4\nu) \ln R] \mathbf{I}, & n = m = 0 \\ (3 - 4\nu)/n \mathbf{I}, & n = -m \quad |n| \geq 1 \\ (3 - 4\nu) \mathbf{I} - \frac{1}{2} \mathbf{A}, & n = -m = \pm 1 \\ 0, & \text{otherwise} \end{cases}$$

$$\oint_{\Gamma} e^{im\theta} \left[\oint_{\Gamma} e^{in\theta} p^* d\Gamma \right] d\Gamma = \frac{\pi R}{2(1-\nu)} \begin{cases} 2(1-\nu) \mathbf{I}, & n = m = 0 \\ \mp (1-2\nu) \mathbf{B}, & n = -m \quad n > 1 \\ (1-2\nu) \mathbf{B} - \frac{1}{2}(1-\nu) \mathbf{A}, & n = -m = \pm 1 \\ 0, & \text{otherwise} \end{cases} \quad (29)$$

where

$$\mathbf{A} = \begin{bmatrix} 1 & \pm i \\ \pm i & 1 \end{bmatrix}, \quad \mathbf{B} = \begin{bmatrix} 0 & 1 \\ -1 & 0 \end{bmatrix} \quad (30)$$

and for the spectral polynomial approximation:

$$\int_{\Gamma} \eta^m \left[\int_{\Gamma} \eta^n u^* d\Gamma \right] d\Gamma = \frac{L^2}{8\pi\mu(1-\nu)(n+1)} \left\{ (3-4\nu) \left[\frac{\ln(1/L)}{m+1} + \frac{1}{(n+m+2)^2} \right. \right. \\ \left. - \sum_{k=0}^{n+m+1} \binom{n+m+1}{k} \frac{(-1)^k}{(k+1)^2} + \sum_{k=0}^m \binom{m}{k} \frac{(-1)^k}{(k+1)^2} \right. \\ \left. + \sum_{k=1}^{n+1} \frac{1}{(n-k+2)(m+k)} \right] \mathbf{I} + \frac{1}{m+1} \mathbf{C} \right\} \\ \int_{\Gamma} \eta^m \left[\int_{\Gamma} \eta^n p^* d\Gamma \right] d\Gamma = \frac{(1-2\nu)L}{4\pi(1-\nu)} \left\{ \frac{1}{(n+m+1)^2} + \sum_{k=0}^{n+m} \binom{n+m}{k} \frac{(-1)^k}{(k+1)^2} \right. \\ \left. - \sum_{k=0}^{n-1} \frac{1}{(n-k)(m+k+1)} \right\} \mathbf{B} \quad (31)$$

The matrix \mathbf{C} is defined as

$$\mathbf{C} = \begin{bmatrix} \cos^2 \beta & \frac{1}{2} \sin 2\beta \\ \frac{1}{2} \sin 2\beta & \sin^2 \beta \end{bmatrix} \quad (32)$$

where β is the orientation angle of the line strip.

ACKNOWLEDGMENT

The authors gratefully acknowledge the financial support of ONR.

REFERENCES

1. 'Spectral and high order methods for partial differential equations', *Proc. ICOSAHOM '89 Conf.*, Villa Olmo, Como (Italy), June 1989, pp. 26-29.

2. D. Gottlieb and S. A. Orszag, 'Numerical analysis of spectral methods: theory and applications', *CBMS-NSF Regional Conf.*, Series in Applied Mathematics, Philadelphia, SIAM, 1977.
3. E. Moses, P. Bar-Yoseph and A. Yarin, 'On finite element solutions of boundary layer equations', *Comput. Fluid Dyn.*, 3, 139-160 (1994).
4. Y. K. Cheung, 'Finite strip method in analysis of elastic plates with two opposite simply supported ends', *Proc. Inst. Civ. Engng.*, 40, 1-7 (1968).
5. D. J. Dawe and S. Wang, 'Vibration of shear-deformable beams using a spline function approach', *Int. J. Numer. Meth. Engng.*, 33, 819-844 (1992).
6. C. A. Brebbia, *The Boundary Element Method for Engineers*, Pentech Press, London, 1978.
7. A. H Schatz, *Mathematical Theory of Finite and Boundary Element Methods*, Birkhauser, Basel 1990.
8. C. A. Brebbia and J. Dominguez, 'Boundary element methods versus finite elements', in C. A. Brebbia (ed.), *Proc. Int. Conf. on Applied Numerical Modeling*, Pentech Press, London, 1978.
9. I. Harari and T. J. R. Hughes, 'A cost comparison of boundary and finite element methods for problems of time-harmonic acoustics', *Comput. Methods Appl. Mech. Engng.*, 97, 77-102 (1992).
10. R. P. Shaw, 'E' can mean eigenfunction in BEM', in C. A. Brebbia (ed.), *Proc. Boundary Element Method XVI*, 1994, pp. 3-10.
11. O. Michael, J. Avrashi and G. Rosenhouse, 'The boundary strip method in elastostatics and potential equations', *Int. J. Numer. Meth. Engng.*, 39, 527-544 (1996).
12. O. Michael, J. Avrashi and G. Rosenhouse, 'A new boundary spectral strip method for non-periodical geometrical entities based on analytical integrations', *Comput. Methods Appl. Mech. Engng.*, 135, 327-342 (1996).
13. P. A. Martin, F. J. Rizzo and I. R. Gonsalves, 'On hyper singular boundary integral equations for certain problems in mechanics', *Mechanics Research Commun.*, 16, 65-71 (1989).
14. T. J. R. Hughes, *The Finite Element Method: Linear Static and Dynamic Finite Element Analysis*, Prentice-Hall, Englewood Cliffs, N.J., 1987.
15. O. Michael, J. Avrashi and G. Rosenhouse, 'Boundary spectral strip for 2D frequency domain elastodynamics', (1996), submitted for publication.
16. O. Michael, J. Avrashi and G. Rosenhouse, 'Steady state elastodynamics solutions using boundary spectral line strip', *Engng Comput.*, (1997), accepted for publication.
17. F. J. Rizzo, D. J. Shippy and M. Rezayat, 'A boundary integral equation method for time-harmonic radiation and scattering in an elastic half-space', in T. A. Cruse, A. Pifko and H. Armen, (eds.), *Advanced Topics in Boundary Element Analysis*, ASME, AMD 72, 1985, pp. 83-90.
18. D. C. Champeney, *Fourier Transforms and their Physical Applications*, Academic Press, New York, 1973.
19. C. F. Gerald and P. O. Wheatley, *Applied Numerical Analysis*, Addison-Wesley Reading, MA, 1989.
20. G. H. Golub and C. F. van Loan, *Matrix Computations*, 2nd edn., The Johns Hopkins University Press, Baltimore and London, 1989.
21. M. Tanaka, V. Sladek and J. Sladek, 'Regularization technique applied to boundary element methods', *Appl. Mech. Rev.*, 40, 457-499 (1994).

C.5 Diffraction from simple shapes by a hybrid asymptotic-numerical method

"Diffraction from simple shapes by a hybrid asymptotic-numerical method," Joshua M. Montgomery and Paul E. Barbone, **Journal of the Acoustical Society of America**, vol 104(4), pp. 1964–1972, October 1998.

Diffraction from simple shapes by a hybrid asymptotic-finite element method

Joshua M. Montgomery^{a)} and Paul E. Barbone

Department of Aerospace and Mechanical Engineering, Boston University, Boston, Massachusetts 02215

(Received 19 May 1997; revised 8 November 1997; accepted 8 June 1998)

The application of a hybrid asymptotic/finite element method to the problem of scattering from two-dimensional, submerged objects is considered. The hybrid method is based on patching a short-wavelength asymptotic expansion of the scattered field to a finite element interpolation of the near field. In patching, the diffracted field shape functions with unknown amplitude are forced to agree smoothly with the solution in the near field along a curve at a prescribed distance from the diffraction points. A new hybrid finite element on this artificial boundary represents the effect of the outer domain on the solution within this new boundary. This allows the replacement of the original boundary value problem with an asymptotically equivalent boundary value problem, the domain of which is small and efficiently discretized. The method is applied to diffraction by a blunted wedge, which in this context represents a degenerate prism. The hybrid scattering solution shall be compared to an analytic field representation found using an exact Dirichlet-to-Neumann map.

© 1998 Acoustical Society of America. [S0001-4966(98)04809-7]

PACS numbers: 43.20.Dk [ANN]

INTRODUCTION

We describe a hybrid method for scattering which combines short-wavelength asymptotics with the finite element method. In the hybrid approach, we attempt to draw on the benefits from both methods while eliminating their largest individual deficiencies. For example, an asymptotic approach can be computationally efficient for acoustically large scatterers; however, its applicability is limited since diffraction coefficients are unavailable for geometries with anything but simple discontinuities. Traditional numerical methods, on the other hand, can accommodate arbitrary geometries but are practically limited by their computational cost.

The hybrid method as presented here is related to the method of matched asymptotic expansions (MAE)¹ where, in the short wavelength limit, the scattered field contains two asymptotic regions. In the inner (local) region, the full Helmholtz equation must be solved. In the outer (global) region, the field can be found by means of a suitable short wavelength asymptotic technique, such as the geometrical theory of diffraction (GTD).² The representation of the outer field is written in terms of certain unspecified amplitude functions called "diffraction coefficients." In the MAE method, the solutions in the two regions would be asymptotically matched, thus determining these coefficients.

In our hybrid method, on the other hand, the inner solution is found numerically by patching smoothly to the outer asymptotic approximation. The patching is imposed on an artificial boundary, Γ_R , which is introduced around diffraction regions. This boundary is chosen to be located in an overlap domain where both the inner and outer solutions are valid. Patching the inner and outer fields on Γ_R is equivalent to using the GTD solution to specify a radiation boundary

condition for the inner numerical problem. Thus, we replace the original boundary value problem (b.v.p.) with an asymptotically equivalent one.

The combination of the geometrical theory of diffraction (GTD) with traditional numerical methods in scattering applications dates back to 1975.³ Burnside *et al.*³ introduced the method and demonstrated its utility by computing the two-dimensional electromagnetic fields scattered by a perfectly conducting wedge and a perfectly conducting cylinder of square cross section. They substituted GTD-based shape functions for the fields diffracted by the vertices into a current-based integral formulation of the scattering problem. The GTD-based shape functions were used for distances greater than $\lambda/2$ from the vertices, while pulse shape functions were used for distances smaller than $\lambda/2$. A set of discrete equations was obtained by collocation. Agreement with exact and benchmark solutions was remarkable, especially considering that the near field "numerical region" extended only to a distance of $\lambda/2$.

Since 1975, Burnside's hybrid method has been applied to scattering from a tetrahedron,⁴ has been augmented to address grazing incidence,⁵ has been included within a Galerkin formulation, and applied to bodies of revolution.⁶

Wang⁷ in 1991 was the first to introduce surface wave-based shape functions in a hybrid method. These he included for two-dimensional scattering and scattering from bodies of revolution. Wang noted that integration of the GTD-based shape functions in order to obtain the discretized equations was computationally expensive, and suggested that these integrals be evaluated asymptotically.

None of these authors address uniqueness issues associated with their boundary integral formulation for Helmholtz equation on exterior domains. Further, all rely on a surface integral equation formulation as a starting point of the analysis. Shape functions motivated by asymptotic expansions are

^{a)}Currently affiliated with Noise and Acoustics Division, The Boeing Company, Seattle, WA 98124.

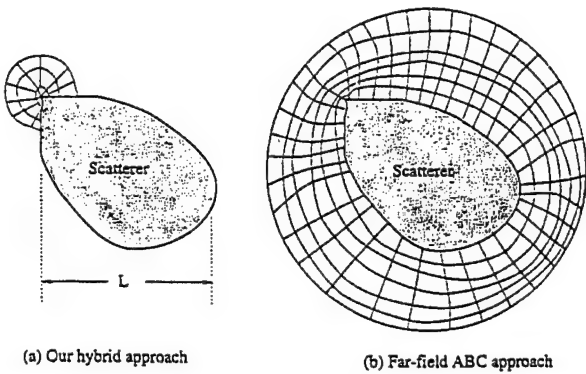


FIG. 1. Conceptual application of our hybrid method compared to a more typical ABC (artificial/absorbing boundary condition) approach. Our method is based on short-wavelength rather than far-field asymptotics. In our method, the condition on the artificial boundary comes from enforcing continuity of the function and its normal derivative with an outer asymptotic expansion. In the ABC approach, a boundary operator (usually a homogeneous differential operator) is applied on the artificial boundary.

then substituted into the equation in a straightforward manner.

There are several distinctions between our approach and these previous approaches. First, we begin with a short wavelength asymptotic expansion of the overall solution, rather than with an integral equation formulation of the overall solution. Within the short-wavelength analysis we embed a well-posed boundary value problem that can be solved numerically. This is in contrast to simply using asymptotics-motivated shape functions in an otherwise traditional numerical formulation as in the works cited above,³⁻⁷ or as in some applications of infinite elements.^{8,9}

Second, we patch the inner numerical solution to the outer short-wavelength asymptotic solution. This concept might be compared to using a far-field asymptotic expansion to derive an approximate boundary condition to be applied on an artificial boundary.^{10,11} Short wavelength expansions are valid when the wavelength λ is much shorter than all other dimensions in the problem. Far-field expansions, on the other hand, are valid when r , the distance from an origin "near" or in the scatterer, is much larger than all other distances in the problem. Only when λ and r are the only characteristic distances in a problem are the two expansions equivalent. (It so happens that the example we shall study in the following sections fits into this category.) One clear distinction between these two approaches is depicted in the cartoons in Fig. 1, which shows the numerical domains associated with each of the two approaches.

Even when the short wavelength expansion and the far-field expansion are equivalent, there is a considerable difference in the implementation of each approach. In the artificial/absorbing boundary condition (ABC) approach,^{10,11} the far-field expansions are used to derive boundary operators that must be satisfied by the numerical solution. The high-order versions of such operators require the evaluation of high-order tangential derivatives of the finite element field. Since most finite element interpolations are only C^0 , these implementations require special attention.¹² Further, this formulation yields only the solution inside the artificial

boundary, and some extra postprocessing is therefore necessary to obtain the field outside the artificial boundary. In the general formulation of our hybrid method described in Sec. IV, on the other hand, we enforce continuity (of both the function and its normal derivative) between the short-wavelength asymptotic approximation and the numerical solution. We thus avoid the need to derive a boundary operator that must be satisfied by the finite-element field. Our boundary condition on the artificial boundary requires no derivatives of the finite-element interpolants for any order asymptotic approximation.

Alternatively, one might compare our hybrid method to an application of infinite elements. One distinction is that, in our formulation, the outer field is required to satisfy the Helmholtz equation (at least asymptotically) before we even formulate the numerical boundary value problem. In typical infinite element applications, on the other hand, the outer field is interpolated in some convenient,¹³⁻¹⁶ or physically inspired,^{8,9} manner. These interpolations are then substituted into a weak form that enforces the approximate satisfaction of the field (Helmholtz, in this case) equation. Further, most infinite element formulations enforce continuity between the inner and outer fields strongly. Finally, our formulation is free of infinite or large domain integrals, while almost all infinite element formulations require infinite integrals of some kind. [The exception to these is the infinite element formulation devised by one of the authors (PEB) in collaboration with I. Harari, as described in Refs. 17 and 18.]

In addition, we remark that our hybrid approach is based on the formulation of an asymptotically equivalent boundary value problem defined on a small domain. We can choose any numerical method to solve this problem. (This is also in clear contrast to infinite elements, for example, in which the treatment of the outer domain is integral in the entire problem formulation.) Here we discuss solving this problem using finite elements, but in another contribution we discuss using the "boundary strip method."¹⁹

The idea of patching a short-wavelength expansion to a collection of numerical solutions (as needed to supplement the validity of the outer expansion) can obviously be applied to a quite complicated scatterer. We have elected to first study and present our method in the context of the most basic of problems, diffraction from a truncated wedge. The formulation and asymptotic solution of this problem is presented in Sec. II. We follow this in Sec. III by discussing the issue of patching inner and outer fields together as opposed to matching them. Our hybrid method depends on patching, yet matching is known to yield the correct directivities. The comparison between patching and matching makes it clear that the patched directivity can provide a good approximation to the exact directivity. More importantly, it shows that the approximation can, in principle, be improved to arbitrarily high accuracy. This gives us reassurance that the proposed technique can be built into a reliable numerical method.

Patching of the numerical solution to the outer asymptotic solution gives rise to a boundary value problem defined on a finite (and relatively small) domain. This boundary value problem is outside the realm of application

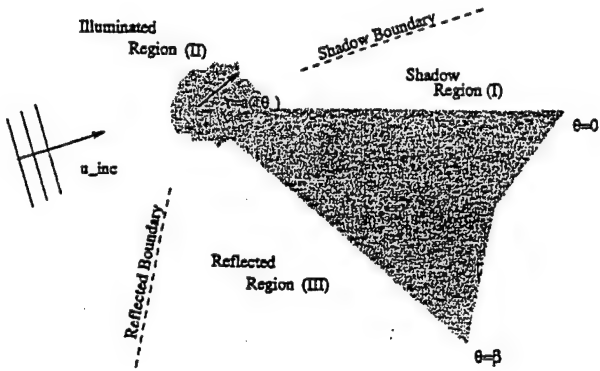


FIG. 2. Blunted wedge with incident plane wave.

of standard finite element methods because of the patching boundary conditions. In Sec. IV, we describe a weak formulation of the asymptotically equivalent b.v.p. as part of a finite element implementation. Here, we enforce the boundary condition by introducing a new “hybrid” finite element. The results from the hybrid method, utilizing this new element, are compared to a reference solution found by means of a Dirichlet-to-Neumann (DtN) map.²⁰

I. FORMULATION

We imagine the wedge, of exterior angle β , positioned such that the tip coincides with the origin while one face lies on the positive x axis. The tip is blunted by a truncation described by $r=a(\theta)$ (see Fig. 2). We assume that the maximum of a is on the order of a wavelength (λ). Thus, $a(\theta)=O(k^{-1})$ or $ka=O(1)$. We let l be a predetermined distance from the tip with which we nondimensionalize all of our spatial coordinates. Then in the limit as $kl\rightarrow\infty$, the wedge appears to be acoustically infinite.

In all that follows we will work in terms of nondimensionalized coordinates as well as wave number, k . We shall also work in terms of a time-harmonic acoustic pressure:

$$p(x,y,t)=\Re\{u_{\text{tot}}(x,y)e^{-i\omega t}\}. \quad (1)$$

The time dependence will be suppressed from here on. The total field is then represented as the sum of an incident plane-wave and scattered field contributions:

$$u_{\text{tot}}=u_{\text{inc}}+u, \quad u_{\text{inc}}=e^{ik(x \cos \theta' + y \sin \theta')}. \quad (2)$$

In the absence of sources, u is governed by the reduced wave equation

$$(\Delta+k^2)u=0. \quad (3)$$

We consider a wedge with soft faces, such that $u_{\text{tot}}=0$ on the wedge. Equation (2) then yields

$$u=-u_{\text{inc}} \begin{cases} r=a(\theta), \\ \theta=0, \quad r \geq a(0), \\ \theta=\beta, \quad r \geq a(\beta). \end{cases} \quad (4)$$

Further, the scattered field must satisfy a radiation condition as $r\rightarrow\infty$.

II. ASYMPTOTIC EXPANSION

We seek an asymptotic approximation of the solution to (1)–(4), valid in the limit as $k\rightarrow\infty$. In this section we discuss the process of obtaining the outer approximation to the field. We follow this by a description of the inner b.v.p. and characteristics of its solution. We then seek to compare the method used in patching these solutions to the method of matched asymptotics.

A. Outer solution

We assume a solution of the form

$$u(x)\sim w(x,k)e^{iks(x)}, \quad k\rightarrow\infty. \quad (5)$$

Here $w(x,k)$ is the amplitude, k is the wave number, and $s(x)$ is the phase. Substituting (5) into (3) yields

$$-k^2[(\nabla s)^2-1]w+2ik\nabla s \cdot \nabla w+ikw\Delta s+\Delta w=0. \quad (6)$$

To solve (6) for large values of k , we assume that w can be expanded in a series of inverse powers of ik :

$$w(x,k)\sim k^{-\alpha} \sum_{m=0}^N w_m(x)(ik)^{-m}+o(k^{-N-\alpha}). \quad (7)$$

Inserting (7) into (6) and equating powers of k yields the eiconal equation

$$(\nabla s)^2=1, \quad (8)$$

and the transport equations

$$2\nabla s \cdot \nabla w_m + w_m \Delta s = -\Delta w_{m-1}, \quad m=0,1,2,\dots, \quad (9)$$

where $w_n=0$ for $n<0$. These equations can be solved by standard characteristic methods which provide the rays of GTD. The phase can be determined using Fermat's principle.² The scattered field can be expressed as the sum of a reflected plane wave, a shadow wave, a diffracted cylindrical wave, plus higher order terms

$$u\sim u_{\text{ref}}+u_{\text{shad}}+u_{\text{diff}}+O(k^{-3/2}). \quad (10)$$

The three different terms in the above equation represent the leading terms of three different expansions, each of the form (5) with (7). By defining an angle $\phi=\theta'-2\beta$, these contributions can be expressed as the following:

$$\begin{aligned} u_{\text{shadow}} &= -e^{ik(x \cos \theta' + y \sin \theta')} && \text{shadow region,} \\ u_{\text{ref}} &= -e^{ik(x \cos \phi + y \sin \phi)} && \text{reflected region,} \\ u_{\text{diff}} &= \frac{D(\theta, \theta')}{\sqrt{kr}} e^{ikr} && \text{everywhere.} \end{aligned} \quad (11)$$

Here, $D(\theta, \theta')$ is not yet determined. It represents the amplitude of the field diffracted into the θ direction due to an incident wave in the θ' direction. It is sometimes referred to as the “diffraction coefficient” associated with the wedge.

An immediate concern regarding this representation (11) is the discontinuity between the regions. In order to obtain a smooth transition across the boundaries, we introduce a boundary layer solution. Such solutions are readily available in many textbooks (e.g., Refs. 21–24).

As an example, we consider the boundary between the shadow region (I) and the illuminated region (II). We introduce a change of coordinates:

$$\xi = x \cos \theta' + y \sin \theta', \quad (12)$$

$$\eta = -x \sin \theta' + y \cos \theta'. \quad (13)$$

In terms of these new variables,

$$u_{\text{shad}} \sim \mathcal{H}(\eta) e^{ik\xi}. \quad (14)$$

Here \mathcal{H} is the Heaviside step function. This solution is clearly not valid on $\eta=0$, where there is a discontinuity predicted. Following the example in Ref. 21 yields the boundary layer solution:

$$u_{bl}(\xi, \eta) = \frac{1}{\sqrt{\pi}} e^{-i(\pi/4)} e^{ik\xi} \int_{-\eta\sqrt{k/2\xi}}^{\infty} e^{iz^2} dz. \quad (15)$$

Equation (15) shows that in the limit of $\|\eta\sqrt{k/\xi}\| \gg 1$ there exists a plane wave, $e^{ik\xi}$, for $\eta > 0$ and no first-order contribution for $\eta < 0$. On the boundary ($\eta=0$) the amplitude of the field is the average of the amplitudes in (I) and (II). Replacing u_{shad} in (11) with u_{bl} in (15) yields an asymptotic expansion for the field which is valid everywhere except at $r=0$. We note that a representation that is uniformly valid in angle can be obtained without specific solution of a "canonical" or inner problem near the wedge tip. Until the solution of the inner problem is obtained, however, the directivity $D(\theta)$ that appears in (11) remains unknown.

B. Inner diffraction problem

It is the solution of the inner problem, or canonical problem, that provides the unknown diffraction coefficient. In the usual GTD or MAE approach, the inner solution is found analytically and then matched asymptotically to the outer solution. In our hybrid method, on the other hand, we shall find the inner solution numerically by patching it smoothly to the outer solution [Eqs. (11) and (15), or an equivalent solution]. In this section, we shall examine (analytically) the process of matching and patching to show that in some sense they are equivalent. This tells us that our hybrid method, based on patching, can provide a good approximation to the diffraction coefficient.

The inner problem is obtained by rescaling in "inner" variables:

$$R = kr; \quad \Theta = \theta; \quad U(R, \Theta) = u(r, \theta). \quad (16)$$

Rewriting the reduced wave equation (3) in polar coordinates gives the inner problem:

$$\left(\frac{\partial^2}{\partial R^2} + \frac{1}{R} \frac{\partial}{\partial R} + \frac{1}{R^2} \frac{\partial^2}{\partial \Theta^2} \right) U + U = 0, \quad (17)$$

$$U = -U_{\text{inc}} \begin{cases} R = ka(\theta), \\ \Theta = 0, \beta, \quad R > ka, \end{cases} \quad (18)$$

$$U \text{ matches } u \text{ as } R \rightarrow \infty. \quad (19)$$

We note that in contrast to the outer equations, the limit $k \rightarrow \infty$ does not simplify the inner differential equation at all. We must solve the full Helmholtz equation.

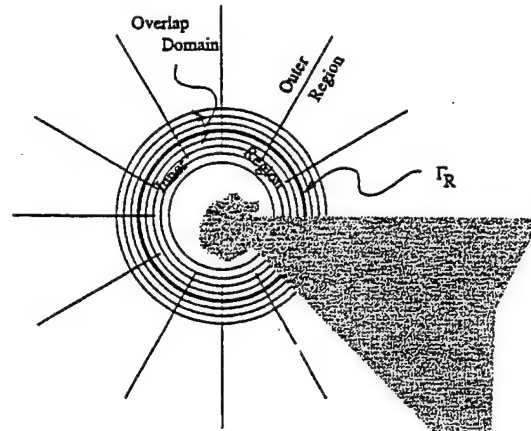


FIG. 3. Inner and outer regions.

In all that follows, we shall find it convenient to work in terms of $\hat{U} = U - U_{\text{sharp}}$. Here U_{sharp} represents the field (with minimum singularity) scattered by a sharp wedge due to an incident field U_{inc} .²² Further, U_{sharp} can be shown to match the plane wave and boundary layer solutions in the outer field. Thus, the function \hat{U} satisfies (17) and

$$\hat{U} = \begin{cases} -U_{\text{inc}} - U_{\text{sharp}} & \text{on } R = ka(\theta), \\ 0 & \text{on } \Theta = 0, \beta. \end{cases} \quad (20)$$

For a general $a(\theta)$, the solution for \hat{U} cannot be obtained in closed form. Without the analytical form, we cannot match U to u as indicated in Eq. (19). Therefore, in Sec. IV, we shall describe a numerical method to find \hat{U} subject to a patching condition replacing (19). For either outer boundary condition, \hat{U} can be uniquely represented outside $R = ka_{\max}$ as

$$\begin{aligned} \hat{U}(R, \Theta) = & \sum_{n=1}^{\infty} A_n H_{\nu_n}^{(1)}(R) \sin \nu_n \Theta \\ & + B_n H_{\nu_n}^{(2)}(R) \sin \nu_n \Theta. \end{aligned} \quad (21)$$

Here, $H_{\nu_n}^{(1)}$ and $H_{\nu_n}^{(2)}$ are the Hankel function of the first and second kind of order ν_n ,²⁵ where $\nu_n = n\pi/\beta$. A_n and B_n are unknown complex constants. For any given $a(\theta)$, there is a set of coefficients S_{nm} such that A_n and B_n can be related as follows:

$$A_n = A_n^0 + \sum_{m=1}^{\infty} S_{nm} B_m. \quad (22)$$

A_n^0 satisfies the inhomogeneous boundary condition (20). The sum $\sum_{m=1}^{\infty} S_{nm} B_m$ represents the amplitude of the n th scattered mode due to all incident modes with amplitude B_m .

We would now like to match (21) to the cylindrical wave in (11) to find $D(\theta)$ in terms of A_n and B_n . In the method of matched asymptotic expansions, this requires an overlap domain in which both (21) and (11) are valid (see Fig. 3). This domain occurs when

$$R = k^\alpha, \quad 0 < \alpha < 1. \quad (23)$$

The hybrid method, on the other hand, relies on patching. The inner solution will be found numerically and forced to agree smoothly with the outer asymptotic solution (11) along Γ_R . Here, Γ_R is chosen to be an arc of a circle lying in the aforementioned overlap domain.

C. Patching versus matching

The method of matched asymptotic expansions yields a solution which is asymptotic to the exact solution. Thus, we are guaranteed that the difference between the exact and asymptotic solutions vanishes in the limit as $k \rightarrow \infty$. Patching on the *fixed* curve $R = \text{const}$, on the other hand, has no such asymptotic validity. Here we shall compare the directivities obtained by patching ($\hat{D}_p(\theta)$) to those obtained by matching ($\hat{D}_m(\theta)$). In particular, we shall show that patching *in the overlap domain* leads to the result that

$$\hat{D}_p(\theta) \sim \hat{D}_m(\theta); \quad k \rightarrow \infty. \quad (24)$$

We denote the outer solutions to be used in the comparison as follows:

$$\hat{u}_p(r, \theta) = u_p - u_{\text{sharp}} = \frac{\hat{D}_p(\theta)}{\sqrt{kr}} e^{ikr}, \quad (25)$$

$$\hat{u}_m(r, \theta) = u_m - u_{\text{sharp}} = \frac{\hat{D}_m(\theta)}{\sqrt{kr}} e^{ikr}. \quad (26)$$

1. Patching

We shall patch along the curve $R = k^\alpha r_0$, or $r = k^{\alpha-1} r_0$:

$$\hat{u}_p(k^{\alpha-1} r_0, \theta) = \hat{U}(k^\alpha r_0, \theta), \quad (27)$$

$$\partial_r \hat{u}_p(k^{\alpha-1} r_0, \theta) = \partial_r \hat{U}(k^\alpha r_0, \theta). \quad (28)$$

Equations (21), (25), (27), and (28) then yield $\hat{D}_p(\theta)$ as

$$\begin{aligned} \hat{D}_p(\theta) &= \sum_{n=1}^{\infty} \frac{-4i}{\pi} \frac{e^{-ik^\alpha r_0}}{\sqrt{k^\alpha r_0}} \\ &\times \frac{A_n \sin \nu_n \theta}{H_{\nu_n}^{(2)'}(k^\alpha r_0) - (i - 1/2k^\alpha r_0) H_{\nu_n}^{(2)}(k^\alpha r_0)}. \end{aligned} \quad (29)$$

In obtaining (29) we have used the identity²⁵

$$H_{\nu_n}^{(1)}(z) H_{\nu_n}^{(2)'}(z) - H_{\nu_n}^{(2)}(z) H_{\nu_n}^{(1)'}(z) = -\frac{4i}{\pi z}. \quad (30)$$

Similarly, we can eliminate $\hat{D}_p(\theta)$ from (27) and (28) to obtain a relation between B_n and A_n :

$$\begin{aligned} B_n &= \frac{(i - 1/2k^\alpha r_0) H_{\nu_n}^{(1)}(k^\alpha r_0) - H_{\nu_n}^{(1)'}(k^\alpha r_0)}{(i - 1/2k^\alpha r_0) H_{\nu_n}^{(2)}(k^\alpha r_0) - H_{\nu_n}^{(2)'}(k^\alpha r_0)} A_n \\ &= O(k^\alpha r_0)^2. \end{aligned} \quad (31)$$

Equations (22) and (31) show that patching yields

$$A_n = A_n^o + O(k^\alpha r_0)^{-2}. \quad (32)$$

2. Matching

We obtain $\hat{D}_m(\theta)$ by using Van Dyke's matching rule.¹ First we express the inner solution (21) in terms of outer variables:

Inner solution:

$$\begin{aligned} \hat{U}^{(0)}(R, \Theta) &= \sum_{n=1}^{\infty} A_n H_{\nu_n}^{(1)}(R) \sin \nu_n \Theta \\ &\quad + B_n H_{\nu_n}^{(2)}(R) \sin \nu_n \Theta. \end{aligned} \quad (33)$$

In outer variables:

$$\begin{aligned} \hat{U}^{(0)}(kr, \theta) &= \sum_{n=1}^{\infty} A_n H_{\nu_n}^{(1)}(kr) \sin \nu_n \theta \\ &\quad + B_n H_{\nu_n}^{(2)}(kr) \sin \nu_n \theta. \end{aligned} \quad (34)$$

We now expand (34) for large k to obtain the outer expansion of the inner solution:²⁵

$$\begin{aligned} \hat{U}^{(0, -1/2)}(kr, \theta) &= \sum_{n=1}^{\infty} \sqrt{\frac{2}{\pi kr}} [A_n e^{i(kr - (\pi/2)\nu_n - \pi/4)} \\ &\quad + B_n e^{-i(kr - (\pi/2)\nu_n - \pi/4)}] \sin \nu_n \theta. \end{aligned} \quad (35)$$

Outer solution:

$$\hat{u}^{(-1/2)}(r, \theta) = \frac{\hat{D}_m(\theta)}{\sqrt{kr}} e^{ikr}. \quad (36)$$

Inner of outer:

$$\hat{u}^{(-1/2, 0)}\left(\frac{R}{k}, \Theta\right) = \frac{\hat{D}_m(\Theta)}{\sqrt{R}} e^{iR}. \quad (37)$$

By Van Dyke's matching rule, (35) and (37) must be equivalent. Thus we conclude that

$$\hat{D}_m(\theta) = \sum_{n=1}^{\infty} \left[\sqrt{\frac{2}{\pi}} A_n e^{-i(\pi/2)(\nu_n + 1/2)} \right] \sin \nu_n \theta, \quad (38)$$

$$B_n = 0. \quad (39)$$

Equations (22) and (39) show that matching yields

$$A_n = A_n^o. \quad (40)$$

Therefore, we conclude from Eqs. (32) and (40) that matching and patching yield the same values for A_n to order $O(k^\alpha r_0)^{-2}$.

3. Error in directivity

We note that $\hat{D}_p(\theta)$ in (29) and $\hat{D}_m(\theta)$ in (38) appear to be different. Further, we note that $\hat{D}_p(\theta)$ depends explicitly on the location of our artificial boundary. This is a typical feature of patching. The matched directivity, $\hat{D}_m(\theta)$, is clearly independent of the purely artificial parameter r_0 .

We measure the error in patching as the difference between $\hat{D}_m(\theta)$ in (38) and $\hat{D}_p(\theta)$ in (29). Thus, we define the following function:

$$\text{error}(\theta) = \sum_n E_n \sin \nu_n \theta \equiv \hat{D}_m(\theta) - \hat{D}_p(\theta). \quad (41)$$

Substituting Eqs. (29) and (38) into (41) leads to

$$E_n = A_n \left[\sqrt{\frac{2}{\pi}} e^{-i(\pi/2)\nu_n - i(\pi/4)} - \frac{-4i}{\pi} \frac{e^{-ik^\alpha r_0}}{\sqrt{k^\alpha r_0}} \right. \\ \times \left. \frac{1}{H_{\nu_n}^{(2)'}(k^\alpha r_0) - (i - 1/2k^\alpha r_0)H_{\nu_n}^{(2)}(k^\alpha r_0)} \right] \\ + O((k^\alpha r_0)^{-2}). \quad (42)$$

Since $0 < \alpha < 1$, $k^\alpha r_0 \rightarrow \infty$ as $k \rightarrow \infty$. Therefore, we can obtain an asymptotic approximation for E_n as $k \rightarrow \infty$ by expanding the Hankel functions for large argument. From Ref. 25 we have

$$H_{\nu_n}^{(2)}(k^\alpha r_0) = \sqrt{\frac{2}{\pi}} \left[1 + i \frac{4\nu_n^2 - 1}{8k^\alpha r_0} \right] \frac{e^{-ik^\alpha r_0}}{\sqrt{k^\alpha r_0}} e^{i(\pi/2) + i(\pi/4)} \\ + O((k^\alpha r_0)^{-5/2}). \quad (43)$$

Combining (42) with (43) yields an asymptotic approximation of the error as

$$E_n \sim -iA_n \sqrt{\frac{2}{\pi}} \frac{4\nu_n^2 - 1}{8k^\alpha r_0} e^{-i(\pi/2)\nu_n - i(\pi/4)} + O((k^\alpha r_0)^{-2}). \quad (44)$$

Clearly, as $k \rightarrow \infty$, $E_n \rightarrow 0$. We note, however, that E_n grows like n^2 for kr_0 fixed. For solutions with bounded energy, however, it can be shown,²⁶ that $A_n = o(\nu_n^{-\nu_n})$ as $\nu_n \rightarrow \infty$. Therefore, (44) vanishes as $k \rightarrow \infty$ for all n .

III. THE HYBRID METHOD

Up to now we have considered the asymptotic aspects of the hybrid asymptotic-numerical method. Here we discuss a numerical formulation suitable for determining the inner solution. Patching the outer asymptotic solution to the numerical solution on the artificial boundary effectively enforces the radiation condition on the inner field. In this section, we describe a weak form developed by us for this purpose. This is followed by a finite element discretization.

A. General formulation

We now describe a weak formulation of our boundary value problem that is suitably incorporated into our hybrid method. We denote the region outside of the scatterer by Ω . The “internal” boundary of Ω is denoted by Γ , which we assume to be piecewise smooth. We consider Γ as being partitioned into Γ_g and Γ_h , where $\Gamma = \Gamma_g \cup \Gamma_h$. The classical or strong form of the problem is to find u in Ω such that

$$(\Delta + k^2)u = -f \text{ in } \Omega, \quad (45)$$

$$u = g \text{ on } \Gamma_g, \quad (46)$$

$$\frac{\partial u}{\partial n} = ikh \text{ on } \Gamma_h, \quad (47)$$

$$\lim_{r \rightarrow \infty} r^{1/2} \left(\frac{\partial u}{\partial r} - iku \right) = 0. \quad (48)$$

The unbounded domain Ω is decomposed by an artificial boundary Γ_R into a bounded inner domain Ω^i and its unbounded outer complement Ω^o . The solution to the original b.v.p. is decomposed into an inner and an outer field:

$$u = \begin{cases} u^i & \text{on } \Omega^i, \\ u^o & \text{on } \Omega^o. \end{cases} \quad (49)$$

In our hybrid method, we choose the outer field, u^o , to be given by the expansion in Eqs. (10) and (11), wherein the directivity $D(\theta)$ is unknown. [Or equivalently, when solving for $u - u_{\text{sharp}}$, by (25) with $\hat{D}_p(\theta)$ unknown.] Equations (45)–(47) are then supplemented by the patching boundary condition on Γ_R :

$$u^i = u^o \text{ on } \Gamma_R, \quad (50)$$

$$\partial_n u^i = \partial_n u^o \text{ on } \Gamma_R. \quad (51)$$

Standard finite element formulations are incompatible with the patching boundary conditions (50) and (51). Here we shall employ the weak formulation of Harari *et al.*²⁷

$$a(\omega^i, u^i) + \left(\omega^i, \frac{\partial u^o}{\partial n^o} \right)_{\Gamma_R} = L(\omega^i), \quad (52)$$

$$\left(\frac{\partial \omega^o}{\partial n^o}, u^i \right)_{\Gamma_R} - \left(\frac{\partial \omega^o}{\partial n^o}, u^o \right)_{\Gamma_R} = 0. \quad (53)$$

It should be noted that $a(\dots)$ and $(\dots)_{\Gamma_R}$ are symmetric bilinear forms which are not inner products. Rather, they are defined as

$$a(\omega, u) = \int_{\Omega^i} (\nabla \omega \cdot \nabla u - \omega k^2 u) d\Omega, \quad (54)$$

$$(\omega, u)_{\Gamma_R} = \int_{\Gamma_R} \omega u d\Gamma, \quad (55)$$

$$L(\omega) = \int_{\Omega^i} w f d\Omega + \int_{\Gamma_h} \omegaikh d\Gamma. \quad (56)$$

We note that to evaluate the terms in (52) and (53), there is integration only over the inner region Ω^i and the artificial boundary, Γ_R . Thus, there is no integration over infinite or even large domains. For (52) and (53) to be valid, the outer solution u^o must satisfy the Helmholtz equation as well as the radiation condition. If the scatterer is not completely contained in Γ_R , then u^o must also satisfy all natural and essential boundary conditions in Ω^o . The functions ω^i and ω^o represent the arbitrary weighting functions of u^i and u^o , respectively. The Euler-Lagrange equations of (52) provide satisfaction of the governing differential equation in Ω^i and enforce continuity of normal derivatives across Γ_R . The relation in (53) enforces continuity of the unknown functions across Γ_R .

B. Finite element formulation

We now turn our attention to the problem of the imperfect wedge. In what follows, we shall be solving for $u_{\text{scat}} - u_{\text{sharp}}$. Thus, u^o will contain only a cylindrical wave contribution. Inside of Γ_R we use standard bilinear, quadrilateral elements with degrees of freedom representing the real and imaginary parts of the field. Let N and D denote shape functions with local support, defined on Ω^i and Γ_R , respectively. Then our inner field can be represented in the context of the finite element method.²⁸

Inner solution:

$$u^i = \sum_A d_A^i N_A^i(r, \theta), \quad (57)$$

$$\omega^i = \sum_A c_A^i N_A^i(r, \theta). \quad (58)$$

Here each sum is over the total number of elements in our mesh. Similarly, we choose a finite element representation for $\hat{D}_p(\theta)$ on Γ_R , and so obtain the following representation of the outer field:

Outer solution:

$$u^o = \sum_M d_M^o D_M^o(\theta) \sqrt{\frac{r_0}{r}} e^{ik(r-r_0)}, \quad (59)$$

$$\omega^o = \sum_M c_M^o D_M^o(\theta) \sqrt{\frac{r_0}{r}} e^{ik(r-r_0)}. \quad (60)$$

Equations (59) and (60) reflect the GTD form of our outer solution (11), normalized by the radius of Γ_R .

To treat the boundary condition on Γ_R we introduce what will be referred to as a "hybrid element." We shall assume that the shape functions N and D are both piecewise linear. Thus, for the special case treated here, the hybrid element has four nodes, two of which are shared with a Helmholtz element. The spatial coordinates of the two pairs match, forming what appears to be a one-dimensional element. We can then use (52) and (53) to find the following element stiffness matrix:

$$K^e = \begin{bmatrix} 0 & \mathcal{H} \\ \mathcal{H} & -\mathcal{H} \end{bmatrix}. \quad (61)$$

Here \mathcal{H} is a 2×2 complex matrix with entries:

$$\mathcal{H}_{AB} = \int_{\Gamma_R^e} C_0 N_A^i N_B^i d\Gamma, \quad (62)$$

$$C_0 = \left(\frac{1}{2r_0} - ik \right). \quad (63)$$

We note that this matrix is symmetric. The lower half of the block weakly enforces continuity between the inner and outer fields. The upper right-hand block contributes to the continuity of normal derivatives.

C. Comparisons

We have implemented the hybrid element and performed calculations for a wedge of angle $\beta = 7\pi/4$. The in-

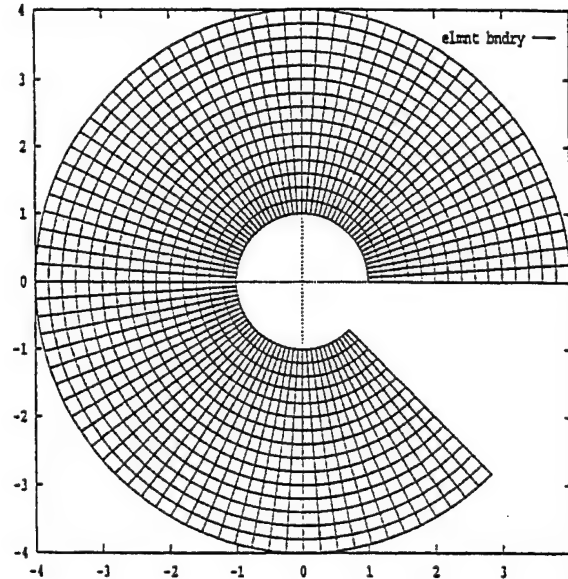


FIG. 4. Mesh used for radiation and scattering from a nonsharp soft wedge.

terior domain Ω^i was meshed with a minimum resolution of ten elements per wavelength (Fig. 4). On the blunted tip, we define $a(\theta) = a_0 = \text{const}$, where $ka_0 = \pi$. We locate the artificial boundary, Γ_R , at $kr_0 = 4\pi$. The solution is forced by the inner boundary condition (20), where the infinite sum for U_{sharp} (Ref. 22) is truncated with negligible error.

Our numerical interpolation is implemented twice: first we use the hybrid elements to represent the radiation boundary condition, and then we compare these results to those obtained using an "exact" DtN boundary condition.²⁹ The DtN map is derived in the Appendix. Although error will occur due to the finite element discretization of the interior problem, we expect this error to be identical in both the hybrid element and DtN methods. Thus, any difference in the results highlights inaccuracies in the hybrid formulation.

Here we consider a plane wave incident from $\theta = 7\pi/6$. At this incident angle, we expect both a shadow and a reflected region to exist. Figure 5 shows the magnitude of the pressure on Γ_R for both the hybrid element and DtN methods. The first thing we notice in comparing the two solutions is that they are hardly distinguishable from one another. The same is true when comparing the phase, although this is not shown. From these results we conclude that the hybrid and exact DtN representations compare favorably.

The shape of the curve (Fig. 5) is another point of interest. We note that the tip blunting does not significantly displace the shadow boundary from that formed by a sharp wedge. Such a displacement would be signaled by two infinities in $\hat{D}(\theta)$. One infinity would be associated with the new position of the shadow boundary. The other would be required to cancel the shadow boundary solution in u_{sharp} .

To better interpret the shape of the previous curve, the magnitude of the pressure on Γ_R is plotted for different incident angles (Fig. 6). In addition, we use our original numerical solution for \hat{u} , along with u_{sharp} , to construct a total field representation (Fig. 7). The repetition in the first plot reinforces our assumption that no shadow boundary correc-

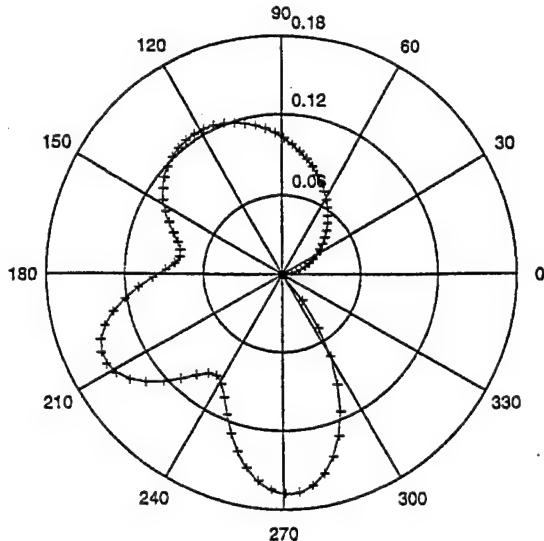


FIG. 5. Magnitude of the pressure on Γ_R as a function of θ . The solid curve represents the results obtained using the hybrid method. The "+" symbols mark the results obtained using an exact DtN boundary condition.

tion is present. The three "lobes" represent backscattering and interference between the diffracted and reflected fields, which differ from the solution to the sharp wedge. This difference is small when compared to the magnitude of the total field (Fig. 7).

In examining the total field representation, given the original angle of incidence, we observe all of the expected phenomena. The first is our soft boundary condition, which requires the pressure to be zero on the wedge. We further observe sharp variations in the field in the reflected region due to interference between the diffracted and reflected fields. But most interesting are the smooth transitions across the shadow and reflected boundaries. In particular, we notice very small pressures in the shadow region compared to those on the other side of the shadow boundary.

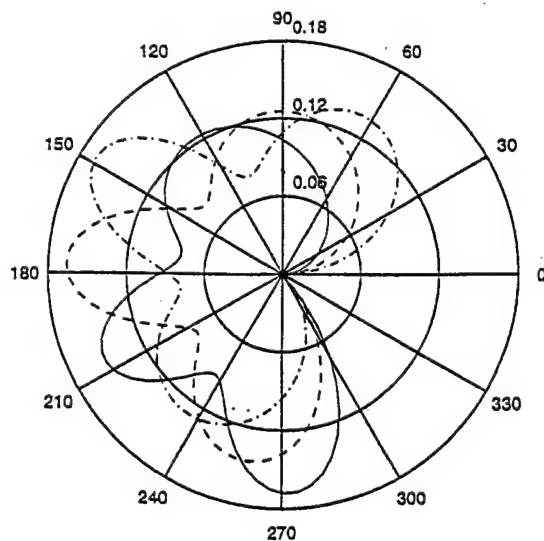


FIG. 6. Magnitude of \hat{u} on Γ_R for incident angles: $5\pi/6$ --, π ---, $7\pi/6$ - - -.

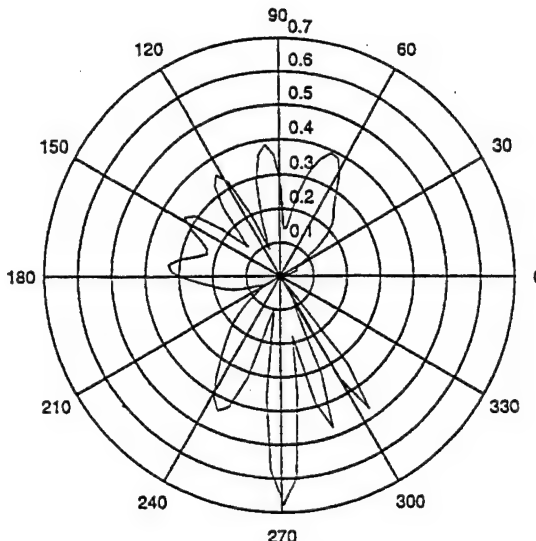


FIG. 7. Magnitude of the total field on Γ_R , due to an incident plane wave of angle $7\pi/6$ on a blunted wedge of angle $7\pi/4$.

IV. CONCLUSIONS

We have described a hybrid GTD/FEM method to evaluate diffraction coefficients. The method depends on first performing an outer GTD analysis (less the diffraction coefficients) to obtain an outer asymptotic approximation of the field. An example of this procedure was presented in Sec. III. The outer approximation necessarily involves undetermined diffraction coefficients. To find those, an inner problem is formulated with a patching boundary condition on an artificial boundary. We found the relation between the patched directivity and the matched directivity in Sec. III C. In particular, we determined how their difference scaled with both kr_o and with ν_n .

In Sec. IV A, we described a weak formulation of the inner boundary value problem that allowed us to enforce the patching boundary condition within a FEM framework. In Sec. IV B, we specialized this to the problem at hand, diffraction from a wedge, and showed that the patching condition can be enforced by introducing a "hybrid element."

The results of our hybrid method in this simple geometry were compared to reference calculations performed using the DtN method. The DtN method provides an exact (modulo the truncation of an infinite series) representation of the artificial boundary condition. The two calculations were performed on the same inner mesh, and so any difference between the two highlights error in the patching boundary condition. We found the methods to be in excellent agreement with each other, and therefore conclude that our hybrid method might be successful in more complicated scattering geometries.

ACKNOWLEDGMENTS

The authors would like to thank Isaac Harari for many helpful discussions and ideas. This work was supported by the Office of Naval Research.

APPENDIX: DERIVATION OF DTN MAP

The DtN map, or Dirichlet-to-Neumann map, is simply the impedance map for the fluid outside the artificial boundary Γ_R . To find the DtN map, we must solve the following problem. Given $\bar{u}(\theta)$, find $\partial_r u|_{\Gamma_R}$ such that

$$(\Delta + k^2)u = 0 \quad \text{in } \beta < \theta < 0; \quad r > r_0, \quad (\text{A1})$$

$$u = \begin{cases} \bar{u} & \text{on } \Gamma_R, \\ 0 & \text{on } \theta = 0, \quad r > r_0, \\ 0 & \text{on } \theta = \beta, \quad r > r_0. \end{cases} \quad (\text{A2})$$

Further, u must satisfy a radiation condition as $r \rightarrow \infty$.

The solution of (A1) and (A2) can be written in the following form:

$$u(r, \theta) = \sum_{n=1}^{\infty} [A_n / H_{\nu_n}^{(1)}(kr_0)] H_{\nu_n}^{(1)}(kr) \sin \nu_n \theta. \quad (\text{A3})$$

We recall that $\nu_n = n\pi/\beta$. The constants A_n are given by

$$A_n = \frac{1}{2\beta} \int_0^{\beta} \bar{u}(\theta) \sin \nu_n \theta \, d\theta. \quad (\text{A4})$$

We now use (A3) to evaluate $\partial_r u$ on $r = r_0$:

$$\partial_r u(r_0, \theta) = k \sum_{n=1}^{\infty} [A_n / H_{\nu_n}^{(1)}(kr_0)] H_{\nu_n}^{(1)'}(kr_0) \sin \nu_n \theta. \quad (\text{A5})$$

The DtN is obtained by combining (A4) with (A5), and substituting $u(r_0, \theta)$ for $\bar{u}(\theta)$. Thus we obtain

$$\begin{aligned} \partial_r u(r_0, \theta) &= \frac{k}{2\beta} \sum_{n=1}^{\infty} \int_0^{\beta} u(r_0, \phi) \sin \nu_n \phi \, d\phi \\ &\times [H_{\nu_n}^{(1)'}(kr_0) / H_{\nu_n}^{(1)}(kr_0)] \sin \nu_n \theta. \end{aligned} \quad (\text{A6})$$

Equation (A6) is the exact DtN boundary condition for scattering from a soft truncated wedge. In practice, the infinite sum must be truncated, which causes the boundary condition to be inexact. In our calculations with $kr_0 = 2\pi$, we included ten terms in the sum.

- ¹M. Van Dyke, *Perturbation Methods in Fluid Mechanics* (Parabolic, Stanford, 1975).
- ²J. B. Keller, "A Geometrical Theory of Diffraction," in *Selected Papers on Geometrical Aspects of Scattering*, edited by P. L. Marston, SPIE Milestone Series, (MS 89):5-25 (SPIE Optical Engineering, Bellingham, WA, 1994); reprinted from *Calculus of Variations and its Applications*, Proc. of Symposia in Applied Mathematics, Vol. 8, pp. 27-51 (American Mathematical Society, New York, 1958).
- ³W. D. Burnside, C. L. Yu, and R. J. Marhefka, "A technique to combine the geometrical theory of diffraction and the moment method," *IEEE Trans. Antennas Propag.* AP-23, 551-558 (1975).
- ⁴J. N. Sahalos and G. N. Thiele, "On the application of the gtd-mm technique and its limitations," *IEEE Trans. Antennas Propag.* AP-29(5), 780-786 (1981).
- ⁵T. J. Kim and G. N. Thiele, "A hybrid diffraction technique-general theory and applications," *IEEE Trans. Antennas Propag.* AP-30(5), 888-897 (1982).
- ⁶L. N. Medgyesi-Mitschang and D. S. Wang, "Hybrid methods for analysis of complex scatterers," *Proc. IEEE* 77(5), 770-779 (1989).
- ⁷D. S. Wang, "Current-based hybrid analysis for surface-wave effects on large scatterers," *IEEE Trans. Antennas Propag.* 39(6), 839-850 (1991).
- ⁸R. J. Astley, G. J. Macaulay, and J.-P. Coyette, "Mapped wave envelope elements for acoustical radiation and scattering," *J. Sound Vib.* 170, 97-118 (1994).
- ⁹D. S. Burnett, "A three-dimensional acoustic infinite element based on a prolate spheroidal multipole expansion," *J. Acoust. Soc. Am.* 96, 2818-2816 (1994).
- ¹⁰A. Bayliss and E. Turkel, "Radiation boundary conditions for wave-like equations," *Commun. Pure Appl. Math.* 33, 707-725 (1980).
- ¹¹A. Khebir, A. Kouki, and R. Mittra, "Higher order asymptotic boundary condition for the finite element modeling of two-dimensional transmission line structures," *IEEE Trans. Microwave Theory Tech.* 38, 1433-1437 (1990).
- ¹²D. Givoli, I. Patlashenko, and J. B. Keller, "High-order boundary conditions and finite elements for infinite domains," *Comput. Methods Appl. Mech. Eng.* 143, 13-39 (1997).
- ¹³M. J. McDougall and J. P. Webb, "Infinite elements for the analysis of open dielectric waveguides," *IEEE Trans. Microwave Theory Tech.* 37, 1724-1731 (1989).
- ¹⁴P. Bettess, "Infinite elements," *Int. J. Numer. Methods Eng.* 11, 53-64 (1977).
- ¹⁵O. C. Zienkiewicz, K. Bando, P. Bettess, C. Emson, and T. C. Chiam, "Mapped infinite elements for exterior wave problems," *Int. J. Numer. Methods Eng.* 21, 1229-1251 (1985).
- ¹⁶O. C. Zienkiewicz, C. Emson, and P. Bettess, "A novel boundary infinite element," *Int. J. Numer. Methods Eng.* 19, 393-404 (1983).
- ¹⁷I. Harari, P. E. Barbone, M. Slavutin, and R. Shalom, "Boundary infinite elements for the Helmholtz equation in exterior domains," accepted in *Int. J. Numer. Methods Eng.* (1997).
- ¹⁸I. Harari, R. Shalom, and P. E. Barbone, "Higher-order boundary infinite elements," accepted in *Comput. Methods Appl. Mech. Eng.* (1997).
- ¹⁹P. E. Barbone and O. Michael, "Scattering from submerged objects by a hybrid asymptotic-boundary integral equation method," submitted to *J. Acoust. Soc. Am.* (1997).
- ²⁰D. Givoli, *Numerical Methods for Problems in Infinite Domains* (Elsevier, Amsterdam, 1992).
- ²¹E. Zauderer, *Partial Differential Equations of Applied Mathematics* (Academic, New York, 1989), 2nd ed.
- ²²D. S. Jones, *Acoustic and Electromagnetic Waves* (Clarendon, Oxford, 1986).
- ²³A. D. Pierce, *Acoustics: An Introduction to its Physical Principles and Applications* (Acoustical Society of America, New York, 1989).
- ²⁴L. B. Felsen and N. Marcuvitz, *Radiation and Scattering of Waves* (IEEE, New York, 1994).
- ²⁵M. Abramowitz and I. A. Stegun, *Handbook of Mathematical Functions* (Dover, New York, 1972).
- ²⁶J. M. Montgomery, "Acoustic Scattering Calculations by a Hybrid Asymptotic-Numerical Method," M.Sc. Thesis, Dept. of Aerospace and Mechanical Engineering, Boston University, Boston, MA, 1997.
- ²⁷I. Harari, P. E. Barbone, and J. M. Montgomery, "Finite Element Formulations for Exterior Problems: Application to Hybrid Methods, Non-reflecting Boundary Conditions, and Infinite Elements," *Int. J. Numer. Methods Eng.* 40, 2791-2805 (1997).
- ²⁸Th. J. R. Hughes, *The Finite Element Method* (Prentice-Hall, Englewood Cliffs, NJ, 1987).
- ²⁹D. Givoli, Revisions of the FEM code DLEARN found in Ref. 28 to accommodate Helmholtz elements.

C.6 Dispersion Free Finite Element Methods for Helmholtz Equation

"Dispersion Free Finite Element Methods for Helmholtz Equation," Paul E. Barbone and Isaac Harari, **Proc. 16th International Congress on Acoustics and 135th Meeting Acoustical Society of America**, Vol. 1, pp. 199-200, Acoustical Society of America, 1998. P.K. Kuhl and L.A. Crum, eds.

16th INTERNATIONAL CONGRESS
ON ACOUSTICS
AND
135th MEETING
ACOUSTICAL SOCIETY OF AMERICA

*The Sound of the Future:
A Global View of Acoustics in the 21st Century*

Seattle, Washington, USA
20–26 June 1998

VOLUME I

EDITORS
Patricia K. Kuhl
Lawrence A. Crum
*University of Washington,
Seattle, WA*

Dispersion Free Finite Element Methods for Helmholtz Equation

Paul E. Barbone* and Isaac Harari†

*Dept. of Aerospace & Mechanical Engineering, Boston Univ., 110 Cummington Ave., Boston, MA 02215 and †Dept. of Solids, Materials and Structures, Tel Aviv Univ., Tel Aviv, Israel.

Abstract

We derive Petrov-Galerkin finite element method. In one-dimension, our method is H^1 optimal and symmetric. In higher dimensions, our formulation must be approximated to maintain local coupling, which results in asymmetry. The formulation itself yields an expression for the "distance" from optimality, related to the lack of symmetry.

1 Introduction

The classical (Bubnov-) Galerkin finite element method is known to produce suboptimal results (sometimes referred to as *quasi-optimal* (Babuška and Sauter (1997)) when applied to problems involving the Helmholtz operator (Harari, *et al.* 1996.) One of the main practical ramifications of this fact is that a solution propagating on a finite element mesh will express a wavenumber other than that specified in the original continuous equation. Thus, even when a particular solution appears to be well resolved, "numerical dispersion" can cause small error to accumulate over large propagation distances. Numerical dispersion leading to the accumulation of large error is also called the "pollution effect" (Babuška and Sauter, 1997).

Formulations proposed to reduce this effect have existed since Courant's time (Courant, 1943), and some of the most recent efforts are described by Harari, *et al.*, (1996), and Brezzi, *et al.* (1997), and in references therein.

We consider the problem of finding $\bar{u}(x)$, the H^1 projection onto a given finite element space $\bar{\mathcal{S}}$ of $u(x)$, a solution of the Helmholtz equation. We show that the problem of finding \bar{u} is approximately equivalent to a Petrov-Galerkin formulation of the original boundary value problem. The optimally chosen weight functions must satisfy several criteria that are specified below. In particular, we show that the weighting functions are the shape functions themselves (i.e. what would be used in a Bubnov-Galerkin procedure) plus bubble functions. The bubbles can be found approximately in a straightforward and systematic manner.

2 Formulation

We consider the problem of finding $\bar{u}(x) \in \bar{\mathcal{S}}$ such that for $u(x)$ in \mathcal{S} :

$$\|u - \bar{u}\|_{H^1(\Omega)} = \text{minimum}. \quad (1)$$

Here, $u(x) : \bar{\Omega} \rightarrow C$ is the (complex valued) unknown solution of Helmholtz equation. $\Omega \subset R^d$ denotes a d -dimensional domain with boundary Γ . We shall consider the function spaces $\bar{\mathcal{S}}$ and \mathcal{S} to be defined as follows:

$$\mathcal{S} = \{u(x) | u(x) \in H^1(\Omega); u(x) = u_o(x) \text{ on } \Gamma_u\} \quad (2)$$

$$\bar{\mathcal{S}} = \{\bar{u}(x) | \bar{u}(x) \in \mathcal{S}; \bar{u}(x) = \sum_A d_A N_A(x)\}. \quad (3)$$

Finally, we suppose that f is a complex valued function in $L_2(\Omega)$ and that $u(x)$ satisfies (k^2 is a given known constant):

$$\nabla^2 u + k^2 u + f = 0 \quad x \in \Omega \quad (4)$$

$$u(x) = u_o(x) \quad x \in \Gamma_u \quad (5)$$

We shall consider $f(x)$ to be known, though $u(x)$ is not.

Minimizing (1) subject to the constraints (4-5) leads to the following weak form:

$$\sum_e \int_{\Omega^e} \left\{ \nabla \nu_o \cdot \nabla \bar{u} - k^2 \nu_o \bar{u} - \nu_o f \right\} dx = \sum_e k^2 \int_{\partial \Omega^e} (u - \bar{u}) \frac{\partial \nu}{\partial n} d\gamma. \quad (6)$$

If we choose to neglect the right hand side term in (6), then what we are left with is just a Petrov-Galerkin formulation based on the original weak form.

In (6), Ω^e is the element domain. $\nu_o(x)$ is the “optimal” weight function, which for a given $N_A(x)$ (a basis function in \bar{S}) satisfies $\nabla^2 \nu_o + k^2 \nu_o = N_A(x)$ in Ω , and $\nu_o = N_A(x)$ on $\partial \Omega^e$.

In one-dimension, $u - \bar{u}$ on the element boundaries is exactly zero, and so the last term in (6) is indeed zero. In that case, the method is truly optimal. In higher dimensions, the method is only approximately optimal. Since the function and the weights are in general different, the formulation is non-symmetric. In the special case that the right hand side of (6) is zero, however, the formulation can be shown to be symmetric (Barbone and Harari, 1997.)

3 Conclusions

We have developed a stabilized Petrov-Galerkin formulation for the Helmholtz equation. Our starting goal was to find an H^1 optimal projection of $u(x)$ onto a given finite element basis. This seems to be a logical starting point for the development of stabilized and bubble methods, as well as a logical target for stabilized methods to try to obtain. Our formulation achieves nearly H^1 optimality in any dimension, and exact H^1 optimality in one dimension.

4 Acknowledgement

This work is supported financially by the Office of Naval Research.

References

- [1] I. M. Babuška and S. A. Sauter. *SIAM J. Numer. Anal.*, 34, 6, (1997) 2392–2423.
- [2] Paul E. Barbone and I. Harari. *BU Tech. Rep.*, BU-AME 97-011, May 7, 1997.
- [3] F. Brezzi, L. P. Franca, T. J. R. Hughes, A. Russo. *Comput. Methods Appl. Mech. Engrg.*, 145 (1995) 329–439.
- [4] R. Courant. *Bull. Am. Math. Soc.*, 49 (1943) 1–23.
- [5] I. Harari, K. Grosh, T. J. R. Hughes, M. Malhotra, P. M. Pinsky, J. R. Stewart, L. L. Thompson. *Arch. Comput. Methods Engrg.*, 3, (1996) 131–309.
- [6] T. J. R. Hughes. *Comput. Methods Appl. Mech. Engrg.*, 127 (1995) 387–401.

C.7 FEM, BEM, Spectral FEM or Spectral BEM?

"FEM, BEM, Spectral FEM or Spectral BEM?" Ofer Michael and Paul E. Barbone, Also as
BU Dept. Aerospace & Mechanical Eng. Technical Report No. AM-97-028, October 1997.

FEM, BEM, SPECTRAL FEM OR SPECTRAL BEM?

Ofer Michael* and Paul E. Barbone

Department of Aerospace & Mechanical Engineering, Boston University
110 Cummington Street, Boston, MA 02215

Abstract

We study the computational cost associated with solving a given boundary value problem by BEM and FEM. The field equations considered relate to Laplace, Helmholtz, elastostatics, and time harmonic elastodynamics. The computational cost in floating point operations is determined as a function of number of nodes per edge (n_{nd}) and element order. We find that for any given element order, there is a crossover point n_{co} such that for $n_{nd} > n_{co}$, BEM is more cost effective, while for $n_{nd} < n_{co}$, FEM is more cost effective. The value of n_{co} is a strong function of element order. Based on the results of the study, we draw the following general conclusions: For high order finite elements, static condensation of FEM is crucial to achieve high efficiency. For 2-D problems, BEM is generally more efficient than both standard FEM and FEM with statically condensed elements for most element orders. For 3-D problems, FEM with statically condensed elements is more cost effective than BEM (and standard FEM) for most practical problem sizes. When using very high order elements ($p \geq 8$), BEM is generally more efficient than standard FEM (but not statically condensed FEM) for all problem sizes.

key words: Computational cost, spectral element, FEM, BEM, Helmholtz, Laplace, elastostatics, elastodynamics, comparison.

*contact author, tel: 617/353-7380, fax: 617/353-5866, email: ofer@bu.edu

1 Introduction

We consider the computational cost associated with solving a given linear boundary value problem using either the finite element method (FEM) [1] or the boundary element method (BEM) [2]. Both BEM and FEM have distinct advantages in different contexts. In many problems, however, which method to choose will depend on the computational cost associated with obtaining a solution. By computational cost, we mean both the CPU time required to get to the solution and the core memory required to obtain a solution. It is the purpose of this paper to determine under which conditions one method is more economical than another.

The relative benefits and drawbacks (in terms of efficiency) of the two methods are easily summarized. In FEM, the entire problem domain must be discretized. This leads to a relatively large number of equations, N_{eq}^{FEM} . The coefficient matrix that must be inverted, however, is banded and (usually) symmetric. Once the coefficient matrix is inverted, the solution is known everywhere in the domain. In BEM, on the other hand, only the boundary of the domain needs to be discretized. This leads to a relatively small number of equations, N_{eq}^{BEM} . The coefficient matrix that must be inverted is full and (usually) non-symmetric. Once the coefficient matrix is inverted, the solution is known only on the boundary. Additional computation is required to obtain the solution everywhere in the domain.

For “equivalent discretizations,” the number of BEM equations required to solve a 3D boundary value problem can be related to the number of FEM equations to solve the same problem by $N_{eq}^{BEM} \propto (N_{eq}^{FEM})^{2/3}$. When N_{eq}^{BEM} is a relatively small number,

the symmetry and bandedness of the FEM matrices gives FEM a cost advantage in direct inversion of the coefficient matrix. On the other hand, when N_{eq}^{BEM} is a relatively large number, the smaller size of the BEM matrix gives BEM a cost advantage in direct inversion of the coefficient matrix. Thus it has long been assumed that for very large problems, BEM is more cost effective than FEM.

This idea was challenged in an enlightening paper by Harari and Hughes [3], who studied the relative cost of the two methods in solving the Helmholtz equation with linear elements. Those authors concluded for N_{eq}^{BEM} large enough so that BEM is more efficient than FEM, the problem was too large for direct inversion techniques to be used. Therefore, in the full range of problem sizes in which direct inversion would be applied, FEM is more efficient. They also compared iterative inversion methods. In this case, they found that BEM was more cost effective for smaller problems, while FEM was more cost effective per iteration for larger problems. They thus concluded that in the range where iterative techniques would be applied, FEM was more cost effective than BEM.

The work of Harari and Hughes [3] is based on comparing the efficiencies of solving the Helmholtz equation using linear elements with FEM or BEM. A simple argument¹ shows that their conclusions do not hold for arbitrarily high order elements. As the element order in a BEM application is increased, the structure of the BEM coefficient matrix remains unchanged. As the element order in a FEM application is increased, however, the bandwidth of the FEM coefficient matrix also grows. Thus, the efficiency advantage of FEM associated with its banded structure is gradually forfeited. Therefore, for any

¹Due to I. Harari.

given number of elements in a computation, one would expect to find an element order at which BEM would become more efficient than FEM.

The goals of this paper include determining the crossover point (the problem size where FEM and BEM have approximately the same cost) as a function of element order. We make the comparison for the Helmholtz equation, Laplace's equation, elastostatics, and (time harmonic) elastodynamics. In each case, we compare spectral (high order) BEM to spectral (high order) FEM. In the FEM case, we consider both statically condensed element-interior nodes and non-condensed element-interior nodes. In the case of BEM, we consider both the typical non-symmetric collocation formulation and a symmetric Galerkin formulation. We also compare the memory requirements for each method. This extends the work of Harari and Hughes [3] to high order elements, and to fields other than time harmonic acoustics.

The organization of this paper is as follows. In the next section, we discuss the basis of our comparison of the two methods. This is followed in section 3 by an evaluation of the factorization cost associated with directly inverting FEM/BEM coefficient matrices. In section 4 we consider the set-up cost of both Galerkin and collocation BEM and compare the overall solution time of the various methods. In section 5 we present the memory requirements of the different methods for the different field problems. This is followed in section 6 with a discussion of issues related to exterior problems. No direct comparisons are made in this context, since relevant conclusions can be drawn based on our earlier results. The final BEM/FEM comparison is made in section 7. There we consider iterative solvers and compare the cost of performing a given number of iterations for

each method. The penultimate section compares different versions of FEM to each other and different versions of BEM to each other. In particular, statically condensed FEM is compared to non-condensed FEM, while Galerkin BEM is compared to collocation BEM.

2 The basis of comparison

2.1 Computational Cost

Several choices must be made to determine a fair basis of comparison between the two methods. The first choice relates to the cost that should be measured. This choice depends to a certain extent on what cost is quantifiable. The main human-time cost associated with a computation is the definition of the computational model. This can be significantly easier in BEM than in FEM since BEM requires only the boundary of the domain to be meshed. In any case, the cost associated with this task is highly application specific. The main computational cost of solving a linear boundary value problem is usually associated with inverting the coefficient matrix in the equation $\mathbf{A}\mathbf{x} = \mathbf{b}$. In smaller BEM problems, the cost associated with evaluating the coefficients in \mathbf{A} , the “set-up cost,” can also be significant, as can the cost associated with evaluating the field in the interior of the domain.

We shall concern ourselves mainly with the cost associated with inverting \mathbf{A} . This cost can be primarily attributed to the factorization cost. This basis of comparison is consistent with that presented in [3]. We shall also consider the set-up cost associated with an *efficient* implementation of the BEM. We neglect the set-up cost associated

with FEM, since it is typically negligible compared to the factorization cost. We also ignore the cost associated with BEM in evaluating the field in the interior of the domain. Though this is not necessarily negligible compared to the factorization cost, the number of field point evaluations is often problem specific and therefore application dependent. Therefore, we believe that focusing on factorization cost and BEM set-up cost is a fair basis of comparison between the two methods.

2.2 Equivalent Meshes

BEM and FEM have different meshing requirements. In comparing the relative efficiency of the two methods, one must choose a basis to compare the space-filling finite element mesh with the on-surface boundary element mesh. There are two obvious choices available. The first is to compare the methods based on equal accuracy. That is, a FEM mesh would be "equivalent" to a BEM mesh if in some measure, they gave equally accurate results. The second choice is to make the BEM mesh the restriction of the FEM mesh to the boundary of the domain. Thus, on the surface of the domain, the FEM and BEM meshes would have an identical number of nodes.

The first basis of comparison is difficult if not impossible to quantify in a general manner. Though error estimates are available, the precise values of the constants in such estimates is problem and mesh specific. The second basis of comparison, on the other hand, is straightforward to consider and apply. Further, there is precedent in this choice in the comparisons that can be found in [3, 4, 5, 6]. For these reasons, we shall choose the second basis of comparison to define our "equivalent meshes."

It is noted in [4] that BEM typically yields more accurate results than FEM on such “equivalent meshes.” Thus, our choice of equivalent meshes may appear to favor FEM over BEM in the cost comparison. On the other hand, discretization requirements in practice are often set by geometrical considerations rather than accuracy requirements. In this case, a fine FEM mesh near the boundary of the domain might be blended into a coarser FEM mesh in the interior. Further, we shall choose a cube (or square in 2D) canonical geometry. (See section 4.) This shape that has the highest volume (area) to surface area (perimeter) ratio of any hexahedron (quadrilateral). These two considerations imply that the ratio of $N_{eq}^{FEM}/N_{eq}^{BEM}$ is higher in our comparison than in most applications. In this respect, our choice of equivalent meshes favors BEM. Therefore, our choice of equivalent meshes favors FEM in one respect, and BEM in another.

2.3 Operation Counts

The computational cost of any given algorithm is difficult to quantify in advance. Since multiplies and divides have the longest latencies of ALU (arithmetic logic unit) instructions, a count of these *floating point operations* (multiplies plus divides) can give *an indication* of algorithm efficiency. We emphasize, however, that this should serve only as an indication. Multiplies, for example, can be 2 – 4 times faster than divides. More important, multiplies are usually pipelined, while divides are usually not [7]. This can make divides a factor of 10 – 20 more costly than multiplies.

Perhaps more important than multiplies versus divides, however, is the branching and memory behavior of an algorithm [7]. In our comparison, we are assuming that the dom-

inant computational cost is in the inversion of the coefficient matrix. In that situation, almost all branching behavior is loop-oriented and can be well predicted. Further, many if not all floating point operations are vectorized with completely predictable memory requirements. Thus the compiler can take full advantage of the processor cache to minimize memory instruction delays.

With these caveats, we believe that our comparison of algorithms based on floating point operation (FLOP) counts can give a reasonable estimate of the relative efficiencies of inverting BEM and FEM coefficient matrices.

3 Direct solution technique

The standard BEM formulation leads to a full non-symmetric system of equations with a non-singular coefficient matrix which can be real or complex², $\mathbf{A} \in \Re^{n_{eq} \times n_{eq}} / \mathcal{C}^{n_{eq} \times n_{eq}}$. The most suitable solver for such a system of equations is LU decomposition. For this solver, two steps are required namely factorization and back-solve. The number of floating point operations-*flops* which are required to factorize a real matrix \mathbf{A} is given by Golub and van Loan ([8] pp. 53-58) as:

$$\mathbf{A} = \mathbf{L}\mathbf{U}, \quad n_{eq}^3/3 \text{ flops} \quad (1)$$

We note that in the second edition of Golub and van Loan [9] a slightly different terminology is used for “flops”. Since we are using the paper of Harari and Hughes [3] as a basis of comparison for this work, we will stick to the terminology of the first edition [8]

²For Laplace and elastostatics it is real and for Helmholtz and elastodynamics it is complex.

which is consistent with [3].

The back-solve step is composed of a forward reduction $\mathbf{Ly} = \mathbf{b}$ and a back-substitution $\mathbf{Ux} = \mathbf{y}$. Each step requires $n_{eq}^2/2$ flops, thus, the back-solve requires a total of n_{eq}^2 flops. For a complex coefficient matrix $\mathbf{A} \in \mathcal{C}^{n_{eq} \times n_{eq}}$ the factorization and the back-solve time must be multiplied by a factor of four.

The FEM coefficient matrix is banded and symmetric and therefore, a more efficient solver can be used ([8], pp. 93-97, [1], pp. 635-643). In this case the factorization will be:

$$\mathbf{A} = \mathbf{U}^t \mathbf{D} \mathbf{U}, \quad n_{eq}b_w^2/2 - b_w^3/3 \text{ flops} \quad (2)$$

where \mathbf{D} is a diagonal matrix and b_w is the mean half-bandwidth of the matrix \mathbf{A} . The corresponding back-solve procedure would be:

$$\begin{aligned} \mathbf{U}^t \mathbf{z} &= \mathbf{b}, \quad \text{forward reduction, } n_{eq}b_w - b_w^2/2, \text{ flops} \\ \mathbf{Dy} &= \mathbf{z}, \quad \text{diagonal scaling, } n_{eq}, \text{ flops} \\ \mathbf{Ux} &= \mathbf{y}, \quad \text{back-substitution, } n_{eq}b_w - b_w^2/2, \text{ flops} \end{aligned} \quad (3)$$

Thus, the FEM back-solve requires a total of $n_{eq}(2b_w + 1) - b_w^2 \approx 2n_{eq}b_w - b_w^2$ flops. Note that we can assume that $b_w \gg 1$. The FEM coefficient matrix is usually real. An exceptional case is wave problems with dissipation. In this case the coefficient matrix becomes complex and the factorization time and the back-solve time should be multiplied by four as in BEM.

4 Interior problems

The test case problem is chosen to be the same model discussed by Harari and Hughes [3] which is a square domain for 2D and a cube for 3D. Each edge or face is discretized using n divisions of p order elements as shown in Figure 1. We emphasize here that the equivalent BEM/FEM models are equivalent in the sense that they have the same number of nodes/elements per side, and they use the same interpolation for the elements.

For the 2D problem, the total number of nodes n_{nd} in the BEM model would be:

$$n_{nd} = 4(n p) \quad (4)$$

and for 3D we get³:

$$n_{nd} = 6(n p)^2 + 2 \approx 6(n p)^2. \quad (5)$$

For a 2D FEM model the total number of nodes will be:

$$n_{nd} = (n p + 1)^2 \approx (n p)^2 \quad (6)$$

and the corresponding bandwidth b_w would be:

$$b_w = n_v [(n p + 1)p + (p + 1)] \approx n_v n p^2. \quad (7)$$

Here, n_v is the number of variables per node. Thus, for Laplace and Helmholtz equations $n_v = 1$, while for elastostatics and elastodynamics $n_v = 2, 3$ for 2D and 3D, respectively. If we statically condense the FEM inner nodes so that the element would have only exterior nodes the total number of nodes and the related bandwidth would be for 2D:

$$n_{nd} = (n p + 1)^2 - n^2(p - 1)^2 \approx n^2(2p - 1) \quad (8)$$

³Note that $n p \gg 1$.

$$b_w = n_v [(n p + 1)p + (p + 1) - n(p - 1)^2] \approx n_v [n(2p - 1) + 2p]. \quad (9)$$

For 3D FEM with inner nodes these values would be:

$$n_{nd} = (n p + 1)^3 \approx (n p)^3 \quad (10)$$

$$b_w = n_v [(n p + 1)^2 p + (np + 1)p + (p + 1)] \approx n_v n^2 p^3, \quad (11)$$

while for statically condensed 3D FEM these values become:

$$n_{nd} = (n p + 1)^3 - n^3(p - 1)^3 \approx n^3(3p^2 - 3p + 1) \quad (12)$$

$$b_w = n_v [(n p + 1)^2 p + (np + 1)p + (p + 1) - n^2(p - 1)^3] \approx n_v [n^2(3p^2 - 3p + 1) + 3np^2]. \quad (13)$$

4.1 Factorization time crossover

Based on eqs.(1,4) and eqs.(1,5) we can evaluate the factorization time for 2D and 3D BEM, respectively:

$$\begin{aligned} t_f &= \frac{64}{3} c_m n_v^3 (n p)^3, \quad \text{for 2D} \\ t_f &= 72 c_m n_v^3 (n p)^6, \quad \text{for 3D.} \end{aligned} \quad (14)$$

Here, c_m is a factor which is unity if \mathbf{A} is real (Laplace and elastostatics) and is $c_m = 4$ if \mathbf{A} is complex (Helmholtz and elastodynamics.)

For the FEM with interior nodes we derive from eqs.(2,6,7) and eqs.(2,10,11) the factorization time for 2D and 3D, respectively:

$$\begin{aligned} t_f &= n_v^3 n^3 (3n - 2)p^6 / 6, \quad \text{for 2D} \\ t_f &= n_v^3 n^6 (3n - 2)p^9 / 6, \quad \text{for 3D.} \end{aligned} \quad (15)$$

By equating eqs.(14) and (15) we find the crossover point from FEM (with inner nodes) to BEM:

$$n_{co} = \left[\left(\frac{128 c_m}{p^3} + 2 \right) / 3 \right], \quad \text{for 2D} \quad (16)$$

$$n_{co} = \left[144 \frac{c_m}{p^3} + 2/3 \right], \quad \text{for 3D.} \quad (17)$$

Note that if $n < n_{co}$ then FEM is more cost effective than BEM and *vice versa* for $n > n_{co}$.

Similarly, using eqs.(2,8,9) and eqs.(2,1213) we find the factorization time for 2D and 3D statically condensed FEM:

$$\begin{aligned} t_f &= n_v^3 [n(2p - 1) + 2p]^2 [3n^2(2p - 1) - 2n(2p - 1) - 4p] / 6, \quad \text{for 2D} \\ t_f &= n_v^3 [n^2(3p^2 - 3p + 1) + 3np^2]^2 \times \\ &\quad [3n^3(3p^2 - 3p + 1) - 2n^2(3p^2 - 3p + 1) - 6np^2] / 6, \quad \text{for 3D.} \end{aligned} \quad (18)$$

By equating (14,18) we can find the crossover between BEM and statically condensed FEM. The expressions for these crossover points can be found only in an implicit form.

The “crossover point” n_{co} is the number of elements on each edge of the domain. This corresponds to $n_{nd_{co}} = n_{co}p + 1$ nodes per edge, which is more closely related to the problem size than the number of elements. Therefore, we shall compare our results in terms of $n_{nd_{co}}$, the number of nodes/edge at the crossover point from FEM to BEM.

We first compare the cost of non-condensed FEM to standard BEM. Figures 2a and 2b depict the number of nodes on each edge for the crossover case versus the order of the elements used. Figure 2a shows the crossover for Laplace and elastostatics where $c_m = 1$, while Figure 2b shows the crossover for Helmholtz and elastodynamics ($c_m = 4$). Figures 2a,2b together show that BEM is more cost effective for all 2D problems where a 6-th or

higher order element is used. For 3D problems, BEM is always more cost effective when using 8-th or higher order element for Laplace or elastostatics equations, and a 9-th or higher order element for Helmholtz or elastodynamics.

We define the “optimal crossover” from statically condensed FEM to BEM is that which yields the smallest problem size. It can be seen that for all types of equations (Laplace, Helmholtz, elastostatics and elastodynamics) the optimal crossover occurs for quadratic elements in 2D problems and for cubic or 4-th order elements in 3D problems.

In the 2D case, the optimal crossover point is $n_{nd_{co}}(p = 2) = 25$ for Laplace and elastostatics and $n_{nd_{co}}(p = 2) \approx 100$ for Helmholtz and elastodynamics. In either case, the model is modest in size and one could conclude that using BEM is generally preferred. For 3D problems the optimal crossover is $n_{nd_{co}}(p = 3, 4) \approx 45$ for Laplace and elastostatics and $n_{nd_{co}}(p = 3, 4) \approx 185$ for Helmholtz and elastodynamics. For the 3D cases, especially for Helmholtz and elastodynamics, these values represent large problems ($\approx 10^5$ fully-coupled, complex equations).

5 Set-up cost

For large problems, the factorization cost is certainly the dominant solution expense. For smaller problems, however, the formulation cost or set-up cost becomes an issue. It has been reported [5] that the set-up costs can dominate especially in relatively small problems. Therefore, we shall attempt to estimate the set-up costs of BEM as a fraction of the total solution costs.

Since we are going to evaluate the set-up cost time for symmetric Galerkin formulation

in BEM we will discuss in the next sub-section issues which are relevant to the Galerkin formulation.

5.1 Symmetric Galerkin formulation for BEM

One way to reduce the factorization time and the required memory when using BEM is to use a symmetric formulation (e.g. Galerkin [10, 11, 12, 13, 14, 15].) In [10, 11, 12, 13] a symmetric formulation is achieved for Dirichlet boundary value problems, while in [14, 15] symmetric formulations are presented for both Neumann and Dirichlet boundary conditions. A symmetric coefficient matrix leads to a reduction of the direct solution time and memory requirements by about half. On the other hand, in order to generate the symmetric matrices of the Galerkin formulation, a second integration must be performed. This might increase the set-up cost significantly and therefore it is not clear whether the overall solution time is reduced at all when a symmetric Galerkin formulation is used. In this section we will try to take into consideration the second integration and to compare between the regular collocation BEM and the symmetric Galerkin BEM.

5.2 Set-up cost evaluation

We will assume that for each nodal/collocation point the values of the Jacobian and the normal are given and stored in the memory, and that their computational cost is negligible compared to the time required to evaluate the coefficient matrix.⁴ For the evaluation of

⁴We remark that the storage and retrieval of such data may not be performed as efficiently as in the case of inverting the coefficient matrix. Therefore, the CPU equivalent of one operation count of this section may differ significantly from that of the last section. Nevertheless, though our relative CPU time estimate may be off by a factor of two, it is unlikely to be off by more than a factor of ten.

the coefficient matrix, we will need the values of the kernel at the collocation points. We will denote this time by t_k , and we will evaluate it later in this section. At this stage we will assume that the kernel is given at all collocation points. We will also neglect the time required for regularization of the singular elements because of the fact that this time scales linearly with the number of elements, and the additional computational cost which is required for this regularization can be reduced considerably if an efficient procedure is used [16, 10].

5.2.1 2-D BEM

We will start by evaluating the set-up cost of 2-D regular collocation. The number of entries in the coefficient matrix is:

$$n_{el}^2(p + 1)^2. \quad (19)$$

For each entry we must evaluate an integral of the form:

$$I = \int_{\Gamma} N(\mathbf{x}_1) K(\mathbf{x}_1, \mathbf{x}_2) d\Gamma \quad (20)$$

where N is a shape function and K is the kernel. This integral can be rewritten in discrete form as:

$$I \approx \sum_{m=1}^{n_{int}} w_m \times N(\mathbf{x}_1^m) \times J(\mathbf{x}_1^m) \times K(\mathbf{x}_1^m, \mathbf{x}_2) \quad (21)$$

Here, n_{int} is the number of integration points, w and J are the integration weight and the Jacobian at the relevant integration point. In the last equation w , N and J are all real numbers and therefore the product of $w_m \times N(\mathbf{x}_1^m) \times J(\mathbf{x}_1^m)$ requires only two flops. The kernel K is an $n_v \times n_v$ real or complex matrix and therefore the multiplication

of the $w_m \times N(\mathbf{x}_1^m) \times J(\mathbf{x}_1^m)$ product by the kernel requires an additional $\bar{c}_m n_v^2$ flops.⁵

Therefore each integration point requires $(2 + \bar{c}_m n_v^2)$. Considering all integration points and all matrix entries we find that the total integration time is:

$$t_{int_{2D}}^G = n_{el}^2(p+1)^2 n_{int} (2 + n_v^2 \bar{c}_m) \quad \text{flops} \quad (22)$$

The Galerkin coefficient matrix is symmetric and therefore requires evaluation of about half the number of matrix entries as does regular collocation. For each entry in the Galerkin matrix, we must evaluate an integral of the form:

$$I = \int_{\Gamma} N_j(\mathbf{x}_2) \left\{ \int_{\Gamma} N_i(\mathbf{x}_1) K(\mathbf{x}_1, \mathbf{x}_2) d\Gamma \right\} d\Gamma \quad (23)$$

and in discrete form:

$$I \approx \sum_{n=1}^{n_{int}} w_n \times N_j(\mathbf{x}_2^n) \times J(\mathbf{x}_2^n) \times \left\{ \sum_{m=1}^{n_{int}} w_m \times N_i(\mathbf{x}_1^m) \times J(\mathbf{x}_1^m) \times K(\mathbf{x}_1^m, \mathbf{x}_2^n) \right\} \quad (24)$$

In the former calculations we found that the product in the curly brackets requires $n_{int}(2 + n_v^2 \bar{c}_m)$ flops. Multiplying this product (which is a real or complex $n_v \times n_v$ matrix) by the product of $w_n \times N_j(\mathbf{x}_2^n) \times J(\mathbf{x}_2^n)$ requires an additional $(2 + n_v^2 \bar{c}_m)$ flops per integration point. Finally, considering all integration points and all the matrix entries we find the integration time for 2-D Galerkin to be:

$$t_{int_{2D}}^G = \frac{1}{2} n_{el}^2 (p+1)^2 n_{int} [(2 + n_v^2 \bar{c}_m) + n_{int}(2 + n_v^2 \bar{c}_m)] \quad \text{flops.} \quad (25)$$

5.2.2 3-D BEM

For 3-D collocation the number of matrix entries is:

$$n_{el}^2 (p+1)^4, \quad (26)$$

⁵ $\bar{c}_m = 1$ or 2 for real or complex problems, respectively.

and the integrand must be evaluated at n_{int}^2 points since it is a 2-D integration. The integrand consists of a kernel, two shape functions, weight function and the Jacobian. The integral to be evaluated for each entry has the form:

$$I = \int_S N_\eta(\mathbf{x}_1) N_\xi(\mathbf{x}_1) K(\mathbf{x}_1, \mathbf{x}_2) dS. \quad (27)$$

The evaluation of the integrand at each integration point requires 3 real number operations (because of the additional shape function) and n_v^2 real or complex operations for the kernel multiplication. The integration cost in this case is:

$$t_{int_{3D}}^C = n_{el}^2(p+1)^4 n_{int}^2 (3 + n_v^2 \bar{c}_m) \quad \text{flops} \quad (28)$$

For 3-D Galerkin, after considering the second integration and symmetry, we obtain:

$$t_{int_{3D}}^G = \frac{1}{2} n_{el}^2 (p+1)^4 n_{int}^2 [(3 + n_v^2 \bar{c}_m) + n_{int}^2 (3 + n_v^2 \bar{c}_m)] \quad \text{flops} \quad (29)$$

We will choose the integration order to be consistent with the element order p , thus, $n_{int} = (p+1)$. After using the fact that $n_{el} = 4n$ and $6n^2$ for 2D and 3D, respectively, we can rewrite the set-up cost as:

$$\begin{aligned} t_{su_{2D}}^C &= 16n^2(p+1)^3(2 + n_v^2 \bar{c}_m) + t_{k_{2D}} && \text{flops} && \text{2D collocation} \\ t_{su_{2D}}^G &= 8n^2(p+1)^3(p+2)(2 + n_v^2 \bar{c}_m) + t_{k_{2D}} && \text{flops} && \text{2D Galerkin} \\ t_{su_{3D}}^C &= 36n^4(p+1)^6(3 + n_v^2 \bar{c}_m) + t_{k_{3D}} && \text{flops} && \text{3D collocation} \\ t_{su_{3D}}^G &= 18n^4(p+1)^6[(p+1)^2 + 1](3 + n_v^2 \bar{c}_m) + t_{k_{3D}} && \text{flops} && \text{3D Galerkin} \end{aligned} \quad (30)$$

We note that the time t_k is identical for Galerkin or collocation.

We shall digress briefly here to compare the relative costs of standard BEM to symmetric Galerkin BEM. From equations (30), we get the difference between the set-up cost

of symmetric Galerkin and regular BEM:

$$\Delta t_{su} = t_{su}^G - t_{su}^C = \begin{cases} 8(2 + n_v^2 \bar{c}_m) n^2 p(p+1)^3 & 2D \\ 18(3 + n_v^2 \bar{c}_m) n^4 p(p+2)(p+1)^6 & 3D \end{cases} \quad (31)$$

We note that the factorization time of the symmetric Galerkin method is half the time of the regular BEM (14). The total difference in the solution time Δt_{sol} , is the sum of Δt_{su} in (31) and the the difference in the factorization time (14). Thus we obtain:

$$\Delta t_{sol} = \Delta t_{su} + \Delta t_f = \begin{cases} 8(2 + n_v^2 \bar{c}_m) n^2 p(p+1)^3 - \frac{32}{3} c_m n_v^3 (np)^3 & 2D \\ 18(3 + n_v^2 \bar{c}_m) n^4 p(p+2)(p+1)^6 - 36 c_m n_v^3 (np)^6 & 3D \end{cases} \quad (32)$$

By using equation (32) we can find the conditions under which Galerkin BEM is more cost effective then regular collocation BEM:

$$\begin{aligned} n &\geq \frac{3(2 + n_v^2 \bar{c}_m)}{4c_m n_v^3} \frac{(p+1)^3}{p^2} && 2D \\ n &\geq \left[\frac{(3 + n_v^2 \bar{c}_m)}{2c_m n_v^3} \frac{(p+1)^6(p+2)}{p^5} \right]^{\frac{1}{2}} && 3D \end{aligned} \quad (33)$$

Figures 3a,b show the crossover from regular BEM to symmetric Galerkin BEM for 2D and 3D problems, respectively. It can be observed from Figure 3a that in 2D, Galerkin is more cost effective for problems with about 5 or more elements per edge for quadratic elements (except for the Laplace equation case). For Laplace's equation, collocation is more cost effective up to about 15 element per edge. Similar trends are seen in the 3D case, as shown in Figure 3b.

From this study we conclude that generally speaking, symmetric Galerkin is more cost-effective than collocation, except in smaller problems where cost is less of an issue. We remind the reader that this conclusion was reached under the integration scheme described above. Other integration methods may lead to different results.

5.2.3 Evaluation of t_k

In order to compare the total solution time to that of FEM we have to estimate t_k explicitly. We will start with the evaluation of t_k for Laplace and Helmholtz equations. For these two equations the kernel is defined as: $G(\mathbf{x}_1, \mathbf{x}_2) = G(r)$ where $r = |\mathbf{x}_1 - \mathbf{x}_2|$. We will assume that the values of G , $\frac{1}{r} \frac{dG}{dr}$ are tabulated as functions of r^2 . Given two points, \mathbf{x}_1 and \mathbf{x}_2 , d -flops are required to evaluate r^2 (d is the dimension of the problem). In order to locate the value of the kernel in the table another flop is required. If a finer value is needed then a linear interpolation can be used and another $2\bar{c}_m$ flops will be required. Higher order interpolation is possible, of course, but at greater expense. This gives a total of $(d + 1 + 2\bar{c}_m)$ flops to evaluate G . To integrate over the normal derivative $\partial G / \partial n = dG/dr \partial r / \partial n$, we must also evaluate $r \partial r / \partial n$. We find that d flops are required to evaluate $r \frac{\partial r}{\partial n}$, since

$$r \frac{\partial r}{\partial n} = (\mathbf{x}_{1j} - \mathbf{x}_{2j}) n_j \quad j = 1..d. \quad (34)$$

The evaluation of $(\partial G / \partial r) / r$ is identical to the evaluation of G and requires the same number of flops. An additional \bar{c}_m flops are required to multiply $r \partial r / \partial n$ by $\frac{1}{r} \frac{dG}{dr}$. This sums to a total of $(2d + 1 + 3\bar{c}_m)$ flops to evaluate $\partial G / \partial n$. Table 5.2.3 summarizes the number of flops required for the evaluation of $\partial G / \partial n$:

We will choose the time to evaluate $\partial G / \partial n$ as representative for kernel evaluation.

We denote by $t_{k_1} = 2d + 1 + 3\bar{c}_m$ the time required to evaluate the kernel once. In order to find t_k , one should multiply t_{k_1} by the total number of nodes in the model, squared:

$$\begin{aligned} t_k &= 16(np)^2(5 + 3\bar{c}_m) \quad 2D \\ t_k &= 36(np)^4(7 + 3\bar{c}_m) \quad 3D \end{aligned} \quad (35)$$

Operation	Number of flops required
evaluate r^2	d
locate $(dG/dr)/r$ in table	1
refine using linear interpolation	$2\bar{c}_m$
evaluate $r(\partial r/\partial n)$	d
multiply $r(\partial r/\partial n)$ by $(dG/dr)/r$	\bar{c}_m
Total	$2d + 1 + 3\bar{c}_m$

Table 1: Number of flops required to find $\partial G/\partial n$ at one node.

Under similar assumptions,⁶ we find t_{k_1} for elastostatics and elastodynamics to be:

$$\begin{aligned} t_{k_1} &= 6d^2 + 2d && \text{for Elastostatics} \\ t_{k_1} &= 13d^2 + 10d + 28 && \text{for Elastodynamics} \end{aligned} \tag{36}$$

After multiplying t_{k_1} by the relevant number of nodes squared we find that:

$$\begin{aligned} t_k &= 512(np)^2 && \text{for 2D Elastostatics} \\ t_k &= 2160(np)^4 && \text{for 3D Elastostatics} \\ t_k &= 1600(np)^2 && \text{for 2D Elastodynamics} \\ t_k &= 8460(np)^4 && \text{for 3D Elastodynamics} \end{aligned} \tag{37}$$

The total set-up cost for BEM is thus given by using the values for t_k together with equation (30). The total solution time for BEM is the sum of the set-up time and the factorization time given in (14).

⁶We use the conservative assumption that we have to evaluate the traction kernel.

The set-up cost time of FEM scales linearly with the number of elements n_{el} , while the factorization time scales like n_{el}^2 and n_{el}^4 for 2D and 3D, respectively. Since in FEM $n_{el} \gg 1$ we will neglect the FEM set-up time as compared to the factorization time.

Finally, we will compare the statically condensed FEM and the BEM for the four equations.

5.3 Comparison of overall solution time

Since the BEM set-up time is non negligible, we will compare the BEM solution time (set-up and factorization) to that of the statically condensed FEM solution time (factorization). This comparison is presented in Figures 4a and 4b for 2D and 3D problems, respectively. It can be seen that for 2D problems the optimal crossover point is for quadratic elements. The crossover for Laplace and elastostatics occurs for relatively small problems while for wave problems the crossover corresponds to much larger problems (more than 100 nodes per edge).

Similar conclusions can be obtained for 3D problems. The optimal crossover point is for quadratic or 4-th order elements. For Laplace and elastostatics BEM becomes more cost effective for relatively small problems while for wave problems BEM becomes better only after using a large number of nodes per edge (more than ≈ 110). Another interesting feature of these graphs is the remarkable reduction of the crossover between linear and quadratic elements. For example, for 3D problems the crossover is about 5 times smaller in the quadratic case. This translates into a problem which is about 125 times smaller than in the linear case.

5.4 Set-up cost as a proportion of the overall solution time in BEM

The crossover between BEM and FEM generally occurs at relatively large problem sizes. At such values, our estimates indicate that set-up costs are relatively unimportant. Nevertheless, we find it interesting to estimate the percentage of total solution time that is dedicated to evaluating the coefficient matrix. We will choose Laplace equation as a representative equation. Figures 5a and 5b show the percentage of the set-up time out of the overall solution time as function of number of nodes on each edge for 2D and 3D, respectively. In both Figures the comparison is done for 4-types of elements (linear, quadratic, cubic and 4-th order). It can be seen that the differences between the elements types are very small.

In Figure 5a we see that the contribution of the set-up cost to the overall solution time is generally not negligible, especially for small to medium problems. For example, for problems smaller than 20 nodes per edge (total of 80 BEM nodes) the set-up cost is more expensive than the solution time.

Figure 5b shows the corresponding results for 3D. We see that the drop in the set-up cost as a function of the number of nodes per edge is much sharper. However, still for 10 nodes per edge (total of 600 BEM nodes) or fewer, the set-up cost is greater than the solution time.

6 Memory

One of the most important issues in solving large problems is the memory required to store the matrices. In many cases the memory issue is more crucial than the CPU time issue. This is because of the fact that a large problem that fits into memory may take a long time to solve, but it would still be solvable. A problem that cannot be fit into memory may never be solvable.

The memory required for BEM is n_{eq}^2 words, while for FEM it is $b_w n_{eq}$ words. In the case of complex equations the number of storage words in BEM is doubled. Using equations (4,5) we can find the number of words required for storage by BEM:

$$\begin{aligned} 16\bar{c}_m n_v^2(n p)^2 &\text{ words for 2D} \\ 36\bar{c}_m n_v^2(n p)^4 &\text{ words for 3D} \end{aligned} \tag{38}$$

Recall that \bar{c}_m is 1 or 2 for a real or complex system of equations, respectively. For the symmetric Galerkin BEM the storage size is reduced by half. Using equations (6,7) and (10,11) we find the required storage for FEM with inner nodes:

$$\begin{aligned} n_v^2 n^3 p^4 &\text{ words for 2D} \\ n_v^2 n^5 p^6 &\text{ words for 3D} \end{aligned} \tag{39}$$

Using equations (8,9) and (12,13) we find the required storage for statically condensed FEM:

$$\begin{aligned} n_v^2 n^2 (2p - 1) [n(2p - 1) + 2p] &\text{ words for 2D} \\ n_v^2 n^4 (3p^2 - 3p + 1) [n(3p^2 - 3p + 1) + 3p^2] &\text{ words for 3D} \end{aligned} \tag{40}$$

By equating (38) and (39) we can find the memory crossover between BEM and FEM

with inner nodes:

$$n_{co} = 16\bar{c}_m/p^2 \quad \text{for 2D} \quad (41)$$

$$n_{co} = 36\bar{c}_m/p^2 \quad \text{for 3D}$$

Similarly, by equating (38) and (40) we find the memory crossover between BEM and statically condensed FEM:

$$\begin{aligned} n_{co} &= 16\bar{c}_m p^2 / (2p - 1)^2 - 2p / (2p - 1) && \text{for 2D} \\ n_{co} &= 36\bar{c}_m p^4 / (3p^2 - 3p + 1)^2 - 3p^2 / (3p^2 - 3p + 1) && \text{for 3D} \end{aligned} \quad (42)$$

We note that for high order elements, the memory crossover point tends to the value of $n_{co} = 4\bar{c}_m - 1$ for both 2D and 3D cases. Thus BEM is more cost effective after using 3 (real) or 8 (complex) elements on each edge.

Figures 6a,6b describe the memory crossover. In comparing BEM and non-condensed FEM, we see that the crossover to BEM decreases as the approximation order grows. The problem size at which the crossover occurs is in fact quite small. We note that the 3D linear case for wave problems is an exception, where the problem size is relatively large.

In comparing statically condensed FEM to BEM, we find the optimal crossover to BEM for quadratic elements, except the 3D Laplace and elastostatics where it is cubic. In the cases of Laplace and elastostatics, the problem sizes for quadratic elements is 13 and 23 nodes per edge for 2D and 3D problems, respectively. For wave problems, it is 27 and 45 nodes per edge for 2D and 3D, respectively. In the case where we use a symmetric Galerkin BEM formulation, the required memory storage is half of the original value, and the crossover values decrease accordingly.

7 Exterior Problems

The FEM in its regular formulation is not capable of treating infinite domains and some modification is necessary. One of the methods which is suitable for exterior problems is the DtN method [17, 18]. The DtN method relates the function to its normal derivative along an artificial boundary. Typically a simple shape such as a circle or a sphere is chosen since the method requires the Green's function (or equivalent solution) on the exterior domain bounded by the artificial boundary. In this case, one must mesh the area between the artificial boundary and the original boundary as shown in Figure 7. The DtN coefficient matrix is full and symmetric and it has to be solved together with the additional elements which are used. Comparing factorization times for the coupled DtN/FEM method to the Galerkin BEM shows that the Galerkin BEM is faster provided the number of elements on the real and artificial boundary are about the same. This is due to the fact that the size of the DtN matrix and the Galerkin BEM would be about the same and they would both be symmetric. The DtN/FEM system, however, has the additional computational effort associated with the interior finite element nodes. This conclusion ignores issues of set-up costs.

An increasingly common way to treat exterior problems in FEM is through infinite elements [19, 20, 21]. The contribution of these elements to the coefficient matrix is similar to regular finite elements. Typically one uses several layers of regular elements to mesh an artificial boundary, outside of which infinite elements are used. In the case where the number of layers is large the comparison of BEM and FEM becomes similar to that of an interior problem. In the case where it is small then the bandwidth of the

FEM becomes much smaller than that in problems that we studied in the interior case, and therefore FEM would be more cost effective. These comparisons ignore the fact that in practice infinite and finite elements are usually different orders.

Some caveats are required in the discussion of exterior wave problems. The standard BIE formulation is known to be non-unique at frequencies of the interior domain [22, 23]. Various methods have been proposed to overcome this difficulty, [24, 25, 26]. The first two [24, 25] methods are more appropriate for lower frequency applications. The third [26], known as the Burton-Miller formulation, involves a highly singular kernel and thus requires additional computational effort in the set-up. For example, using Burton-Miller approximately doubles t_k (eq. 30) since both the kernel and its normal derivative must be evaluated. The cost of implementing such strategies has not been considered.

8 Iterative Solvers

Unlike direct solvers, the efficiency of iterative solvers depends strongly on the problem itself, including the boundary conditions and initial solution guess. In general, of course, there is no way to predict *a priori* the number of iterations required for convergence. Therefore it is impossible to determine in general which of the methods FEM or BEM will converge faster. We can estimate, however, the time required to perform k iterations for each method. Therefore, we will compare only the cost for the same number of iterations for FEM and BEM and neglect the cost of pre-conditioning.

We shall consider the generalized minimal residual procedure - GMRES [27, 28] as our iterative solver. The solution is based on an iterative substitution which consists of

two steps[3]. The first is the $\mathbf{A}\mathbf{u}$ product:

$$\mathbf{u}_{k+1} = \mathbf{A}\mathbf{u}_k \quad (43)$$

The second is an orthonormalization with respect to the Krylov space, and requires $c_m k n_{eq}$ flops, where k is the iteration number.

The $\mathbf{A}\mathbf{u}$ product requires $c_m n_{eq}^2$ flops in the case of BEM and $\bar{c}_m n_{el} n_{edof}^2$ flops for FEM.

Here n_{el} is the number of elements and n_{edof} is the number of DOF of each element. Note that the orthonormalization time is a linear function of the iteration number.

Using the former definitions we can tabulate the cost per iteration for the different methods:

Mesh	No. of equations n_{eq}	$\mathbf{A}\mathbf{u}$ product	Orthonormalization
		[flops] $c_m n_{eq}^2$	[flops] $c_m k n_{eq}$
$n \times n$	$4n_v np$	$16c_m n_v^2 (np)^2$	$4c_m n_v k np$
$n \times n \times n$	$6n_v (np)^2$	$36c_m n_v^2 (np)^4$	$6c_m n_v k (np)^2$

Table 2: Cost of k -th iteration using BEM.

Mesh	No. of equations n_{eq}	No. of elements n_{el}	No. of DOF per element n_{edof}	$\mathbf{A}\mathbf{u}$ product	Orthonormalization
				[flops] $\bar{c}_m n_{el} n_{edof}^2$	[flops] $c_m k n_{eq}$
$n \times n$	$n_v (np)^2$	n^2	$n_v (p+1)^2$	$\bar{c}_m n_v^2 n^2 (p+1)^4$	$c_m n_v k (np)^2$
$n \times n \times n$	$n_v (np)^3$	n^3	$n_v (p+1)^3$	$\bar{c}_m n_v^2 n^3 (p+1)^6$	$c_m n_v k (np)^3$

Table 3: Cost of k -th iteration using non-condensed FEM.

Mesh	No. of equations n_{eq}	No. of elements n_{el}	No. of DOF per element n_{edof}	\mathbf{Au} product [flops] $\bar{c}_m n_{el} n_{edof}^2$	Orthonormalization [flops] $c_m k n_{eq}$
$n \times n$	$n_v n^2 (2p - 1)$	n^2	$4n_v p$	$16\bar{c}_m n_v^2 (np)^2$	$c_m n_v k n^2 (2p - 1)$
$n \times n \times n$	$n_v n^3 (3p^2 - 3p + 1)$	n^3	$2n_v (3p^2 + 1)$	$4\bar{c}_m n_v^2 n^3 (3p^2 + 1)^2$	$c_m n_v k n^3 (3p^2 - 3p + 1)$

Table 4: Cost of k -th iteration using statically condensed FEM.

Since the orthonormalization time behaves like $k f(c_m, n_v, n, p)$, we find that the orthonormalization time required for k iterations is: $\frac{1}{2}k(k+1) f(c_m, n_v, n, p) \approx \frac{1}{2}k^2 f$ for $k \gg 1$. The \mathbf{Au} product time is not a function of the iteration number and therefore the time required for k iterations is simply k times the time of one iteration. The sum of these two steps is the total time required to perform k -iterations. These times are summarized in Table 5.

	2D	3D
BEM	$2k c_m n_v np (8n_v np + k)$	$3k c_m n_v (np)^2 [12n_v (np)^2 + k]$
Non-condensed FEM	$\frac{1}{2}k \bar{c}_m n_v n^2 \times [2n_v (p+1)^4 + k \bar{c}_m p^2]$	$\frac{1}{2}k \bar{c}_m n_v n^3 \times [2n_v (p+1)^6 + k \bar{c}_m p^3]$
Statically condensed FEM	$\frac{1}{2}k \bar{c}_m n_v n^2 \times [32n_v p^2 + k \bar{c}_m (2p-1)]$	$\frac{1}{2}k \bar{c}_m n_v n^3 \times [8n_v (3p^2+1)^2 + k \bar{c}_m (3p^2-3p+1)]$

Table 5: Cost of k iterations.

Based on the times given in Table 5, we find the crossover conditions for which BEM

becomes more cost effective: For non-condensed FEM:

$$\begin{aligned} k &\geq \frac{2n_v n [16\bar{c}_m p^2 - (p+1)^4]}{\bar{c}_m p (np-4)} \quad \& \quad np > 4 \quad \text{for 2D} \\ k &\geq \frac{2n_v n [36\bar{c}_m np^4 - (p+1)^6]}{\bar{c}_m p^2 (np-6)} \quad \& \quad np > 6 \quad \text{for 3D} \end{aligned} \quad (44)$$

and for condensed FEM:

$$\begin{aligned} k &\geq \frac{32n_v np^2 (\bar{c}_m - 1)}{\bar{c}_m [n(2p-1) - 4]} \quad \& \quad n > 4p/(2p-1) \quad \text{for 2D} \\ k &\geq \frac{8n_v n [7\bar{c}_m np^4 - (3p^2 + 1)^2]}{\bar{c}_m [n(3p^2 - 3p + 1) - 6p^2]} \quad \& \quad np > 6 \quad \text{for 3D} \end{aligned} \quad (45)$$

We emphasize again that these results reflect only which of the two methods is faster for the same number of iterations.

The second issue that we would like to investigate here is the memory consumption. We note here that this comparison is applicable to those situations in which all element stiffness matrices are stored prior to solution. The comparison will be based again on the same number of iterations for both methods. We will use the assumption that the number of the equations n_{eq} is much larger than the number of iterations k , thus, $n_{eq} \gg k$. From this assumption we find that the storage space for regular BEM would be $\bar{c}_m n_{eq}^2$ words, and half of that when a symmetric Galerkin BEM is used. In the case of FEM $\bar{c}_m k n_{eq}$ words are required for the storage of the Krylov vectors from the former iterations and $n_{el} n_{edof}^2$ words are required for the storage of the coefficient matrix non-zero terms. The storage space for the different methods can be written as:

Using the values in Table 6 we can find the memory crossovers. In the 2D case we find that for Laplace and elastostatics, BEM always requires less memory space for the same number of iterations, while for waves problems the crossover from statically condensed FEM to Galerkin BEM occurs when $k \geq 4n_v p^2 / (2p-1)$. For 3D problems the crossover

	2D	3D
Regular BEM	$16\bar{c}_m n_v^2 (np)^2$	$36\bar{c}_m n_v^2 (np)^4$
Galerkin BEM	$8\bar{c}_m n_v^2 (np)^2$	$18\bar{c}_m n_v^2 (np)^4$
Non-condensed FEM	$n_v^2 n^2 (p+1)^4 + \bar{c}_m k n_v (np)^2$	$n_v^2 n^3 (p+1)^6 + \bar{c}_m k n_v (np)^3$
Condensed FEM	$16n_v^2 (np)^2 + \bar{c}_m k n_v n^2 (2p-1)$	$4n_v^2 n^3 (3p^2+1)^2 + \bar{c}_m k n_v n^3 (3p^2-3p+1)$

Table 6: Memory required for k iterations [words].

between statically condensed FEM and Galerkin BEM will occur approximately when $k \geq 18n_v np^4 / (3p^2 - 3p + 1)$ (for $n \gg p$).

9 FEM static condensation

Here we compare FEM to statically condensed FEM. Thus we evaluate the importance of static condensation in high order FEM approaches. Based on equations (15,18) we can find the factorization time ratio between the condensed and the non-condensed FEM for direct solvers. The memory ratio for direct solvers can be found from equations (39,40). For iterative solvers we can find the ratio of solution time for k iteration from Table 5 and the memory ratio from Table 6. These ratios are summarized in Table 7 under the assumption of $n \gg p$.

The results in Table 7 neglect the cost of static condensation. The assumption that this cost is negligible becomes invalid when $p = \mathcal{O}(n) \gg 1$. The cost associated with static condensation can be estimated to be that of inverting a $n_v(p-1)^d$ square, full

	2D	3D
Factorization time direct solvers	$p^6/(2p - 1)^3$	$p^9/(3p^2 - 3p + 1)^3$
Memory direct solvers	$p^4/(2p - 1)^2$	$p^6/(3p^2 - 3p + 1)^2$
Solution time for k iterations	$[2n_v(p+1)^4 + (k+1)\bar{c}_m p^2] / [32n_vp^2 + (k+1)\bar{c}_m(2p-1)]$	$[2n_v(p+1)^6 + (k+1)\bar{c}_m p^3] / [8n_v(3p^2+1)^2 + (k+1)\bar{c}_m(3p^2-3p+1)]$
Required memory for k iterations	$[n_v(p+1)^4 + \bar{c}_m k p^2] / [16n_vp^2 + \bar{c}_m k(2p-1)]$	$[n_v(p+1)^6 + \bar{c}_m k p^3] / [4n_v(3p^2+1)^2 + \bar{c}_m k(3p^2-3p+1)]$

Table 7: Ratios between non-condensed and condensed FEM.

symmetric matrix for each element. This is given by the expression:

$$t_{condensation} = n_{el} n_v^3 (p-1)^{3d} / 6 = \begin{cases} n^2 n_v^3 (p-1)^6 / 6 & \text{flops, for 2D} \\ n^3 n_v^3 (p-1)^9 / 6 & \text{flops, for 3D} \end{cases} \quad (46)$$

Comparing (14) to (46) shows that condensation cost is indeed negligible for $p < n$.

10 Remarks and Conclusions

We have presented an extensive theoretical cost comparison between FEM and BEM for low and high order elements. The work applies to four equations: Laplace, Helmholtz, elastostatics and elastodynamics in 2D and 3D. This comparison dealt both with direct and iterative solvers. We evaluated the set-up cost time for BEM in its regular form and in its symmetric Galerkin form and compared those two methods to each other. Finally

we compared pure FEM with statically condensed FEM. In this section we will summarize our conclusions from each comparison separately.

10.1 Direct solvers: Solution time

From the comparison between standard FEM and BEM, we find that there is a significant drop in the crossover values of high order elements as compared to linear elements. For Laplace and elastostatics BEM, becomes more cost effective when using just one element per edge of 6-th and 8-th order, for 2D and 3D, respectively. For waves problems, the order of that element is 9 and 13 for 2D and 3D, respectively.

From the comparison between statically condensed FEM and BEM, we find that the minimal crossover is obtained for quadratic elements in 2D and cubic in 3D. In 2D for quadratic elements the crossover occurred at about 100 nodes per edge for wave problems (equivalent to a total of 400 BEM nodes or 7,500 condensed FEM nodes). For 2D Laplace and elastostatics the crossover is at about 40 nodes per edge (equivalent to 160 BEM nodes or 1,200 condensed FEM nodes). These problems are well within the range of application of direct solutions methods.

The optimal crossover in 3D occurred for cubic elements at about 50 nodes per edge for Laplace and elastostatics equations. This corresponds to 15,000 BEM nodes or 10^5 condensed FEM nodes. For the Helmholtz and elastodynamics equations, the corresponding figures are 190 nodes per edge giving 200,000 BEM nodes or $6 \cdot 10^6$ condensed FEM nodes. These problem sizes challenge the current capabilities of direct solvers. Therefore, we conclude that in 3D, FEM is more cost effective for the full range of applicability of direct

solvers.

10.2 Direct solvers: Memory

From the comparison of the memory between statically condensed FEM and BEM we find that the minimal crossover is for quadratic elements (except for 3D Laplace and elastostatics where it is for cubic elements). In 2D, the crossover is about 15 or 30 nodes per edge for real or complex equations, respectively. This is equivalent to a total of 3,800 BEM nodes or 12,000 condensed FEM nodes for the static equations, and 12,000 BEM or 75,000 statically condensed FEM nodes for the dynamics equations. Since memory is typically a problem only for very large coefficient matrices, we conclude that BEM is generally more memory efficient than statically condensed FEM for 2D problems and for 3D Laplace and elastostatics. The case of 3D wave problems, where 12,000 BEM nodes with complex values need to be stored might be considered borderline. For Helmholtz, this corresponds to 4 GB of memory for double precision arithmetic, which is *currently* available on a few high performance computers.

10.3 BEM set-up cost

The BEM set-up cost might be a very significant part out of the overall solution time. We chose the Laplace equation as representative to find that the set-up cost is more expensive than the factorization cost for meshes of fewer than 10 (20) nodes per edge for 3D (2D) problems (equivalent to a total of 600 (80) BEM nodes). The set-up cost drops very rapidly with increasing number of nodes, and for large problems, has a small

contribution for the overall solution time. For example, for the Laplace equation the set-up cost is less than 10% of the overall solution time for a mesh of 40 (200) nodes per edge in 3D (2D) (equivalent to a total of 9,600 (800) BEM nodes).

We note that the set-up procedure is typically much more memory and data intensive than the matrix inversion procedure. Therefore, the unpredictable memory behavior of any given application would tend to make the true time estimates larger than those described here. Therefore, we can consider our estimates of the set-up costs to be lower bounds on what a user might expect in practice.

10.4 Standard BEM versus symmetric Galerkin BEM

The optimal element order where the symmetric Galerkin BEM formulation is more cost effective than collocation BEM is quadratic or cubic in 2D or 3D, respectively. For 2D quadratic elements in elastostatics and wave problems, Galerkin becomes more cost effective after using only 5 elements per edge. For Laplace's equation, this crossover is at 15 elements per edge. In 3D for cubic elements the crossover to symmetric Galerkin BEM is at 7 elements per edge for elastostatics and wave problems and 13 elements per edge for Laplace. From these results (especially in the 2D case) we conclude that the expense of the extra set-up in the symmetric Galerkin BEM formulation is compensated in factorization time savings in most problems of interest. These conclusions were reached on the basis of the integration strategy described in section 5, which was developed for efficiency rather than accuracy. The use of other integration strategies would certainly affect our conclusions.

10.5 Iterative solvers

We compared the iterative solution of FEM equations to BEM equations for equal numbers of iterations. We found that the solution time crossover occurs at k_{co} iterations, where $k_{co} \approx 72n_vnp$ for $np \gg 1$. When using 50 cubic elements per edge in 3D to solve the elastostatics equation, the $k_{co} \approx 32,000$ iterations. For problems that converge in fewer than k_{co} iterations, FEM is more cost effective.

10.6 Static condensation

Our comparison of standard FEM to FEM with static condensation show the great efficiency improvements that static condensation provides with a direct solver. For example, Table 7 shows that using 4-th order elements and condensing out the interior degrees of freedom is about 12 times faster in 2D and 5 times faster in 3D than standard FEM. In the same case, pure FEM demands 5 times the storage space used by condensed FEM in 2D and 3 times in 3D.

Acknowledgment

The authors are grateful to Dr. Isaac Harari for helpful discussions on many aspects of this comparison, and to Dr. Margaret Martonosi for guidance in scrutinizing the use of flop counts to measure computational efficiency. Finally, the authors gratefully acknowledge the financial support of ONR.

References

- [1] T.J.R. Hughes, The Finite Element Method: Linear Static and Dynamic Finite Element Analysis (Prentice Hall, Englewood Cliffs, NJ, 1987).
- [2] C.A. Brebbia and J. Domiguez, Boundary Elements An Introductory Course, (Computational Mechanics Publications, McGraw-Hill 1992).
- [3] I. Harari and T. J.R. Hughes, *Comput. Methods in Appl. Mech. and Engrg.*, A cost comparison of boundary element and finite element methods for problems of time-harmonic acoustics, **97**, 77-102, (1992).
- [4] W. Krajewski and S.J. Salon, Comparison of the BEM and FEM approach for the electromagnetic field analysis in a zoned medium, Communications in Numerical Methods in Engineering, **9** (1993) 847-856.
- [5] C. Setbon, A numerical comparison of the finite element method and the boundary element method in acoustics, MSc. thesis, Tel-Aviv University, Israel, 1996.
- [6] E.C. Hume, R.A. Brown and W.M. Deen, Comparison of boundary and finite element methods for moving boundary problems governed by a potential, International Journal for Numerical Methods in Engineering **21** (1985) 1295-1314.
- [7] M. Martonosi, Private communication, May 1997.
- [8] G.H. Golub and C.F. van Loan, Matrix computations, 1-st edition, (Johns Hopkins Univ. Press, Baltimore, MD, 1983).

- [9] G.H. Golub and C.F. van Loan, Matrix computations, 2-nd edition, (Johns Hopkins Univ. Press, Baltimore, MD, 1989).
- [10] O. Michael and P.E. Barbone, Galerkin formulation and singularity subtraction for spectral solutions of boundary integral equations, Accepted for publication: Int. J. for Num. Meth. in Engng., (1997).
- [11] M. Bonnet, *Regularized direct and indirect symmetric variational BIE formulations for three-dimensional elasticity*, Engineering Analysis with Boundary Elements, **15**, 93-102, (1995).
- [12] P. Parreira and M. Guiggiani, *On the implementation of the Galerkin approach in the boundary element method*, Computers and Structures, **33**, 269-79, (1989).
- [13] A. Kanarachos and C. Provatidis, *On the symmetrization of the BEM formulation*, Computer Methods in Applied Mechanics and Engineering, **71**, 151-65, (1988).
- [14] S. Sirtori, G. Maier, G. Novati and S. Miccoli, A Galerkin symmetric boundary-element method in elasticity: formulation and implementation, International Journal for Numerical Methods in Engineering, **35** (1992) 255-282.
- [15] A. Aimi, M. Diligenti and G. Monegato, New numerical integration schemes for applications of Galerkin BEM to 2-D problems, International Journal for Numerical Methods in Engineering, **40** (1997) 1977-1999.
- [16] M. Tanaka, V. Sladek and J. Sladek, Regularization techniques applied to boundary element methods, Appl. Mech. Rev., **40** (1994), 457-499.

- [17] J.B. Keller and D. Givoli, Exact non-reflecting boundary conditions, *J. Comput. Phys.* 82 (1989) 172-192.
- [18] D. Givoli, Numerical methods for problems in infinite domains (Studies in applied mechanics, Vol. 33, Elsevier, 1992).
- [19] D.S. Burnett, A three dimensional acoustic infinite element based on a spheroidal multipole expansion, *J. Acoust. Soc. Am.*, 96 (1994), 2798-2816.
- [20] P. Bettess, Infinite Elements, *Int. J. Numer. Methods Eng.*, 11 (1977), 53-64.
- [21] I. Harari and P.E. Barbone, Finite element formulation for exterior problems: application to hybrid methods, non-reflecting boundary conditions, and infinite elements, Boston University Technical Report AM-96-001, (1996).
- [22] L.G. Copely, Fundamental results concerning integral representations in acoustic radiation, *J. Acoust. Soc. Amer.* 44 (1968) 28-32.
- [23] V.D. Kupradze, Fundamental Problems in Mathematical Theory of Diffraction (Steady State Processes), 1935; translated by C.D. Benster, N.B.S. Rep. 2008, 1952.
- [24] H.A. Schenck, Improved integral formulation for acoustic radiation problems, *J. Acoust. Soc. Amer.* 44 (1968) 41-58.
- [25] D.S. Jones, Integral equations for exterior acoustic problem, *Quart. J. Mech. Appl. Math.*, 27 (1974) 129-142.

-
- [26] A.J. Burton and G.F. Miller, The application of integral equation methods to the numerical solution of some exterior boundary-value problems, Proc. Roy. Soc. London Ser. A 323 (1971) 201-210.
- [27] F. Shakib, T.J.R. Hughes and Z. Johan, A multi-element group preconditioned GMRES algorithm for nonsymmetric systems arising in finite element analysis, Comput. Methods Appl. Mech. Engrg. 75 (1989) 415-456.
- [28] Y. Saad and M.H. Schultz, GMRES: A generalized minimal residual algorithm for solving nonsymmetric linear systems, Research Report YALEU/DCS/RR-254, Dept. of Computer Science, Yale University, 1983.

Figures caption

Fig. 1: FEM/BEM models of a square and a cube.

Fig. 2: Factorization time, crossover from FEM to BEM.

- a) Laplace and elastostatics.
- b) Helmholtz and elastodynamics.

Fig. 3: Set-up cost + solution time, crossover from regular collocation BEM to Galerkin BEM.

- a) 2D problems.
- b) 3D problems.

Fig. 4: Solution time, crossover from condensed FEM to BEM.

- a) 2D problems.
- b) 3D problems.

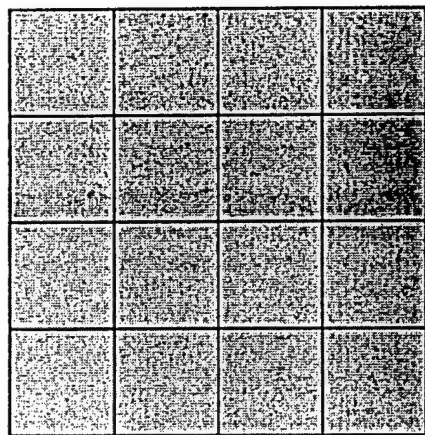
Fig. 5: Set-up cost time out of the over all solution time.

- a) 2D Laplace equation.
- b) 3D Laplace equation.

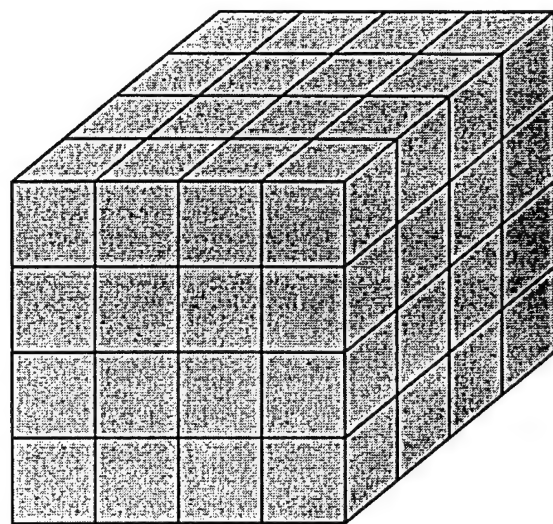
Fig. 6: Memory, crossover from FEM to BEM.

- a) Laplace and elastostatics.
- b) Helmholtz and elastodynamics.

Fig. 7: Exterior problem.

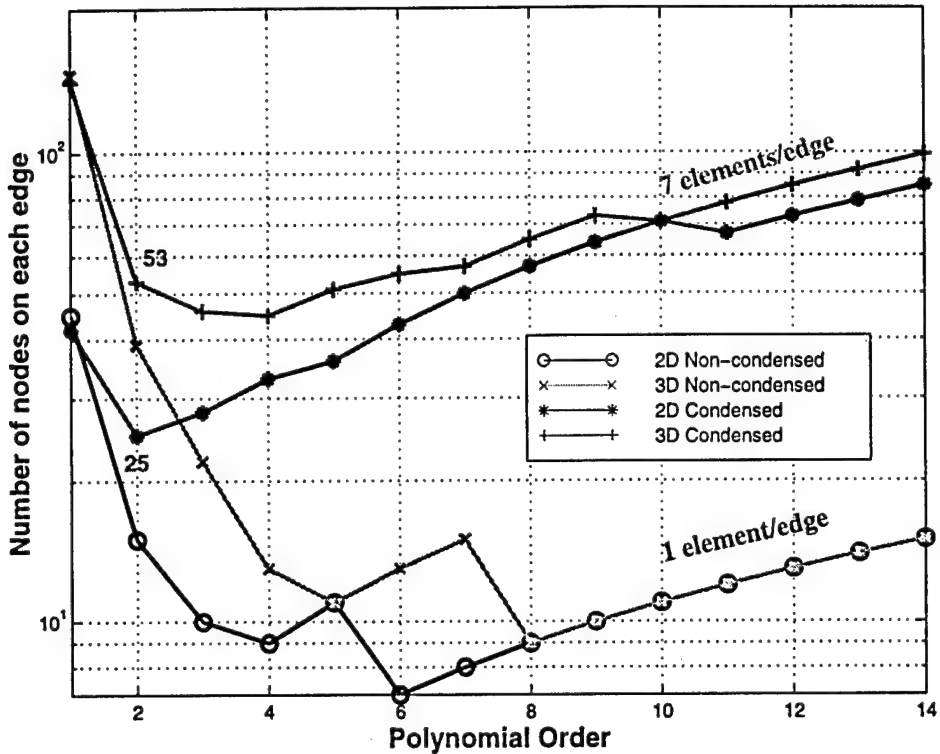


2D

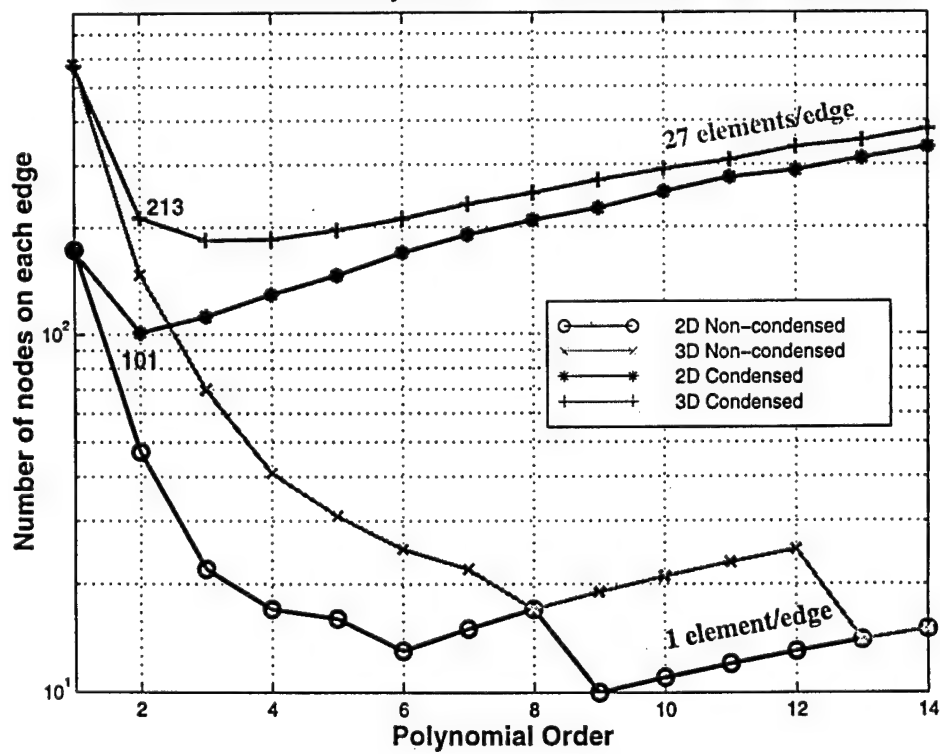


3D

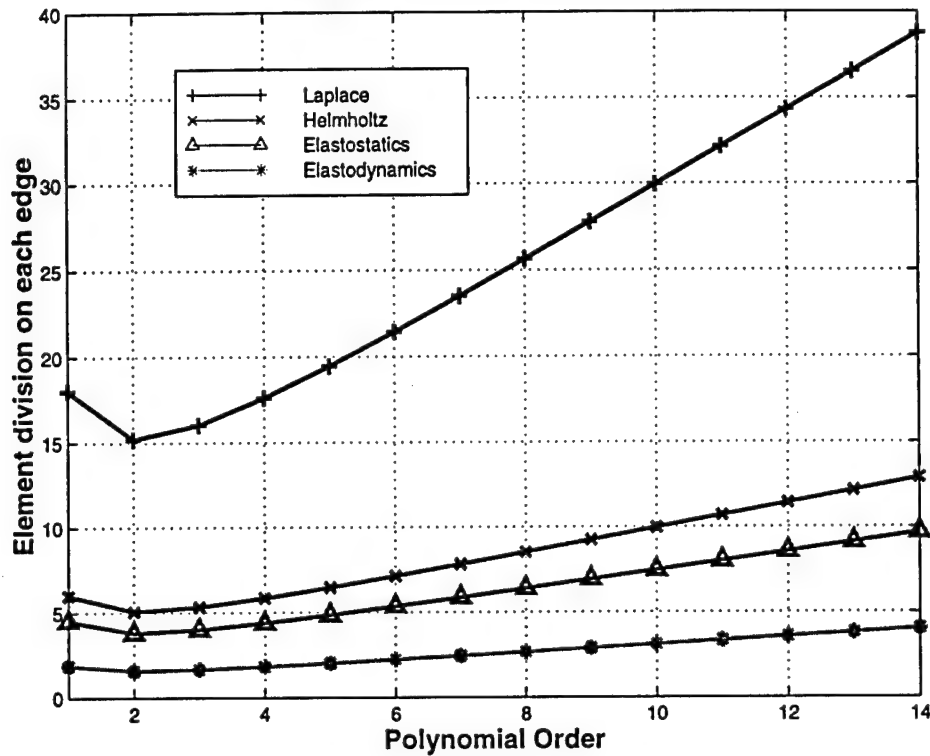
Laplace and Elastostatics – Factorization Time Crossover



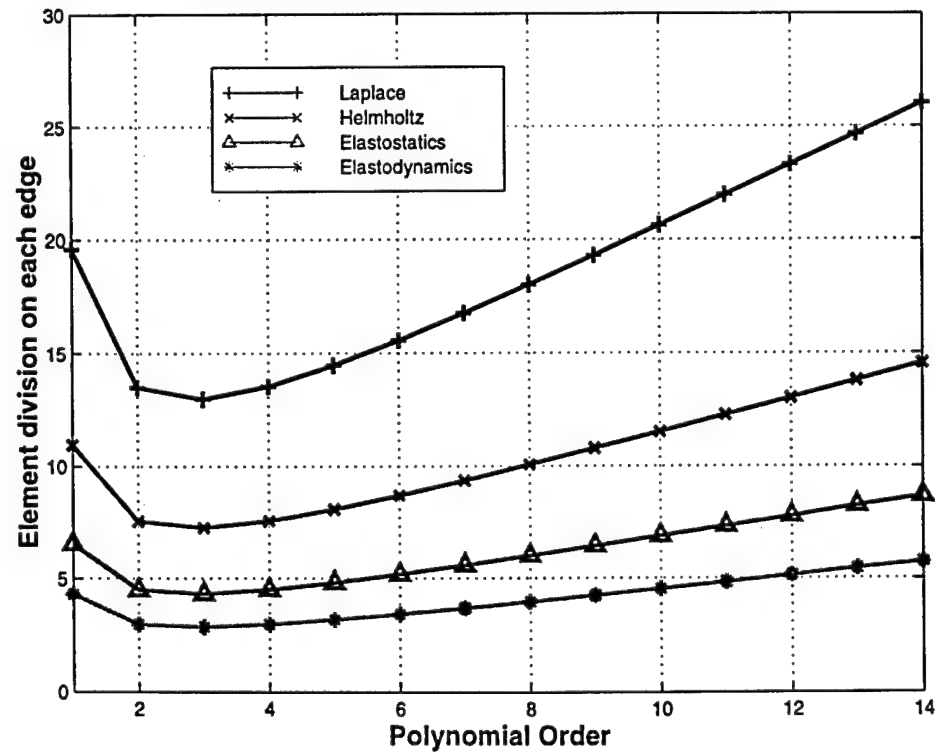
Helmholtz and Elastodynamics – Factorization Time Crossover



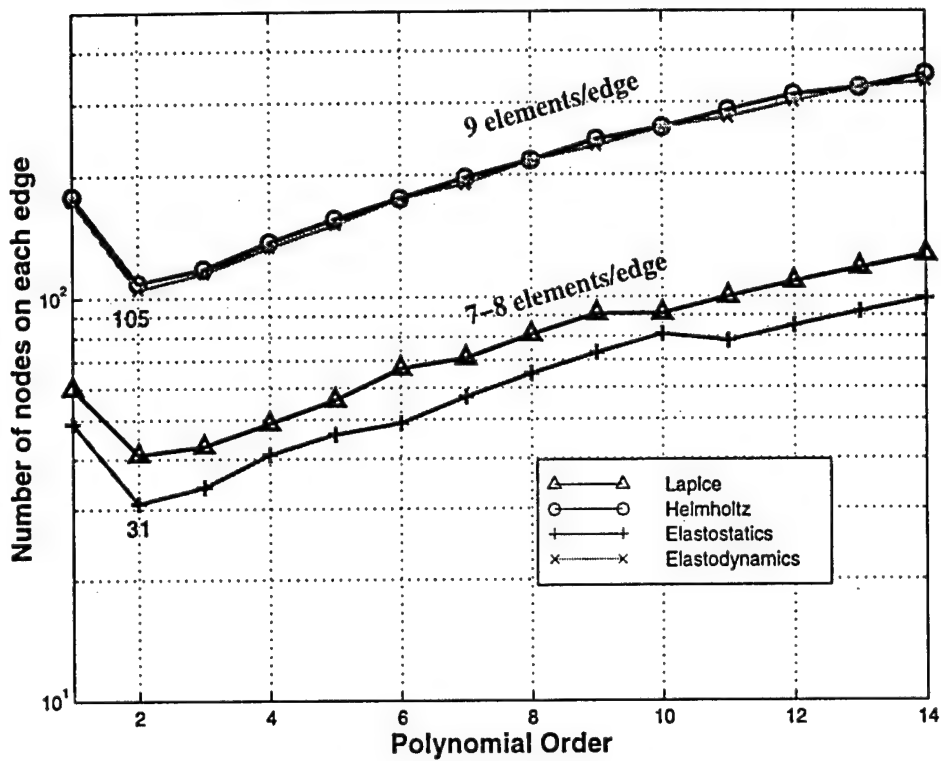
2-D Problems: crossover Galerkin/collocation



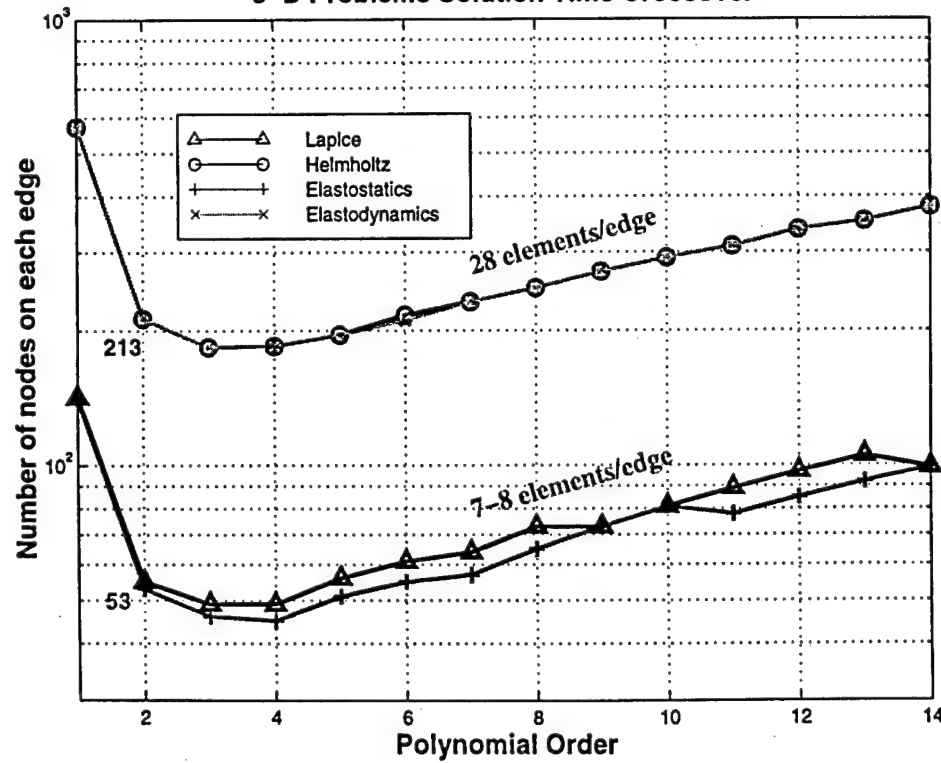
3-D Problems: crossover Galerkin/collocation

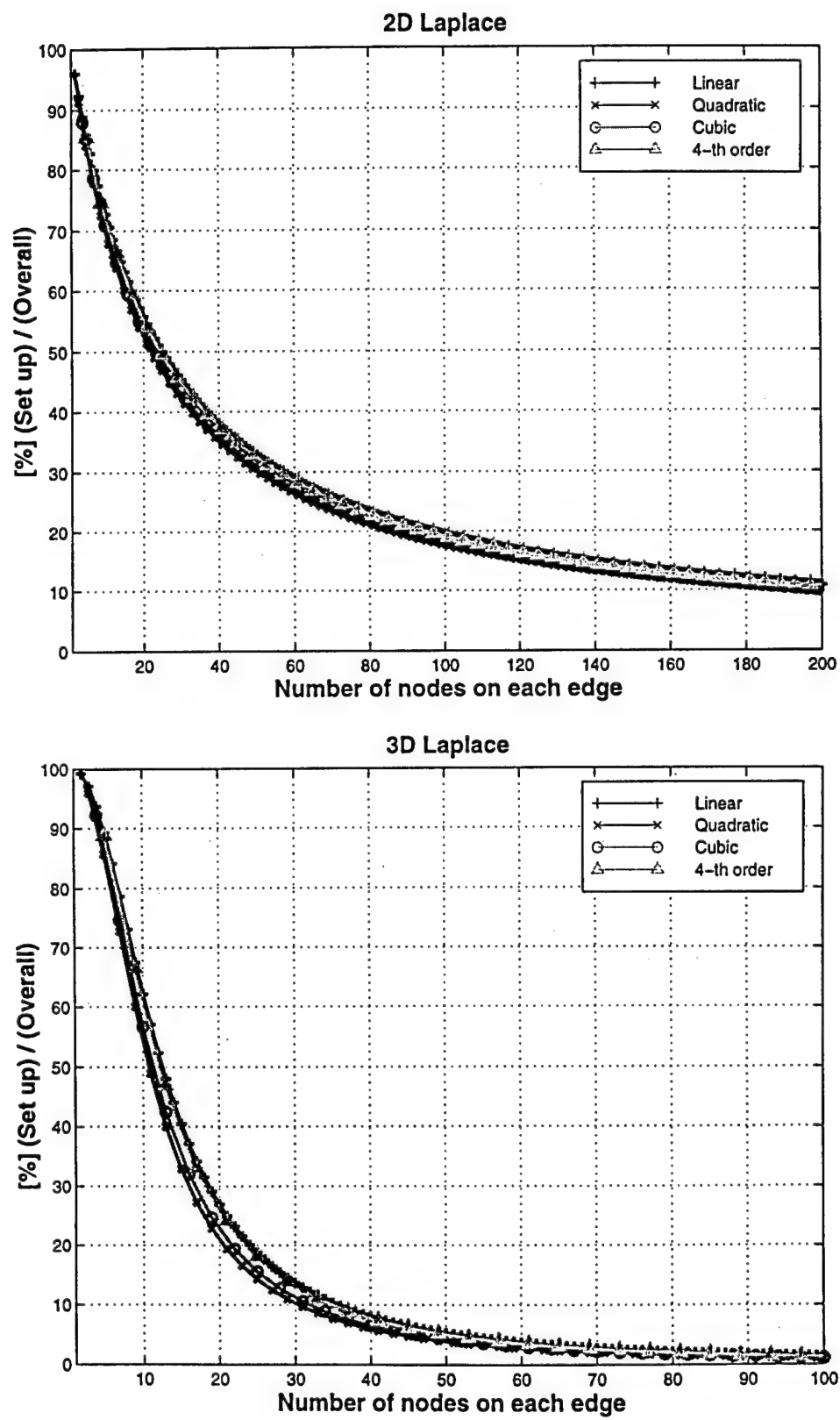


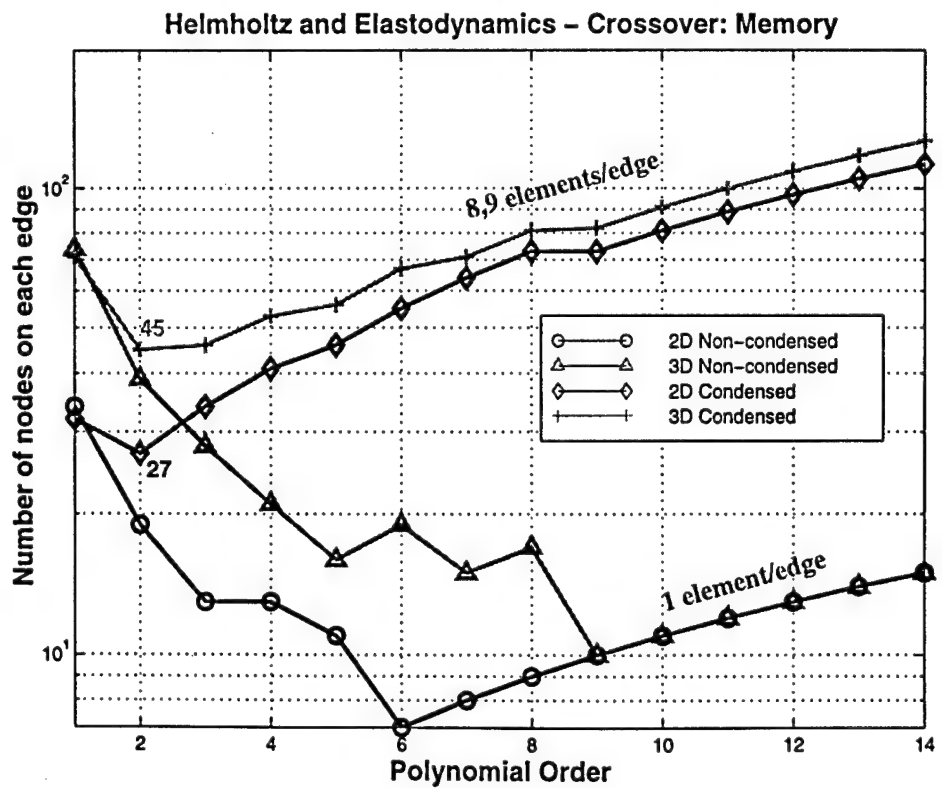
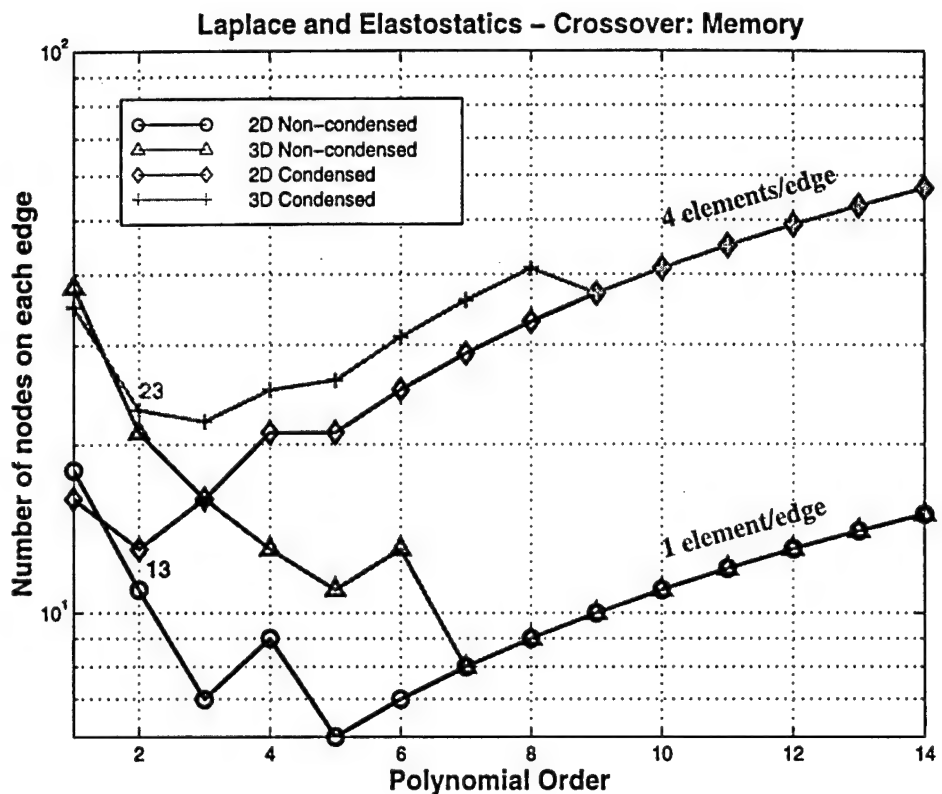
2-D Problems Solution Time Crossover

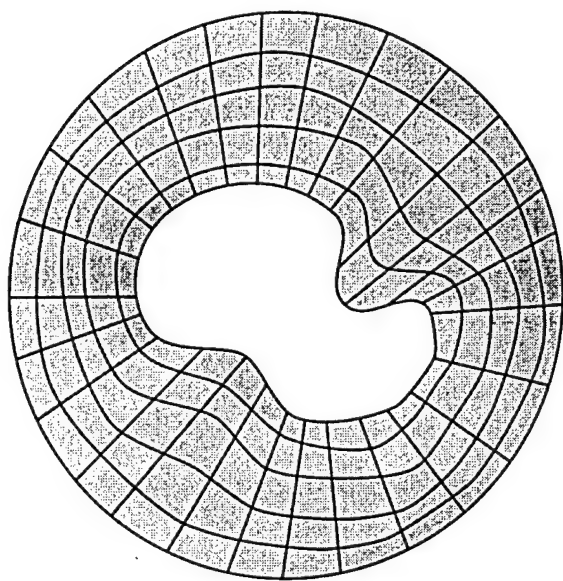
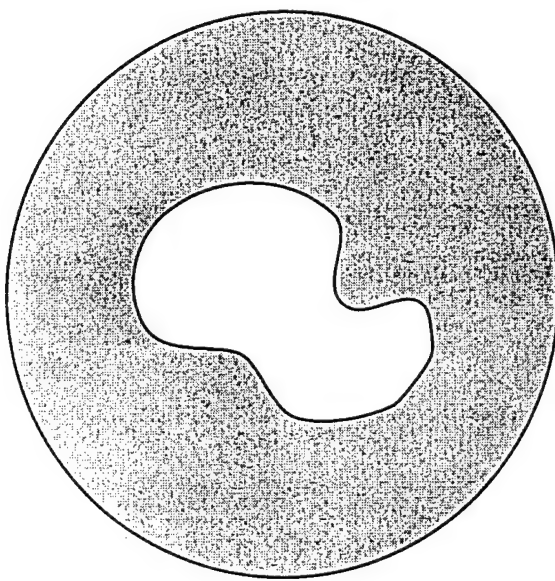


3-D Problems Solution Time Crossover









C.8 Nearly H^1 Optimal Finite Element Method for the Helmholtz Equation

"Nearly H^1 Optimal Finite Element Method for the Helmholtz Equation," Paul E. Barbone and Isaac Harari, BU Dept. Aerospace & Mechanical Eng. Technical Report No. AM-97-011, May 7, 1997.

Nearly H^1 Optimal Finite Element Method
for the Helmholtz Equation

Paul E. Barbone
Isaac Harari

May 7, 1997

Technical Report No. AM-97-011

**Nearly H^1 Optimal FEM for the
Helmholtz Equation**

Paul E. Barbone

Isaac Harari

Sept. 30, 1996

May 1, 1997

1 Introduction

We consider the problem of finding $\bar{u}(x)$, the H^1 projection onto a given finite element space $\bar{\mathcal{S}}$ of $u(x)$, a solution of the Helmholtz equation. We show that the problem of finding \bar{u} is approximately equivalent to a Petrov-Galerkin formulation of the original boundary value problem. The optimally chosen weight functions must satisfy several criteria that are specified below. In particular, we show that the weighting functions are the shape functions themselves (i.e. what would be used in a Bubnov-Galerkin procedure) plus bubble functions. The bubbles can be found approximately in a straightforward and systematic manner.

We shall formulate the problem of finding the desired projection in a rather straightforward way. We desire to minimize the norm of the difference between the interpolant and the unknown function, subject to the constraint that the unknown function satisfies the desired differential equation. Upon manipulating the resulting equations, a “stabilized finite element method” results. For definiteness, we shall work in terms of the Helmholtz equation and the H^1 semi-norm, though generalization to other equations or norms is possible.

2 Formulation

We consider the problem of finding $\bar{u}(x) \in \bar{\mathcal{S}}$ such that for $u(x)$ in \mathcal{S} :

$$\|u - \bar{u}\|_{H^1(\Omega)} = \text{minimum.} \quad (1)$$

Here, $u(x) : \bar{\Omega} \rightarrow C$ is the (complex valued) unknown solution of Helmholtz equation. $\Omega \subset R^d$ denotes a d -dimensional domain with boundary Γ . We shall consider the function spaces $\bar{\mathcal{S}}$ and \mathcal{S} to be defined as follows:

$$\mathcal{S} = \{u(x) | u(x) \in H^1(\Omega); u(x) = u_o(x) \text{ on } \Gamma_u\} \quad (2)$$

$$\bar{\mathcal{S}} = \{\bar{u}(x) | \bar{u}(x) \in \mathcal{S}; \bar{u}(x) = \sum_A d_A N_A(x)\}. \quad (3)$$

By assuming that $\bar{\mathcal{S}} \subset \mathcal{S}$, we are assuming that our chosen basis can exactly represent the essential boundary conditions $u = u_o$ on Γ_u . That may or may not be the case in practice, but we shall restrict ourselves to this case for simplicity. We further introduce two spaces of admissible variations:

$$\mathcal{V} = \{w(x) | w(x) \in H^1(\Omega); w(x) = 0 \text{ on } \Gamma_u\} \quad (4)$$

$$\bar{\mathcal{V}} = \{\bar{w}(x) | \bar{w}(x) \in \mathcal{V}; \bar{w}(x) = \sum_A c_A N_A(x)\}. \quad (5)$$

Finally, we suppose that f is a complex valued function in $L_2(\Omega)$ and that $u(x)$ satisfies (k^2 is a given known *constant*):

$$\nabla^2 u + k^2 u + f = 0 \quad x \in \Omega \quad (6)$$

$$u(x) = u_o(x) \quad x \in \Gamma_u \quad (7)$$

$$\frac{\partial u}{\partial n} = p(x) \quad x \in \Gamma_p \quad (8)$$

We shall consider $f(x)$ to be known, though $u(x)$ is not.

We wish to find $\bar{u}(x)$ which denotes the H^1 projection of $u(x)$ onto $\bar{\mathcal{S}}$. Therefore, we introduce the functional:

$$\Pi[u, \bar{u}, \lambda] = \frac{1}{2} \int_{\Omega} [\nabla u^* - \nabla \bar{u}^*][\nabla u - \nabla \bar{u}] d\mathbf{x} - \int_{\Omega} \lambda [(\nabla^2 + k^2)u + f] d\mathbf{x} \quad (9)$$

Here, $\lambda(x) \in L_2(\Omega)$ is a Lagrange multiplier enforcing the constraint equation (6). Its variations $\nu(x)$ are also in $L_2(\Omega)$. The complex conjugate of a quantity (\cdot) is denoted by a star: $(\cdot)^*$.

We now make Π stationary with respect to variations in u (w), \bar{u} (\bar{w}) and λ (ν):

$$\frac{\delta \Pi}{\delta u} = 0 = \frac{1}{2} \int_{\Omega} \nabla w^* \cdot [\nabla u - \nabla \bar{u}] d\mathbf{x} + \frac{1}{2} \int_{\Omega} \nabla w \cdot [\nabla u^* - \nabla \bar{u}^*] d\mathbf{x} - \int_{\Omega} \lambda (\nabla^2 + k^2)w d\mathbf{x} \quad (10)$$

$$\frac{\delta \Pi}{\delta \bar{u}} = 0 = \int_{\Omega} \nabla \bar{w} \cdot [\nabla u - \nabla \bar{u}] d\mathbf{x} \quad (11)$$

$$\frac{\delta \Pi}{\delta \lambda} = 0 = - \int_{\Omega} \nu(x) [(\nabla^2 + k^2)u + f] d\mathbf{x} \quad (12)$$

Integrating (11) by parts yields

$$-\int_{\Omega} \nabla \bar{w} \cdot \nabla \bar{u} d\mathbf{x} - \int_{\Omega} \bar{w} \nabla^2 u d\mathbf{x} + \int_{\partial \Omega} \bar{w} \frac{\partial u}{\partial n} d\mathbf{x} = 0 \quad (13)$$

From equation (6), we have

$$\nabla^2 u = -f - k^2 u. \quad (14)$$

Combining equations (13) and (14) yields

$$\int_{\Omega} [\nabla \bar{w} \cdot \nabla \bar{u} - k^2 \bar{w} u] d\mathbf{x} = \int_{\Omega} \bar{w} f d\mathbf{x} + \int_{\partial \Omega} \bar{w} \frac{\partial u}{\partial n} d\mathbf{x}. \quad (15)$$

We note that equation (15) is almost the Galerkin weak form for \bar{u} . If we were to replace $u(x)$ in (15) with $\bar{u}(x)$, arguing that their difference is negligible, then we would recover the Galerkin equations. Instead, we turn our attention to equation (12), which is the Euler-Lagrange equation that determines $u(x)$. We use this to approximate the term (\bar{w}, u) in (15).

3 Evaluating (\bar{w}, u)

From (12) we have

$$\sum_e \int_{\Omega^e} \nu(x)[\nabla^2 u + k^2 u + f] d\mathbf{x} = 0. \quad (16)$$

Here we have introduced the “element domains”, Ω^e , $e = 1, \dots, N$. We now restrict our attention to those functions ν which are piecewise continuous. Integrating the first term of (16) twice by parts then yields

$$\sum_e \int_{\Omega^e} u(\nabla^2 + k^2)\nu + f \nu d\mathbf{x} - \sum_e \int_{\partial\Omega^e} u \frac{\partial\nu}{\partial n} d\gamma - \int_{\partial\Omega} \nu \frac{\partial u}{\partial n} d\gamma = 0. \quad (17)$$

We now choose $\nu(x)$ (which is arbitrary) to satisfy the following over each element domain, Ω^e :

$$(\nabla^2 + k^2)\nu = \bar{w} \quad \text{on } \Omega^e \quad (18)$$

$$\nu = k^{-2}(\bar{w} - \nu_o) \quad (19)$$

$$\nu_o = \bar{w} \quad \text{on } \partial\Omega^e \quad (20)$$

It is clear from (18-20) that $\nu(x)$ so chosen is continuous across element boundaries. For the remainder of this presentation, $\nu(x)$ is no longer arbitrary, but that special function associated with $\bar{w}(x)$ as defined in equations (18-20). Combining equations (17) and (18) now yields

$$\sum_e \int_{\Omega^e} \bar{w} u d\mathbf{x} = - \sum_e \int_{\Omega^e} f \nu d\mathbf{x} + \sum_e \int_{\partial\Omega^e} u \frac{\partial\nu}{\partial n} d\gamma. \quad (21)$$

3.1 The closure assumption

Equation (21) requires the knowledge of $u(x)$ on the element boundaries in order to evaluate $\int_{\Omega^e} \bar{w} u d\mathbf{x}$. We shall replace integrations of $u(x)$ over element boundaries by corresponding integrals of $\bar{u}(x)$. There we set

$$\int_{\partial\Omega^e} u \frac{\partial\nu}{\partial n} d\gamma = \int_{\partial\Omega^e} \bar{u} \frac{\partial\nu}{\partial n} d\gamma + \text{err}_e. \quad (22)$$

The quantity err_e introduced in (22) represents the “error” of our “closure” assumption. That is, we shall later neglect err_e in (22) to relate integrals of $u(x)$ over element boundaries to integrals of $\bar{u}(x)$.

Replacing $u(x)$ with $\bar{u}(x)$ on $\partial\Omega^e$ is exact pointwise in one dimension, but is satisfied pointwise only approximately in higher dimensions. That is the approximation that has been used and discussed by Hughes in his multi-scale work [1]. Equation (22) is a relaxation of the pointwise requirement $u(x) = \bar{u}(x)$ on $\partial\Omega^e$.

4 Deriving the final weak form

Before we substitute everything back into our main equation (15), we simplify the result from (21) and (22). We begin by applying the divergence theorem to the right hand side of (22):

$$\int_{\partial\Omega^e} \bar{u} \frac{\partial \nu}{\partial n} d\gamma = \int_{\Omega^e} \nabla \cdot (\bar{u} \nabla \nu) dx \quad (23)$$

$$= \int_{\Omega^e} \nabla \bar{u} \cdot \nabla \nu + \bar{u} \Delta \nu dx. \quad (24)$$

We now use equations (18) and (19) to replace $\Delta \nu$ and ν in (24):

$$k^2 \int_{\partial\Omega^e} \bar{u} \frac{\partial \nu}{\partial n} d\gamma = \int_{\Omega^e} \nabla \bar{u} \cdot \nabla (\bar{w} - \nu_o) + k^2 \bar{u} \nu_o dx. \quad (25)$$

Equations (21), (22) and (25) can be combined to obtain:

$$k^2 \sum_e \int_{\Omega^e} \bar{w} u dx = \sum_e \int_{\Omega^e} (\nabla \bar{u} \cdot \nabla \bar{w} - f \bar{w}) - (\nabla \bar{u} \cdot \nabla \nu_o - k^2 \bar{u} \nu_o - f \nu_o) dx + \sum_e k^2 \text{err}_e. \quad (26)$$

Finally, we substitute (26) into (15) and use (20) to obtain:

$$\sum_e \int_{\Omega^e} \left\{ \nabla \nu_o \cdot \nabla \bar{u} - k^2 \nu_o \bar{u} \right\} dx = \int_{\Omega} \nu_o f dx + \int_{\partial\Omega} \nu_o \frac{\partial u}{\partial n} d\gamma + \sum_e k^2 \text{err}_e. \quad (27)$$

If we choose to neglect err_e in (27), then what we are left with is just a Petrov-Galerkin formulation based on the original weak form. It is in a suitable form to determine $\bar{u}(x)$ given a set of shape functions defining $\bar{\mathcal{S}}$, and given functions $f(x)$ and $p(x)$. We shall now examine the implications of neglecting err_e .

5 Analysis of closure assumption (22)

We can rewrite equation (22) as follows:

$$\text{err}_e = \int_{\partial\Omega^e} (u - \bar{u}) \frac{\partial \nu}{\partial n} d\gamma. \quad (28)$$

We shall now examine equation (28) and show that equations (11), (16) and (27) are consistent with err_e vanishing.

In this section, we shall assume only that $u(x)$ satisfies (16) for all functions $\nu(x) \in L_2(\Omega)$, and that $\nu(x)$ and $\nu_o(x)$ are related as in (18-20). We begin by applying the divergence theorem to the right hand side of (28):

$$\text{err}_e = \int_{\Omega^e} \nabla \cdot ((u - \bar{u}) \nabla \nu) dx, \quad (29)$$

$$= \int_{\Omega^e} (\nabla(u - \bar{u}) \cdot \nabla \nu + (u - \bar{u}) \nabla^2 \nu) dx. \quad (30)$$

Equation (18) allows us to replace $\nabla^2\nu$ with $\bar{w} - k^2\nu$. Combining this with (19) allows us to write

$$\nabla^2\nu = \nu_o. \quad (31)$$

We use (31) in the second term of (30), and (19) in the first term to write

$$\text{err}_e = \int_{\Omega^e} (k^{-2}\nabla(u - \bar{u}) \cdot \nabla(\bar{w} - \nu_o) + (u - \bar{u})\nu_o) d\mathbf{x}, \quad (32)$$

$$= k^{-2} \int_{\Omega^e} \nabla \bar{w} \cdot \nabla(u - \bar{u}) d\mathbf{x} - k^{-2} \int_{\Omega^e} (\nabla \nu_o \cdot \nabla(u - \bar{u}) - k^2 \nu_o(u - \bar{u})) d\mathbf{x} \quad (33)$$

Summing $k^2 \text{err}_e$ over all elements and separating the contributions on the right hand side of (33) yields:

$$\begin{aligned} \sum_e k^2 \text{err}_e &= \sum_e \int_{\Omega^e} \nabla \bar{w} \cdot \nabla(u - \bar{u}) d\mathbf{x} \\ &\quad + \sum_e \int_{\Omega^e} (\nabla \nu_o \cdot \nabla \bar{u} - k^2 \nu_o \bar{u}) d\mathbf{x} \\ &\quad - \sum_e \int_{\Omega^e} (\nabla \nu_o \cdot \nabla u - k^2 \nu_o u) d\mathbf{x}. \end{aligned} \quad (34)$$

To evaluate the last term on the right hand side of (34), we integrate equation (16) by parts once:

$$0 = \sum_e \int_{\Omega^e} [-\nabla \nu \cdot \nabla u + k^2 \nu u + \nu f] d\mathbf{x} + \sum_e \int_{\partial \Omega^e} \nu \frac{\partial u}{\partial n} d\gamma, \quad (35)$$

$$= \sum_e \int_{\Omega^e} [-\nabla \nu \cdot \nabla u + k^2 \nu u + \nu f] d\mathbf{x} + \int_{\partial \Omega} \nu \frac{\partial u}{\partial n} d\gamma. \quad (36)$$

The last term simplifies since both ν and ∇u are continuous functions. We note that (36) holds for all allowable functions ν , and so in particular holds for $\nu = \nu_o$.

We now substitute (36) into (34) to obtain

$$\begin{aligned} \sum_e k^2 \text{err}_e &= \sum_e \int_{\Omega^e} \nabla \bar{w} \cdot \nabla(u - \bar{u}) d\mathbf{x} \\ &\quad + \sum_e \int_{\Omega^e} (\nabla \nu_o \cdot \nabla \bar{u} - k^2 \nu_o \bar{u} - \nu_o f(x)) d\mathbf{x} - \int_{\partial \Omega} \nu_o \frac{\partial u}{\partial n} d\gamma. \end{aligned} \quad (37)$$

We see from (37) that the approximation (22) (i.e. with $\text{err}_e = 0$) is consistent with both our formulation (27) and our objective (11). That is not to say that our closure assumption $\text{err}_e = 0$ is always satisfied in practice! If *both* (27) and (11) are satisfied, then our closure assumption is valid. In practice, however, we would evaluate \bar{u} with (27); there is no way to impose either of the *additional* conditions that $\text{err}_e = 0$ or equation (11). If, in fact, it turns out that $\text{err}_e = 0$ as a result of a particular calculation using (27), then we see that (37) implies (11). Thus, we have optimality in that case. In general, however, computing with (27) under the *assumption* that $\text{err}_e = 0$ does not yield H^1 optimality, because that assumption is not always justified.

In certain cases, the closure assumption (22) is always satisfied. In particular, in one dimension the assumption is satisfied since $u(x) = \bar{u}(x)$ at element boundaries. Further, in the limit $kh \rightarrow 0$, the assumption is asymptotically satisfied to $o(kh)^2$ in any dimension.

We now turn our attention to evaluating $\nu_o(x)$ in certain cases.

6 Determining $\nu_o(x)$

6.1 Piecewise linear shape functions in one dimension

The weighting function in (27) is determined by solving equations (18-20) over each element. In one dimension, with element nodes at points x_{n-1} , x_n , and x_{n+1} , $\nu_o(x)$ is given by

$$\nu_o(x) = \begin{cases} \frac{\sin k(x - x_{n-1})}{\sin k(x_n - x_{n-1})} & \text{for } x_{n-1} \leq x \leq x_n \\ \frac{\sin k(x_{n+1} - x)}{\sin k(x_{n+1} - x_n)} & \text{for } x_n \leq x \leq x_{n+1} \end{cases} \quad (38)$$

We note that as $kh \rightarrow 0$ (where h represents the element size) then $\nu_o(x) \rightarrow \bar{w}(x)$. Thus in the limit of mesh refinement, we recover the standard Bubnov-Galerkin approximation, which we know to be optimal in that case.

6.2 Rectangular elements in two dimensions

Here we consider bilinear rectangular elements with dimensions h_x and h_y in the x and y directions, respectively. We write $\nu_o(x)$ as

$$\nu_o(x) = \bar{w}(x) + \nu_1(x), \quad (39)$$

and note that $\nu_1(x)$ satisfies

$$\Delta \nu_1 + k^2 \nu_1(x) = -k^2 \bar{w} \quad x \in \Omega^e \quad (40)$$

$$\nu_1 = 0 \quad x \in \partial\Omega^e. \quad (41)$$

In local (element) coordinates, equations (40) and (41) become

$$\left[\frac{1}{h_x^2} \frac{\partial^2}{\partial \xi^2} + \frac{1}{h_y^2} \frac{\partial^2}{\partial \eta^2} \right] \nu_1 + k^2 \nu_1 = -k^2 N_a(\xi, \eta) \quad \xi, \eta \in (-1, 1) \times (-1, 1) \quad (42)$$

$$\nu_1 = 0 \quad \xi = \pm 1; \eta = \pm 1. \quad (43)$$

Here, $N_a(\xi, \eta) = \frac{1}{4}(1 + \xi_a \xi)(1 + \eta_a \eta)$.

We can solve (42) and (43) by writing $\nu_1(x)$ as a series of eigensolutions; *viz.*

$$\nu_1(x) = \sum_{n,m=1} A_{nm}^a \sin \frac{n\pi(1+\xi)}{2} \sin \frac{m\pi(1+\eta)}{2}. \quad (44)$$

We note that each term in (44) satisfies (43). The superscript ‘*a*’ indicates that this $\nu_1(x)$ is associated with the shape function N_a . Substituting (44) into (42) yields

$$\sum_{n,m=1} \left[k^2 - \frac{1}{h_x^2} \frac{n^2\pi^2}{4} - \frac{1}{h_y^2} \frac{m^2\pi^2}{4} \right] \sin \frac{n\pi(1+\xi)}{2} \sin \frac{m\pi(1+\eta)}{2} A_{nm}^a = -k^2 N_a(\xi, \eta). \quad (45)$$

We now multiply (45) by $\sin \frac{p\pi(1+\xi)}{2} \sin \frac{q\pi(1+\eta)}{2}$ and integrate over the (local) element domain to obtain:

$$A_{pq}^a = -\frac{1}{pq\pi^2} \frac{[(1-\xi_a) - (-1)^p(1+\xi_a)][(1-\eta_a) - (-1)^q(1+\eta_a)]}{1 - \frac{p^2\pi^2}{4k^2h_x^2} - \frac{q^2\pi^2}{4k^2h_y^2}} \quad (46)$$

Equations (39), (44) and (46) give $\nu_o(x)$ associated with each of the element shape functions, N_a , $a = 1, 2, 3, 4$.

6.3 Series approximations for other elements

That $\nu_o(x)$ is approximated by $\bar{w}(x)$ can be used to find an expansion for $\nu_o(x)$ in the general case. In fact, equations (18-20) combine to show that $\nu_o(x)$ satisfies:

$$\Delta\nu_o + kh^2\nu_o = \Delta\bar{w} \quad \text{on } \Omega^e \quad (47)$$

$$\nu_o = \bar{w} \quad \text{on } \partial\Omega^e \quad (48)$$

Here we have introduced a nondimensional distance $\hat{x} = x/h$. We can find a useful approximate formula for $\nu_o(x)$ based on the following asymptotic approximation:

$$\nu_o(x) \sim \bar{w}(x) + kh^2\nu_1(x) + kh^4\nu_2 + \dots \quad (49)$$

Substituting (49) into equations (47-48) yields

$$\Delta\nu_1 = -\nu_o \quad \text{on } \Omega^e \quad (50)$$

$$\Delta\nu_n = -\nu_{n-1} \quad \text{on } \Omega^e \quad (51)$$

$$\nu_1 = \nu_n = 0 \quad \text{on } \partial\Omega^e. \quad (52)$$

The boundary condition (52) shows that $\nu_1(x)$, $\nu_2(x)$, etc. are bubble functions. They can be approximated optimally from (50) (or (51)) by using the Bubnov-Galerkin method and a bubble shape function. The approximation can theoretically be refined indefinitely. Doing so yields the approximations to be described next.

6.4 (Bubnov-)Galerkin approximations to ν_o

Here we write $\nu_o(x)$ as

$$\nu_o(x) = \bar{w}(x) + \nu_1(x), \quad (53)$$

and note that $\nu_1(x)$ satisfies

$$\Delta\nu_1 + k^2\nu_1(x) = -k^2\bar{w} \quad x \in \Omega^e \quad (54)$$

$$\nu_1 = 0 \quad x \in \partial\Omega^e. \quad (55)$$

We approximate $\nu_1(x)$ by a (combination of) bubble shape function(s) satisfying (55):

$$\nu_1(x) \approx \sum_{b=1}^{n_b} B_b(x)\beta_b. \quad (56)$$

The coefficients β_b can be obtained by requiring (54) be satisfied weakly via a (Bubnov-) Galerkin approximation. This leads to the equations:

$$\sum_{b=1}^{n_b} K_{ab}^B \beta_b^B = -k^2 W_a^B \quad (57)$$

$$K_{ab}^B = \int_{\Omega^e} \nabla B_a(x) \cdot \nabla B_b(x) - k^2 B_a(x) B_b(x) dx \quad (58)$$

$$W_a^B = \int_{\Omega^e} B_a(x) N_B(x) dx. \quad (59)$$

We recall that $N_B(x)$ was introduced in equation (3) as one of the shape functions spanning $\bar{\mathcal{V}}$. Equation (58) can be solved on each element to determine β_b , and thus $\nu_o(x)$.

6.5 Relation to bubble functions

The above discussion points out that $\nu_o(x)$ differs from $\bar{w}(x)$ only by a bubble function. Here we investigate the relation between $\nu_o(x)$ and the use of bubbles. For simplicity, we shall neglect forcing. For sake of this discussion, we shall consider a bilinear quadrilateral element and consider augmenting this element with a quadratic bubble corresponding to a node entirely in the interior of the element. We shall denote the four “original” shape functions (without the bubble) by $N_i(x)$, $i = (1, 2, 3, 4)$. The bubble shape function will be denoted by $B_b(x)$, $b = 1, \dots, n_b$.

This leads us to the following stiffness elements:

$$k_{ij}^e = \int_{\Omega^e} \nabla N_i(x) \cdot \nabla N_j(x) - k^2 N_i(x) N_j(x) dx \quad i, j = 1, 2, 3, 4. \quad (60)$$

$$k_{ib}^e = \int_{\Omega^e} \nabla N_i(x) \cdot \nabla B_b(x) - k^2 N_i(x) B_b(x) dx \quad i = 1, 2, 3, 4; b = 1, \dots, n_b. \quad (61)$$

$$K_{ab}^B = \int_{\Omega^e} \nabla B_a(x) \cdot \nabla B_b(x) - k^2 B_a(x) B_b(x) dx \quad a, b = 1, \dots, n_b. \quad (62)$$

Thus the reduced stiffness for the bubble element can be written as

$$[\hat{k}_{ij}^e] = [k_{ij}^e] - [k_{ia}^e][K_{ab}^B]^{-1}[k_{bj}^e]. \quad (63)$$

For the sake of comparison, we now consider the element stiffness matrix that would arise from the approximation to $\nu_o(x)$ given in the previous section. Thus, with $\nu_o(x)$ given by (53) and (56), equation (27) leads to the following element stiffness matrix:

$$[k_{ij}^p] = [k_{ij}^e] - [k_{ja}^e][k_{ab}^e]^{-1}[k^2 W_b^i]. \quad (64)$$

We note that (64) is not identical to (63), nor is (63) the symmetric part of (64). The two are similar, though, and differ only in the extent that $k^2 W_b^i$ differs from k_{ib}^e . Interestingly, these differ only in the gradient terms.

7 Example in one dimension

Here we consider a simple example in one dimension utilizing linear shape functions. The element stiffness matrix is obtained from (27) with $\nu_o(x)$ given by (38). This yields

$$k_{11}^e = k_{22}^e = \frac{k \cos kh}{\sin kh} \quad (65)$$

$$k_{12}^e = k_{21}^e = \frac{-k}{\sin kh} \quad (66)$$

We consider a problem on the unit interval ($x \in (0, 1)$) with $k = 80$, subject to the boundary conditions

$$u(0) = 1 \quad ; \quad u'(1) = 0. \quad (67)$$

We choose a mesh of 50 randomly sized elements. The largest and smallest values of kh in the mesh are 3.04 and 0.16, respectively.

A plot of the results are shown in the figure. We note that nodal exactness is obtained for any degree of mesh distortion.

8 Conclusions

We have developed a stabilized Petrov-Galerkin formulation for the Helmholtz equation. Our starting goal was to find an H^1 optimal projection of $u(x)$ onto a given finite element basis. This seems to be a logical starting point for the development of stabilized and bubble methods, as well as a logical target for stabilized methods to try to obtain.

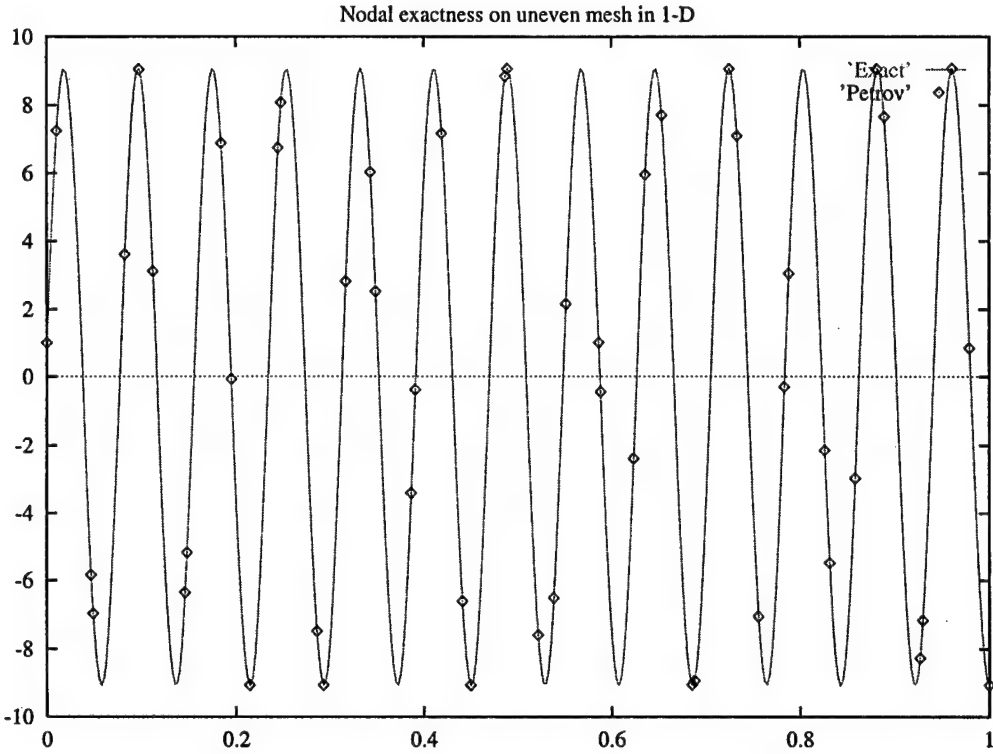


Figure 1: Exact solution compared to nodal values of FEM approximation

Our formulation achieves nearly H^1 optimality in any dimension, and exact H^1 optimality in one dimension. We have demonstrated the nodal exactness of the method in one dimension in a numerical example. (It is easy to prove nodal exactness in one dimension since the Green's function can be represented by a combination of weighting functions.)

The weighting functions to be used in our Petrov-Galerkin formulation depend on the choice of basis of the trial solution space. In particular, the weighting functions $\nu_o(x)$ must satisfy equations (18-20). In one dimension, we have described $\nu_o(x)$ exactly (for piecewise linear shape functions). We have also described a method to approximate $\nu_o(x)$ for applications in higher dimensions. Further work is required to test the usefulness of the approximate $\nu_o(x)$ functions described in section 6.

9 Acknowledgement

This work is supported financially by the Office of Naval Research.

10 References

References

- [1] T. J. R. Hughes. Multiscale phenomena: Green's functions, the Dirichlet-to-Neumann formulation, subgrid scale models, bubbles, and the origins of stabilized methods. *Computer Methods in Applied Mechanics and Engineering*, 1995. Accepted.
- [2] T.J.R. Hughes. *The Finite Element Method*. Prentice-Hall, Englewood Cliffs, 1987.

C.9 Acoustic Scattering Calculations by a Hybrid Asymptotic Numerical Method

Joshua M. Montgomery, Acoustic Scattering Calculations by a Hybrid Asymptotic Numerical Method. M.Sc. Thesis, Boston University, Dept. of Aerospace & Mechanical Eng., Boston, MA. 1997.

BOSTON UNIVERSITY
COLLEGE OF ENGINEERING

THESIS

ACOUSTIC SCATTERING CALCULATIONS BY A HYBRID
ASYMPTOTIC-NUMERICAL METHOD

BY

JOSHUA M. MONTGOMERY

Bachelor of Science, Physics, University of Puget Sound, 1994

Bachelor of Arts, Mathematics, University of Puget Sound, 1994

Submitted in partial fulfillment of the

requirements for the degree of

Master of Science

1997

Acknowledgments

I would like to express my sincere appreciation to those who have contributed towards the success of this project:

Professor Paul E. Barbone for his seemingly endless guidance and support. His experience and insight have been an invaluable asset. I am truly grateful for the opportunity to have worked with him and look forward to future collaboration.

Professor Isaac Harari for teaching me the Finite Element Method as well as for his direct collaboration on this project.

Professor Allan Pierce for expanding my understanding of and appreciation for the theory of acoustics. His guidance and teaching were instrumental in my research.

Professors Guido Sandri and Ray Nagem for believing in my ability as a scientist. Their passion for education is truly inspirational.

Professors Ali Nadim and Leopold Felsen for their efforts as members of my thesis committee and for challenging me in their teaching.

Dr. Ofer Michael for his interest in this work and his assistance in many aspects of the numerical simulations.

Brian Collins, Brian Rush, and Aravind Cherukuri for their support and insight, the examples of which are too numerous and diverse to possibly mention.

This work was supported by the Office of Naval Research.

ACOUSTIC SCATTERING CALCULATIONS BY A HYBRID
ASYMPTOTIC-NUMERICAL METHOD

JOSHUA M. MONTGOMERY

Boston University, College of Engineering, 1997

Major Professor: Paul E. Barbone

Assistant Professor of: Mechanical Engineering

Abstract

We develop and apply a hybrid asymptotic-finite element method to the problem of acoustic scattering from two-dimensional, submerged objects. The hybrid method is based on patching a short-wavelength asymptotic expansion of the scattered field to a finite element interpolation of the near field. In patching, the diffracted field shape functions with unknown amplitude are forced to agree smoothly with the solution in the near field along a specified curve. This curve is chosen to contain any local diffraction points. This procedure allows us to replace the original boundary value problem with an asymptotically equivalent boundary value problem, the domain of which is small and efficiently discretized. A new hybrid finite element on this artificial boundary represents the effect of the outer domain on the solution within this new boundary. The method is applied to diffraction and scattering by a blunted wedge, which in this context represents a degenerate prism. The hybrid solutions are compared to two bench-mark solutions: an exact analytic solution and a numerical solution found using an exact Dirichlet-to-Neumann map.

Contents

1	Introduction	1
2	Formulation	4
2.1	Motivation	5
2.2	Model Problem	6
3	Asymptotic Expansion Method	9
3.1	Outer Asymptotic Expansion: Geometrical Theory of Diffraction	10
3.1.1	Outer Solution	11
3.1.2	Boundary Layer Theory	12
3.2	Inner Asymptotic Expansion: A Canonical Problem	15
3.3	Patching vs. Matching	16
3.3.1	Matching	17
3.3.2	Patching	19
3.3.3	Error Analysis	20
4	Variational Formulation for FEM Solution	22
4.1	Strong Formulation	23

4.2	Weak Formulation	24
4.3	Hybrid Formulation	27
4.3.1	Cylindrical Wave Field	27
4.3.2	Cylindrical and Plane Wave Fields	28
5	Hybrid Finite Element Formulation	31
5.1	Diffracted Field	33
5.1.1	FEM Formulation	33
5.1.2	DtN Representation	35
5.1.3	Results	36
5.2	Scattered Field	40
5.2.1	Plane Wave Contributions	40
5.2.2	FEM Formulation	42
5.2.3	Results	43
6	Error Analysis	50
6.1	Dispersion Error	51
6.2	Patching Error	52
6.3	Optimal Location of the Artificial Boundary	53
7	Conclusions	59
A	Boundary Conditions and Surface Waves	62
A.1	Fluid Loaded Elastic Plate	63
A.1.1	Formulation	64

A.1.2	Surface Wave Contributions	66
A.2	Impedance Boundary Condition	70
A.3	Summary	72
B	Exact Analytical Representation	74
C	Stationary Phase	78

Chapter 1

Introduction

We describe a hybrid method for scattering calculations which combines short-wavelength asymptotics with the finite element method. In the hybrid approach, we attempt to draw on the benefits from both methods while eliminating their largest individual deficiencies. For example, an asymptotic approach can be computationally efficient for acoustically large scatterers; however, its applicability is limited since diffraction coefficients are unavailable for geometries with anything but simple discontinuities. Traditional numerical methods, on the other hand, can accommodate arbitrary geometries but are practically limited by their computational cost.

The hybrid method is related to the method of matched asymptotic expansions (MAE) where, in the short wavelength limit, the scattered field contains two asymptotic regions [1]. In the inner (local) region, the full Helmholtz equation must be solved. In the outer (global) region, the field can be found by means of the Geometrical Theory of Diffraction (GTD) [2]. The representation of the outer field is written in terms of certain unspecified amplitude functions called ‘diffraction coefficients.’ In the MAE method, the solutions in the two regions would be asymptotically matched, thus determining these coefficients.

In the hybrid method, on the other hand, the inner solution is found numerically and is patched smoothly to the outer asymptotic approximation. The patching is imposed on an artificial boundary, Γ_R , which is introduced around diffraction regions. This boundary is chosen to be located in an ‘overlap domain’ where both the inner and outer solutions are valid. Patching the inner and outer fields on Γ_R is equivalent to using the GTD solution to specify a radiation boundary condition for the inner numerical problem. Thus, we replace the original boundary value problem (b.v.p.) with an asymptotically equivalent one.

We discuss the hybrid formulation in detail in its application to scattering from a trun-

cated wedge. In this example, the wedge represents a degenerate case of a simple two dimensional object. We begin by obtaining asymptotic approximations to the inner and outer fields. We seek a complete representation of the outer field which we specify on Γ_R . We obtain the inner asymptotic solution and discuss the issue of patching these fields together as opposed to matching them.

We then describe a weak formulation of the asymptotically equivalent b.v.p. as part of a finite element implementation. Here, we enforce the radiation boundary condition by introducing a new ‘hybrid’ finite element. The results from the hybrid method, utilizing this new element, are then compared to a reference calculation of the field. In one case, we compare the computed diffracted field to that found by means of an exact Dirichlet-to-Neumann (DtN) map[3]. In another case, we compare the entire scattered field to an exact analytic solution of the blunted wedge.

Chapter 2

Formulation

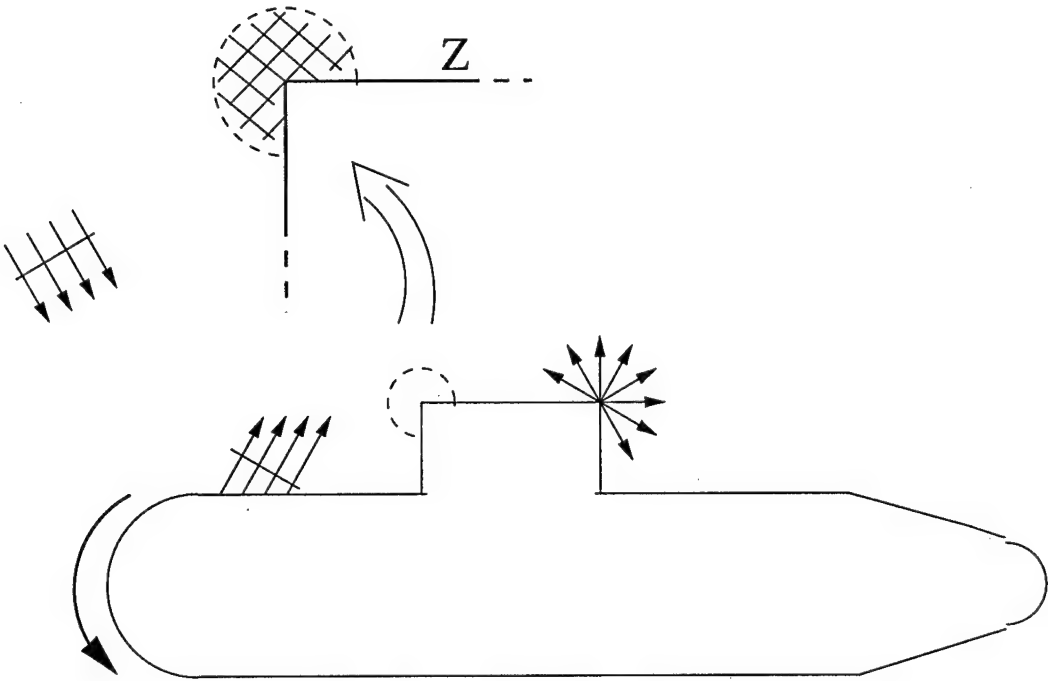


Figure 2.1: Example of a complex, submerged elastic structure

The hybrid method is motivated by a desire to compute acoustic fields scattered by complex, submerged elastic structures which are large in comparison to a wavelength. Scattering from these objects gives rise to a number of interesting phenomena which can be difficult to model. Such aspects include reflection from smooth surfaces, diffraction from geometric discontinuities, and surface waves which propagate along fluid-elastic interfaces (see Figure 2.1).

2.1 Motivation

To solve such a complicated problem analytically would require information about the field near the diffraction points. In order to solve the problem using the Finite Element

Method, on the other hand, the domain exterior to the object must be discretized with enough elements per wavelength to sufficiently represent the solution. As the wavelength of the incident field decreases or as the size of the object increases, the number of elements required also increases. Thus, in the limit of a well refined mesh, the computational cost of the problem can become unmanageable.

In the hybrid method, we propose a combination of these two approaches. The local regions around the diffraction points are discretized and the field there is found numerically. The field in the rest of the domain is represented using the Geometrical Theory of Diffraction.

We examine the field in the short wavelength limit, where the diffracted field evolves rapidly in the spatial domain. Because of this, each diffraction point can be examined in isolation from the rest of the object (Figure 2.1). We then replace the large complicated object with a canonical problem of an infinite wedge with impedance boundaries. The impedance condition is chosen because it is the simplest boundary condition that can exhibit some of the same wave phenomena as an elastic boundary (see Appendix A).

2.2 Model Problem

We imagine the wedge, of exterior angle β , positioned such that the tip coincides with the origin while one face lies on the positive x-axis. The tip is blunted by a truncation described by $r = a(\theta)$ (see figure 2.2). We assume that the maximum of $a(\theta)$ is on the order of a wavelength. Thus, $a(\theta) = O(k^{-1})$ or $ka = O(1)$. We let l be a predetermined distance from the tip with which we non-dimensionalize all of our spatial coordinates. Then in the limit

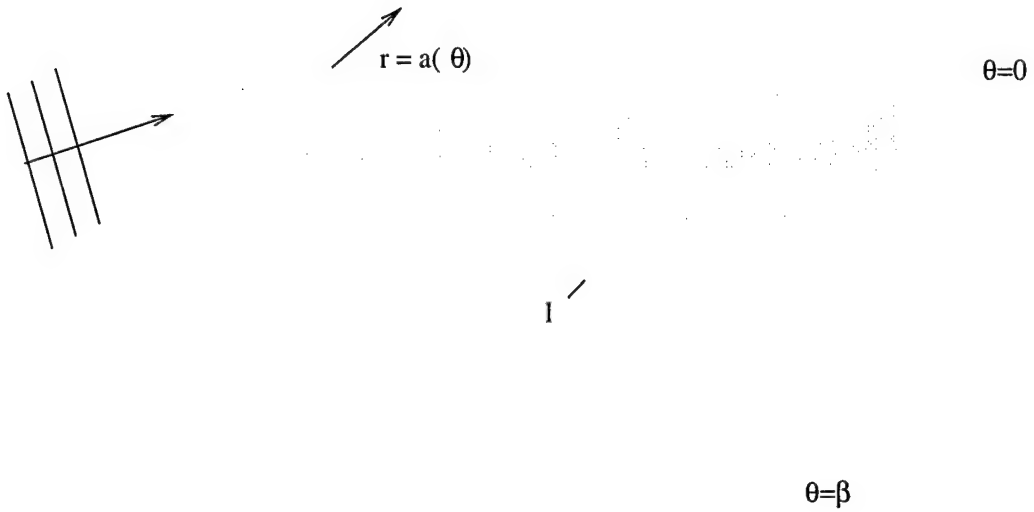


Figure 2.2: Blunted wedge with incident plane wave

as $kl \rightarrow \infty$, the wedge appears to be acoustically infinite.

In all that follows we will work in terms of non-dimensionalized coordinates as well as wavenumber, k . We shall also work in terms of a time harmonic acoustic pressure:

$$p(x, y, t) = \Re\{u_{\text{tot}}(x, y)e^{-i\omega t}\} \quad (2.1)$$

The time dependence will be suppressed from here on. The total field is then represented as the sum of an incident plane-wave and scattered field contributions:

$$u_{\text{tot}} = u_{\text{inc}} + u \quad u_{\text{inc}} = e^{ik(x \cos \theta' + y \sin \theta')} \quad (2.2)$$

In the absence of sources, u is governed by the reduced wave equation

$$(\Delta + k^2)u = 0. \quad (2.3)$$

We first consider a wedge with soft faces, such that $u_{\text{tot}} = 0$ on the wedge. This is a limiting

case of infinite impedance. Equation (2.2) then yields:

$$u = -u_{\text{inc}} \text{ on } \begin{cases} r = a(\theta) \\ \theta = 0 & r \geq a(0) \\ \theta = \beta & r \geq a(\beta) \end{cases} \quad (2.4)$$

Further, the scattered field must satisfy a radiation condition at $r = \infty$.

Chapter 3

Asymptotic Expansion Method

We seek a solution to the problem of scattering from this truncated wedge. We begin by finding asymptotic approximations to both the inner and outer fields. The inner expansion will be useful in analyzing the method of patching. We will compare the solution found by patching to that found by matching in order to obtain an asymptotic error estimate. Because it is used directly in the hybrid method, we begin by examining the outer field.

3.1 Outer Asymptotic Expansion: Geometrical Theory of Diffraction

We assume a solution to the outer problem of the form

$$u(\mathbf{x}) \sim z(\mathbf{x}, k) e^{iks(\mathbf{x})} \quad k \rightarrow \infty. \quad (3.1)$$

Here $z(x)$ is the amplitude, k is the wave number, and $s(x)$ is the phase. Substituting this solution (3.1) into the reduced wave equation (2.3) yields

$$-k^2[(\nabla s)^2 - 1]z + 2ik\nabla s \cdot \nabla z + ikz\Delta s + \Delta z = 0 \quad (3.2)$$

To solve this for large values of k , we assume that z can be expanded in an asymptotic series in inverse powers of ik :

$$z(\mathbf{x}, k) \sim \sum_{m=0}^N z_m(\mathbf{x})(ik)^{-m} + o(k^{-N}) \quad (3.3)$$

In the limit as $k \rightarrow \infty$, we can truncate this series with negligible error. Inserting (3.3) into (3.2) and equating powers of k yields the eiconal equation

$$(\nabla s)^2 = 1 \quad (3.4)$$

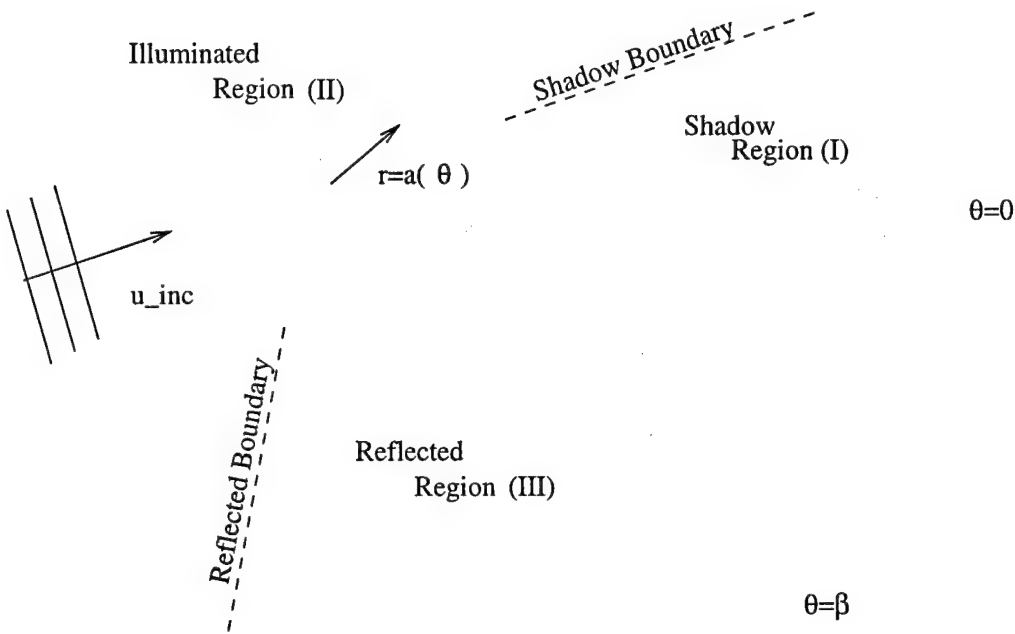


Figure 3.1: Illuminated and Shadow Regions

and the transport equations

$$2\nabla s \cdot \nabla z_m + z_m \Delta s = -\Delta z_{m-1} \quad m = 0, 1, 2, \dots \quad (3.5)$$

where $z_n = 0$ for $n < 0$. These equations can be solved using the Geometrical Theory of Diffraction [2].

3.1.1 Outer Solution

The Geometrical Theory of Diffraction shows that the scattered field can be expressed as the sum of a reflected plane wave, a shadow wave, a diffracted cylindrical wave, plus higher order terms

$$u \sim u_{\text{refl}} + u_{\text{shad}} + u_{\text{diff}} + O(k^{-\frac{3}{2}}) \quad (3.6)$$

In terms of an angle $\theta^R = 2\beta - 2\pi - \theta'$, these contributions can be expressed as the following:

$$\begin{aligned}
u_{\text{shadow}} &= \begin{cases} -e^{ik(x \cos \theta' + y \sin \theta')} & \theta < \theta' \\ 0 & \theta > \theta' \end{cases} \\
u_{\text{refl}} &= \begin{cases} -e^{ik(x \cos \theta^R + y \sin \theta^R)} & \theta > \theta^R \\ 0 & \theta < \theta^R \end{cases} \\
u_{\text{diff}} &= \frac{D(\theta, \theta')}{\sqrt{kr}} e^{ikr} \quad \text{Everywhere}
\end{aligned} \tag{3.7}$$

The function $D(\theta, \theta')$ is not yet determined. It represents the amplitude of the field diffracted in the θ -direction due to an incident wave in the θ' -direction. It is sometimes referred to as the diffraction coefficient associated with the wedge. The amplitudes of the shadow wave and reflected wave are determined by satisfying the boundary conditions on $\theta = 0, \beta$, respectively.

An immediate concern regarding this representation (3.7) is the discontinuity between the regions. In order to obtain a smooth transition across the boundaries, we make use of boundary layer theory [4]. We first examine the boundary between the shadow region and the illuminated region.

3.1.2 Boundary Layer Theory

We begin by introducing a change of coordinates:

$$\xi = x \cos \theta' + y \sin \theta' \tag{3.8}$$

$$\eta = x \sin \theta' - y \cos \theta' \tag{3.9}$$

In terms of these new variables,

$$u_{\text{shad}} \sim \mathcal{H}(\eta) e^{ik\xi} \tag{3.10}$$

Here \mathcal{H} is the Heaviside step function. This solution is clearly not valid on $\eta = 0$, where it has a discontinuity. We seek a boundary layer solution valid near $\eta = 0$ which describes the transition between the shadow and the illumination. We assume that the boundary layer solution will have the form:

$$u_{\text{b.l.}}(\xi, \eta) = w(\xi, \eta)e^{ik\xi}. \quad (3.11)$$

Inserting (3.11) into (2.3) yields:

$$\frac{\partial^2 w}{\partial \eta^2} + \frac{\partial^2 w}{\partial \xi^2} + 2ik \frac{\partial w}{\partial \xi} = 0. \quad (3.12)$$

We magnify the region near the shadow boundary to establish a local solution by introducing stretched local coordinates

$$\Xi = \xi ; H = k^{\frac{1}{2}} \eta ; W(\Xi, H) = w(\xi, \eta). \quad (3.13)$$

We insert (3.13) into (3.12) to find

$$k \frac{\partial^2 W}{\partial H^2} + \frac{\partial^2 W}{\partial \Xi^2} + 2ik \frac{\partial W}{\partial \Xi} = 0. \quad (3.14)$$

We now assume that W has the following asymptotic expansion:

$$W \sim W_0 + o(1) ; k \rightarrow \infty \quad (3.15)$$

Inserting (3.15) into (3.14) and keeping the first order in k yields the equation:

$$\frac{\partial^2 W_0}{\partial H^2} + 2i \frac{\partial W_0}{\partial \Xi} = 0 \quad (3.16)$$

Following [4], we consider a general solution of this parabolic equation (3.16) of the form

$$W_0(\Xi, H) = \int_{-\infty}^{\infty} \left[\frac{1}{\sqrt{\Xi}} e^{i(H-S)^2/2\Xi} \right] F(S) dS. \quad (3.17)$$

Here $F(S)$ is an arbitrary function. Equation (3.17) with (3.11) and (3.13) is our inner solution, valid in the region of the shadow boundary. The function F is found by matching our inner (3.17) and outer (3.10) solutions using VanDyke's matching rule [1]. We first write the inner solution in terms of outer variables

$$W_0(\xi, k^{\frac{1}{2}}\eta) = \int_{-\infty}^{\infty} [\sqrt{\frac{k}{\xi}} e^{ik(\eta-s)^2/2\xi}] f(s) ds. \quad (3.18)$$

Here we have defined the following:

$$S = k^{\frac{1}{2}} s ; F(S) = f(s) \quad (3.19)$$

We now expand (3.18) to $O(k^0)$ by the method of stationary phase:

$$W(\xi, k^{\frac{1}{2}}\eta)e^{ik\xi} \sim \sqrt{2\pi}f(\eta)e^{i\frac{\pi}{4}}e^{ik\xi} + O(k^{-\frac{1}{2}}) \quad (3.20)$$

For (3.20) to match with the outer solution (3.10) we require:

$$f(\eta) \equiv \frac{1}{\sqrt{2\pi}}e^{-i\frac{\pi}{4}}\mathcal{H}(\eta). \quad (3.21)$$

Using (3.18) and (3.21) allows the boundary layer solution to be written as

$$w(\xi, \eta) = \sqrt{\frac{k}{2\pi\xi}}e^{-i\frac{\pi}{4}} \int_0^{\infty} e^{ik(\eta-s)^2/2\xi} ds. \quad (3.22)$$

Alternatively, changing the integration variable allows us to rewrite the boundary layer solution as

$$w_{\text{b.l.}}(\xi, \eta) = \frac{1}{\sqrt{\pi}}e^{-i\frac{\pi}{4}}e^{ik\xi} \int_{-\eta\sqrt{k/2\xi}}^{\infty} e^{iz^2} dz. \quad (3.23)$$

Equation (3.23) shows that in the limit of $\|\eta\sqrt{k/\xi}\| \gg 1$ there exists a plane wave, $e^{ik\xi}$, for $\eta > 0$ and no first order contribution for $\eta < 0$. On the boundary ($\eta = 0$) the amplitude of the field is the average of the amplitudes in the two regions.

We now have a complete solution to the outer asymptotic problem. We note that the boundary layer solution has been obtained without reference to the inner diffraction problem. So we turn our attention to the inner diffraction problem and seek a similar asymptotic solution.

3.2 Inner Asymptotic Expansion: A Canonical Problem

We begin by introducing inner variables

$$R = kr ; \Theta = \theta ; U(R, \Theta) = u(r, \theta) \quad (3.24)$$

Rewriting the reduced wave equation (2.3) in polar coordinates gives the inner problem:

$$\left(\frac{\partial^2}{\partial R^2} + \frac{1}{R} \frac{\partial}{\partial R} + \frac{1}{R^2} \frac{\partial^2}{\partial \Theta^2} \right) U + U = 0 \quad (3.25)$$

$$U = -U_{\text{inc}} \text{ on } \begin{cases} R = ka(\theta) \\ \Theta = 0, \beta \quad R > ka \end{cases} \quad (3.26)$$

$$U \text{ matches } u \text{ as } R \rightarrow \infty \quad (3.27)$$

In what follows, we shall find it convenient to work in terms of $\hat{U} = U - U_{\text{sharp}}$. Here, U_{sharp} represents the field (with minimum singularity) scattered by a sharp wedge due to an incident field U_{inc} [5]. Further, U_{sharp} can be shown to match the plane wave and boundary layer solutions in the outer field. Thus, the function \hat{U} satisfies equation (3.25) as well as:

$$\hat{U} = \begin{cases} -U_{\text{inc}} - U_{\text{sharp}} & \text{on } R = ka(\theta) \\ 0 & \text{on } \Theta = 0, \beta \end{cases} \quad (3.28)$$

For a general $a(\theta)$, the solution for \hat{U} cannot be obtained in closed form. Outside $R = ka_{\max}$, however, the solution can be uniquely represented. We assume \hat{U} to be separable such that:

$$\hat{U} = F(R) G(\Theta) \quad (3.29)$$

Inserting this into the wave equation yields relations for the two separated functions:

$$\begin{aligned} G''(\Theta) + \nu G(\Theta) &= 0 \\ R^2 F''(R) + RF'(R) + (R^2 - \nu^2)F &= 0 \end{aligned} \quad (3.30)$$

Utilizing these equations with the boundary conditions on $\theta = 0, \beta$ results in the representation:

$$\hat{U}(R, \Theta) = \sum_{n=1}^{\infty} A_n H_{\nu_n}^{(1)}(R) \sin \nu_n \Theta + B_n H_{\nu_n}^{(2)}(R) \sin \nu_n \Theta \quad (3.31)$$

Here, $H_{\nu_n}^{(1)}$ and $H_{\nu_n}^{(2)}$ are the Hankel function of the first and second kind, respectively [6]. They are of order ν_n , where $\nu_n = n\pi/\beta$. The A_n are complex constants which depend on the particular details of $a(\theta)$. We seek to relate equation (3.31) to the cylindrical wave in (3.7), resulting in an expression for $D(\theta)$ in terms of A_n and B_n .

3.3 Patching vs. Matching

The method of matched asymptotic expansions requires an overlap domain in which both the inner (3.31) and outer (3.7) solutions are valid (see Figure 3.2). This domain occurs where

$$R = k^\alpha \quad 0 < \alpha < 1 \quad (3.32)$$

The hybrid method, on the other hand, relies on patching. The inner solution will be found numerically and forced to agree smoothly with the outer asymptotic solution (3.7), along Γ_R . Here Γ_R is chosen to be an arc of a circle lying in the aforementioned overlap domain.

The method of matched asymptotic expansions yields a solution which is asymptotic to the exact solution. Thus, we are guaranteed that the difference between the exact and

asymptotic solutions vanishes in the limit as $k \rightarrow \infty$. Patching on $R = const$, on the other hand, has no such asymptotic validity. Here we shall compare the directivities obtained by patching ($\hat{D}_p(\theta)$) to those obtained by matching ($\hat{D}_m(\theta)$). In particular, we shall show that patching in the overlap domain leads to the the result that

$$\hat{D}_p(\theta) \sim \hat{D}_m(\theta) ; k \rightarrow \infty. \quad (3.33)$$

3.3.1 Matching

In general, the inner and outer expansions complement each other, one being valid in the region where the other fails. In order to find a uniform first approximation, the inner and outer solutions are asymptotically matched. We denote the outer expansion of the diffracted field in terms of a cylindrical wave with unknown directivity:

$$\hat{u}_m(r, \theta) = u_m - u_{\text{sharp}} = \frac{\hat{D}_m(\theta)}{\sqrt{kr}} e^{ikr} \quad (3.34)$$

We obtain $\hat{D}_m(\theta)$ by using VanDyke's matching rule [1]. First we express the inner solution (3.31) in terms of outer variables:

Inner solution:

$$\hat{U}^{(0)}(R, \Theta) = \sum_{n=1}^{\infty} A_n^{(m)} H_{\nu_n}^{(1)}(R) \sin \nu_n \Theta + B_n^{(m)} H_{\nu_n}^{(2)}(R) \sin \nu_n \Theta \quad (3.35)$$

In outer variables:

$$\hat{U}^{(0)}(kr, \theta) = \sum_{n=1}^{\infty} A_n^{(m)} H_{\nu_n}^{(1)}(kr) \sin \nu_n \theta + B_n^{(m)} H_{\nu_n}^{(2)}(kr) \sin \nu_n \theta \quad (3.36)$$

Expand (for large k) [6] to obtain the outer expansion of the inner solution:

$$\hat{U}^{(0, -\frac{1}{2})}(kr, \theta) = \sum_{n=1}^{\infty} A_n^{(m)} \sqrt{\frac{2}{\pi kr}} e^{ikr - i\frac{\pi}{2}\nu_n - i\frac{\pi}{4}} \sin \nu_n \theta + B_n^{(m)} \sqrt{\frac{2}{\pi kr}} e^{-ikr + i\frac{\pi}{2}\nu_n + i\frac{\pi}{4}} \sin \nu_n \theta \quad (3.37)$$

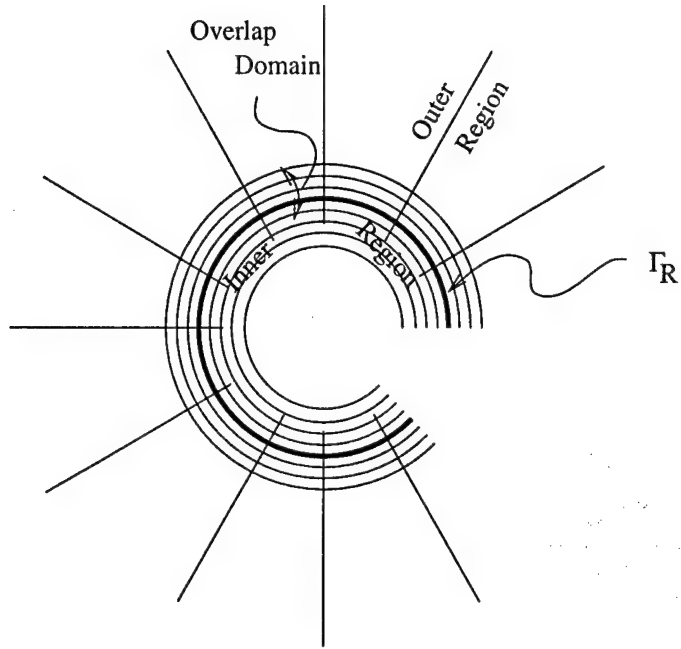


Figure 3.2: Inner and Outer Regions

Next, we find the inner expansion of the outer solution.

Outer Solution:

$$\hat{u}^{(-\frac{1}{2})}(r, \theta) = \frac{\hat{D}_m(\theta)}{\sqrt{kr}} e^{ikr} \quad (3.38)$$

Inner of outer:

$$\hat{u}^{(-\frac{1}{2}, 0)}\left(\frac{R}{k}, \Theta\right) = \frac{\hat{D}_m(\Theta)}{\sqrt{R}} e^{iR} \quad (3.39)$$

By VanDyke's matching rule [1], (3.37) and (3.39) must be equivalent. Thus

$$\hat{D}_m(\theta) = \sum_{n=1}^{\infty} \left[\sqrt{\frac{2}{\pi}} A_n^{(m)} e^{-i\frac{\pi}{2}(\nu_n + \frac{1}{2})} \right] \sin \nu_n \theta ; \quad B_n^{(m)} = 0. \quad (3.40)$$

3.3.2 Patching

We again denote the outer solution in terms of a cylindrical wave. We shall patch along the curve $R = k^\alpha r_0$, or $r = k^{\alpha-1}r_0$, where $0 \leq \alpha \leq 1$. Along this curve we enforce continuity of the field and its normal derivative:

$$\hat{u}_p(k^{\alpha-1}r_0, \theta) = \hat{U}(k^\alpha r_0, \theta) \quad (3.41)$$

$$\frac{\partial \hat{u}_p}{\partial r}(k^{\alpha-1}r_0, \theta) = k \frac{\partial \hat{U}}{\partial R}(k^\alpha r_0, \theta) \quad (3.42)$$

The first of these two conditions leads to:

$$\hat{D}_p(\theta) = \sum_{n=1}^{\infty} \sqrt{k^\alpha r_0} e^{-ik^\alpha r_0} [A_n^{(p)} H_{\nu_n}^{(1)}(k^\alpha r_0) + B_n^{(p)} H_{\nu_n}^{(2)}(k^\alpha r_0)] \sin \nu_n \theta. \quad (3.43)$$

The second condition (3.42) on Γ_R yields the relation:

$$C_k D_p(\theta) \frac{e^{ik^\alpha r_0}}{\sqrt{k^\alpha r_0}} = \sum_{n=1}^{\infty} [A_n^{(p)} H_{\nu_n}^{(1)\prime}(k^\alpha r_0) + B_n^{(p)} H_{\nu_n}^{(2)\prime}(k^\alpha r_0)] \sin \nu_n \theta. \quad (3.44)$$

$$C_k = i - \frac{1}{2k^\alpha r_0} \quad (3.45)$$

We recall that matching the two solutions resulted in $B_n^{(m)} = 0$ (3.40). We expect a similar result in patching, such that B_n/A_n is asymptotically small. To find a representation for B_n , we multiply equation (3.44) by $\sin \nu_m \theta$ and integrate from 0 to β :

$$B_n^{(p)} = \frac{C_k}{H_{\nu_n}^{(2)\prime}(k^\alpha r_0)} \frac{e^{ik^\alpha r_0}}{\sqrt{k^\alpha r_0}} \frac{2}{\beta} \int_0^\beta D_p(\theta) \sin \nu_n \theta d\theta - A_n^{(p)} \frac{H_{\nu_n}^{(1)\prime}(k^\alpha r_0)}{H_{\nu_n}^{(2)\prime}(k^\alpha r_0)} \quad (3.46)$$

Using equation (3.43), we evaluate the integral in the above relation (3.46) and eliminate $D_p(\theta)$:

$$B_n^{(p)} = -\frac{C_k H_{\nu_n}^{(1)}(k^\alpha r_0) - k H_{\nu_n}^{(1)\prime}(k^\alpha r_0)}{C_k H_{\nu_n}^{(2)}(k^\alpha r_0) - k H_{\nu_n}^{(2)\prime}(k^\alpha r_0)} A_n^{(p)} \quad (3.47)$$

Since $0 < \alpha < 1$, $k^\alpha r_0 \rightarrow \infty$ as $k \rightarrow \infty$. Therefore, we can obtain an asymptotic approximation for B_n/A_n as $k \rightarrow \infty$ by expanding the Hankel functions for large argument. From [6] we have:

$$H_{\nu_n}^{(1)}(k^\alpha r_0) = \sqrt{\frac{2}{\pi}} \left[1 + i \frac{4\nu_n^2 - 1}{8k^\alpha r_0} \right] \frac{e^{ik^\alpha r_0}}{\sqrt{k^\alpha r_0}} e^{-i\frac{\pi}{2}\nu_n - i\frac{\pi}{4}} + O((k^\alpha r_0)^{-\frac{5}{2}}) \quad (3.48)$$

$$H_{\nu_n}^{(2)}(k^\alpha r_0) = \sqrt{\frac{2}{\pi}} \left[1 - i \frac{4\nu_n^2 - 1}{8k^\alpha r_0} \right] \frac{e^{-ik^\alpha r_0}}{\sqrt{k^\alpha r_0}} e^{i\frac{\pi}{2}\nu_n + i\frac{\pi}{4}} + O((k^\alpha r_0)^{-\frac{5}{2}}) \quad (3.49)$$

Using these expansions, we can express the ratio of the constants in the following way:

$$\frac{B_n^{(p)}}{A_n^{(p)}} = \frac{N(\nu_n)(k^\alpha r_0)^{-5/2} e^{ik^\alpha r_0} + o((k^\alpha r_0)^{-5/2})}{D(\nu_n)(k^\alpha r_0)^{-1/2} e^{-ik^\alpha r_0} + O((k^\alpha r_0)^{-3/2})} = O((k^\alpha r_0)^{-2}) \quad (3.50)$$

As expected, we find that the contributions from the B_n terms are asymptotically small in comparison to the A_n terms. Equation (3.50) and linearity of the problem implies that

$$A_n^{(m)} = A_n^{(p)} + O((k^\alpha r_0)^{-2}) \equiv A_n \quad (3.51)$$

3.3.3 Error Analysis

We measure the error in patching as the difference between $\hat{D}_m(\theta)$ in equation (3.40) and $\hat{D}_p(\theta)$ in equation (3.43). Thus, we define the following function:

$$\text{error}(\theta) = \sum_n E_n \sin \nu_n \theta \equiv \hat{D}_m(\theta) - \hat{D}_p(\theta). \quad (3.52)$$

Substituting equations (3.43), (3.40), and (3.51) into equation (3.52) leads to:

$$E_n = A_n \left[\sqrt{\frac{2}{\pi}} e^{-i\frac{\pi}{2}\nu_n - i\frac{\pi}{4}} - \sqrt{k^\alpha r_0} e^{-ik^\alpha r_0} H_{\nu_n}^{(1)}(k^\alpha r_0) \right] + O((k^\alpha r_0)^{-2}). \quad (3.53)$$

Using equation (3.48) to expand the Hankel functions, we find an asymptotic approximation for the error:

$$E_n \sim i A_n \sqrt{\frac{2}{\pi}} \frac{4\nu_n^2 - 1}{8k^\alpha r_0} e^{-i\frac{\pi}{2}\nu_n - i\frac{\pi}{4}} + O((k^\alpha r_0)^{-2}) \quad (3.54)$$

Clearly, as $k \rightarrow \infty$, $E_n \rightarrow 0$. We note, however, that since $\nu_n \sim n$, there is a potential for E_n to grow like n^2 for kr_0 fixed.

We must now examine the constants, A_n , to see if this is the case. We examine the series [8]

$$U_o = \sum_{n=1}^{\infty} A_n \sin \nu_n \Theta H_{\nu_n}^{(1)}(R) \quad (3.55)$$

for arbitrary but fixed values of R and θ . We assume that this series converges, and thus conclude that the constants A_n must compensate for the dependence of the Hankel functions on n . In the limit of large n , we can express this dependence as [6]:

$$H_{\nu_n}^{(1)}(kr) \sim \left[\left(\frac{e kr}{2\nu_n} \right)^{\nu_n} - i2 \left(\frac{e kr}{2\nu_n} \right)^{-\nu_n} \right] / \sqrt{2\pi\nu_n} = O(\nu_n^{\nu_n}) \quad \nu_n \rightarrow \infty \quad (3.56)$$

which clearly grows without bounds for large ν_n . In order for our series (3.55) to converge, we require that

$$A_n = o(\nu_n^{-\nu_n}) \quad \nu_n \rightarrow \infty \quad (3.57)$$

Thus we see that our error coefficients are not only small in the limit of large k , but vanish in the limit of large ν_n as well.

Chapter 4

Variational Formulation for FEM

Solution

Up to now we have considered a typical MAE approach in examining the asymptotic aspects of the hybrid method. Here we discuss a numerical formulation suitable for determining the inner solution. By patching, we use the outer solution to formulate a radiation boundary condition along the artificial boundary. In this chapter, we discuss the strong and weak formulations used and follow this by discussing the hybrid finite element implementation [10].

4.1 Strong Formulation

We now describe a weak formulation of our boundary value problem that is suitably incorporated into our hybrid method. We denote the region outside of the scatterer by Ω . We further denote the ‘internal’ boundary of Ω by Γ_{im} and assume it to be piecewise smooth. On Γ_{im} we shall impose an impedance boundary condition. This allows for a boundary that supports surface waves, yet also provides the simple limits of a hard or a soft boundary.

The classical or strong form of the problem is to find u in $\overline{\Omega}$ such that:

$$(\Delta + k^2)u = -f \text{ in } \Omega \quad (4.1)$$

$$\frac{\partial u}{\partial n} + Zu = -\frac{\partial u_{inc}}{\partial n} - Zu_{inc} \text{ on } \Gamma_{im} \quad (4.2)$$

$$u = \text{outgoing as } r \rightarrow \infty \quad (4.3)$$

The unbounded domain Ω is decomposed by an artificial boundary Γ_R into a bounded inner domain Ω^i and its unbounded outer complement Ω^o . The solution to the original b.v.p. is decomposed into an inner and an outer field:

$$u = \begin{cases} u^i & \text{on } \Omega^i \\ u^o & \text{on } \Omega^o \end{cases} \quad (4.4)$$

We assume that the forcing, f , vanishes in the outer field. Further, we enforce the continuity of the solution across Γ_R weakly in a variational setting.

4.2 Weak Formulation

Following [11], we define the functional of our weak formulation:

$$\Pi(u, \lambda) = \frac{1}{2}a(u^i, u^i) + \frac{1}{2}a(u^o, u^o) - L(u^i) - L(u^o) + (\lambda, u^i - u^o)_{\Gamma_R}. \quad (4.5)$$

$$a(\omega, u) = \int_{\Omega} (\nabla \omega \cdot \nabla u - \omega k^2 u) d\Omega - \lim_{r \rightarrow \infty} \int_{\Gamma_r} i\omega k u d\Gamma + \int_{\Gamma_{im}} \omega Z u d\Gamma \quad (4.6)$$

$$(\omega, u)_{\Gamma_R} = \int_{\Gamma_R} \omega u d\Gamma \quad (4.7)$$

$$L(\omega) = \int_{\Omega} \omega f d\Omega - \int_{\Gamma_{im}} \omega (Z u_{\text{inc}} + \frac{\partial u_{\text{inc}}}{\partial n}) d\Gamma \quad (4.8)$$

Here, λ represents a Lagrange multiplier, introduced to enforce continuity across the artificial boundary. We restrict our choice of functions such that:

$$|a(u, u)| < \infty \quad (4.9)$$

For the purposes of this discussion, we employ the method of limiting absorption. That is, we allow the natural wavenumber of the fluid to contain a small imaginary part:

$$k = k_0(1 + i\alpha) \quad \alpha \ll 1. \quad (4.10)$$

Next, we perform the integration over the boundary at infinity, which we now denote by Γ_∞ . We then take the limit as $\alpha \rightarrow 0$. Assuming that our outer solution is of a cylindrical wave form:

$$u, \omega \sim \frac{e^{ikr}}{\sqrt{kr}} \quad (4.11)$$

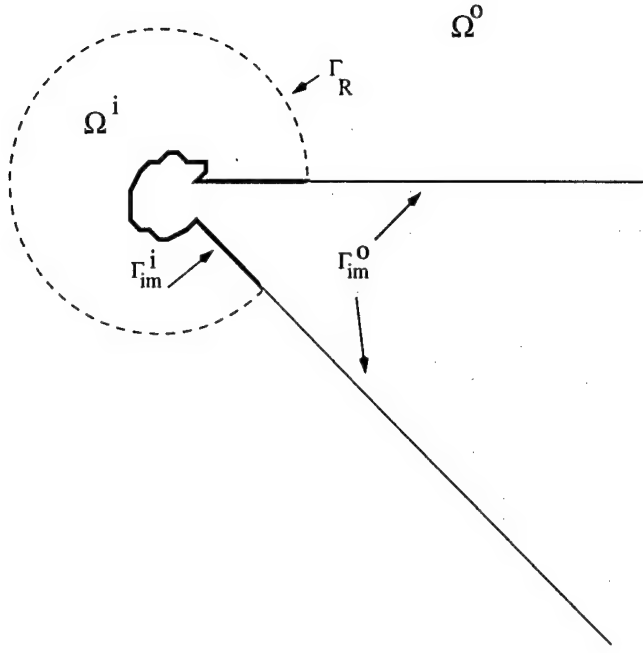


Figure 4.1: Boundaries and Domains for the Hybrid Formulation

then the integral over Γ_∞ in equation (4.6) becomes

$$\int_{\Gamma_\infty} i\omega k u \, d\Gamma \sim \lim_{r \rightarrow \infty} \int_0^{2\pi} ik \frac{e^{i2k_0 r}}{kr} e^{-2\alpha k_0 r} r \, d\theta = 0. \quad (4.12)$$

Subject to the constraint of equation (4.9), we seek to find the functions u and corresponding Lagrange multiplier λ that render $\Pi(u, \lambda)$ stationary. We examine the variation in the Lagrange multiplier:

$$\frac{\delta \Pi}{\delta \lambda} = \lim_{\varepsilon \rightarrow 0} \frac{\partial}{\partial \varepsilon} (\Pi(u, \lambda + \varepsilon \nu)) = 0 \quad (4.13)$$

which leads to a condition enforcing continuity of the solution across Γ_R :

$$(\nu, u^i - u^o)_{\Gamma_R} = 0 \quad (4.14)$$

We then examine the variation in the trial solution:

$$\frac{\delta \Pi}{\delta u} = \lim_{\varepsilon \rightarrow 0} \frac{\partial}{\partial \varepsilon} (\Pi(u + \varepsilon \omega, \lambda)) = 0 \quad (4.15)$$

Utilizing the arbitrariness of the weighting functions, equation (4.15) yields the relations:

$$\begin{aligned} a(\omega^o, u^o) - (\lambda, \omega^o)_{\Gamma_R} &= L(\omega^o) \\ a(\omega^i, u^i) + (\lambda, \omega^i)_{\Gamma_R} &= L(\omega^i) \end{aligned} \quad (4.16)$$

Examining the first equation, we obtain the following:

$$\begin{aligned} \int_{\Omega^o} (\nabla \omega^o \cdot \nabla u^o - \omega^o k^2 u^o) d\Omega - \int_{\Gamma_\infty} i\omega^o k u^o d\Gamma \\ + \int_{\Gamma_{im}^o} \omega^o (Z u^o + Z u_{inc} + \frac{\partial u_{inc}}{\partial n^o}) d\Gamma - \int_{\Gamma_R} \lambda \omega^o d\Gamma = 0 \end{aligned} \quad (4.17)$$

We define the boundary of Ω^o as $\Gamma^o = \Gamma_R + \Gamma_{im}^o + \Gamma_\infty$. We note that:

$$\nabla \cdot (\omega^o \nabla u^o) = \nabla \omega^o \cdot \nabla u^o + \omega^o \Delta u^o. \quad (4.18)$$

We now use equation (4.18) in (4.17), and employ Gauss' integral theorem to obtain:

$$\begin{aligned} - \int_{\Omega^o} \omega^o (\Delta u^o + k^2 u^o) d\Omega + \int_{\Gamma_\infty} \omega^o (\frac{\partial u^o}{\partial n^o} - iku^o) d\Gamma + \int_{\Gamma_R} \omega^o (\frac{\partial u^o}{\partial n^o} - \lambda) d\Gamma \\ + \int_{\Gamma_{im}^o} \omega^o (\frac{\partial u^o}{\partial n^o} + Z u^o + \frac{\partial u_{inc}}{\partial n^o} + Z u_{inc}) d\Gamma = 0 \end{aligned} \quad (4.19)$$

Because ω^o is arbitrary, we require each of the integrands to equal zero independently. The first two terms in equation (4.19) require u^o to satisfy the Helmholtz equation as well as a radiation condition:

$$(\Delta + k^2) u^o = 0 \quad (4.20)$$

$$\lim_{r \rightarrow \infty} r^{1/2} (\frac{\partial u^o}{\partial r} - iku^o) = 0 \quad (4.21)$$

Next, u^o must satisfy the impedance condition on the boundary of the scatterer which is contained in the outer field:

$$\frac{\partial u^o}{\partial n^o} + Z u^o = -\frac{\partial u_{inc}}{\partial n^o} - Z u_{inc} \quad \text{on } \Gamma_{im}^o. \quad (4.22)$$

A final condition yields an expression for the Lagrange multiplier, and we assume an analogous relation for the weighting function:

$$\lambda = \frac{\partial u^o}{\partial n^o} ; \quad \nu = \frac{\partial \omega^o}{\partial n^o} \quad (4.23)$$

We now choose u^o to satisfy equations (4.20-4.22) and eliminate λ and ν using (4.23).

Equations (4.14) and (4.16) thus reduce to:

$$a(u^i, \omega^i) + (\frac{\partial u^o}{\partial n^o}, \omega^i)_{\Gamma_R} = L(\omega^i) \quad (4.24)$$

$$(\frac{\partial \omega^o}{\partial n^o}, u^i)_{\Gamma_R} - (\frac{\partial \omega^o}{\partial n^o}, u^o)_{\Gamma_R} = 0 \quad (4.25)$$

This is our weak formulation. In this formulation, we integrate only over the bounded domain and the artificial boundary. In the hybrid method, the outer solution u^o is represented by a set of functions which asymptotically satisfy the wave equation. This solution is determined by the GTD representation discussed in Chapter 3.

4.3 Hybrid Formulation

4.3.1 Cylindrical Wave Field

We introduce the hybrid formulation by considering the simple problem of computing the diffracted field \hat{u} . We specify the outer field using equation (3.38):

$$\hat{u}^o \sim D(\theta) \sqrt{\frac{r_0}{r}} e^{ik(r-r_0)} \quad (4.26)$$

$$\hat{w}^o \sim \tilde{D}(\theta) \sqrt{\frac{r_0}{r}} e^{ik(r-r_0)} \quad (4.27)$$

Substituting equations (4.26)-(4.27) into equation (4.24)-(4.25) yields a weak form for u^i with arbitrary ω^i :

$$\int_{\Omega^i} (\nabla \omega^i \cdot \nabla u^i - \omega^i k^2 u^i) d\Omega + \int_{\Gamma_{im}^i} Z \omega^i u^i d\Gamma - \int_0^\beta ikr_0 D(\theta) \omega^i d\theta = 0 \quad (4.28)$$

$$- \int_0^\beta ikr_0 \tilde{D}(\theta) u^i d\theta + \int_0^\beta ikr_0 D(\theta) \tilde{D}(\theta) d\theta = 0 \quad (4.29)$$

4.3.2 Cylindrical and Plane Wave Fields

We now examine the hybrid formulation for the full scattered field, including reflected plane waves, shadow forming plane waves, and surface waves. The shadow and reflected waves are dependent on the characteristic angles associated with the shadow (θ^S) and reflected (θ^R) boundaries. The surface wave contributions have a similar dependence on the complex angles associated with the subsonic waves on the faces of the wedge.

We specify the outer solution to be of the form:

$$u_o \sim D(\theta) \sqrt{\frac{r_0}{r}} e^{ik(r-r_0)} + B^S(r, \theta, \theta^S) + B^R(r, \theta, \theta^R) + d_{s0} \mathcal{B}^0(r, \theta, \theta_{s0}) + d_{s\beta} \mathcal{B}^\beta(r, \theta, \theta_{s\beta}) \quad (4.30)$$

$$\omega_o \sim \tilde{D}(\theta) \sqrt{\frac{r_0}{r}} e^{ik(r-r_0)} + \tilde{d}_{s0} \mathcal{B}^0(r, \theta, \theta_{s0}) + \tilde{d}_{s\beta} \mathcal{B}^\beta(r, \theta, \theta_{s\beta}) \quad (4.31)$$

Both the B and \mathcal{B} functions exactly satisfy the wave equation. Further, they are asymptotically equivalent to functions found by boundary layer theory in Chapter 3. They contain a smooth transition from plane wave to $o(1)$ contributions across the boundary defined by their characteristic angles. The B functions match the inhomogeneous part of the boundary condition on the scatterer in equation (4.22). Knowing the incident field, we can then solve for the reflection coefficients from that equation. The \mathcal{B} functions, on the other hand, satisfy the homogeneous form of the impedance boundary condition, thus determining θ_{s0}

and $\theta_{s\beta}$. The corresponding complex coefficients, d_{s0} and $d_{s\beta}$, are unknown. They represent the amplitudes of the diffracted surface waves.

Substituting equations (4.30-4.31) into the weak form (4.24-4.25) once again yields a hybrid formulation for u^i with arbitrary ω^i :

$$A_{11} + A_{12} = F_1 \quad (4.32)$$

$$A_{21} + A_{22} = F_2 \quad (4.33)$$

where we define:

$$A_{11} = \int_{\Omega^i} (\nabla \omega^i \cdot \nabla u^i - \omega^i k^2 u^i) d\Omega + \int_{\Gamma_{im}} Z \omega^i u^i d\Gamma \quad (4.34)$$

$$A_{12} = - \int_0^\beta ikr_0 D\omega^i d\theta - \int_0^\beta (d_{s0} \frac{\partial \mathcal{B}^0}{\partial r} + d_{s\beta} \frac{\partial \mathcal{B}^\beta}{\partial r}) \omega^i r_0 d\theta \quad (4.35)$$

$$A_{21} = - \int_0^\beta ikr_0 \tilde{D}u^i d\theta - \int_0^\beta (\tilde{d}_{s0} \frac{\partial \mathcal{B}^0}{\partial r} + \tilde{d}_{s\beta} \frac{\partial \mathcal{B}^\beta}{\partial r}) u^i r_0 d\theta \quad (4.36)$$

$$A_{22} = \int_0^\beta (D + d_{s0} \mathcal{B}^0 + d_{s\beta} \mathcal{B}^\beta) (ik \tilde{D} + \tilde{d}_{s0} \frac{\partial \mathcal{B}^0}{\partial r} + \tilde{d}_{s\beta} \frac{\partial \mathcal{B}^\beta}{\partial r}) r_0 d\theta \quad (4.37)$$

$$F_1 = \int_0^\beta \left(\frac{\partial B^R}{\partial r} + \frac{\partial B^S}{\partial r} \right) \omega^i r_0 d\theta \quad (4.38)$$

$$F_2 = - \int_0^\beta (B^R + B^S) (ik \tilde{D} + \tilde{d}_{s0} \frac{\partial \mathcal{B}^0}{\partial r} + \tilde{d}_{s\beta} \frac{\partial \mathcal{B}^\beta}{\partial r}) r_0 d\theta \quad (4.39)$$

This is the hybrid formulation for the field scattered from a blunted wedge with impedance boundaries. Equations (4.32)-(4.39) define, in a weak form, the ‘asymptotically equivalent boundary value problem’ for u^i in Ω^i .

For simplicity, we examine the problem in the limit of infinite impedance, or soft boundaries:

$$\left. \begin{array}{l} \theta_{s\beta} \rightarrow \beta \\ \theta_{s0} \rightarrow 0 \end{array} \right\} \quad Z \rightarrow \infty. \quad (4.40)$$

This effectively eliminates the \mathcal{B} functions from equations (4.34)-(4.39). What remains is a hybrid formulation for the scattered field which contains both cylindrical and plane wave terms. With this formulation, as well as equations (4.28) and (4.29) for the diffracted field, we now seek to introduce finite elements and the numerical implementation of the hybrid method.

Chapter 5

Hybrid Finite Element Formulation

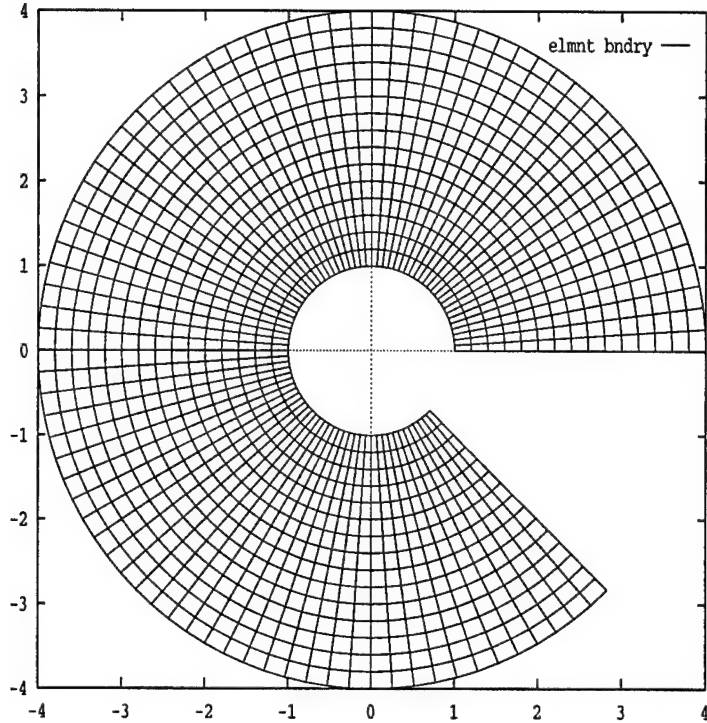


Figure 5.1: Example of the mesh used for radiation and scattering from a non-sharp soft wedge

We now turn our attention to the problem of the imperfect wedge. In order to implement our weak formulation, we express the inner and outer fields in terms of shape functions with unknown amplitudes. We choose the inner domain shape functions such that the corresponding unknowns represent the real and imaginary parts of the field.

We will implement our finite element formulation in two cases. In the first case, we shall solve for $\hat{u} = u_{\text{bl}} - u_{\text{sharp}}$. Thus u^o will contain only a cylindrical wave contribution. We then compare the hybrid solution of this diffracted field to a reference calculation found by means of an exact DtN map.

In the second case, we solve for the entire scattered field. To do so, we must first represent the plane wave contributions in the shadow and reflected regions. We combine

this with the previous representation of the diffracted field. We then compare this result to an exact analytic representation of the scattered field.

5.1 Diffracted Field

In the asymptotic outer region, we express the radial dependence of the diffracted field according to the GTD solution. The outgoing cylindrical waves are represented by exponentials, normalized with respect to the artificial boundary. The inner field and the outer angular dependence are modeled with simple piecewise linear shape functions.

5.1.1 FEM Formulation

Let N and D denote linear shape functions with local support. The field can then be represented in the context of the finite element method [10] as:

Inner Solution:

$$u^i = \sum_A d_A^i N_A^i(r, \theta) \quad (5.1)$$

$$\omega^i = \sum_A c_A^i N_A^i(r, \theta) \quad (5.2)$$

Outer Solution:

$$u^o = \sum_M d_M^o D_M^o(\theta) \sqrt{\frac{r_0}{r}} e^{ik(r-r_0)} \quad (5.3)$$

$$\omega^o = \sum_M c_M^o D_M^o(\theta) \sqrt{\frac{r_0}{r}} e^{ik(r-r_0)} \quad (5.4)$$

Here each sum is over the total number of elements in our mesh. Inserting equations (5.1-5.4) into our weak formulation (4.24-4.25) and recognizing that the c 's are arbitrary yields a matrix equation of the form:

$$K d = f. \quad (5.5)$$

K denotes a stiffness matrix, d a vector of the unknown pressures or wave amplitudes, and f a force vector. In the case of the diffracted field with plane wave incident, the force vector can be derived from the stiffness matrix, using the prescribed incident displacements.

Following this analysis, we seek an element representation of the stiffness matrix. In an element domain which lies interior to Γ_R , the stiffness is governed by the Helmholtz equation. The element stiffness for such an element is [10]:

$$K_{AB}^e = \int_{\Omega^e} \nabla N_A^i \cdot \nabla N_B^i - k^2 N_A^i N_B^i d\Omega \quad (5.6)$$

To treat the boundary condition on Γ_R we introduce what will be referred to as a ‘hybrid element.’ It has four nodes, two of which are shared with a Helmholtz element. The spatial coordinates of the two pairs of nodes match, forming what appears to be a one-dimensional element. It could be thought of as the connection between a quadrilateral element in Ω^i and an infinite element in Ω^o .

Recall that the shape functions N and D were both assumed to be linear. On the local, element domain these functions look identical. Using this, we find the following hybrid element stiffness matrix:

$$K^e = \begin{bmatrix} 0 & \kappa \\ \kappa & -\kappa \end{bmatrix} \quad (5.7)$$

where:

$$\kappa_{AB} = - \int_{\Gamma_R^e} C_0 N_A^i N_B^i d\Gamma \quad (5.8)$$

$$C_0 = (ik - \frac{1}{2r_0}) \quad (5.9)$$

5.1.2 DtN Representation

The exact DtN method is very similar to the hybrid method in its approach to infinite domain problems. Again, we introduce an artificial boundary, Γ_R , which divides the domain into inner and outer regions. We then solve the outer problem analytically and derive an exact relation between the unknown function and its derivative. This relation is imposed on Γ_R and is used as a boundary condition on the inner problem. This inner problem is then solved numerically, typically by means of the finite element method.

In a simple case, the exact boundary condition has the form:

$$u_{,n} = -Mu \quad \text{on } \Gamma_R. \quad (5.10)$$

Here u represents the unknown function and $u_{,n}$ is its normal derivative on the boundary. The operator M is called the Dirichlet-to-Neumann (DtN) map.

The constraint on the problem in the outer domain is that it must be simple enough so that the DtN map can be easily computed. This implies that a relatively simple boundary is chosen, such as a circle or a sphere. We further assume that the outer domain is ‘regular.’

We seek a DtN map suitable for our diffracted field representation on Γ_R . We express the function and its derivative as the following sums:

$$u(r_0, \theta) = \sum_{n=1}^{\infty} A_n H_{\nu_n}^{(1)}(kr_0) \sin(\nu_n \theta) \quad (5.11)$$

$$\frac{\partial u}{\partial n}(r_0, \theta) = - \sum_{n=1}^{\infty} k A_n H'_{\nu_n}^{(1)}(kr_0) \sin(\nu_n \theta). \quad (5.12)$$

We then multiply equation (5.11) by $\sin(\nu_m \theta)$ and integrate from 0 to β . This results in an expression for the unknowns:

$$A_m = \frac{2}{\beta H_{\nu_m}^{(1)}(kr_0)} \int_0^{\beta} u(r_0, \theta) \sin(\nu_m \theta) d\theta \quad (5.13)$$

We now substitute this expression into equation (5.12) and find the following representation:

$$Mu(r_0, \theta) = \sum_n k \frac{H_{\nu_n}^{(1)}(kr_0)}{\beta H_{\nu_n}^{(1)}(kr_0)} \sin(\nu_n \theta) \int_0^\beta u(r_0, \theta) \sin(\nu_n \theta) d\theta \quad (5.14)$$

This is our DtN map, valid on the artificial boundary $r = r_0$. We employ the DtN boundary condition in the variational formulation. The finite element formulation is then constructed similar to that in the hybrid method. Because we use the same discretization, any error due to mesh refinement is removed from the comparison.

5.1.3 Results

We have implemented the hybrid element and performed calculations for a wedge of angle $\beta = 7\pi/4$. The interior domain Ω^i was meshed with a minimum resolution of 10 elements per wavelength (Figure 2.2). On the blunted tip, we define $a(\theta) = a_0 = \text{constant}$, where $ka_0 = \pi$. We locate the artificial boundary, Γ_R , at $kr_0 = 4\pi$. The solution is forced by the inner boundary condition (3.28), where the infinite sum for U_{sharp} [5] is truncated with negligible error.

Our numerical interpolation is implemented twice: first we use the hybrid elements to represent the radiation boundary condition, and then we compare these results to those obtained using an exact DtN boundary condition [12]. Although error will occur due to the finite element discretization of the interior problem, we expect this error to be identical in both the hybrid element and DtN methods. Thus, any difference in the results highlights inaccuracies in the hybrid formulation.

Here we consider a plane wave incident from $\theta = 7\pi/6$. At this incident angle, we expect both a shadow and a reflected region to exist. Figure 5.2 shows the magnitude of

the pressure on Γ_R for both the hybrid element and DtN methods. The first thing we notice in comparing the two solutions is that they are hardly distinguishable from one another. The same is true when comparing the phase, although this is not shown. From these results we conclude that the hybrid and exact DtN representations compare favorably.

The shape of the curve (Figure 5.2) is another point of interest. We note that the tip blunting does not significantly displace the shadow boundary from that formed by a sharp wedge. Such a displacement would be signaled by two infinities in $\hat{D}(\theta)$. One infinity would be associated with the new position of the shadow boundary. The other would be required to cancel the shadow boundary solution in u_{sharp} .

To better interpret the shape of the previous curve, the magnitude of the pressure on Γ_R is plotted for different incident angles (Figure 5.3). In addition, we use our original numerical solution for \hat{u} , along with u_{sharp} , to construct a total field representation (Figure 5.4). The repetition in the first plot reinforces our assumption that no shadow boundary correction is present. The three ‘lobes’ represent interference between the diffracted and reflected fields, which differ from the solution to the sharp wedge. This difference is small when compared to the magnitude of the total field (Figure 5.4).

In examining the total field representation, given the original angle of incidence, we observe all of the expected phenomena. The first is our soft boundary condition, which requires the pressure to be zero on the wedge. We further observe sharp variations in the field in the reflected region due to interference between the diffracted and reflected fields. But most interesting are the smooth transitions across the shadow and reflected boundaries. In particular, we notice very small pressures in the shadow region compared to those on the other side of the shadow boundary.

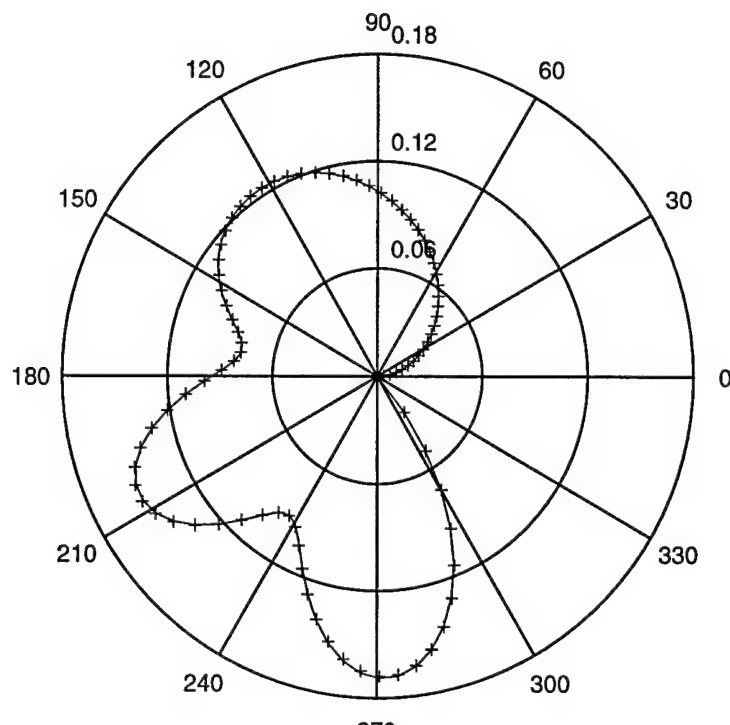


Figure 5.2: Magnitude of the pressure on Γ_R as a function of θ . Hybrid (−) compared to exact DtN (+).

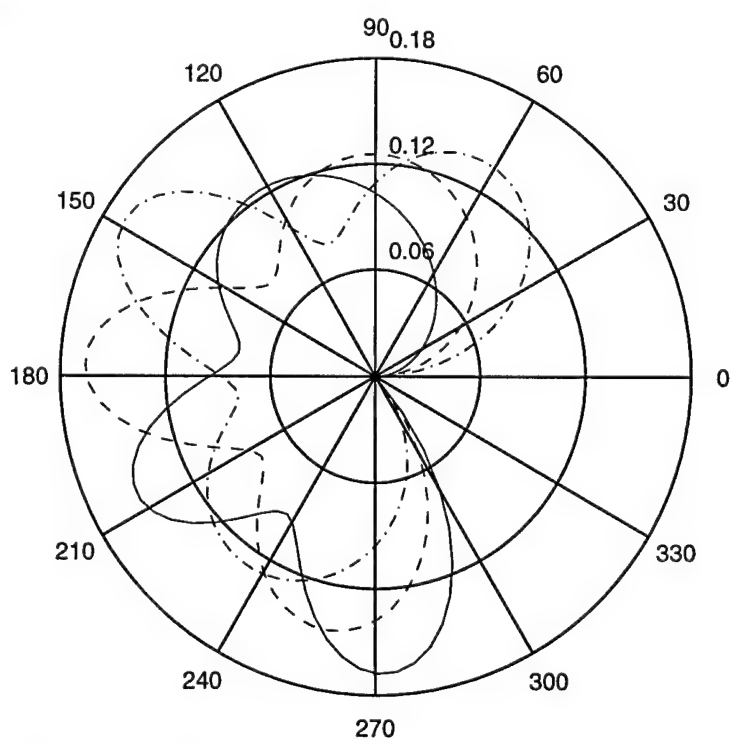


Figure 5.3: Magnitude of \hat{u} on Γ_R for incident angles: $5\pi/6$ - .-, π - -, $7\pi/6$ - .

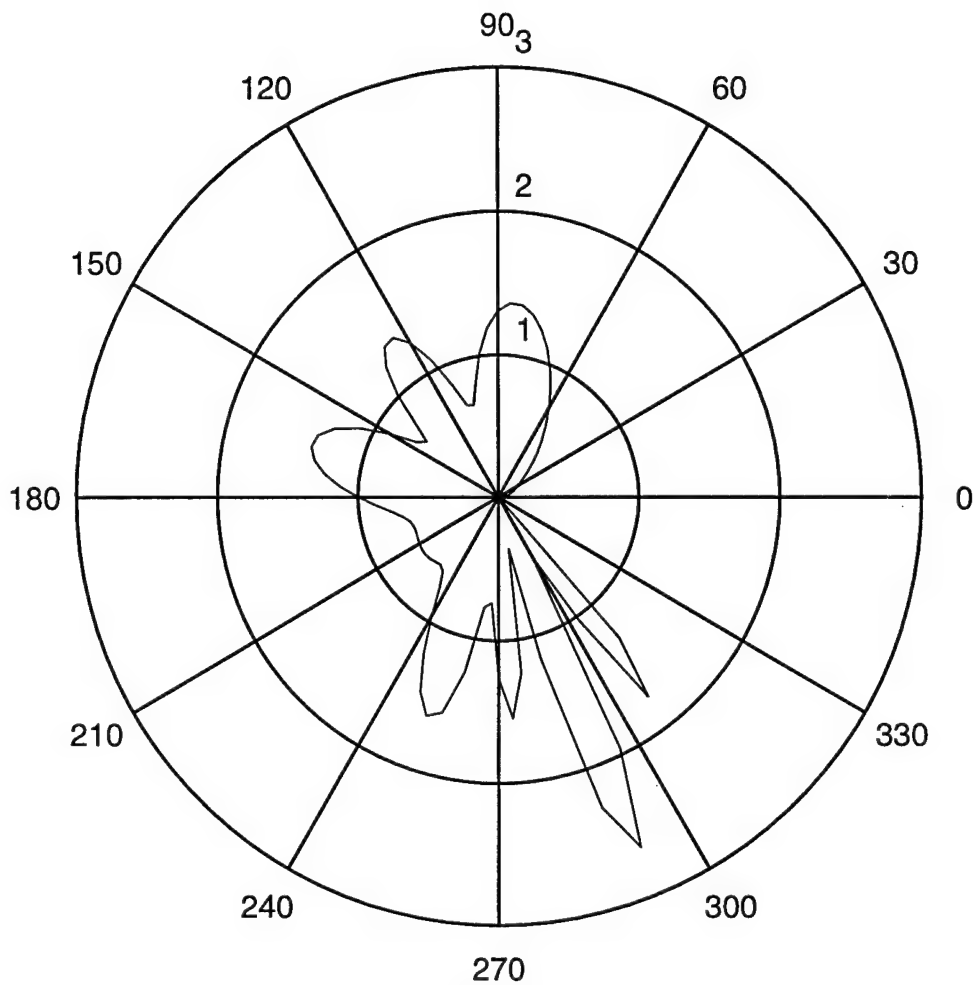


Figure 5.4: Magnitude of the total field on Γ_R , due to an incident plane wave of angle $\pi/6$ on a blunted wedge of angle $7\pi/4$.

5.2 Scattered Field

A similar approach to the problem of the diffracted field is taken to examine the full scattered field. Here we are solving for u_{bl} rather than $\hat{u} = u_{bl} - u_{sharp}$. Thus we must represent the shadow and reflected plane waves. We insert the trial solutions into the weak formulation in order to obtain element level representations for the stiffness matrix and force vector. But first we need to obtain a representation for the plane wave shape functions in the outer domain.

5.2.1 Plane Wave Contributions

To find a specific representation for the reflected and shadow forming fields, we consider the following exact solution of the Helmholtz equation [5]:

$$p_s = -\frac{1}{2}e^{ikr}w\{-e^{i\pi/4}\sqrt{2kr}\sin\frac{1}{2}(\phi - \phi^i)\} \quad (5.15)$$

$$w\{z\} = e^{-z^2} \frac{2}{\sqrt{\pi}} \int_{-iz}^{\infty} e^{-t_1^2} dt_1 = e^{-z^2} \text{erfc}(-iz) \quad (5.16)$$

In the above expression there exists a transition from plane wave to smaller order contributions in a small region about $\phi = \phi^i$. The plane wave terms exist when z in (5.16) is negative.

For the wedge, we use the above solutions to create a representation which combines a shadow forming field in the region $0 \leq \theta \leq \theta^S$ with a reflected field in the region $\theta^R \leq \theta \leq \beta$, where $\theta^R = 2\beta - 2\pi - \theta^S$. Here β still represents the exterior angle of the wedge. By recognizing the behavior of the error function in (5.16), we can express the shadow and reflected fields as the following:

$$B^S(r, \theta) = -\frac{1}{2}e^{ikr}w\{e^{i\pi/4}z_s\} \quad (5.17)$$

$$B^R(r, \theta) = -\frac{1}{2}e^{ikr}w\{e^{i\pi/4}z_r\} \quad (5.18)$$

$$z_s = \sqrt{2kr} \sin \frac{1}{2}(\theta - \theta^S) \quad (5.19)$$

$$z_r = \sqrt{2kr} \sin \frac{1}{2}(\theta^R - \theta) \quad (5.20)$$

The plane wave and cylindrical wave components are more readily apparent when examining the asymptotic approximation of equation (5.16) [6]:

$$w(z) \sim \frac{i}{\sqrt{\pi}} \left[\frac{1}{z} + \sum_{m=1}^{\infty} \frac{1 \cdot 3 \cdots (2m-1)}{2^m z^{2m+1}} \right] \quad z \rightarrow \infty, |\arg z| < \frac{3\pi}{4} \quad (5.21)$$

Equation (5.21) is valid when $z_s, z_r \gg 1$, i.e.:

$$|\sqrt{kr} \sin \frac{1}{2}(\theta - \theta^S), \sqrt{kr} \sin \frac{1}{2}(\theta - \theta^R)| \gg 1. \quad (5.22)$$

In the region where (5.22) holds, we insert (5.21) into (5.17) to find the following:

$$B^S(r, \theta) = -e^{ikr \cos(\theta^S - \theta)} + A(\theta) \frac{e^{ikr}}{\sqrt{kr}} + O((kr)^{-3/2}) \quad \theta < \theta^S \quad (5.23)$$

$$B^S(r, \theta) = A(\theta) \frac{e^{ikr}}{\sqrt{kr}} + O((kr)^{-3/2}) \quad \theta^S < \theta \quad (5.24)$$

$$A(\theta, \theta^S) = \frac{e^{i\pi/4}}{\sqrt{8\pi} \sin \frac{1}{2}(\theta^S - \theta)} \quad (5.25)$$

In the limit as θ approaches θ^S , the amplitude A of the cylindrical wave is singular to ensure that B^S is smooth across the boundary. Further, B^S has outgoing behavior in the limit as $r \rightarrow \infty$. A similar expression can be found for B^R , with the plane wave term existing in the reflected region. On the boundary of the wedge, they asymptotically satisfy the conditions:

$$B^S \sim -u_{\text{inc}} \text{ on } \theta = 0, r > a(\theta) \quad (5.26)$$

$$B^R \sim -u_{\text{inc}} \text{ on } \theta = \beta, r > a(\theta) \quad (5.27)$$

In order to implement these functions in our weak formulation, we will also need to represent their radial derivatives. Making use of the r -dependence in z we find that:

$$\frac{\partial B}{\partial r}(r, \theta) = ikB + e^{ikr} \frac{z}{2r} (izw\{e^{i\pi/4}z\} + \frac{1}{\sqrt{\pi}}e^{-i\pi/4}) \quad (5.28)$$

Now that we can represent the plane wave contributions, we turn our attention back to the finite element formulation.

5.2.2 FEM Formulation

We define our inner numerical solution in the same way as in the diffracted field case. The outer solution is then defined as:

$$u^o = d^S B^S(r, \theta) + d^R B^R(r, \theta) + \sum_M d_M^o N_M^o \sqrt{\frac{r_0}{r}} e^{ik(r-r_0)} \quad (5.29)$$

$$\omega^o = \sum_M c_m^o N_M^o \sqrt{\frac{r_0}{r}} e^{ik(r-r_0)} \quad (5.30)$$

The weighting function only contains the cylindrical wave shape function because we are taking d^S and d^R to be known. This is necessary for u^o to satisfy the essential boundary conditions (5.26-5.27) on Γ_{im}^o . We determine the values of these displacements by making use of our knowledge of the magnitude of the incident field and the boundary condition on the wedge. In our case of scattering from a soft wedge, we have $d^S = d^R = 1$.

Inserting this outer solution into the weak formulation results in an identical stiffness matrix as in the diffracted field case. Additional terms appear in the force vector. We can then express the governing equation for the hybrid degrees of freedom in the following

complex matrix notation:

$$\begin{bmatrix} 0 & 0 & K_{13} & K_{14} \\ 0 & 0 & K_{23} & K_{24} \\ K_{31} & K_{32} & -K_{33} & -K_{34} \\ K_{41} & K_{42} & -K_{43} & -K_{44} \end{bmatrix} \begin{bmatrix} d_1 \\ d_1 \\ d_3 \\ d_4 \end{bmatrix} = \begin{bmatrix} f_1 \\ f_2 \\ \hat{f}_3 \\ \hat{f}_4 \end{bmatrix} \quad (5.31)$$

Here the d 's are the complex unknowns. Recalling the definition $C_0 = ik - 1/2r_0$ allows us to write the stiffness and force contributions as:

$$K_{AB} = - \int_{\Gamma_R^e} C_0 N_A N_B d\Gamma \quad (5.32)$$

$$f_A = \int_{\Gamma_R^e} \left(\frac{\partial B^S}{\partial r} + \frac{\partial B^R}{\partial r} \right) N_A d\Gamma \quad (5.33)$$

$$\hat{f}_A = \int_{\Gamma_R^e} C_0 (B^S + B^R) N_A d\Gamma \quad (5.34)$$

In order to have some way of validating our numerical results, we seek an exact analytic solution for the field scattered from a blunted wedge. The derivation of this solution can be found in Appendix B. With this exact representation as a benchmark, we wish to examine the hybrid scattered field solution.

5.2.3 Results

We compare the hybrid solution to a nodally exact, analytic solution on $kr_0 = 4\pi$. We implement the hybrid method using the same physical parameters as in the diffracted field case. Figure 5.5 contains the real and imaginary components of these two solutions on the

artificial boundary. We first observe that the essential boundary conditions are satisfied on the faces of the wedge. We then note that the magnitude of the field is noticeably larger in the reflected region. We attribute this to the positive interference between the diffracted and reflected components of the field.

We further observe the hybrid solution to be extremely accurate everywhere on Γ_R . The regions near the shadow and reflected boundaries tend to produce the most error. However, even the error in these regions decreases as we adjust the size and refinement of our mesh.

To study the interior, we compute the scattered field for a fixed angle, along the shadow and reflected boundaries (Figure 5.6). In doing so, we observe an extremely favorable correlation between the hybrid and the exact solutions. We further notice that the magnitude on the shadow boundary remains approximately constant, while the magnitude on the reflected boundary appears to fluctuate. This could be attributed to a number of things, including interference in the reflected region or spatial decay.

We now seek to compare the hybrid solution on the artificial boundary for both the inner and outer fields. Recall that our outer solution is of the form (5.29):

$$u^o = \hat{u}^o(r, \theta) + B^R(r, \theta, \theta^R) + B^S(r, \theta, \theta^S) \quad (5.35)$$

$$\hat{u}^o = \hat{D}(\theta) \sqrt{\frac{r_0}{r}} e^{ik(r-r_0)} \quad (5.36)$$

In order for the field to be continuous across Γ_R , we require:

$$u^i(r_0, \theta) = \hat{D}(\theta) + B^R(r_0, \theta, \theta^R) + B^S(r_0, \theta, \theta^S) \quad (5.37)$$

We indeed observe an excellent correlation between the two solutions (Figure 5.7), indicating that the boundary condition on Γ_R has been enforced correctly.

Next, we wish to examine the cylindrical wave components of the scattered field. We begin by expressing the asymptotic expansion of the B functions as in Section 5.2.1:

$$B(r, \theta, \theta_c) \sim -e^{ikr \cos(\theta - \theta_c)} \mathcal{H}(\theta - \theta_c) + A(\theta, \theta_c) \frac{e^{ikr}}{\sqrt{kr}} + O((kr)^{-3/2}) \quad (5.38)$$

$$A^S(\theta, \theta^S) = \frac{-e^{i\pi/4}}{\sqrt{8\pi \sin(\theta - \theta^S)/2}} \quad (5.39)$$

$$A^R(\theta, \theta^R) = \frac{e^{i\pi/4}}{\sqrt{8\pi \sin(\theta - \theta^R)/2}} \quad (5.40)$$

We combine equations (5.39-5.40) with equation (5.36) to produce:

$$D(\theta) = \hat{D}(\theta) + A^S(\theta, \theta^S) + A^R(\theta, \theta^R) \quad (5.41)$$

We call the quantity $D(\theta)$ in (5.41) the directivity. We plot the real and imaginary components of $D(\theta)$ in figure 5.8 and the magnitude as a function of θ in figure 5.9. We observe its singular nature at the critical angles, θ^S and θ^R . The existence of the step in equation (5.38) causes these singularities to arise. They allow for a ‘smoothing’ of the solution across the shadow and reflected boundaries.

These results were all computed for large kr_0 and a well refined mesh. We assume that the size of the artificial boundary and refinement of the mesh result in the largest contributions to the error. We now seek to examine the effect of altering the FEM mesh and compute an asymptotic estimate for the total error.

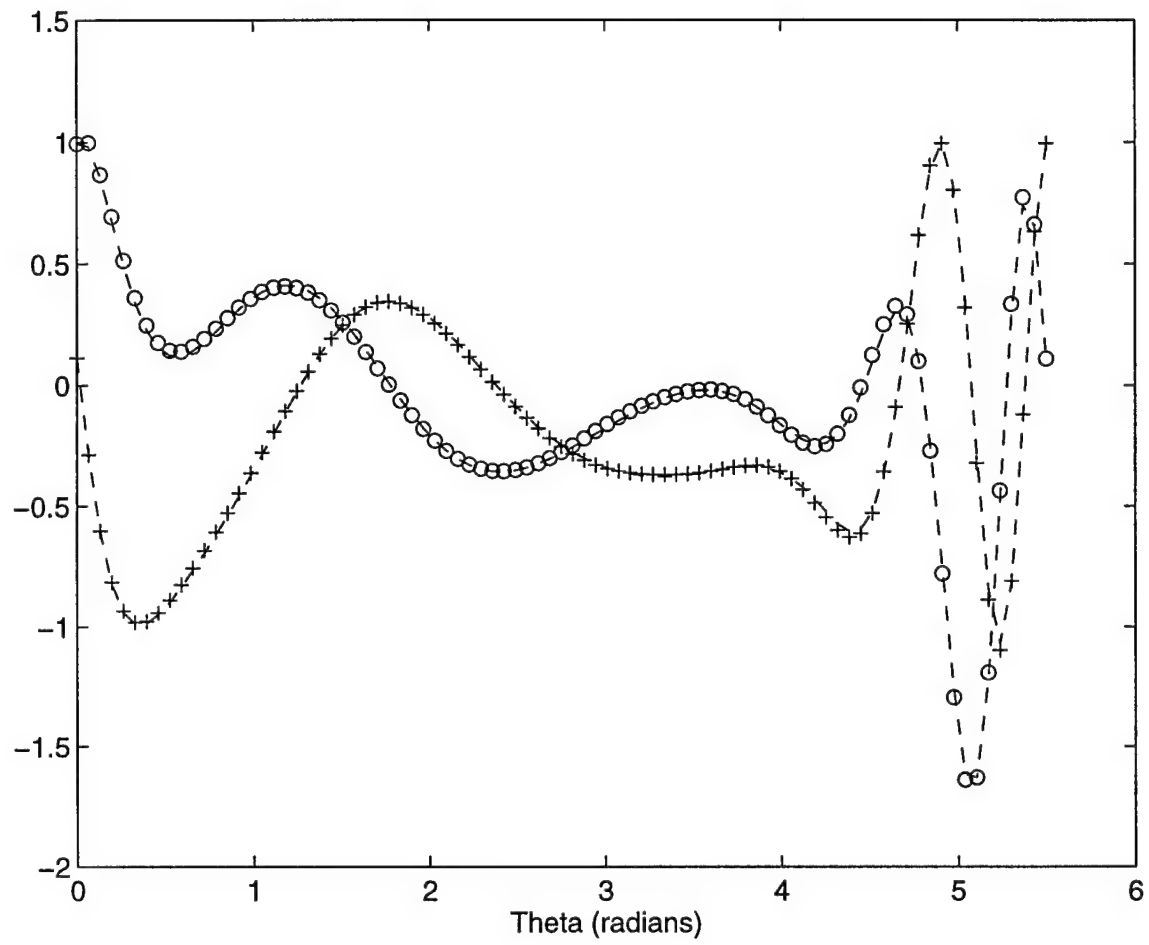


Figure 5.5: Real(+) and imaginary(o) parts of the hybrid solution compared to a nodally exact solution(- -) on Γ_R .

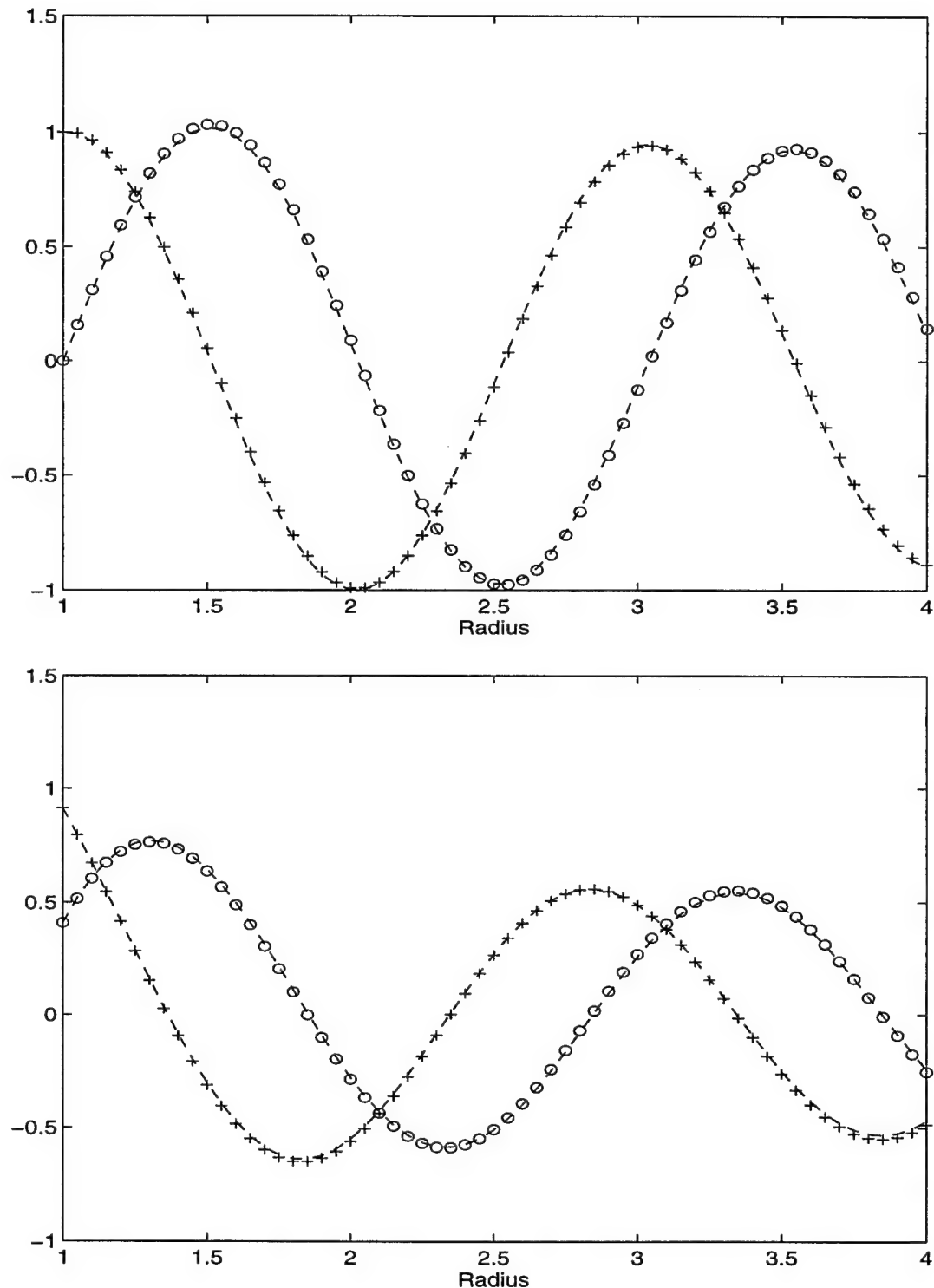


Figure 5.6: Real(+) and imaginary(o) parts of the hybrid solution for the scattered field compared to a nodally exact solution(- -) along the shadow (top) and reflected (bottom) boundaries.

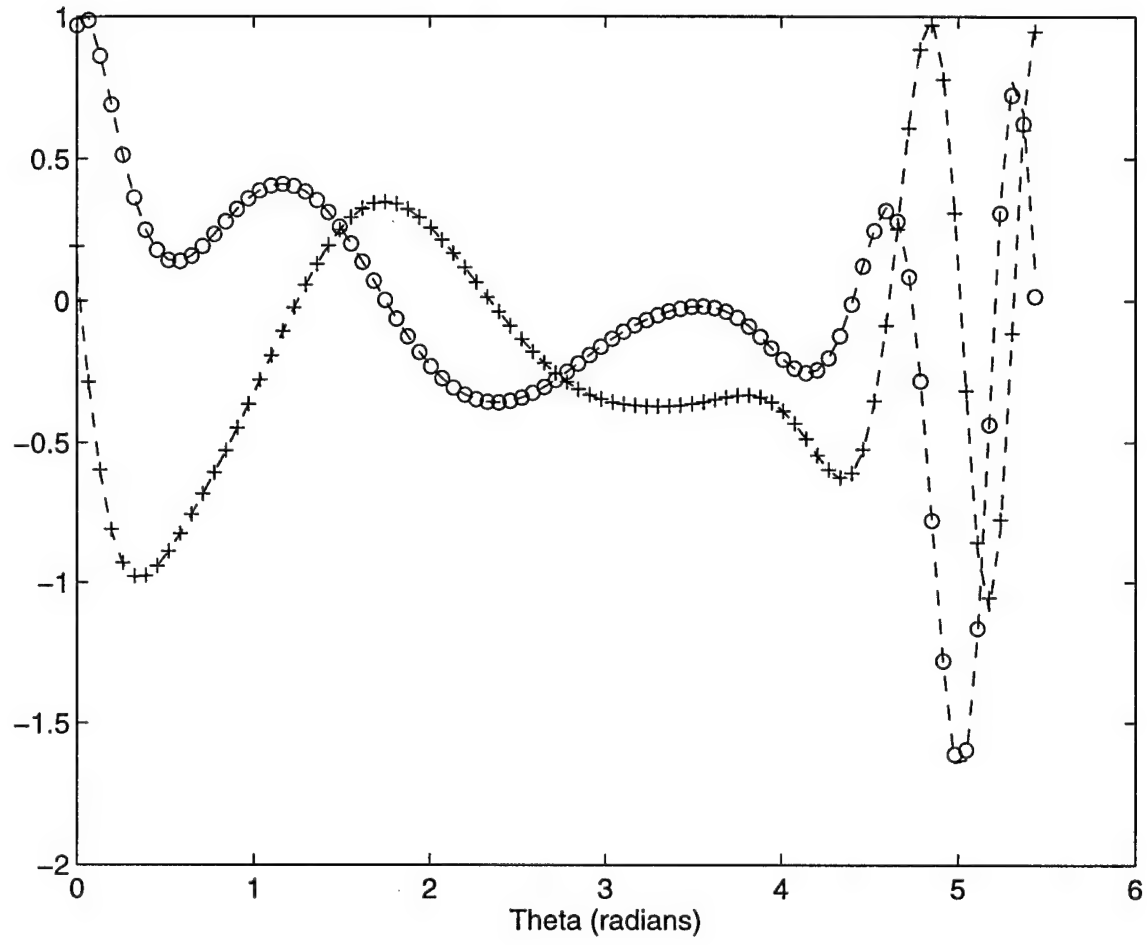


Figure 5.7: Real(+) and imaginary(o) parts of the hybrid solution for the scattered field, computed using the outer hybrid nodes, compared to the solution computed using the inner hybrid nodes(- -).

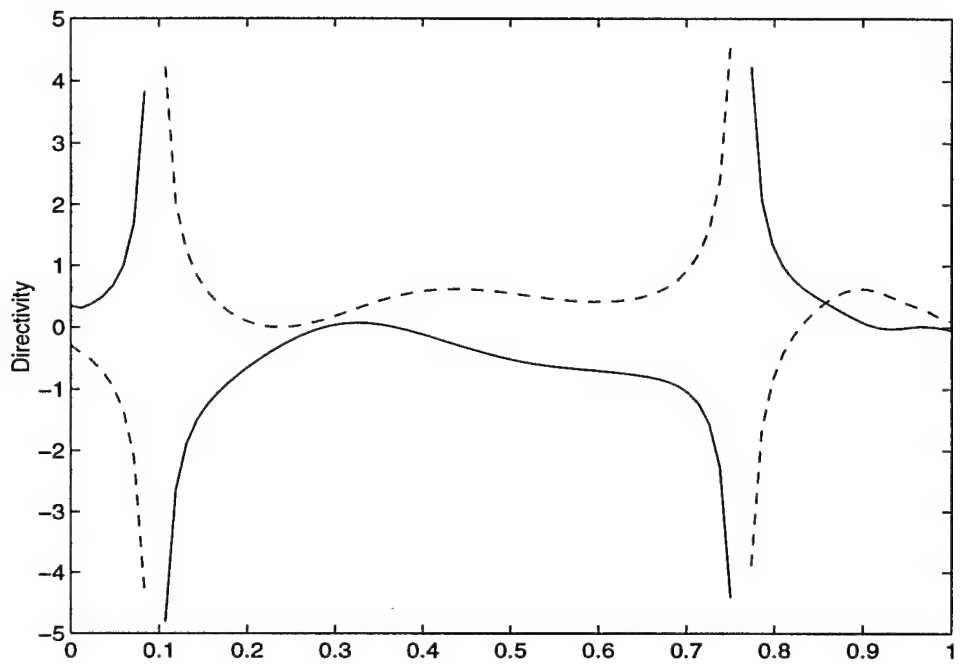


Figure 5.8: Real(—) and imaginary(- -) parts of the directivity as a function of θ/β . This expression is singular at $\theta = \theta^S = \pi/6$ and $\theta = \theta^R = 4\pi/3$.

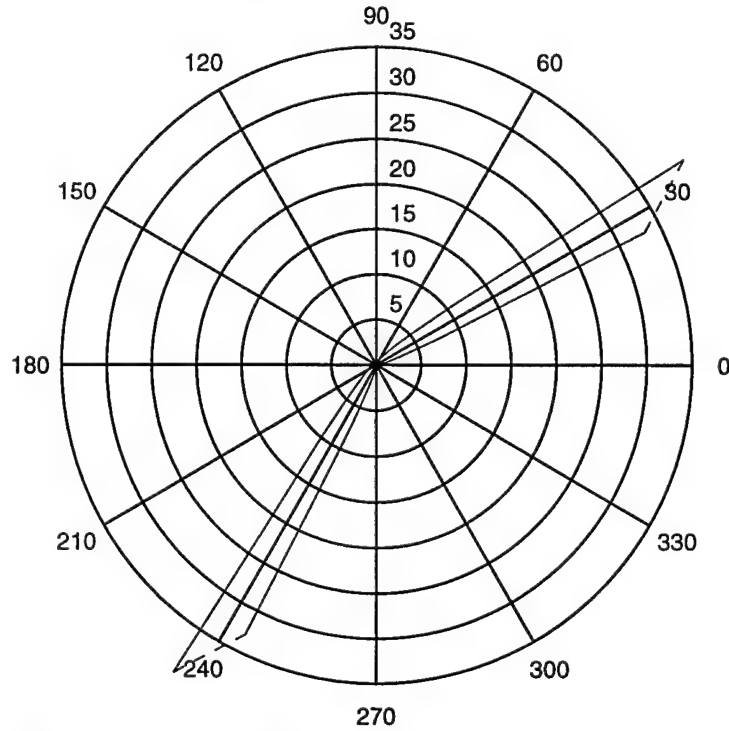


Figure 5.9: Magnitude of the directivity as a function of θ , truncated at the node values adjacent to θ^S and θ^R .

Chapter 6

Error Analysis

In order for a numerical or analytical method to be reliable, we must characterize and understand the sources of error. In this chapter we consider error arising from both numerical dispersion and our asymptotic boundary condition. We express the error in the hybrid method as the sum of the error due to patching the inner and outer solutions and the error due to dispersion in the finite element mesh:

$$E = E_p + E_d. \quad (6.1)$$

Minimizing the overall error associated with the location of the artificial boundary Γ_R results in guidelines for choosing the value of kr_0 .

6.1 Dispersion Error

We assume that numerical dispersion of cylindrical waves is qualitatively similar to that of plane waves. In an analysis of the dispersion, we begin by representing an exact solution u and an approximate FEM solution u^h as the following:

$$u = H_{\nu_n}^{(1)}(kr) \quad (6.2)$$

$$u^h = H_{\nu_n}^{(1)}(k^h r) \quad (6.3)$$

Here k^h is the approximate wavenumber associated with the FEM solution. The parameter h defines the relative discretization of the mesh. We define a non-dimensional parameter as the product $k^h h$. For plane waves in a regular mesh of piecewise linear shape functions, $k^h h$ is given by [13]:

$$k^h h \approx kh - \frac{(kh)^3}{24} < kh \quad (6.4)$$

Equation (6.4) implies that the approximate solution propagates in the radial direction with a characteristic wavelength such that:

$$\lambda^h > \lambda. \quad (6.5)$$

We compute the scattered field along a line of constant θ (Figures 6.1 and 6.2). It is apparent from the output that equation (6.5) is satisfied. We further observe that $|\lambda - \lambda^h|$ decreases as we decrease kh .

Inserting equation (6.4) into equation (6.3), we find:

$$u^h \approx H_{\nu_n}^{(1)}(kr) - H_{\nu_n}^{(1)\prime}(kr) \frac{(kh)^2}{24} kr \quad kh \ll 1. \quad (6.6)$$

From this we can express an asymptotic approximation for the FEM error as the following:

$$E_d = |u - u^h| \sim C_1(kh)^2 kr \quad kh \rightarrow 0 \quad (6.7)$$

As we would expect, this pointwise error depends on the propagation distance as well as the mesh refinement. In Figure 6.3, we compare the hybrid and exact solutions on the artificial boundary. Holding kr_0 fixed, we double the value of kh . What results is an increase in the error in agreement with equation (6.7).

6.2 Patching Error

In chapter 3, we found an asymptotic approximation of the error due to patching of the form:

$$E_p \sim \frac{C_2}{kr_0} \quad \alpha = 1. \quad (6.8)$$

We now consider holding kh fixed and observe the effects of varying kr_0 . Combining equations (6.8) and (6.7) yields an expression for the total error on Γ_R :

$$E|_{\Gamma_R} \sim C_1(kh)^2 kr_0 + \frac{C_2}{kr_0} \quad kr_0 \rightarrow \infty, kh \rightarrow 0. \quad (6.9)$$

We verify an asymptotic error estimate in our numerical solution as follows. We choose kh small enough so that:

$$C_1(kh_0)^2 kr_0 \ll \frac{C_2}{kr_0} \quad kr_0 \gg 1 \quad (6.10)$$

Then we compare the hybrid and exact solutions at this fixed kh_0 for five different values of kr_0 . The cases for the largest and smallest kr_0 are plotted in Figure 6.4. We further plot the maximum error for each kr_0 versus $(kr_0)^{-1}$. As equation (6.9) predicts, the relation between the error and $(1/kr_0)$ appears fairly linear (Figure 6.5).

6.3 Optimal Location of the Artificial Boundary

In order to find an optimal approximate solution, we seek to minimize the error with respect to kr_0 while holding kh fixed. In doing so, we are left with the relation:

$$\frac{dE}{d(kr_0)}|_{kh} = C_1(kh)^2 - \frac{C_2}{(kr_0)^2} = 0. \quad (6.11)$$

Solving for kr_0 yields

$$kr_0 = \frac{C}{kh} \quad (6.12)$$

which is equivalent to what results in balancing E_p with E_d . Thus, for optimal convergence to the exact solution, using piecewise linear shape functions and for $kh \rightarrow 0$, kr_0 must tend to infinity as $1/kh$.

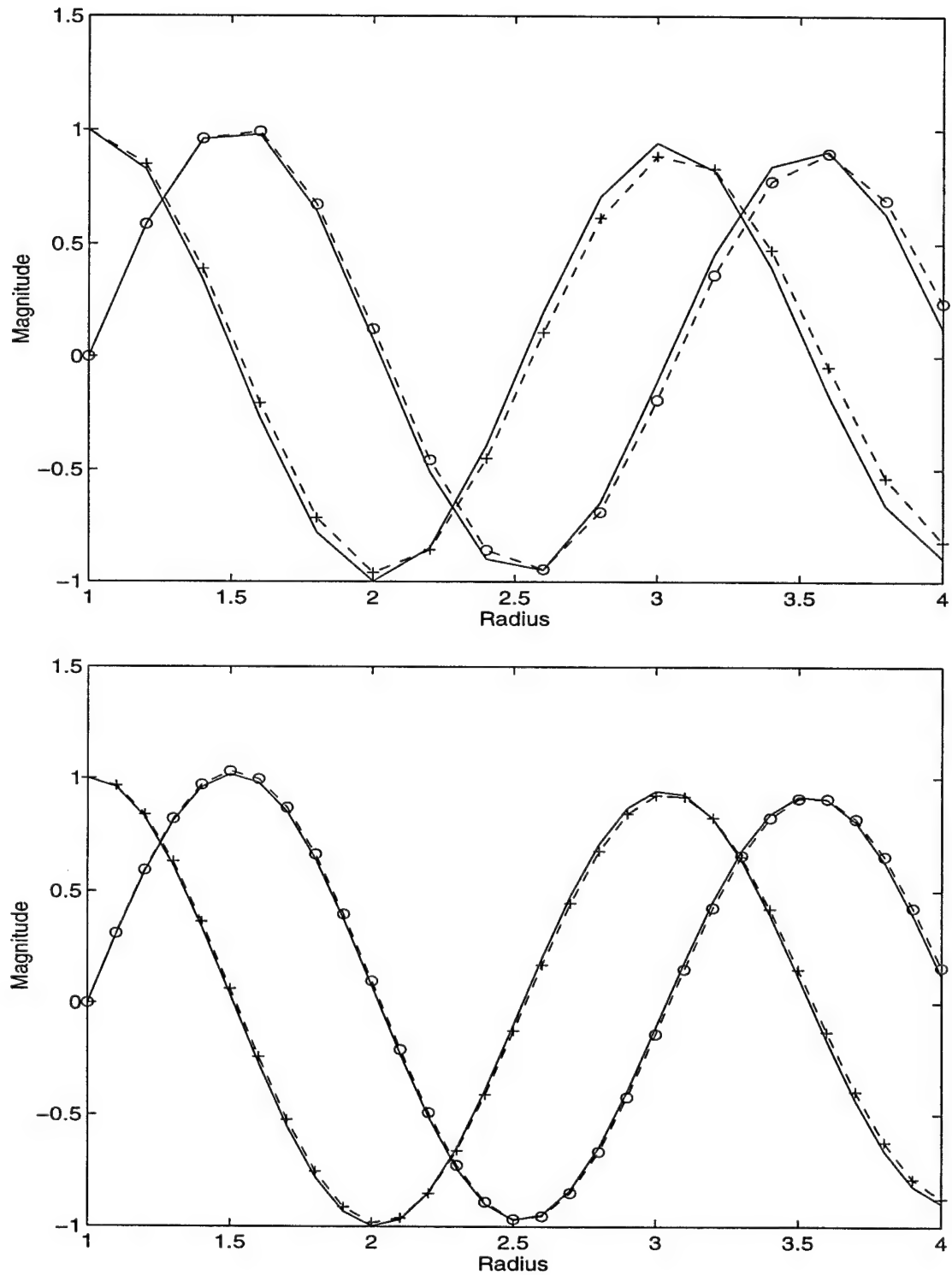


Figure 6.1: Real(+) and imaginary(o) parts of the hybrid scattered field compared to a nodally exact solution on the shadow boundary. $kh = kh_1$ in the lower plot, $kh = 2kh_1$ in the upper.

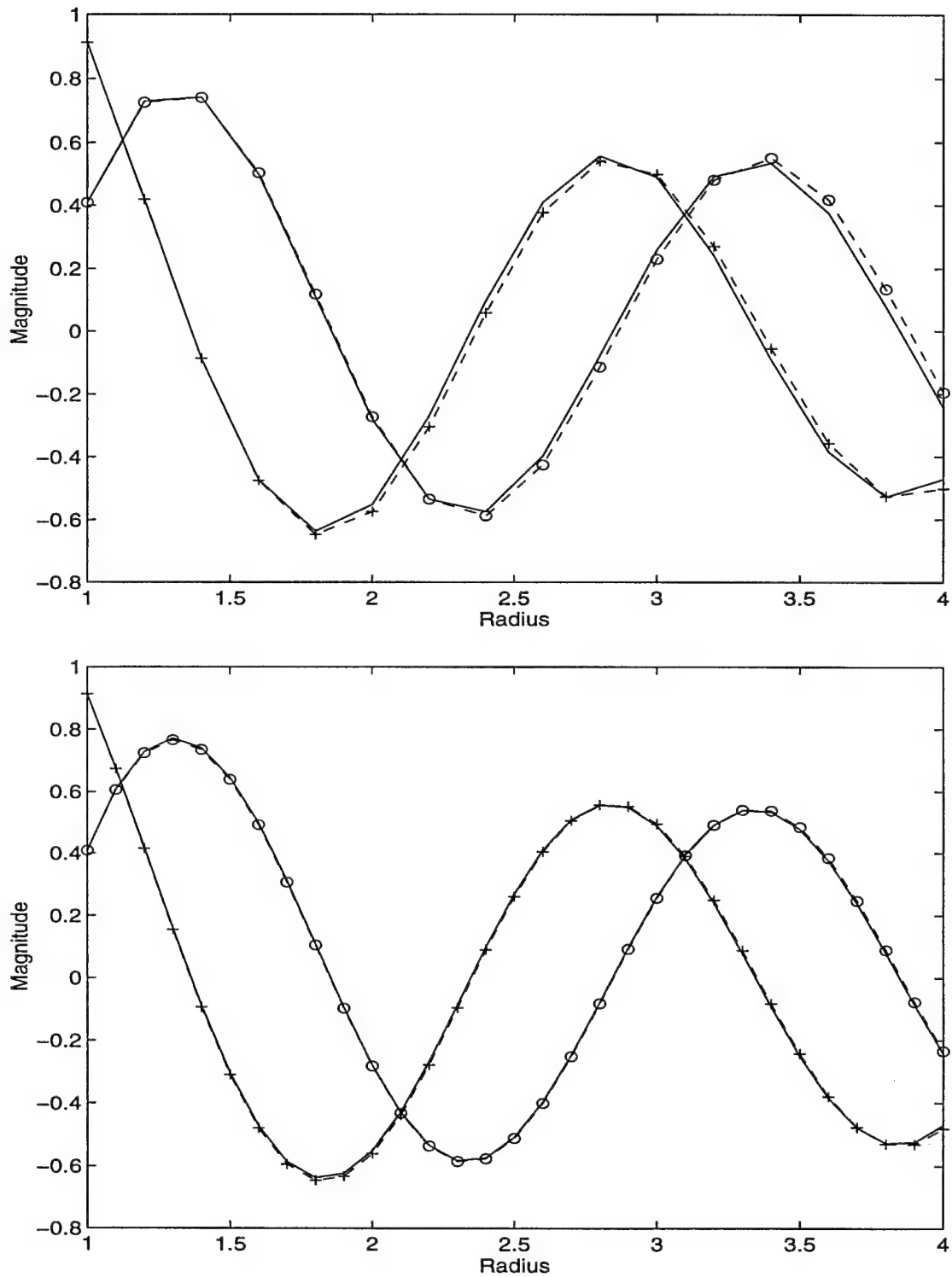


Figure 6.2: Real(+) and imaginary(o) parts of the hybrid scattered field compared to a nodally exact solution on the reflected boundary. $kh = kh_1$ in the lower plot, $kh = 2kh_1$ in the upper.

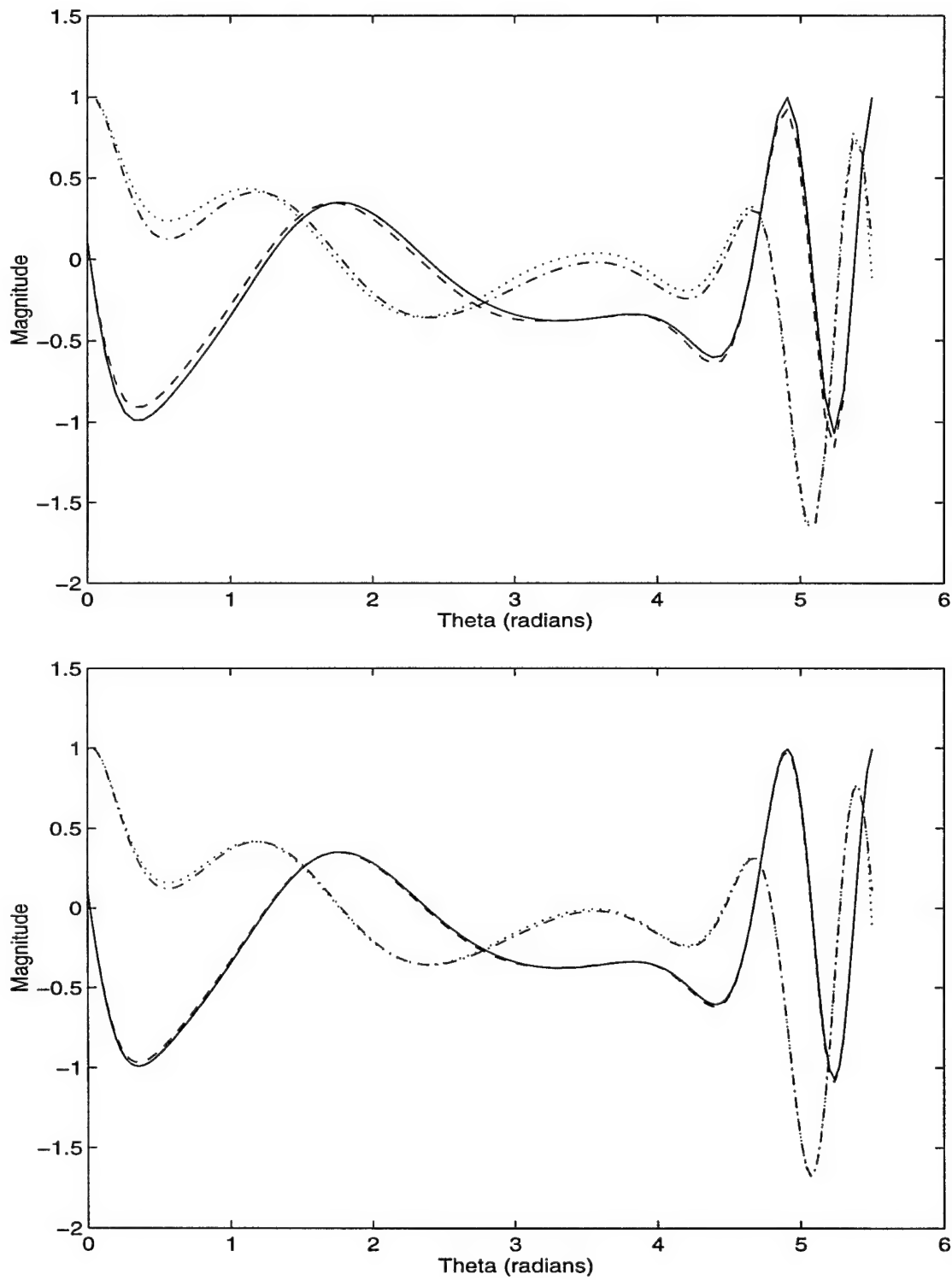


Figure 6.3: Real(--) and imaginary(--) parts of the hybrid scattered field compared to a nodally exact solution on Γ_R . $kh = kh_1$ in the lower plot, $kh = 2kh_1$ in the upper.

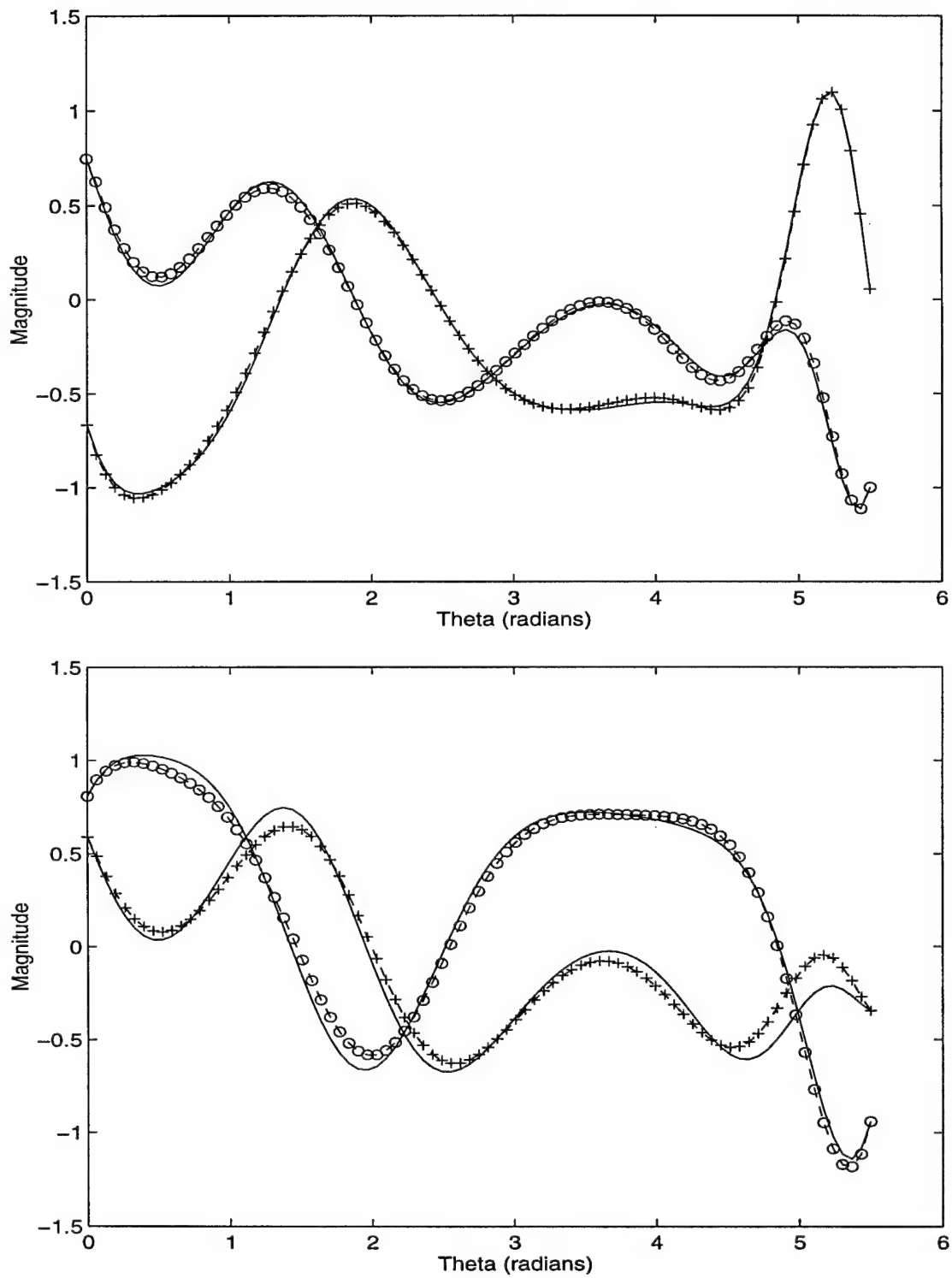


Figure 6.4: Real(+) and imaginary(o) parts of the scattered field compared to a nodally exact solution for $kr_0 = 2\pi$ (top) and $kr_0 = 3\pi/2$ (bottom).

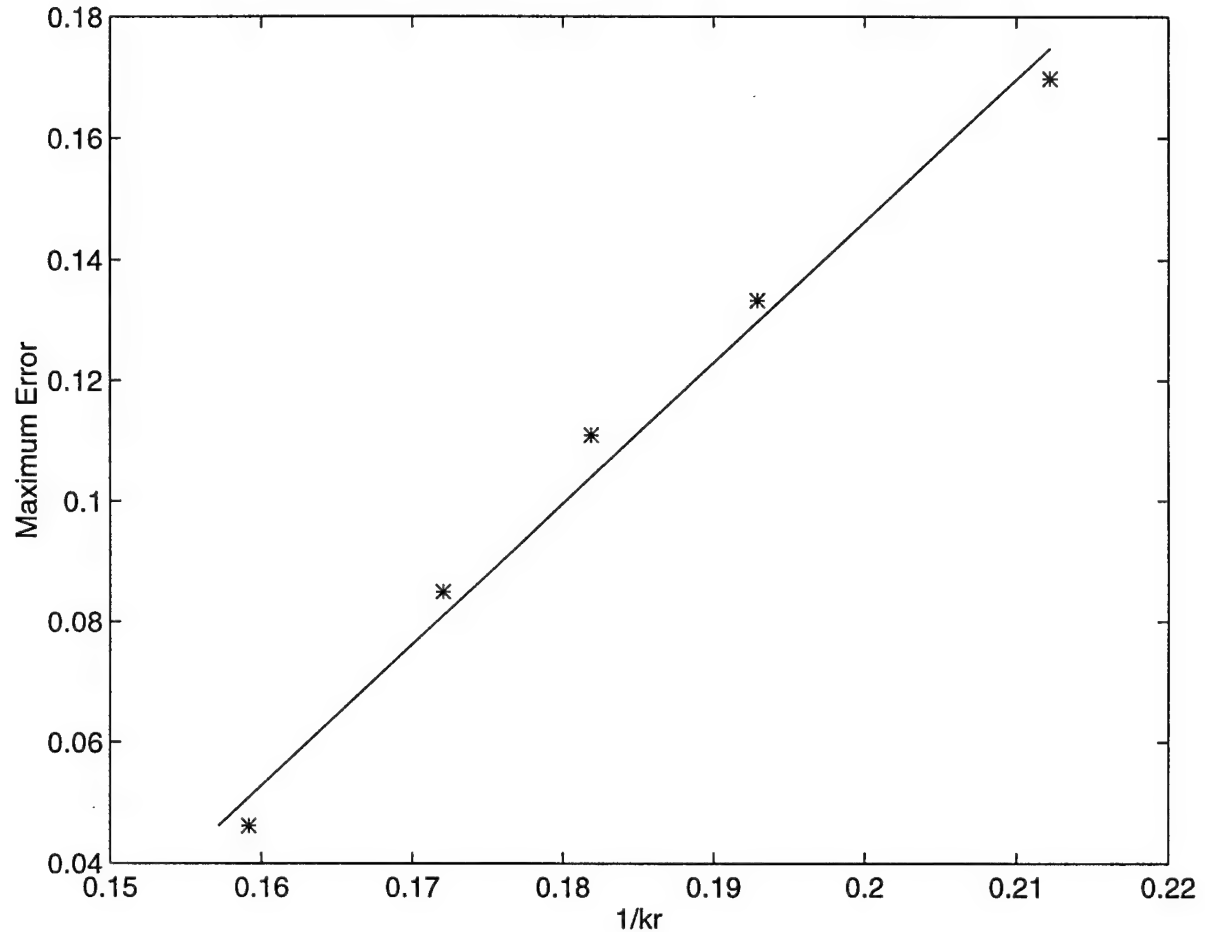


Figure 6.5: Maximum error in $|u - u^h|$ for extremely small kh , $kr_0 : 3\pi/2 \rightarrow 2\pi$.

Chapter 7

Conclusions

Short wavelength asymptotics and the finite element method are two fundamentally different approaches which are successfully combined in the hybrid method. What results from this union of analytic and numerical methods is a highly efficient and extremely accurate tool for solving complicated scattering problems.

The success of the hybrid approach relies on the accuracy of the method of patching the inner numerical solution to the outer asymptotic approximation. It is this boundary condition which allows us to replace an infinite domain problem with a finite domain one which is readily discretized.

In the MAE method, an outer solution was matched exactly to an inner solution in an asymptotic overlap domain. Patching, on the other hand, does not yield a similar guarantee of convergence. However, our analytic error analysis clearly shows an asymptotic equivalence between the methods of matching and patching, provided we always patch in the overlap domain.

Our numerical solutions of the scattered field reinforce this analytic argument. We also observe that the error in the hybrid method is dependent on both the discretization of the mesh as well as the propagation distance from the scatterer. Thus, by adjusting the size of the artificial boundary and mesh refinement, we obtain a hybrid solution nearly identical to an exact analytic solution. For any fixed discretization, we are then able to find a corresponding optimal location for the artificial boundary.

In patching the inner and outer solutions, we assume some knowledge of the outer field. This representation of the field typically contains the form of the solution with unknown coefficients. We can choose a particular component of the solution, however, to be partially prescribed without altering the overall solution. This was observed in our analysis of

the directivity of the outgoing scattered field, which consisted of both computed (\hat{D}) and prescribed (B^R, B^S) data.

We compare the hybrid solution to reference calculations in two separate cases. In one case, we have a nodally exact analytic solution where the error in the comparison represents both the asymptotic error inherent in the method as well as the error due to discretization. The DtN map, on the other hand, provides an exact representation of the boundary condition. Using the same discretization in both the DtN and hybrid methods then eliminates the error due to mesh refinement from the comparison. In both cases, the results from the hybrid method were nearly identical to the bench-mark calculations.

Although the DtN method provides an exact representation for this problem, we expect the hybrid method to be better suited to accommodate interactions between diffraction regions. Looking forward, we seek to model these interactions. To do so, we discretize each inner domain separately as before. The outer field, however, must represent the combined problems. This effectively couples the different inner problems, requiring that they be solved simultaneously.

We further seek to introduce ‘impedance’ elements on the surface of the scatterer. These local, one-dimensional elements are used to satisfy the homogeneous form of the impedance boundary condition. We implement these elements without introducing any additional degrees of freedom on the boundary of the object, although there are unknowns which are introduced on the artificial boundary. These unknowns represent the amplitudes of the diffracted surface waves.

Appendix A

Boundary Conditions and Surface Waves

Two of the most interesting aspects of a complicated scattering problem can be observed in edge effects and along fluid-solid interfaces. We model scattering from edges by means of the Geometrical Theory of Diffraction. To understand the interactions on the interface, we first examine a simple problem containing elastic boundaries. We will then examine a similar problem with a less complicated boundary condition which produces some of the same wave phenomena.

A.1 Fluid Loaded Elastic Plate

Here we discuss the vibration of an elastic plate in contact with a fluid. [16] These vibrations cause unsteady pressures in the fluid which in turn exert a surface loading on the plate. This loading is in addition to that which is caused by mechanical excitation or boundary layers.

We seek a solution for the fluid acoustic field above a thin elastic plate driven by a time harmonic line force. We examine the problem in the wavenumber domain and then obtain a space domain description of the field by approximating the Fourier transform. Even this simple model problem involves competition between several distinct physical attributes, causing the acoustic near field to have a very complicated structure.

In the limit as $kr \rightarrow \infty$, however, the main contribution to the field can be obtained by the method of stationary phase (see Appendix C). Features of the directivity of this asymptotic solution can then be attributed to specific wave phenomena on the fluid-elastic interface. Although this method ignores certain phenomena exclusive to the near field, we seek to find a representation of the field in the asymptotic outer region.

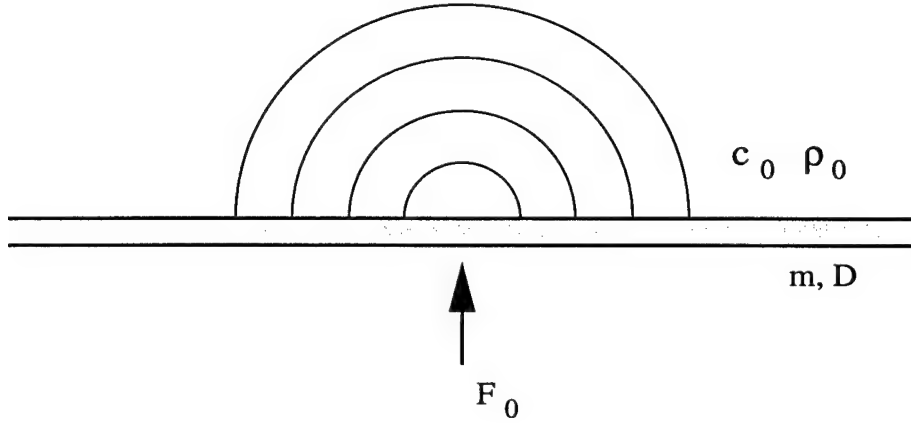


Figure A.1: Elastic plate excited by a time-harmonic line source

A.1.1 Formulation

We imagine a thin elastic plate with specific mass m and bending stiffness D , lying in the $y = 0$ plane. Above the plate is a fluid of density ρ_0 and sound speed c_0 , while the region below is taken to be a vacuum. We excite the plate with a time harmonic line force $F_0 e^{-i\omega t}$ along the z -axis, generating two-dimensional fluid motion in the xy -plane and one-dimensional motion along the plate.

In terms of a time harmonic acoustic pressure, the field in the fluid is governed by the reduced wave equation

$$\left(\frac{\partial^2}{\partial x^2} + \frac{\partial^2}{\partial y^2} + k_0^2 \right) p(x, y) = 0 \quad (\text{A.1})$$

where $k_0 = \omega/c_0$. This field must satisfy a radiation condition at $r = \infty$ as well as the boundary conditions associated with the plate [15]:

$$\frac{1}{i\omega\rho_0} \frac{\partial p}{\partial y}(x, 0) = v_p(x) \quad (\text{A.2})$$

$$(D \frac{\partial^4}{\partial x^4} - m\omega^2) \frac{v_p(x)}{-i\omega} = F_0 \delta(x) - p(x, 0) \quad (\text{A.3})$$

Here v_p denotes the velocity of the plate in the y direction. The first term in the parenthesis of equation (A.3) is the biharmonic while the second term represents the acceleration of the plate. The terms on the right represent the line forcing and pressure exerted by the fluid. For convenience, we introduce a constant with units of wavenumber:

$$\mu = \rho_0/m \quad (\text{A.4})$$

and non-dimensionalize our pressure field such that:

$$\hat{p} = \frac{p}{\mu F_0}. \quad (\text{A.5})$$

From here on we shall ignore the $\hat{\cdot}$ notation. It is then convenient to examine these equations in the wavenumber domain, so we now define a Fourier transform:

$$\tilde{p}(k, y) = \frac{1}{2\pi} \int_{-\infty}^{\infty} p(x, y) e^{-ikx} dx. \quad (\text{A.6})$$

The solution of the transformed Helmholtz equation can then be written in the form:

$$\tilde{p}(k, y) = \tilde{p}(k, 0) e^{ik_y y} \quad (\text{A.7})$$

$$\begin{aligned} k_y &= \sqrt{k_0^2 - k^2} \quad |k| \leq k_0 \quad \text{supersonic} \\ k_y &= i\sqrt{k^2 - k_0^2} \quad |k| \geq k_0 \quad \text{subsonic} \end{aligned} \quad (\text{A.8})$$

This choice of sign on the square roots is determined in accordance with the radiation condition, such that the supersonic waves propagate while the subsonic waves decay up into the fluid. If we were to ignore fluid loading but imagine wave-like behavior having been established on the plate, then there would be an associated spatial frequency from (A.3):

$$k_p = (m\omega^2/D)^{1/4}. \quad (\text{A.9})$$

Substituting (A.7) into the boundary conditions (A.2)-(A.3) yields:

$$\tilde{p}(k, 0) = \frac{k_p^4}{2\pi} \frac{1}{(k^4 - k_p^4)ik_y + \mu k_p^4}. \quad (\text{A.10})$$

By the inverse Fourier transform (A.6), the acoustic pressure in the space domain can be expressed as:

$$p(x, y) = \frac{k_p^4}{2\pi} \int_{-\infty}^{\infty} \frac{e^{ikx} e^{ik_y y} dk}{(k^4 - k_p^4)ik_y + \mu k_p^4} \quad (\text{A.11})$$

A.1.2 Surface Wave Contributions

To examine this integral, we first allow the wavenumber to be complex, such that equation (A.11) becomes a contour integral in the complex k -plane. The contour is initially taken to be along the real axis. We then allow the natural wavenumber in the fluid, k_0 , to have a small positive imaginary part. The effect of this is to push any poles off of the real axis, below for negative values and above for positive values. This ensures that singularities initially on the real axis correspond to outgoing waves.

The main items of interest in the evaluation of the integral (A.11) are the poles, the choice of branch cuts, and the stationary point. The poles are simple zeros of the denominator of the integral. Each corresponds to a different surface wave phenomenon. For this problem, we find poles to be located as pictured in Figure A.2 [17]. The surface waves corresponding to $k = \pm k_s$ propagate along the fluid-solid interface with a phase speed $c_s < c_0$. Although they propagate in the x -direction, the subsonic waves decay away from the plate. Therefore, these waves can be observed only in the region near $y = 0$.

The poles which do not lie on the real axis in figure A.2 correspond to surface waves that propagate above the natural speed in the fluid. The behavior of these two sets of supersonic

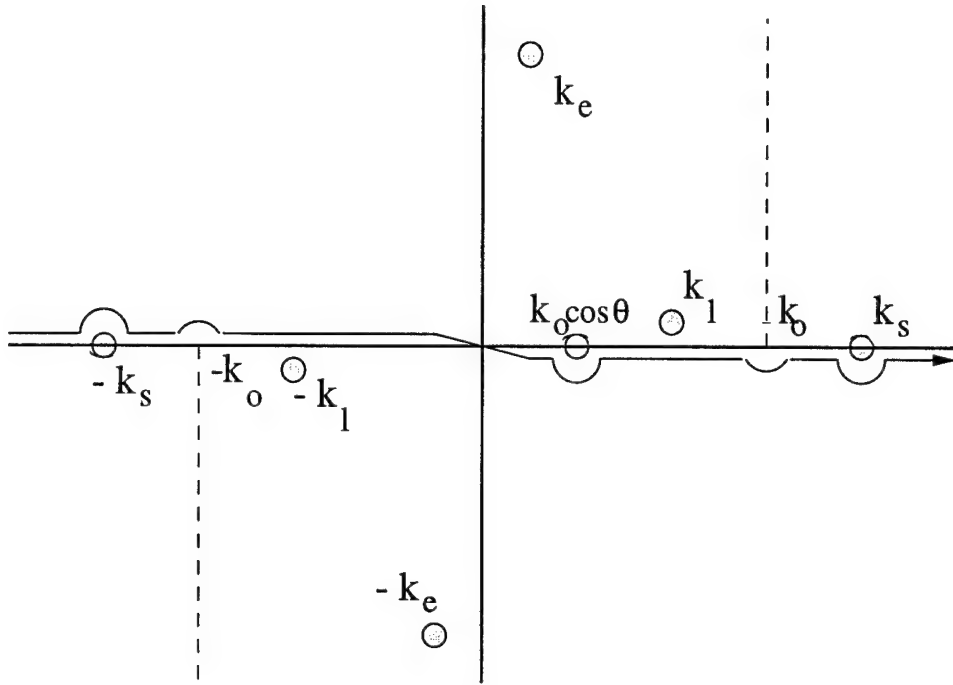


Figure A.2: Poles, branch cuts, and the stationary point

waves are essentially the same. The surface wave decays as it propagates in the x -direction, shedding energy into the fluid at some critical angle θ_c . Along a line of constant x , we then observe an exponential *growth* in the field in the y -direction. This seemingly non-physical result is justified by recognizing that a line taken at the critical angle, originating at the source, serves as a cut-off for the wave shed into the fluid.

The main difference between the leaky ($k = \pm k_l$) and evanescent ($k = \pm k_e$) supersonic waves is evident in the limit of small fluid loading ($\mu = 0$). In this limit, $\Im\{k_l\} \rightarrow 0$ while $\Re\{k_e\} \rightarrow 0$. The evanescent wave therefore decays rapidly and is observed only in the very near field. Although the leaky wave also decays, the rate is much slower and it has a greater effect on the far field.

We introduce branch cuts that extend from the branch points of equation (A.8) to

infinity in the complex plane [16]. The choice of branch cuts is important, as it effects how the poles contribute in the mathematical analysis. Regardless of the choice of branch cuts, however, we shall not ignore any of the pole contributions discussed.

The stationary point represents the dominant contribution to the acoustic far field. Examining the integral (A.11) in this limit:

$$p = \int_C f(k) e^{ik_0 r q(k)} dk \quad k_0 r \rightarrow \infty \quad (\text{A.12})$$

where $q(k)$ is the phase. We seek a particular value of $k = \bar{k}$ such that $\partial q / \partial k(\bar{k}) = 0$. This is called a stationary point (see Appendix C). The method of stationary phase yields the following:

$$p(r, \theta) \sim f(\bar{k}) e^{ik_0 r q(\bar{k})} \sqrt{2\pi/k_0 r q''(\bar{k})} e^{i\pi/4} \quad (\text{A.13})$$

In this particular problem, we find $\bar{k} = k_0 \cos \theta$. Thus, the dominant contribution to $p(r, \theta)$ is dependent on the observation angle. We further observe from equation (A.8) that this contribution is restricted to the supersonic domain.

For convenience, we introduce two more constants

$$M = k_0/k_p \quad \alpha = \mu/k_0. \quad (\text{A.14})$$

Here, α is a fluid-loading parameter and M is called a phase Mach number. Combining equations (A.11)-(A.13) allows us to express the pressure field as:

$$p(r, \theta) \sim \frac{e^{i\pi/4}}{\sqrt{2\pi}} \frac{\sin \theta}{(1 - M^4 \cos^4 \theta) \sin \theta + i\alpha} \frac{e^{ik_0 r}}{\sqrt{k_0 r}} \quad (\text{A.15})$$

We now wish to use this expression to examine the power radiated to the outer region. In the frequency domain, we calculate the acoustic intensity in the radial direction as [14]:

$$I(r, \theta) = \frac{pp^*}{2\rho_0 c_0}. \quad (\text{A.16})$$

Integrating this intensity over an arc of constant radius, we express the radiated power as:

$$\Pi = \frac{1}{\rho_0 \omega} \frac{1}{4\pi} \int_0^\pi \frac{\sin^2 \theta}{(1 - M^4 \cos^4 \theta)^2 \sin^2 \theta + \alpha^2} d\theta \quad (\text{A.17})$$

We imagine the driving frequency to be larger than some critical frequency, $\omega_c = \sqrt{mc_0^4/D}$, such that $M > 1$. This frequency is not necessarily large, depending on the material properties in the problem. We further assume that $\alpha \ll 1$ which, for a typical problem of a steel plate submerged in water, is a fair assumption. The main contribution to the power integral can then be attributed to a critical angle, θ_c , where

$$\cos \theta_c = 1/M. \quad (\text{A.18})$$

We examine the integral (A.17) in the region near the critical angle, such that $\theta = \theta_c + \alpha\theta'$.

The integral then becomes:

$$\Pi \approx \frac{1}{\rho_0 \omega} \frac{1}{4\pi} \int \frac{1}{\alpha} \frac{\sin^2 \theta}{16(M\theta')^2 \sin^4 \theta_c + 1} d\theta' \quad (\text{A.19})$$

From this we observe that $\Pi = O(\alpha^{-1})$ for $\|\theta - \theta_c\| = O(\alpha)$ and that $\Pi = O(1)$ otherwise. The significance of this is that the plate motion is equivalent to a large projector or antenna, resulting in beams at the critical angles. The surface response is dominated by the contribution from a leaky wave, whose imaginary part is proportional to α . The wave contribution is bounded by a line emanating from the source slightly below the critical angle and decays with respect to x as the surface wave loses energy. What results is a beam which eventually diffracts into a highly directive cylindrical wave.

Our expressions for the pressure (A.15) and radiated power (A.19) are not valid for all values of the fluid loading parameter, α , and observation angle, θ . This is most apparent when examining the field near the surface. When $\theta = 0$, the integral for the pressure (A.11)

does not contain a stationary point. Therefore, the method of stationary phase does not apply. What results is the following nonuniform limit:

$$\lim_{\theta \rightarrow 0} \lim_{\alpha \rightarrow 0} p(r, \theta, \alpha) \neq \lim_{\alpha \rightarrow 0} \lim_{\theta \rightarrow 0} p(r, \theta, \alpha) \quad (\text{A.20})$$

In the limit $\theta = 0$, we can wrap the contour of the integral (A.11) around the vertical branch cut at $k = k_0$. In doing so, we pick up contributions from the poles at $k = k_e$, $k = k_l$ and $k = k_s$. From [17], we know that the branch cut integral is $O((kx)^{-3/2})$. Further, pole contributions from all the poles except $k = k_s$ decay exponentially with respect to kx . Thus, the dominant contribution observed in this region is the subsonic surface wave; i.e., the residue from $k = k_s$. This contribution does not present itself in equation (A.11), however, since that approximation is not valid at $\theta = 0$.

Because surface wave phenomena are not unique to fluid-elastic interfaces, we seek to replace the elastic boundary condition with a less complicated one. We now consider surface wave phenomena on an impedance boundary.

A.2 Impedance Boundary Condition

We assume a fluid in the region $y > 0$, bounded by an impedance boundary. The governing equation for the total field in the fluid can be expressed as:

$$\frac{\partial^2 u_t}{\partial x^2} + \frac{\partial^2 u_t}{\partial y^2} + k_o^2 u_t = 0 \quad (\text{A.21})$$

$$u_t = u_{\text{inc}} + u \quad (\text{A.22})$$

We define the impedance as a complex parameter, Z , and represent the boundary condition in the following way:

$$\frac{\partial u_t}{\partial y} + k_0 Z u_t = 0 \quad \text{on } y = 0 \quad (\text{A.23})$$

We wish to consider free modes that will propagate on the boundary. We assume a solution for these modes to be of the form:

$$u = e^{ik_0(\sigma x + \mu y)} \quad (\text{A.24})$$

Inserting this solution (A.24) into the governing equation (A.21) yields:

$$\sigma^2 + \mu^2 = 1 \quad (\text{A.25})$$

Imposing the boundary condition (A.23) on the solution yields:

$$u = e^{ik_0\sqrt{1+Z^2}x} e^{-k_0 Z y} \quad (\text{A.26})$$

We now explore different options for the value of Z in expression (A.26). Choosing $Z > 0$ to be purely real results in a wave which propagates in the x -direction while exponentially decaying in the y -direction. The surface wave on the plate has an associated wavenumber:

$$|k_s| = k_0\sqrt{1+Z^2} > k_0 \quad (\text{A.27})$$

This corresponds to a subsonic wave such that $c_s < c_0$. It is observed only for the region where $y \ll 1/k_0 Z$.

Next, we examine a complex value for the impedance:

$$Z = -\alpha - i\eta \quad \alpha \ll \eta < 1. \quad (\text{A.28})$$

Here, both α and η are positive, real numbers. In order for the solution (A.24) to satisfy the boundary condition, we require:

$$\sigma = \sqrt{1 - \eta^2} \left[1 + \frac{i\alpha\eta}{(1 - \eta^2)} \right] \quad (\text{A.29})$$

$$\mu = \eta - i\alpha \quad (\text{A.30})$$

This choice of Z yields a leaky wave solution. The wavenumber along the boundary can be determined as:

$$| k_l | = k_0 \sqrt{1 - \eta^2 + \alpha^2 \eta^2 / (1 - \eta^2)} < k_0 \quad (\text{A.31})$$

Thus, the wave propagates along the boundary at a speed faster than the natural velocity in the fluid. The exponential decay in the x -direction can be attributed to energy which is shed into the fluid at the critical angle, θ_c . As before, the amplitude of the wave in the fluid grows in the y -direction. However, it is again bounded by a line emanating at an angle θ_c from the point of excitation.

A.3 Summary

In comparing an elastic boundary condition with an impedance boundary, we observe that certain surface wave phenomena are common to both. We further observe that the analysis of even a simple problem involving elastic boundaries can be extremely complicated. By choosing an appropriate value for the impedance Z , we replace the elastic boundary with a less complicated boundary condition which exhibits some of the same wave phenomena.

In our analysis of scattering by a hybrid method, we seek to represent aspects of the field such as diffraction and surface waves while keeping our canonical problem as simple

as possible. Thus, we require the surfaces of our truncated wedge to have an impedance boundary condition and seek to model the resulting diffracted surface waves of the scattered field.

Appendix B

Exact Analytical Representation

In order to compare the results obtained using the hybrid method, we seek an exact analytic representation for the field scattered by a blunted wedge. We begin by examining the solution to the problem of the sharp wedge. One solution that is readily available [5] represents a line source at (r_o, θ_{inc}) , incident on a sharp wedge with soft boundaries. We express the incident and resulting total field as:

$$u_i = -\frac{1}{4}iH_0^{(1)}(k\|\mathbf{x} - \mathbf{x}_0\|) \quad (\text{B.1})$$

$$u_t = \frac{\pi i}{\beta} \sum_{n=1}^{\infty} H_{\nu_n}^{(1)}(kr_o) J_{\nu_n}(kr) \sin(\nu_n \theta) \sin(\nu_n \theta_{inc}) \quad (\text{B.2})$$

where H is the Hankel function, J_{ν_n} is the Bessel function, and $\nu_n = n\pi/\beta$.

Since we wish to model an incident plane wave, we now examine the source term (B.1). We note that the first term in the asymptotic expansion of the Hankel function is as follows:

$$H_{\nu_n}^{(1)}(kr_o) \sim \sqrt{\frac{2}{\pi}} e^{-i\nu_n\pi/2-i\pi/4} \frac{e^{ikr_o}}{\sqrt{kr_o}} \quad kr_o \rightarrow \infty. \quad (\text{B.3})$$

We then modify the amplitude of the incident field to be dependent on the distance from the scatterer and expand the argument of the Hankel function in the limit as this distance tends to infinity:

$$u_i = (\sqrt{\pi kr_o/2} e^{-ikr_o+i\pi/4}) H_0^{(1)}(k\|\mathbf{x} - \mathbf{x}_0\|) \quad (\text{B.4})$$

$$k\|\mathbf{x} - \mathbf{x}_0\| \sim kr_o - kr \cos(\theta - \theta_{inc}) \quad kr_o \rightarrow \infty. \quad (\text{B.5})$$

In this limit, we combine equations (B.3)-(B.5) with (B.1)-(B.2) to form a new expression for the total field:

$$u_{\text{inc}} = e^{-ikr \cos(\theta - \theta_{inc})} \quad (\text{B.6})$$

$$u_{\text{sharp}} = (4\pi/\beta) \sum_{n=1}^{\infty} e^{-i\nu_n\pi/2} J_{\nu_n}(kr) \sin(\nu_n \theta_{inc}) \sin(\nu_n \theta). \quad (\text{B.7})$$

This is the solution u_{sharp} for scattering from a sharp wedge with plane wave incident. The problem of interest, however, is that of scattering from a blunted wedge u_{bl} . We now wish to find a representation for the difference $u_{\text{bl}} - u_{\text{sharp}}$ which can be added to the solution of the sharp wedge.

In both problems, the total field can be expressed as the sum of an incident and a scattered field:

$$\begin{aligned} u_{\text{sharp}} &= u_{\text{inc}} + u_{\text{sct}} \\ u_{\text{bl}} &= u_{\text{inc}} + u \end{aligned} \quad (\text{B.8})$$

For convenience, we introduce

$$\hat{u} = u_{\text{bl}} - u_{\text{sharp}} \quad (\text{B.9})$$

where

$$\hat{u} = \begin{cases} -u_{\text{sharp}} & \text{on } r = a \\ \text{outgoing} & \text{as } r \rightarrow \infty \end{cases} \quad (\text{B.10})$$

Because of the outgoing nature of \hat{u} , we can represent it in the following form:

$$\hat{u} = \sum_{n=1}^{\infty} A_n H_{\nu_n}^{(1)}(kr) \sin(\nu_n \theta) \quad (\text{B.11})$$

Satisfying the boundary condition in (B.10) results in an expression for the unknown constants:

$$A_n = -(4\pi/\beta) e^{-i\nu_n \pi/2} \sin(\nu_n \theta_{\text{inc}}) J_{\nu_n}(ka) / H_{\nu_n}^{(1)}(ka). \quad (\text{B.12})$$

Having solved for these constants, we combine the expressions for \hat{u} (B.11) and u_{sharp} (B.7). This results in the following series representation for the total field in the blunted wedge problem:

$$u_{\text{bl}}(r, \theta) = (4\pi/\beta) \sum_{n=1}^{\infty} e^{-i\nu_n \pi/2} M_n \sin(\nu_n \theta_{\text{inc}}) \sin(\nu_n \theta) \quad (\text{B.13})$$

where

$$M_n = J_{\nu_n}(kr) - [J_{\nu_n}(ka)/H_{\nu_n}^{(1)}(ka)] H_{\nu_n}^{(1)}(kr) \quad (\text{B.14})$$

In comparing (B.13) to the hybrid solution, we subtract out the incident field and evaluate the resulting scattered field nodally. This solution is then interpolated linearly between the nodes, consistent with our FEM representation. Thus, we are comparing the hybrid scattered field solution to a nodally exact analytic solution.

Appendix C

Stationary Phase

A useful tool for evaluating certain integrals is the method of stationary phase. Here we discuss a general integral representation which was motivated by the complicated transform integral in Appendix B. We first assume that this integral has the following form:

$$I(k) = \int_a^b f(x)e^{ik\phi(x)} dx \quad (\text{C.1})$$

Here, k is a *large* parameter and the amplitude function $f(x)$ varies slowly compared to the exponential function. For convenience, we choose the phase $\phi(x)$ in this discussion to have a single stationary point at the value $x = x_0$. We further require this to be a local minimum, such that $\phi''(x_0) > 0$. These restrictions are for simplicity, and one can easily account for several stationary points of different type.

Due to the magnitude of k , the exponential is a highly oscillatory function for all values of x except those very close to x_0 . Because of this, we make the following approximation:

$$I(k) \sim \int_{-\infty}^{\infty} f(x_0)e^{ik\phi(x)} dx \quad (\text{C.2})$$

Since the main contribution to the integral comes from values near $x = x_0$, we can integrate over all space without losing much accuracy. Expanding $\phi(x)$ around the stationary point yields:

$$\phi(x) = \phi(x_0) + \frac{1}{2}\phi''(x_0)(x - x_0)^2 + \dots \quad (\text{C.3})$$

We then insert equation (C.3) into (C.2), resulting in the following approximation:

$$I(k) \sim f(x_0)e^{ik\phi(x_0)} \int_{-\infty}^{\infty} e^{ik\frac{1}{2}\phi''(x_0)(x-x_0)^2} dx \quad (\text{C.4})$$

For convenience, we introduce a new variable:

$$\xi = \sqrt{-ik\frac{1}{2}\phi''(x_0)} (x - x_0) \quad (\text{C.5})$$

$$d\xi = \frac{-ik\phi''(x_0)dx}{2\sqrt{-ik\frac{1}{2}\phi''(x_0)}}. \quad (\text{C.6})$$

Expressing (C.4) in terms of this new variable yields:

$$I(k) \sim f(x_0)e^{ik\phi(x_0)} \frac{i2\sqrt{-ik\frac{1}{2}\phi''(x_0)}}{k\phi''(x_0)} \int_{-\infty}^{\infty} e^{-\xi^2} d\xi \quad (\text{C.7})$$

We define the integral component in (C.7) as:

$$J = \int_0^{\infty} e^{-x^2} dx \quad (\text{C.8})$$

Further examination of this function (C.8) yields a solution to the integral in closed form:

$$J^2 = \int_0^{\frac{\pi}{2}} \int_0^{\infty} e^{-r^2} r dr d\theta = \frac{\pi}{4} \quad (\text{C.9})$$

Combining equation (C.9) with (C.7) yields a final asymptotic representation of the integral using the method of stationary phase:

$$I(k) \sim f(x_0)e^{ik\phi(x_0)} \sqrt{\frac{2\pi}{k\phi''(x_0)}} e^{i\pi/4} \quad (\text{C.10})$$

We consider a final question regarding the sign on the square root in equation (C.5).

This is resolved by examining the contour in x . With ϕ'' positive, the change from x to ξ deforms the contour from the real axis so that it is rotated forty-five degrees in the counter-clockwise direction about the point $x = x_0$.

If the sign on the square root is positive, the contour extends in the direction of increasing x . If the sign on the square root is negative, the opposite is true. In the first case, we can connect the deformed contour with the original through the first and third quadrants. At infinity, the first and third quadrants produce a negative real part in the exponential (C.7) such that the contributions to the integral are negligible. In the other case, however, the contributions at infinity are large. Therefore, we choose the positive sign on the square root in our change of variables.

Bibliography

- [1] Milton Van Dyke, *Perturbation Methods in Fluid Mechanics*, The Parabolic Press, Stanford 1975.
- [2] Joseph B. Keller, “Geometrical Theory of Diffraction,” *Calculus of Variations and Its Applications*, Proc. of Symposia in Applied Mathematics Vol. 8, pp. 27-51 (1958) as it appears in *Selected Papers on Geometrical Aspects of Scattering*, P.L. Marston, ed., SPIE Milestone Series, (MS 89):5-25, SPIE Optical Engineering Press, Bellingham, WA 1994.
- [3] Dan Givoli, *Numerical Methods for Problems in Infinite Domains*, Elsevier, Amsterdam 1992.
- [4] Erich Zauderer, *Partial Diff. Equations of Applied Mathematics*, Academic Press, New York 1989, 2nd Edition.
- [5] D.S. Jones, *Acoustic and Electromagnetic Waves*, Clarendon Press, Oxford 1986.
- [6] M. Abramowitz and I. A. Stegun, *Handbook of Mathematical Functions*, Dover, New York 1972.
- [7] E. J. Hinch, *Perturbation Methods*, Cambridge University Press 1991.

- [8] Joseph B. Keller, Using the convergence of the series to note limits on A_n was suggested by Professor J. B. Keller in a conversation with Dr. Paul Barbone.
- [9] Isaac Harari and Paul E. Barbone, Finite Element Formulations for Exterior Problems, *Boston University Dept. Aero/Mech Eng. Technical Report*, (AM-96-001):1-12, 1996.
- [10] Thomas J.R. Hughes, *The Finite Element Method*, Prentice-Hall, Inc., Englewood Cliffs, NJ 1987.
- [11] I. Harari, Paul E. Barbone, and J. M. Montgomery, Finite Element Formulations for Exterior Problems: Application to Hybrid Methods, Non-reflecting Boundary Conditions, and Infinite Elements, Submitted to *I. J. Num. Meth. in Eng.* (1996).
- [12] Dan Givoli, Revisions of the FEM code *DLEARN* found in [10] to include Helmholtz elements and DtN boundary conditions. We modified Dr. Givoli's DtN code to accommodate wedge geometries.
- [13] Isaac Harari, Computational Methods for Problems of Acoustics with Particular Reference to Exterior Domains, Ph.D. Dissertation, Department of Mechanical Engineering, Stanford University, Stanford, CA, 1991.
- [14] Allan D. Pierce, *ACOUSTICS : An Introduction to Its Physical Principles and Applications*, 42-45, Acoustical Society of America, Woodbury, New York 1989 (second printing 1991).
- [15] Lee A. Segel, *Mathematics Applied to Continuum Mechanics*, Dover Publications, Inc., New York 1987.

[16] D. G. Crighton, "The Free and Forced Waves on a Fluid-Loaded Elastic Plate," in *Journal of Sound and Vibration*, **63**(2):225-235, Academic Press Inc. Limited, London 1979.

[17] D. G. Crighton, "The 1988 Rayleigh Medal Lecture:Fluid Loading-The Interaction Between Sound and Vibration," in *Journal of Sound and Vibration*, **133**(1):1-27, Academic Press Limited 1989.

C.10 Finite Element Formulations for Exterior Problems: Application to Hybrid Methods, Non-reflecting Boundary Conditions, and Infinite Elements

"Finite Element Formulations for Exterior Problems: Application to Hybrid Methods, Non-reflecting Boundary Conditions, and Infinite Elements," Isaac Harari, Paul E. Barbone and Joshua M. Montgomery, **International Journal for Numerical Methods in Engineering**, Vol. 40, 1997, pp. 2791–2805.

FINITE ELEMENT FORMULATIONS FOR EXTERIOR PROBLEMS: APPLICATION TO HYBRID METHODS, NON-REFLECTING BOUNDARY CONDITIONS, AND INFINITE ELEMENTS

ISAAC HARARI *

Department of Solid Mechanics, Materials & Structures, Tel-Aviv University, 69978 Ramat Aviv, Israel

PAUL E. BARBONE AND JOSHUA M. MONTGOMERY

Department of Aerospace & Mechanical Engineering, Boston University, 110 Cummington Street, Boston, MA 02215, U.S.A.

SUMMARY

We develop formulations for finite element computation of exterior acoustics problems. A prominent feature of the formulations is the lack of integration over the unbounded domain, simplifying the task of discretization and potentially leading to numerous additional benefits. These formulations provide a suitable basis for hybrid asymptotic-numerical methods in scattering, non-reflecting boundary conditions and infinite elements. © 1997 by John Wiley & Sons, Ltd.

KEY WORDS: finite element methods; unbounded domains; acoustics; Lagrange multipliers; absorbing boundary conditions; infinite elements

1. INTRODUCTION

Finite element methods are the numerical technique of choice for numerous classes of boundary-value problems. In order to use domain-based discretization in a problem with an infinite domain, a finite computational domain is formed by introducing an artificial boundary. The ‘far-field’ behaviour is then represented either by boundary conditions specified on the artificial boundary, or by interpolation assumed in the complement of the computational domain.¹ The former approach is associated with non-reflecting boundary conditions (see, e.g. Reference 1 and pp. 95–116 of Reference 2) and in particular the DtN (Dirichlet-to-Neumann) method, which was conceived as a general procedure for exterior boundary-value problems by Givoli and Keller³ and is related to earlier work in acoustics.^{4,5} The latter approach is termed infinite elements.^{6–9} A third approach currently being explored by the authors is called a ‘hybrid asymptotic-numerical method’ in that it utilizes analytical asymptotic approximations of the field to formulate approximate DtN conditions.¹⁰

Global DtN boundary conditions can be very accurate, but all of the degrees of freedom on the artificial boundary are coupled, potentially increasing the cost of computation. In contrast, infinite

* This research was performed in part while the author was visiting the Department of Aerospace & Mechanical Engineering, Boston University

elements retain the element-based data structure of finite elements. This preserves the bandedness of the discrete equations, but typically at the cost of including extra unknowns in the formulation arising from discretization of the unbounded domain. The hybrid method will be described more fully in a future contribution.

In what follows, we introduce a framework for finite element computation in an unbounded domain which has applications to the hybrid approach, the DtN method and to infinite elements. We describe the basic ideas in the context of the Helmholtz equation governing time-harmonic acoustic radiation and scattering. This framework may also be employed as a basis for finite element solution of exterior problems in other fields such as steady heat conduction and elastostatics, as well as elastic and electromagnetic waves.

We arrive at our formulation as follows: We first introduce an artificial boundary which partitions the domain into sub-domains. The variational form of the problem depends explicitly on the partition, regardless of discretization, as in hybrid finite element methods, e.g. p. 24 of Reference 11 (to be distinguished from the hybrid asymptotic-numerical approach discussed herein). We enforce continuity at the interface between the sub-domains weakly via Lagrange multipliers. The concept of finite element methods with Lagrange multipliers enforcing boundary constraints is well known,¹² with application to contact and interaction problems, as well as analyses combining different types of elements¹³ and independently modelled sub-domains.^{14,15} Least-squares stabilization permits arbitrary choice of finite element interpolations.^{16,17} We solve for the Lagrange multiplier exactly and thus remove it from the formulation, in a manner similar to Nitsche's method.¹⁸ Integration by parts further simplifies the formulation by removing all integrations over the unbounded domain. This results in a formulation which is exact, is free of any constraint degrees of freedom, and can be used to recover many well-known formulations developed previously.

A similar procedure of removing the Lagrange multiplier was described in the context of elasticity problems by Key.¹⁹ Key's formulation, sometimes referred to as a 'Simplified Variational Principle,' was explored with mixed results by Mang, Gallagher and Haugeneder in various studies.²⁰⁻²³ Our formulation differs significantly from Key's, however, in at least two respects. First, we integrate by parts in the unbounded domain and therefore require our basis functions there to exactly satisfy the differential equation. Further, and perhaps more importantly, we choose our outer domain so that the problem is homogeneous there. The analytical and numerical results presented below show that our procedure can lead to an effective and accurate numerical method.

The boundary-value problem related to acoustic radiation and scattering governed by the Helmholtz equation is described in Section 2. We present the details of the derivation of our formulation in Section 3 and follow that discussion with examples in Section 4.

2. EXTERIOR BOUNDARY-VALUE PROBLEM OF ACOUSTICS

Let $\mathcal{R} \subset \mathbb{R}^d$ be an unbounded region, where d is the number of space dimensions. The boundary of \mathcal{R} , denoted by Γ , is internal and assumed piecewise smooth (Figure 1). The outward unit vector normal to Γ is denoted by \mathbf{n} . We assume that Γ admits the partition $\Gamma = \overline{\Gamma_g \cup \Gamma_h}$, where $\Gamma_g \cap \Gamma_h = \emptyset$.

We consider a boundary-value problem related to acoustic radiation and scattering governed by the Helmholtz equation: find $u: \mathcal{R} \rightarrow \mathbb{C}$, the spatial component of the acoustic pressure or velocity potential, such that

$$-\mathcal{L}u = f \quad \text{in } \mathcal{R} \quad (1)$$

$$u = g \quad \text{on } \Gamma_g \quad (2)$$

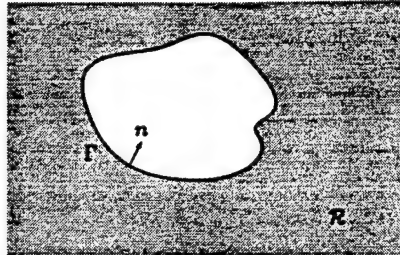


Figure 1. An unbounded region with an internal boundary

$$\frac{\partial u}{\partial n} = ikh \quad \text{on } \Gamma_h \quad (3)$$

$$\lim_{r \rightarrow \infty} r^{(d-1)/2} \left(\frac{\partial u}{\partial r} - iku \right) = 0 \quad (4)$$

Here $\mathcal{L}u := \Delta u + k^2 u$ is the Helmholtz operator, Δ is the Laplace operator and $k \in \mathbb{C}$ is the wave number, $\partial u / \partial n := \nabla u \cdot \mathbf{n}$ is the normal derivative and ∇ is the gradient operator; $i = \sqrt{-1}$ is the imaginary unit; r is the distance from the origin; and $f: \mathcal{R} \rightarrow \mathbb{C}$, $g: \Gamma_g \rightarrow \mathbb{C}$ and $h: \Gamma_h \rightarrow \mathbb{C}$ are the prescribed data.

Equation (4) is the *Sommerfeld radiation condition* and allows only outgoing waves at infinity. The radiation condition requires energy flux at infinity to be positive, thereby guaranteeing that the solution to the boundary-value problem (1)–(4) is unique (See Reference 24, pp. 296–299; Reference 25, pp. 55–60 and references cited therein.) Appropriate representation of this condition is crucial to the reliability of any numerical formulation of the problem (1)–(4).

3. MIXED VARIATIONAL FORMULATION IN A BOUNDED DOMAIN

Here we outline the development of a simple variational formulation that couples two parts of an acoustics problem in a partitioned domain by weakly enforcing continuity at the interface. Our starting point is a generalization of the procedure presented by Hughes²⁶ as a basis for his multi-scale interpretation.

3.1. Partitioned problem in strong form

The unbounded domain \mathcal{R} is decomposed by a smooth artificial boundary Γ_R into a bounded inner domain Ω^i and its unbounded outer complement Ω^o (Figure 2), expressed analytically as

$$\mathcal{R} = \overline{\Omega^i \cup \Omega^o} \quad (5)$$

where $\Omega^i \cap \Omega^o = \emptyset$ and $\Gamma_R = \overline{\Omega^i} \cap \overline{\Omega^o}$.

Following Hughes,²⁶ the solution of the original boundary-value problem (1)–(4) is decomposed into the inner field u^i and outer field u^o :

$$u = u^i + u^o \quad (6)$$

where $u^i|_{\Omega^o} = 0$ and $u^o|_{\Omega^i} = 0$, so that

$$u = \begin{cases} u^i & \text{on } \Omega^i \\ u^o & \text{on } \Omega^o \end{cases} \quad (7)$$

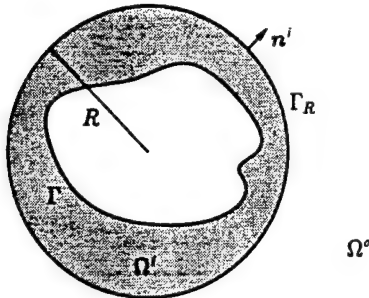


Figure 2. The partitioned domain

Continuity requirements across Γ_R are discussed below. We assume that f vanishes in the outer domain:

$$f = 0 \quad \text{in } \Omega^o \quad (8)$$

An example in which such a decomposition is desirable is short-wavelength scattering problems, where Ω^i contains regions of diffraction, while the ray ansatz is valid in Ω^o . In order to accommodate such configurations we treat the continuity of u across Γ_R (i.e. $u^i = u^o$ on Γ_R) weakly in a variational setting, rather than as an essential requirement that is enforced strongly. Weakly enforcing continuity across the interface is our point of departure from the derivation of Hughes.²⁶

3.2. Variational statement with weak continuity

The variational form of the boundary-value problem is stated in terms of sets of trial solutions, \mathcal{S}^i and \mathcal{S}^o for u^i and u^o , respectively. For Neumann problems ($\Gamma_g = \emptyset$), $\mathcal{S}^i = \{u^i | u^i \in H^1(\Omega^i), u^i = 0 \text{ in } \Omega^o\}$. Otherwise, Dirichlet boundary conditions on Γ_g must also be satisfied by functions in \mathcal{S}^i . The space \mathcal{S}^o is described below.

A variational form of the original boundary-value problem (1)–(4) is augmented to enforce continuity across the artificial boundary by Lagrange multipliers λ . Thus we seek to find $u^i \in \mathcal{S}^i$, $u^o \in \mathcal{S}^o$ and $\lambda \in H^{-1/2}(\Gamma_R)$ that render $\Pi(u, \lambda)$ stationary, where

$$\Pi(u, \lambda) = \frac{1}{2}a(u^i, u^i) + \frac{1}{2}a(u^o, u^o) - L(u^i) + (\lambda, u^i - u^o)_{\Gamma_R} \quad (9)$$

$$a(w, u) = \int_{\Omega^i \cup \Omega^o} (\nabla w \cdot \nabla u - wk^2 u) d\Omega - \lim_{r \rightarrow \infty} \int_{\Gamma_r} w iku d\Gamma \quad (10)$$

$$(w, u)_{\Gamma_R} = \int_{\Gamma_R} w u d\Gamma \quad (11)$$

$$L(w) = \int_{\Omega} wf d\Omega + \int_{\Gamma_R} wikh d\Gamma \quad (12)$$

and Γ_r is a d -dimensional sphere of radius r . Here $a(\cdot, \cdot)$ and $(\cdot, \cdot)_{\Gamma_R}$ are symmetric bilinear forms which are *not* inner products.

The limit in $a(\cdot, \cdot)$ must be evaluated in the context of the principle of limiting absorption (see p. 261 of Reference 24 and p. 360 of Reference 27). That is, we consider $k \leftarrow k + i\mu$, with $\mu > 0$.

The limit $r \rightarrow \infty$ is evaluated with μ held fixed and positive. Then the limit $\mu \downarrow 0$ is taken. Thus:

$$a(w, u) = \int_{\Omega^i \cup \Omega^o} (\nabla w \cdot \nabla u - wk^2 u) d\Omega - \lim_{\mu \downarrow 0} \lim_{r \rightarrow \infty} \int_{\Gamma_r} wi(k + i\mu) u d\Gamma \quad (13)$$

Where no confusion can arise, the limiting absorption shall not be written explicitly.

We define \mathcal{S}^o as the set of functions u^o for which (13) is defined and bounded, namely $\mathcal{S}^o = \{u^o \mid a(u^o, u^o) < \infty, u^o = 0 \text{ in } \Omega^i\}$. For cases in which the artificial boundary does not completely contain the scatterer, all essential boundary conditions on the boundaries of Ω^o must be satisfied by u^o and contributions of inhomogeneous natural boundary data must be included.

The stationary point of this functional is obtained by setting its first variation equal to zero, which is equivalent to:

$$a(w^i, u^i) + (w^i, \lambda)_{\Gamma_R} + a(w^o, u^o) - (w^o, \lambda)_{\Gamma_R} + (v, u^i - u^o)_{\Gamma_R} = L(w^i) \quad (14)$$

Here, $w^i \in \mathcal{V}^i$, $w^o \in \mathcal{V}^o$, and $v \in H^{-1/2}(\Gamma_R)$, are the arbitrary variations of u^i , u^o and λ , respectively. Accordingly, for Neumann problems $\mathcal{V}^i = \{w^i \mid w^i \in H^1(\Omega^i), w^i = 0 \text{ in } \Omega^o\}$; otherwise, homogeneous counterparts of Dirichlet boundary conditions on Γ_g must also be satisfied by functions in \mathcal{V}^i . In the outer field $\mathcal{V}^o = \mathcal{S}^o$. Note that no constraints are specified on the values of u^i and u^o across Γ_R , or on the values of w^i and w^o across Γ_R .

The mixed formulation (14) may be recast in partitioned form

$$\begin{aligned} a(w^i, u^i) &+ (w^i, \lambda)_{\Gamma_R} = L(w^i) \\ a(w^o, u^o) - (w^o, \lambda)_{\Gamma_R} &= 0 \\ (v, u^i)_{\Gamma_R} - (v, u^o)_{\Gamma_R} &= 0 \end{aligned} \quad (15)$$

The key stability condition for mixed formulations is the Babuška-Brezzi (inf-sup) condition (e.g. p. 57 of Reference 11) governing the selection of finite element interpolations. Discretization of (15) entails additional degrees of freedom enforcing the constraint and the typical ‘zero’ diagonal block (see p. 74 of Reference 11) which may lead to ill conditioning. We now discuss removing some of these drawbacks by eliminating λ from the formulation. In general, elimination of the Lagrange multiplier does not guarantee stability. However, in support of the plausibility of the procedure proposed herein, we note that one of the applications of its outcome leads to a new derivation of a known formulation (see Section 4), for which stability in the Babuška-Brezzi sense is not an issue.

3.3. Eliminating the Lagrange multiplier

The Euler-Lagrange equations of the second variational equation in (15) are the homogeneous Helmholtz equation

$$\mathcal{L}u^o = 0 \quad \text{in } \Omega^o \quad (16)$$

and the radiation condition (4) for u^o , and

$$\lambda = \frac{\partial u^o}{\partial n^o} \quad \text{on } \Gamma_R \quad (17)$$

where n^o denotes the outward normal with respect to Ω^o .

Equation (17) gives the interpretation of the Lagrange multiplier. We eliminate the Lagrange multipliers from the formulation by making this substitution and the analogous one for the weighting functions

$$v = \frac{\partial w^o}{\partial n^o} \quad \text{on } \Gamma_R \quad (18)$$

Therefore, for functions u^o that satisfy the homogeneous Helmholtz equation (16) and the radiation condition, equations (15) simplify considerably

$$a(w^i, u^i) + \left(w^i, \frac{\partial u^o}{\partial n^o} \right)_{\Gamma_R} = L(w^i) \quad (19)$$

$$\left(\frac{\partial w^o}{\partial n^o}, u^i \right)_{\Gamma_R} - \left(\frac{\partial w^o}{\partial n^o}, u^o \right)_{\Gamma_R} = 0$$

In this formulation there is integration only over the bounded domain and the artificial boundary. Thus, the outer field u^o may be viewed as specifying boundary conditions on the artificial boundary Γ_R , thereby defining a boundary-value problem for the inner field w^i in the bounded domain Ω^i . Continuity across the artificial boundary is weakly enforced by energy flux-like terms. Specifically, the second variational equation in (19) enforces continuity of the unknown functions across the artificial boundary. The Euler-Lagrange equations of the first of equations (19) provide satisfaction of the differential equation in Ω^i and enforce continuity of normal derivatives across the artificial boundary. Previous investigations of the well-posedness of bounded-domain formulations for exterior problems^{28,29} indicate that enforcing continuity of the functions *and* their normal derivatives is fitting.

Equations (19) have many advantages over the previous formulation, (15). The zero diagonal block associated with Lagrange multiplier methods is absent from (19). Similarly, there are no extra degrees of freedom enforcing the constraint. Perhaps most significantly, there is no integration over the unbounded domain Ω^o .

4. APPLICATIONS

Formulation (19) may be viewed as a general framework into which many existing finite element formulations for unbounded domains can fit as special cases. This framework is based on a rigorous derivation in which each requirement and assumption is explicitly stated. Therefore, it can serve not only as a starting point for the development of new methods, but also as a basis for theoretical evaluation and comparison of existing methods. In the following we specialize our framework to three different applications.

4.1. Hybrid asymptotic-numerical methods in scattering

The development of hybrid methods for short-wavelength scattering problems formed the original motivation for deriving our formulation. The essential idea is to utilize a ray ansatz for a geometrical description of the scattered field in those parts of the domain where it is valid, based on the Geometrical Theory of Diffraction^{30,31} (GTD), and to use traditional discretization in other parts of the domain. This approach requires one to be able to use entirely different basis functions over adjacent domains.

In the region Ω^o , the ray ansatz is valid. There the differential equation is *approximately* satisfied pointwise to a specified asymptotic order $\beta > 0$, as $kR \rightarrow \infty$:

$$\mathcal{L}u^o = O((kR)^{-\beta}) \quad \text{in } \Omega^o \quad (20)$$

On certain points, curves or surfaces, however, the ray ansatz is invalid. Ω^i is chosen to completely contain all such points and their neighbourhoods. In Ω^i , a numerical solution is sought which is patched to the ray ansatz along the artificial boundary. The location of the artificial boundary is selected on one hand to control the asymptotic approximation error of u^o and on the other hand to minimize the size of the computational domain. In this application the artificial boundary often does not completely contain the scatterer, so that *all* essential boundary conditions on the boundaries of Ω^o (except on Γ_R) must be satisfied by u^o .

A GTD-type analysis of the scattered solution yields the geometrical form of the field u^o with unknown 'diffraction coefficients'. This may be considered an approximation with global basis functions. The approximation of u^i in the diffraction region is in terms of traditional finite element interpolation with local support. These expressions (and admissible analogues for weighting functions) are substituted into equations (19). The lack of continuity across the artificial boundary, inherent in this approach, poses no difficulty. In solving (19), approximations of the diffraction coefficients of u^o and the nodal values of u^i are obtained simultaneously. Thus the geometrical form of u^o is employed to specify boundary conditions on a problem for u^i in the bounded Ω^i . Solving for u^i provides the unknown diffraction coefficients.

4.2. Absorbing boundary conditions, the DtN formulation

Formulations of exterior problems that are amenable to domain-based computation are often derived by introducing an artificial boundary into the problem to bound a computational domain Ω^i . Correct far-field behaviour is enforced by specifying non-reflecting (or absorbing) boundary conditions on this boundary. Numerous such schemes have been proposed, many of which are surveyed in the exhaustive reviews of References 1 and 2, pp. 95–116.

A noteworthy class of non-reflecting boundary conditions is obtained by the DtN method. This is a general scheme for handling boundary-value problems in unbounded domains, which employs a rigorous derivation to yield accurate boundary conditions. The method in its general form was developed by Givoli and Keller^{3,32} and is related to similar work in acoustics.^{4,5}

In terms of the notation employed herein, the boundary conditions in the Givoli–Keller derivation are obtained from an analytical solution u^o in the exterior region Ω^o . For this purpose, the artificial boundary is constructed in a relatively simple geometric shape (often a d -dimensional sphere, but not necessarily so, e.g. References 33 and 34), and located so that all geometric irregularities, non-linearities and source terms, as well as material anisotropy and inhomogeneity are contained within it. The analytical solution u^o , obtained for arbitrary Dirichlet conditions on the artificial boundary, is used to form a relation between the function and its derivatives, called a Dirichlet-to-Neumann (hence, DtN) map. This relation, which is the exact impedance, is then imposed as the boundary condition on the artificial boundary, completing the definition of the computational problem. Solving this problem determines the solution in the entire original region \mathcal{R} .

4.2.1. New derivation. The DtN boundary conditions have been derived anew recently in the multi-scale approach²⁶ based on the Green's function for the homogeneous Dirichlet problem in Ω^o . We now re-derive the DtN boundary conditions in the framework of our formulation (19), at first in abstract form, followed by an example in two dimensions.

We denote the homogeneous Dirichlet Green's function in Ω^o by $g(\mathbf{x}, \mathbf{x}')$. Here, $g(\mathbf{x}, \mathbf{x}')$ satisfies $\mathcal{L}g = -\delta(\mathbf{x} - \mathbf{x}')$, $g|_{\Gamma_R} = 0$, and g is outgoing. Consequently,

$$u^o(\mathbf{x}) = K(\mathbf{x}, \mathbf{x}') u^o(\mathbf{x}'), \quad \mathbf{x} \in \Omega^o, \quad \mathbf{x}' \in \Gamma_R \quad (21)$$

Here,

$$Ku^i = \int_{\Gamma_R} \frac{\partial g}{\partial n^o} u^i d\Gamma$$

Using g as the weighting function in the second of equations (19) together with (21) yields

$$u^o(\mathbf{x}) = K(\mathbf{x}, \mathbf{x}') u^i(\mathbf{x}'), \quad \mathbf{x} \in \Omega^o, \quad \mathbf{x}' \in \Gamma_R \quad (22)$$

Equation (22) is a relation for the outer field in terms of the inner field on the interface.

In the Givoli-Keller derivation of the DtN boundary condition, the analogue of equation (22) is an expression for the outer field in terms of arbitrary Dirichlet data on the artificial boundary. In Hughes's multi-scale approach, the analogous equation relates the outer field in Ω^o to the outer field on Γ_R . The interface Γ_R is usually chosen as a separable boundary. The Green's function may then be represented as a series of the products of d -dimensional spherical surface harmonics and Hankel functions in the radial direction.

The normal derivative of u^o is required for the first of equations (19)

$$\frac{\partial u^o}{\partial n^o}(\mathbf{x}) = M(\mathbf{x}, \mathbf{x}') u^i(\mathbf{x}'), \quad \mathbf{x} \in \Omega^o, \quad \mathbf{x}' \in \Gamma_R \quad (23)$$

Here $M = \partial K / \partial n^o$ is the standard DtN map. Substituting this expression into the first equation of (19) yields

$$a(w^i, u^i) + (w^i, Mu^i)_{\Gamma_R} = L(w^i) \quad (24)$$

Equation (24) is identical to the variational equation for u^i in the computational domain obtained by the Givoli-Keller derivation.^{3,32} It is equivalent to specifying the boundary condition

$$\frac{\partial u^i}{\partial n^i} = -Mu^i, \quad \text{on } \Gamma_R \quad (25)$$

in the strong form of the inner-field problem, where n^i denotes the outward normal with respect to Ω^i (Figure 2).

In the simple two-dimensional case the artificial boundary is a full circle, $\Gamma_R = \{(r, \theta) | r=R, 0 \geq 2\pi\}$. The general outgoing solution of the Helmholtz equation in Ω^o is

$$u^o = \sum_{n=0}^{\infty} H_n^{(1)}(kr) (a_n \cos n\theta + b_n \sin n\theta) \quad (26)$$

The prime on the sum indicates that the first term is halved. $H_n^{(1)}$ are Hankel functions of the first kind.

The coefficients a_n and b_n are unknown. By the Givoli-Keller derivation, these coefficients are expressed in terms of arbitrary Dirichlet data on the artificial boundary. The normal derivative on the artificial boundary is determined by differentiating (26), and is thus valid for arbitrary Dirichlet boundary data. The relation between u^o and its normal derivative on the artificial boundary is specified as the boundary condition for u^i on Γ_R , thereby completing the definition of the computational boundary-value problem in Ω^i .

The procedure just described is contained naturally in the variational equations (19). We assume that the outer weighting function has the same circumferential variation as the trial solution:

$$\frac{\partial w^o}{\partial n^o} = \sum_{n=0}^{\infty} \tilde{a}_n \cos n\theta + \tilde{b}_n \sin n\theta \quad (27)$$

Here, \tilde{a}_n and \tilde{b}_n are arbitrary. We note that the variation in the radial direction is unspecified since only values on the artificial boundary are required. Substituting the expressions into the second equation in (19) yields the coefficients in terms of u^i on Γ_R

$$\begin{aligned} a_n &= \frac{1}{\pi H_n^{(1)}(kR)} \int_0^{2\pi} \cos n\theta u^i(R, \theta) d\theta \\ b_n &= \frac{1}{\pi H_n^{(1)}(kR)} \int_0^{2\pi} \sin n\theta u^i(R, \theta) d\theta \end{aligned} \quad (28)$$

These expressions are substituted into the series representation of the outer-field solution (26), resulting in a specific definition of K and the well-known DtN map for this case

$$Mu^i = \sum_{n=0}^{\infty} a_n' \int_0^{2\pi} \cos n(\theta - \theta') u^i(R, \theta') d\theta' \quad (29)$$

The coefficients are

$$a_n := -\frac{k}{\pi} \frac{H_n^{(1)\prime}(kR)}{H_n^{(1)}(kR)} \quad (30)$$

The prime on functions denotes differentiation with respect to the argument.

Substituting the normal derivative of outer-field solution (26), with the computed coefficients a_n and b_n , into the first equation of (19) leads to a variational equation for u^i that is identical to the one obtained by Givoli and Keller. There is no difficulty in duplicating existing DtN formulations for more general configurations by this procedure.

We close this section by noting that we employed our procedure, starting with the mixed variational form (14), to derive a known formulation for which stability in the Babuška–Brezzi sense is not an issue.

4.2.2. Numerical examples. Numerical evaluations were performed on two-dimensional configurations of problems representing infinite cylinders of radius a . Soft boundary conditions are specified on the wet surface to represent a pressure-release cylinder. DtN non-reflecting boundary conditions with eight terms in the operator are employed on an artificial boundary Γ_R at $R=2a$. The inner domain Ω^i is discretized by 3×32 linear quadrilateral elements, so that element sides are roughly equal in length (Figure 3). The resolution is six node points per wavelength ($ka=\pi$, the wavelength is equal to the diameter of the cylinder). Eight terms in the DtN operator are sufficient to guarantee well-posedness of the computational problem under these conditions.^{28,29}

Radiation from an element of a cylinder: We consider the non-uniform radiation from an infinite circular cylinder with a constant inhomogeneous value on an arc ($-\alpha < \theta < \alpha$) and vanishing elsewhere. The normalized analytical solution to this problem for a cylinder of radius a is

$$u = \frac{2}{\pi} \sum_{n=0}^{\infty} \frac{\sin n\alpha}{n} \frac{H_n^{(1)}(kr)}{H_n^{(1)}(ka)} \cos n\theta \quad (31)$$

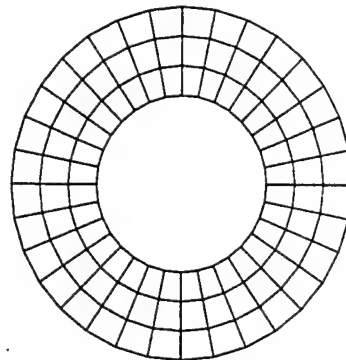


Figure 3. The computational domain exterior to a cylinder of radius a , with an artificial boundary at $R=2a$, discretized by 3×32 linear quadrilateral elements

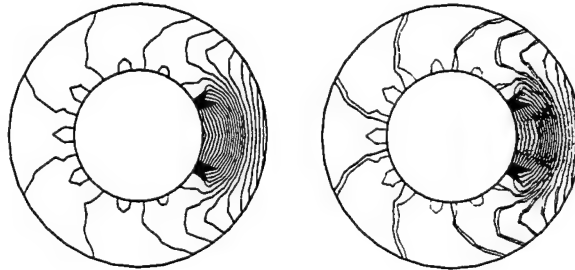


Figure 4. Radiation from an element of a cylinder of radius a , $R=2a$, $ka=\pi$, nodal interpolation of the series solution (31) by on the left, finite element solution on the right

For low wave numbers this solution is relatively uniform in the circumferential direction. The directionality of the solution grows as the wave number is increased, and the solution becomes attenuated at the side of the cylinder opposite the radiating element.

We select $\alpha=5\pi/32$. Figure 4 (left) shows the real part of the analytical solution, nodally interpolated by the mesh employed. The low-amplitude oscillations in the vicinity of the wet surface are merely an artifact of the truncated series representation of the discontinuity in the boundary condition, and are not relevant to the validation of the numerical results. The real part of the finite element solution with DtN boundary conditions is presented in Figure 4 (right), in comparison to the series solution denoted by the dotted contours. The numerical solution captures the essential features of the problem, demonstrating the effectiveness of the DtN boundary conditions in representing the radiation condition on the artificial boundary.

Scattering of a plane wave by a soft cylinder: The difference between an undisturbed wave and the field generated when the wave encounters an obstacle is called a scattered wave. As an example we compute the scattering, by an infinite cylinder of radius a , of a plane wave travelling along the positive x axis ($\theta=0$) in a direction perpendicular to the cylinder's axis. The normalized analytical solution of this problem is

$$u = -2 \sum_{n=0}^{\infty} i^n \frac{J_n(ka)}{H_n^{(1)}(ka)} H_n^{(1)}(kr) \cos n\theta \quad (32)$$

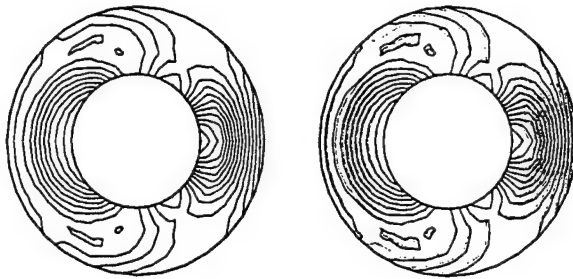


Figure 5. Scattering of a plane wave (at $\theta=0$) from a cylinder of radius a , series (left) and finite element (right) solutions

The directionality of the response increases with wave number, and the distribution becomes more complicated.

The real parts of the analytical solution (nodally interpolated by the mesh employed) and the finite element solution with DtN boundary conditions (in comparison to the series solution denoted by the dotted contours) are presented in Figure 5. Again the numerical solution represents the expected behaviour of the solution.

4.3. Infinite elements

The variational formulation (19) can provide a suitable basis for finite element computation in unbounded domains based on the infinite element concept. This is attained by considering the artificial boundary to be a closed surface, and by letting the infinite element interpolation satisfy the assumptions on the behaviour in the exterior domain (as outgoing solutions of the Helmholtz equation). Under these conditions we have an *infinite element formulation that is free of integration over the unbounded domain, and in which continuity of infinite element interpolation with piecewise polynomial finite element functions need not be assumed in advance*. As such, this approach may offer superior computational performance in practice (in addition to the advantage in eliminating the discretization of the unbounded domain). Further, we hope that the apparent simplicity of the formulation will ease the analytical burden associated with convergence proofs and error estimates of infinite element approximations.

Two approaches in developing infinite element interpolations are possible in this framework. In one approach, infinite element shape functions exactly satisfying the Helmholtz equation are used directly with equations (19). Weak continuity between the finite element shape functions and the infinite element shape functions on Γ_R is then enforced naturally. An alternative is to assume strong continuity between the finite element shape functions and the infinite element shape functions on Γ_R . Then, the infinite element shape functions (generally) do not identically satisfy the Helmholtz equation and a different error is introduced. Both cases may easily be developed within the wave envelope procedure,⁶ and the simplicity of the underlying formulation may provide a suitable setting to evaluate the merits of this procedure.

4.3.1. Approximation. The first class of shape functions consists of outgoing solutions of the Helmholtz equation. In most cases, the circumferential behaviour of these functions on the artificial boundary differs from piecewise polynomial variation of finite element shape functions. Weak enforcement of continuity across the artificial boundary is then performed naturally within the framework of our formulation (19). The infinite element mesh need not be the restriction of the finite element mesh to the artificial boundary. For each unknown in the infinite

element interpolation, the associated weighting function provides an equation to evaluate that unknown.

The basic two-noded element is obtained by combining linear interpolation in the circumferential direction, with $H_0^{(1)}(kr)/H_0^{(1)}(kR)$ in the radial direction. Strong continuity is satisfied when this infinite element mesh matches the restriction of a linear finite element mesh to the artificial boundary. This implementation is equivalent to the lowest-order local DtN boundary conditions.^{28,35} A high-wave number asymptotic approximation is obtained by replacing the Hankel function in the radial direction with $e^{ik(r-R)}\sqrt{R/r}$. Subsequent numerical results are based on this approximation. Generalizations involving trigonometric interpolation in the circumferential direction are possible.³⁶

An alternative approach is to require continuity across the artificial boundary in advance. In this case the second equality in (19) is satisfied identically and all that is required is an expression for $(\partial u^0/\partial n^0)|_{\Gamma_R}$ in terms of $u^i|_{\Gamma_R}$. Such an expression may be obtained by high-wave number asymptotic approximations of outgoing solutions of the Helmholtz equation

$$u^0 = A(r, \theta) e^{ik(r-R)} \quad (33)$$

Here A is expressed as an asymptotic expansion in inverse powers of ik . Such an expansion 'converges' as kR tends to infinity.

Higher-order approximations contain higher-order tangential derivatives, leading to increased coupling on the artificial boundary. For example, the approximation

$$A \sim A_0 + A_1(ik)^{-1} + O((ik)^{-2}) \quad (34)$$

yields the relation

$$\frac{\partial u^0}{\partial n^0} \sim \frac{-ik}{2} \left[(2 + i(kR)^{-1} + (kR)^{-2}) u^i + (kR)^{-2} \frac{\partial^2 u^i}{\partial \theta^2} \right] \quad \text{on } \Gamma_R \quad (35)$$

This may be compared to the two-term local DtN boundary conditions

$$\frac{\partial u}{\partial r} = k \left[\frac{H_0^{(1)'}(kR)}{H_0^{(1)}(kR)} u + \left(\frac{H_0^{(1)'}(kR)}{H_0^{(1)}(kR)} - \frac{H_1^{(1)'}(kR)}{H_1^{(1)}(kR)} \right) \frac{\partial^2 u}{\partial \theta^2} \right] \quad \text{on } \Gamma_R \quad (36)$$

where the derivatives on the Hankel functions are with respect to their argument.

This framework offers an unconventional perspective on infinite element computation that may be used to shed light on some of the outstanding issues in the field, such as integration over the surface at infinity and cancellation of ill-defined integrals in the unbounded domain. This formulation also provides a suitable basis for comparing infinite elements with other common representations of the radiation condition, namely, non-reflecting boundary conditions such as the Bayliss-Turkel conditions,³⁷ and the global and local DtN conditions.

4.3.2. Numerical examples. Numerical evaluations of two-noded infinite elements with asymptotic radial behaviour were performed on the problem of radiation from an element of an infinite cylinder with the parameters described previously, except where otherwise noted. The analytic solution is given in equation (31). The mesh employed is shown in Figure 3.

We select $\alpha = \pi/2$. Figure 6 shows the variation of the infinite element solution along the artificial boundary Γ_R , compared to the DtN solution. The results are virtually indistinguishable.

This infinite element is based on a high wave number approximation, so its performance deteriorates at lower wave numbers. This is demonstrated in Figure 7 which shows the variation of the

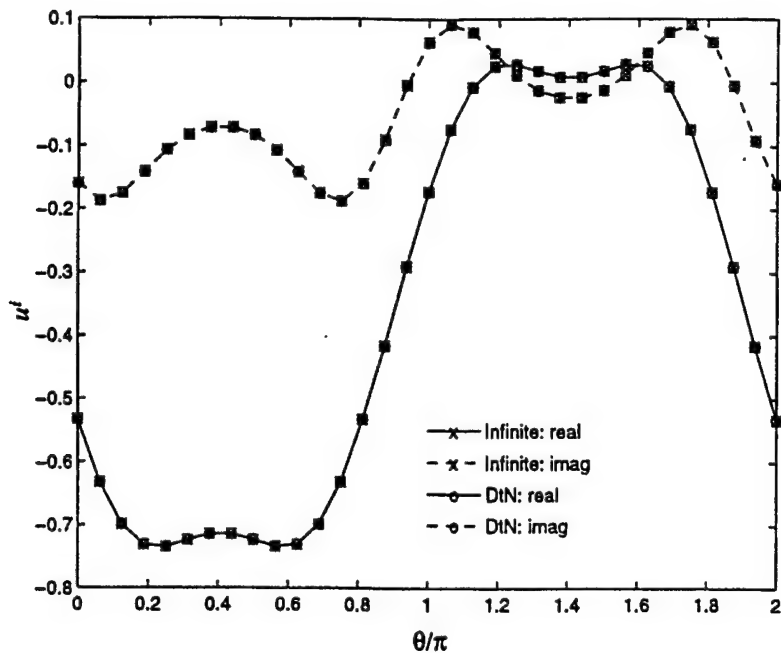


Figure 6. Radiation from an element of a cylinder of radius a , $R=2a$, $ka=\pi$, infinite element and DtN solutions along by artificial boundary Γ_R

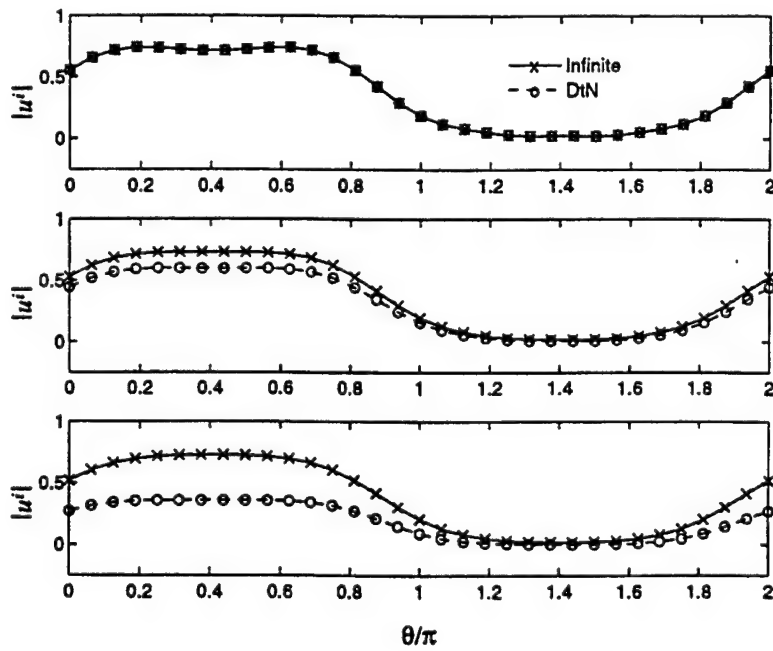


Figure 7. Radiation from an element of a cylinder of radius a , $R=2a$, magnitude of infinite element and DtN solutions by along artificial boundary Γ_R at $kR=2\pi$ (top), $kR=3\pi/2$ (middle), and $kR=\pi$

infinite element solution along the artificial boundary Γ_R at different wave numbers, again compared to the DtN solution. There is good agreement at $kR=2\pi$, but the infinite element solution progressively degrades at $kR=3\pi/2$ and $kR=\pi$. This is merely an indication of too low a wave number for the asymptotic approximation, which may be alleviated by increasing the size of the computational domain.

5. CONCLUSIONS

A general framework for developing finite element formulations for solving exterior problems is presented in this work, with particular application to time-harmonic acoustics. The original motivation for constructing this framework is the development of hybrid analytic-numerical methods for acoustic scattering. The unbounded domain is partitioned into a bounded domain containing diffraction regions and its unbounded complement, in which a geometrical description is employed. The functions in this application lack strong continuity across the interface, so it is enforced weakly via Lagrange multipliers. By identifying the Lagrange multipliers as normal derivatives on the interface, they are eliminated from the formulation. With the additional assumption that the outer field satisfies the differential equation, this leads to a mixed formulation (19) defined only in the bounded domain and on the interface. In terms of hybrid methods, the analytic representation of the outer field may be viewed as specifying boundary conditions for the inner field on the interface, thereby completing the definition of a problem in a bounded domain which is amenable to finite element computation.

By selecting specific representations of the outer field, several methods underlying finite element computation of exterior problems are obtained as specific instances of the mixed variational equations (19). Examples of formulations employing DtN non-reflecting boundary conditions are reproduced. Employing infinite element interpolations for the outer field in (19) yields methods that are devoid of integration over the unbounded domain, simplifying the task of discretization. Strong continuity with finite element interpolation is not a prerequisite. This unconventional approach to infinite element computation has the potential of leading to numerous theoretical and practical benefits.

ACKNOWLEDGEMENTS

The authors wish to thank Ivo Babuška, Helio Barbosa, Luise Couchman, Danny Givoli, Tom Hughes, Geoff Main, Allan Pierce and Joseph Shirron for helpful comments and discussions. This research was supported by the U.S. Office of Naval Research.

REFERENCES

1. D. Givoli, *Numerical Methods for Problems in Infinite Domains*, Elsevier, Amsterdam, 1992.
2. N. N. Abboud, 'A mixed finite element formulation for the transient and harmonic exterior fluid-structure interaction problem', *Ph.D. Thesis*, Stanford University, 1990.
3. D. Givoli and J. B. Keller, 'A finite element method for large domains', *Comput. Methods Appl. Mech. Eng.*, **76**, 41–66 (1989).
4. K. Feng, 'Asymptotic radiation conditions for reduced wave equation', *J. Comp. Math.*, **2**, 130–138 (1984).
5. M. Masmoudi, 'Numerical solution for exterior problems', *Numer. Math.*, **51**, 87–101 (1987).
6. R. J. Astley, G. J. Macaulay and J.-P. Coyette, 'Mapped wave envelope elements for acoustical radiation and scattering', *J. Sound Vib.*, **170**, 97–118 (1994).
7. P. Bettess, 'Infinite elements', *Int. j. numer. methods eng.*, **11**, 53–64 (1977).
8. D. S. Burnett, 'A three-dimensional acoustic infinite element based on a prolate spheroidal multipole expansion', *J. Acoust. Soc. Am.*, **96**, 2798–2816 (1994).
9. O. C. Zienkiewicz, K. Bando, P. Bettess, C. Emson and T. C. Chiam, 'Mapped infinite elements for exterior wave problems', *Int. j. numer. methods eng.*, **21**, 1229–1251 (1985).

10. P. E. Barbone and I. Harari, 'Hybrid asymptotic-numerical method for evaluating diffraction coefficients', *J. Acoust. Soc. Am.*, **98**, 2910 (1995). Presented at 130th Meeting of the Acoust. Soc. Am., St. Louis, Mo, November 1995.
11. F. Brezzi and M. Fortin, *Mixed and Hybrid Finite Element Methods*, Springer, New York, 1991.
12. I. Babuška, 'The finite element method with Lagrangian multipliers', *Numer. Math.*, **20**, 179–192 (1973).
13. J. R. O'Leary and I. Harari, 'Finite element analysis of stiffened plates', *Comp. Struct.*, **21**, 973–985 (1985).
14. M. A. Aminpour, J. B. Ransom and S. L. McCleary, 'Coupled analysis method for structures with independently modelled finite element subdomains', *Int. j. numer. methods eng.*, **38**, 3695–3718 (1995).
15. C. Farhat and M. Geradin, 'Using a reduced number of Lagrange multipliers for assembling parallel incomplete field finite element approximations', *Comput. Methods Appl. Mech. Eng.*, **97**, 333–354 (1992).
16. H. J. C. Barbosa and T. J. R. Hughes, 'The finite element method with Lagrange multipliers on the boundary: Circumventing the Babuška-Brezzi condition', *Comput. Methods Appl. Mech. Eng.*, **85**, 109–128 (1991).
17. R. Stenberg, 'On some techniques for approximating boundary conditions in the finite element method', *J. Comp. Appl. Math.*, **63**, 139–148 (1995).
18. J. Nitsche, 'Über ein variationsprinzip zur lösung von Dirichlet-problemen bei verwendung von Teilräumen, die keinen randbedingungen unterworfen sind', *Abh. Math. Univ. Hamburg*, **36**, 9–15 (1971).
19. S. A. Key, 'A specialization of Jones' generalization of the direct-stiffness method of structural analysis', *AIAA J.*, **9**, 984–985 (1971).
20. H. A. Mang and R. H. Gallagher, 'A critical assessment of the simplified hybrid displacement method', *Int. j. numer. methods eng.*, **11**, 145–167 (1977).
21. R. H. Gallagher, E. Haugeneder and H. A. Mang, 'Limitations on methods of handling incompatible basis functions in boundary value problems', *Trans. Am. Nucl. Soc.*, **33**, 326–327 (1979).
22. E. Haugeneder and H. A. Mang, 'On an improper modification of a variational principle for finite element plate analysis', *Zeitschrift für Angewandte Mathematik und Mechanik*, **59**, 637–640 (1979).
23. E. Haugeneder and H. A. Mang, 'Admissible and inadmissible simplifications of variational methods in finite element analysis', in S. Nemat Nasser (ed.) *Variational Methods in the Mechanics of Solids*, Pergamon Press, Oxford, 1980.
24. I. Stakgold, *Boundary Value Problems of Mathematical Physics*, Vol. II, Macmillan, New York, 1968.
25. C. H. Wilcox, *Scattering Theory for the d'Alembert Equation in Exterior Domains*, Springer, Berlin, 1975.
26. T. J. R. Hughes, 'Multiscale phenomena: Green's functions, the Dirichlet-to-Neumann formulation, subgrid scale models, bubbles, and the origins of stabilized methods', *Comput. Methods Appl. Mech. Eng.*, **127**, 387–401 (1995).
27. J. Sanchez Hubert and E. Sanchez Palencia, *Vibration and Coupling of Continuous Systems*, Springer, Berlin, 1989.
28. I. Harari and T. J. R. Hughes, 'Analysis of continuous formulations underlying the computation of time-harmonic acoustics in exterior domains', *Comput. Methods Appl. Mech. Eng.*, **97**, 103–124 (1992).
29. I. Harari and T. J. R. Hughes, 'Studies of domain-based formulations for computing exterior problems of acoustics', *Int. j. numer. methods eng.*, **37**, 2935–2950 (1994).
30. J. B. Keller, 'Geometrical theory of diffraction', *J. Opt. Soc. Am.*, **52**, 116–130 (1962).
31. J. B. Keller, 'One hundred years of diffraction theory', *IEEE Trans. Ant. Prop.*, AP-33, 123–126 (1985).
32. J. B. Keller and D. Givoli, 'Exact non-reflecting boundary conditions', *J. Comp. Phys.*, **82**, 172–192 (1989).
33. M. J. Grote and J. B. Keller, 'On nonreflecting boundary conditions', *J. Comp. Phys.*, **122**, 231–243 (1995).
34. J. M. Montgomery and P. E. Barbone, 'Diffraction from simple shapes by a hybrid asymptotic-numerical method', *Technical Report No. AM-96-011*, Boston University, Department of Aerospace & Mechanical Engineering, 2 May 1996.
35. D. Givoli and J. B. Keller, 'Non-reflecting boundary conditions for elastic waves', *Wave Motion*, **12**, 261–279 (1990).
36. I. Harari, P. E. Barbone and M. Slavutin, Boundary infinite elements, *Technical Report No. AM-96-009*, Boston University, Department of Aerospace & Mechanical Engineering, 27 March 1996.
37. A. Bayliss and E. Turkel, 'Radiation boundary conditions for wave-like equations', *Commun. Pure Appl. Math.*, **33**, 707–725 (1980).

C.11 Approximate Diffraction Coefficients by the Method of Matched Asymptotic Expansions

"Approximate Diffraction Coefficients by the Method of Matched Asymptotic Expansions,"
Paul E. Barbone, **Wave Motion**, Vol. 22, pp. 1-16, 1995.

Reprinted from

WAVE MOTION

An International Journal
Reporting Research on Wave Phenomena

Wave Motion 22 (1995) 1-16

Approximate diffraction coefficients by the method of matched asymptotic expansions

Paul E. Barbone

Department of Aerospace & Mechanical Engineering, Boston University, Boston, MA 02215, USA

Received 24 May 1994





Approximate diffraction coefficients by the method of matched asymptotic expansions

Paul E. Barbone

Department of Aerospace & Mechanical Engineering, Boston University, Boston, MA 02215, USA

Received 24 May 1994

Abstract

We treat the problem of scattering by an impedance surface as a singular perturbation from scattering by a hard surface. We suggest that this method of approach can yield useful approximations to diffraction coefficients where exact solutions are unavailable or complicated. We substantiate this claim by considering a simple problem where an exact solution is available. We use matched asymptotic expansions to develop a description of the field radiated by a source near an impedance surface. From this calculation, we extract a one-term uniformly valid (in angle) approximation to the far-field directivity, and a one-term approximation to the surface wave excitation coefficient. The uniform directivity is within 10% of the exact solution for values of ϵ (the small parameter) up to unity. The approximate surface wave amplitude is within approximately 10% for values of $0 < \epsilon \leq 1/2$.

1. Introduction

The plane wave reflection coefficient for an impedance surface is -1 at grazing angles of incidence. This limit is independent of the magnitude of the impedance of the surface. The reflection coefficient of a hard surface, on the other hand, is $+1$, independent of the angle of incidence. Thus, the grazing limit of a hard surface is not equal to the hard surface limit of grazing incidence. The source of the singular behavior of acoustic fields propagating near a nearly-hard surface has been the subject of many studies in the past.

In 1951, both Ingard [6] and Lawhead and Rudnick [8] published papers examining the field near an impedance plane due to a point source above that plane. The results of the two papers were found to disagree. Resolution of the disagreement was not possible without a full treatment of the interaction between a saddle point and a pole in a Fourier integral, as was being developed during the 1960s [3]. Wenzel's results [9] in the early 1970s have since been confirmed by Chien and Soroka [4], and a full review of the problem is presented by Attenborough et al. [2]. In all these papers, the authors present approximate evaluations of the formally exact expression of the field radiated by a point source above an infinite impedance plane.

The problem of scattering by a nearly rigid object can be thought of as a perturbation from a rigid surface. Though it is a singular perturbation, we show here that it is amenable to solution by the method of matched asymptotic expansions. Matched asymptotic expansions have the benefit that a uniformly valid expansion can be derived, even when an exact solution is not known for that geometry. Thus we anticipate that similar perturbation procedures can be used to find approximations to diffraction coefficients from objects with complicated boundary conditions and shapes.

Here we examine the problem of an acoustic line source above an impedance plane. We derive a solution uniformly valid near the surface of the impedance plane using matched asymptotic expansions. The leading order behavior in each of four separate regions of the domain is identified and shown to match with the neighboring regions. These four regions can be identified as: the inner region near the source, the outer region, the near surface region, and a surface wave boundary layer region. The results derived here agree asymptotically with a uniformly valid expansion of the exact solution, presented in the appendix.

As a means of quantitative comparison, we compare the far-field directivity and surface wave amplitude predicted by the method of matched asymptotics to those from the exact solution. Based on the agreement found in this comparison, we conclude that the method of matched asymptotics can be used to compute diffraction coefficients by solving singular perturbation problems from a hard surface.

2. Formulation

We consider an acoustic line source located on the surface bounding a half-space. The half-space is filled with an acoustic fluid with sound speed c , the surface is characterized by a specific admittance β , and a time dependence of $e^{-i\omega t}$ shall be assumed throughout.

The boundary value problem governing the acoustic pressure $\tilde{p}(\tilde{x}, \tilde{z})$ is:

$$\frac{\partial^2}{\partial \tilde{x}^2} \tilde{p} + \frac{\partial^2}{\partial \tilde{z}^2} \tilde{p} + k^2 \tilde{p} = 0, \quad \text{in } \tilde{z} > 0, \quad (1)$$

$$\frac{\partial \tilde{p}}{\partial \tilde{z}} + \beta \tilde{p} = \delta(\tilde{x}), \quad \text{on } \tilde{z} = 0, \quad (2)$$

$$\tilde{p}(\tilde{x}, \tilde{z}) \text{ is outgoing} \quad \text{as } \tilde{r} \rightarrow \infty. \quad (3)$$

Here, $k = \omega/c$ is the wavenumber and β is the specific acoustic admittance. We have already scaled the pressure linearly with the source strength. The parameter that naturally arises as a perturbation parameter, $\epsilon \equiv \beta/k$, is the ratio of two lengths. Therefore, we can expect that the perturbation may be singular [5].

2.1. Inner problem and solution

We shall now define our inner problem by non-dimensionalizing the distances that appear in (1)–(3) with respect to the wavelength. Thus, we define

$$X = k\tilde{x}, \quad Z = k\tilde{z}, \quad \epsilon = \beta/k. \quad (4)$$

We now substitute (4) into (1)–(3) to find:

$$\frac{\partial^2 P}{\partial X^2} + \frac{\partial^2 P}{\partial Z^2} + P = 0, \quad \text{in } Z > 0, \quad (5)$$

$$\frac{\partial P}{\partial Z} + \epsilon P = \delta(X), \quad \text{on } Z = 0. \quad (6)$$

Here, $P(X, Z) = \tilde{p}(\tilde{x}, \tilde{z})$ is the acoustic pressure and is denoted by a capital letter to indicate that it depends on the inner variables (X, Z) .

We now solve equations (5) and (6) by seeking a solution in the form

$$P(X, Z) = P_0(X, Z) + \epsilon P_1(X, Z) + O(\epsilon^2). \quad (7)$$

It is a straightforward matter to calculate $P_0(X, Z)$ and $P_1(X, Z)$. Therefore we present only the results here:

$$P_0(X, Z) = \frac{1}{2\pi i} \int_{-\infty}^{\infty} \mu^{-1}(\sigma) e^{i\sigma X + i\mu(\sigma)Z} d\sigma, \quad (8)$$

$$P_1(X, Z) = \frac{1}{2\pi} \int_{-\infty}^{\infty} (1 - \sigma^2)^{-1} e^{i\sigma X + i\mu(\sigma)Z} d\sigma. \quad (9)$$

Here $\mu(\sigma) = (1 - \sigma^2)^{1/2}$, with the branch chosen to satisfy the radiation condition at infinity. We note that P_0 may be written in a more familiar form in terms of a Hankel function, but that given in (8) is convenient for our purposes. It is interesting to evaluate (9) on the boundary $Z=0$. Then the integral in (9) can be evaluated exactly via Cauchy's residue theorem yielding

$$P_1(X, 0) = (-i/2) e^{i|X|}. \quad (10)$$

We note that (10) resembles a plane wave propagating along the surface without attenuation or algebraic decay.

2.2. Outer problem and solution

We now define the outer problem. In the previous section, we nondimensionalized distances by the small length scale, k^{-1} (wavelength). Here we rescale the problem in terms of the longer length scale, β^{-1} (impedance). Therefore, we define the outer variables:

$$x = \beta \tilde{x}, \quad z = \beta \tilde{z}. \quad (11)$$

We now substitute (11) into (1)–(3) to find:

$$\frac{\partial^2 p}{\partial x^2} + \frac{\partial^2 p}{\partial z^2} + \epsilon^{-2} p = 0, \quad \text{in } z > 0, \quad (12)$$

$$\frac{\partial p}{\partial z} + p = \delta(x), \quad \text{on } z = 0, \quad (13)$$

$$p(x, z) \text{ is outgoing,} \quad \text{as } r \rightarrow \infty. \quad (14)$$

Here, $p(x, z) = P(X, Z)$ is the acoustic pressure and is denoted by a lower case letter to indicate that it depends on the outer variables.

We note that the expansion for small ϵ in equations (12)–(14) is equivalent to a short wavelength expansion. Therefore, we seek a solution of equations (12)–(14) in the form:

$$p = \epsilon^m A(x, z) e^{i\phi(x, z)/\epsilon}, \quad (15)$$

$$A(x, z) = A_0(x, z) + \epsilon A_1(x, z) + O(\epsilon^2). \quad (16)$$

The factor ϵ^m is inserted for scaling purposes. The value of m shall be determined by matching to the inner solution.

2.2.1. Determination of $A_0(x, z)$ and $A_1(x, z)$

To determine the forms of $A_0(x, z)$ and $A_1(x, z)$, we substitute (15) and (16) into Eq. (12), and set each power of ϵ to zero independently. Thus we find:

$$(\nabla \phi(x, z))^2 - 1 = 0, \quad (17)$$

$$2\nabla \phi \cdot \nabla A_0 + \Delta \phi A_0 = 0, \quad (18)$$

$$2\nabla \phi \cdot \nabla A_1 + \Delta \phi A_1 = i\Delta A_0. \quad (19)$$

We assume the initial condition for $\phi(x, z)$ is $\phi(0, 0) = 0$. Solving (17) subject to this initial condition yields

$$\phi(x, z) = r \equiv (x^2 + z^2)^{1/2}. \quad (20)$$

The solution $\phi = -r$ is excluded by the radiation condition. Upon substituting (20) into (18) and (19), we find that

$$A_0(x, z) = D_0(\theta) r^{-1/2}, \quad (21)$$

$$A_1(x, z) = D_1(\theta) r^{-1/2} - \frac{i}{2} \left(\frac{1}{4} D_0(\theta) + D_0''(\theta) \right) r^{-3/2}. \quad (22)$$

Here, $D_0(\theta)$ and $D_1(\theta)$ are as yet undetermined functions of θ . The angle θ is measured from the positive x -axis so that $x = r \cos \theta$. We note that the field thus derived represents a cylindrical wave emanating from the source and propagating into the fluid.

We now consider the boundary condition, (13). We substitute (15) into (13) and obtain (for $x \neq 0$)

$$\frac{\partial \phi}{\partial z} A_0 = 0, \quad (23)$$

$$\frac{\partial \phi}{\partial z} A_1 = \frac{\partial A_0}{\partial z} - A_0. \quad (24)$$

We note that ϕ as given in (20) automatically satisfies (23). Upon considering Eq. (24), however, we see that $\partial \phi / \partial z = 0$ leads to an unbounded prediction for A_1 . Therefore, we must reconsider our ansatz in the vicinity of the surface $z = 0$. We shall address this issue once the matching has been accomplished.

3. Matching inner and outer solutions

We shall now match the inner and outer solutions and thus determine the functions $D_0(\theta)$, $D_1(\theta)$. For this purpose, we appeal to Van Dyke's matching principle [5] using two terms in both the inner and outer expansions.

We begin the matching by writing the inner solution ((7) with (8) and (9)) in terms of outer variables:

$$P \sim \frac{1}{2\pi i} \int_{-\infty}^{\infty} \mu^{-1} e^{i\alpha x/\epsilon + i\mu z/\epsilon} d\sigma + \frac{\epsilon}{2\pi} \int_{-\infty}^{\infty} \mu^{-2} e^{i\alpha x/\epsilon + i\mu z/\epsilon} d\sigma. \quad (25)$$

Expanding (25) for small ϵ by the method of steepest descents yields

$$P \sim \frac{1}{2i} \sqrt{\frac{2\epsilon}{\pi r}} e^{ir/\epsilon - i\pi/4} [1 - i\epsilon/8r + O(\epsilon/r^2)] + \frac{\epsilon}{2} \sqrt{\frac{2\epsilon}{\pi r}} \frac{e^{-i\pi/4}}{\sin \theta} e^{ir/\epsilon} [1 + O(\epsilon/r)], \quad z \neq 0. \quad (26)$$

Eq. (26) is what Van Dyke refers to as the "outer expansion of the inner expansion".

We now find the inner expansion of the outer expansion. The outer expansion consists of an expanding cylindrical wave, described by (15) with (20) and (21).

$$p \sim \epsilon^n [[D_0(\theta) + \epsilon D_1(\theta)] r^{-1/2} - i\epsilon \frac{1}{2} (\frac{1}{4} D_0(\theta) + D_0''(\theta)) r^{-3/2}] e^{ir/\epsilon}. \quad (27)$$

Writing (27) in terms of inner variables, expanding to two terms, and then rewriting in terms of outer variables simply recovers (27) back again. Thus, the matching in this case can be carried out by a simple comparison of (26) and (27), which shows that

$$D_0 = \frac{1}{2i} \sqrt{\frac{2}{\pi}} e^{-i\pi/4}, \quad (28)$$

$$D_1 = \frac{1}{2} \sqrt{\frac{2}{\pi}} \frac{e^{-i\pi/4}}{\sin \theta}, \quad (29)$$

$$m = 1/2. \quad (30)$$

The unknown coefficients in the outer expansion (27) are thus determined. We note that the inner expansion in this case yields as much information as the outer expansion. That is, the far-field form of the inner expansion is equivalent to the outer expansion (27) *in this case*. So, we can conclude that (25) is valid at least wherever (27) is valid.

We note that $D_1(\theta)$ becomes infinite at $\theta=0, \pi$, thus confirming our conjecture that the outer expansion would break down on $z=0$. We shall now describe how to overcome the non-uniformity at $z=0$.

4. Surface waves

The term $A_1(r, \theta)e^{ir/\epsilon}$ becomes unbounded on $z=0$. This can be understood to be necessary because the outer expansion (27) does not satisfy the boundary condition there. To overcome this nonuniformity in the expansion, we must reconsider the form of the solution on the boundary. In particular, we must match $A_1(r, \theta)e^{ir/\epsilon}$ to a solution defined near the boundary that satisfies the boundary condition.

We expect that the solution near the surface will include propagating free waves. We determine the characteristics of these waves by assuming the form

$$p_{\text{surface}} \propto \exp(i\sigma_0 x + i\mu_0 z). \quad (31)$$

We then substitute the assumed form (31) into the governing Eq. (12) and boundary condition (13), to find

$$\sigma_0 = \pm \epsilon^{-1} \sqrt{1 + \epsilon^2}, \quad (32)$$

$$\mu_0 = i. \quad (33)$$

The positive (negative) sign in (32) corresponds to a wave propagating in the positive (negative) X direction. These considerations, combined with the radiation condition, indicate that the field near the impedance surface is:

$$p_{\text{surface}} = E\epsilon \exp[i\sqrt{1 + \epsilon^2} |x|/\epsilon - z]. \quad (34)$$

Here E is an unknown constant, representing the *excitation coefficient* of the surface wave. The power of ϵ is chosen to facilitate matching to the first order field in the outer solution (27). The surface wave field decays exponentially with distance from the surface and is therefore “trapped” near the surface.

4.1. Boundary layer between the surface wave and the cylindrical wave

We shall now derive a boundary layer solution that describes the transition from the outer cylindrical wave field (27) to the surface wave field (34) near the surface. We assume that the field in the boundary layer has the form

$$p_{\text{bdry layer}} = E\epsilon \alpha(x, z) \exp[i\sqrt{1 + \epsilon^2} x/\epsilon - z]. \quad (35)$$

We must find $\alpha(x, z)$ so that $p_{\text{bdry layer}}$ in (35) matches to the cylindrical wave field (27) away from the boundary, and matches the surface wave field (34) near the boundary. We shall show this calculation explicitly only for $x > 0$. The field in the region $x < 0$ can be obtained by symmetry.

To do so, we substitute (35) into (12) and find that $\alpha(x, z)$ satisfies

$$\frac{\partial^2}{\partial x^2} \sigma + \frac{\partial^2}{\partial z^2} \alpha + 2i\epsilon^{-1} \sqrt{1+\epsilon^2} \frac{\partial}{\partial x} \alpha - 2 \frac{\partial}{\partial z} \alpha = 0. \quad (36)$$

The third and fourth terms in (36) represent a gradient in a particular direction. We find it convenient to work in a coordinate system aligned with that direction. Therefore, we introduce the variables (ξ, η) such that

$$\begin{pmatrix} x \\ z \end{pmatrix} = \begin{bmatrix} \sqrt{1+\epsilon^2} & -i\epsilon \\ i\epsilon & \sqrt{1+\epsilon^2} \end{bmatrix} \begin{pmatrix} \xi \\ \eta \end{pmatrix}. \quad (37)$$

The matrix appearing on the right hand side of Eq. (37) is orthogonal, thus the transformation of coordinates can be thought of as a simple rotation¹. In terms of the new variables (37), Eq. (36) becomes

$$\frac{\partial^2}{\partial \xi^2} \alpha + \frac{\partial^2}{\partial \eta^2} \alpha + 2i\epsilon^{-1} \frac{\partial}{\partial \xi} \alpha = 0. \quad (38)$$

We now magnify the η direction so as to balance the highest derivatives in η with the ϵ^{-1} term in (38). Therefore, we introduce the inner boundary layer variables (Ξ, H) as

$$\Xi = \xi, \quad H = \epsilon^{-1/2} \eta. \quad (39)$$

In terms of these variables, we seek solutions of (38) in the form

$$\alpha(x, z) \sim \alpha_0(\Xi, H). \quad (40)$$

Upon substituting (39) and (40) into (38), we find

$$\frac{\partial^2}{\partial H^2} \alpha_0 + 2i \frac{\partial}{\partial \Xi} \alpha_0 = O(\epsilon). \quad (41)$$

The general solution of Eq. (41) can be written in the form [10]

$$\alpha_0 = \frac{1}{\sqrt{\Xi}} \int_{-\infty}^{\infty} f(s) e^{i(H-s)^2/2\Xi} ds. \quad (42)$$

The function $f(s)$ is to be determined by matching the boundary layer solution to the surface wave solution.

To carry out the matching procedure, we write (42) in terms of outer variables and expand for small ϵ by the method of stationary phase. This process yields

$$\alpha_0 \sim \sqrt{2\pi} e^{i\pi/4} / (z\sqrt{1+\epsilon^2} - i\epsilon z). \quad (43)$$

Here, we have changed back to the outer variables. Using (43) in (35) gives the near surface pressure as

$$p_{\text{bdry layer}} \sim E\epsilon \sqrt{2\pi} e^{i\pi/4} f(z - i\epsilon z) e^{i\sqrt{1+\epsilon^2}|x|/\epsilon - z}. \quad (44)$$

When $z=0$, we require $f(-i\epsilon z) = e^{-i\pi/4}/\sqrt{2\pi}$ so that (44) matches (34). When $z=O(1)$, on the other hand, we require the surface wave to vanish and so $f=0$. Therefore, we choose $f(\eta)$ to be

¹ The angle of rotation corresponding to the change of coordinates in Eq. (37) is complex. It represents the direction of the complex surface wave ray being shed from the surface to the real point (x, z) . A full motivation and interpretation of complex surface wave rays can be found in the landmark paper of Keller and Karal [7]. Here, the rotation into the complex plane is introduced merely as a mathematical convenience. The necessity to analytically continue the solution into the complex plane in order to achieve matching, however, is dictated by the fact that the line $z=0$ is a "Stokes line", and $z=\epsilon z/\sqrt{1+\epsilon^2}$ is an "anti-Stokes line". Therefore the complex angles introduced on a purely geometrical basis by Keller and Karal are seen to be relevant in the current context. (We warn the reader that some authors use the reverse terminology for Stokes lines. We choose to follow the nomenclature in Ref. [3]).

$$f(\eta) = \begin{cases} e^{-i\pi/4}/\sqrt{2\pi}, & \text{for } \Re\eta < -\Im\eta \\ 0 & \text{for } \Re\eta > -\Im\eta. \end{cases} \quad (45)$$

We now combine Eqs. (35), (42) and (45) to obtain the form of the boundary layer solution

$$p_{\text{bdry layer}} \sim \frac{E\epsilon e^{i\xi/\epsilon - i\pi/4}}{\sqrt{\epsilon 2\pi\xi}} \int_{-\infty}^0 e^{i(\eta-s)^2/2\epsilon\xi} ds = \frac{E\epsilon}{2} e^{i\xi/\epsilon} \operatorname{erfc}[e^{-i\pi/4}\eta/\sqrt{2\epsilon\xi}]. \quad (46,47)$$

Here, the complimentary error function is defined to be [1]

$$\operatorname{erfc} z = \frac{2}{\sqrt{\pi}} \int_z^\infty e^{-t^2} dt. \quad (48)$$

Eq. (46), or equivalently (47), describes the transition between the surface wave near the boundary and the cylindrical wave field far from the boundary. The transition occurs with a region where $|\eta^2/2\epsilon\xi| \ll 1$, or when

$$|z - i\epsilon x| \ll (\epsilon x)^{1/2}. \quad (49)$$

Equation (49) shows that along $z=0$, the boundary layer solution (47) describes the leading order correction to the field for distances $x \ll O(\epsilon^{-1})$. Therefore, the surface wave does not fully reveal itself until $|x| \sim \epsilon^{-1}$.

4.2. Matching the surface wave to the cylindrical wave

The excitation coefficient of the surface wave, E , has yet to be determined. This shall be found by matching the boundary layer solution (46) to the outer solution (27).

Eq. (46) is already written in terms of the outer variables (ξ, η) . The two leading terms of the expansion of the integral in (46) come from the stationary point and the endpoint, respectively. Thus expanding (46) for small ϵ yields

$$p_{\text{bdry layer}} \sim E\epsilon \mathcal{H}(-\Im(e^{i\pi/4}\eta)) \exp[i\xi/\epsilon] + \frac{E\epsilon^2 e^{i\pi/4}}{\sqrt{2\pi\epsilon\xi}} \frac{\xi}{\eta} \exp i\xi(1 + \eta^2/2\xi^2)/\epsilon. \quad (50)$$

Here, $\mathcal{H}(z)$ is the Heaviside step function. Eq. (50) is the “outer of the inner” expansion. We now proceed to find the “inner of the outer”.

From (22) and (28)–(30) we have

$$\epsilon^{3/2} A_1(r, \theta) e^{ir/\epsilon} = \epsilon^{3/2} \frac{e^{-i\pi/4}}{\sqrt{2\pi}} \left[\frac{1}{\sin \theta} - 1/8r \right] r^{-1/2} e^{ir/\epsilon}. \quad (51)$$

We now write (51) in terms of the inner (boundary layer) variables (Ξ, H) and expand to find

$$\epsilon^{3/2} A_1(r, \theta) e^{ir/\epsilon} \sim \epsilon \frac{e^{-i\pi/4}}{\sqrt{2\pi}} \left[\frac{\Xi}{H} - O(\epsilon^{1/2}) \right] \Xi^{-1/2} \exp i\Xi(1 + \epsilon H^2/2\Xi^2)/\epsilon. \quad (52)$$

For purposes of comparison, we now rewrite (52) in terms of outer variables

$$\epsilon^{3/2} A_1(r, \theta) e^{ir/\epsilon} \sim \epsilon^{3/2} \frac{e^{i\pi/4}}{\sqrt{2\pi}} \frac{\xi}{\eta} \xi^{-1/2} \exp i\xi(1 + \eta^2/2\xi^2)/\epsilon. \quad (53)$$

A direct comparison of equations (50) and (53) where $-\Im(e^{i\pi/4}\eta) < 0$ yields

$$E = -i. \quad (54)$$

We note that $-\mathcal{I}(e^{i\pi/4}\eta) > 0$ corresponds to angles $\theta = O(\epsilon)$. With E determined, the solution is complete. We shall now collect and discuss our results.

5. Summary and discussion

We can now collect the results from previous sections together. At distances $r \ll 1$, the acoustic pressure is described to first order in ϵ by the inner expansion, (7) with (8) and (9). The outer expansion (27) with (28)–(30) is valid for $r \gg 1$, except at angles $\theta = 0$ and $\theta = \pi$. Near the impedance surface at distances $|x| \gg \epsilon^{-1}$, the pressure is well described by the surface wave field (34). $p_{\text{bdry layer}}$ describes the development of the surface wave field (34) and the transition to the outer solution (27). It represents a first order correction to the hard surface solution that is uniformly valid in the vicinity of the surface, i.e. at angles $\theta = O(\epsilon)$. A similar expression can be derived for $\theta = \pi - O(\epsilon)$. Combining these results, we have:

$$p \sim \begin{cases} \frac{1}{2\pi i} \int_{-\infty}^{\infty} [\mu^{-1}(\sigma) + i\epsilon(1-\sigma^2)^{-1}] e^{i\alpha x/\epsilon + i\mu(\sigma)z/\epsilon} d\sigma, & r \ll 1, \\ \frac{\epsilon^{1/2} e^{-i\pi/4}}{i\sqrt{2\pi r}} e^{ir/\epsilon} \left[1 + \frac{i\epsilon}{\sin \theta} - i\epsilon/8r \right], & r \gg 1, z \neq 0, \\ \frac{\epsilon^{1/2} e^{-i\pi/4}}{i\sqrt{2\pi r}} e^{ir/\epsilon} - \frac{i\epsilon}{2} e^{i|x|\sqrt{1+\epsilon^2}/\epsilon - z} \operatorname{erfc} \left[\frac{e^{-i\pi/4}(z\sqrt{1+\epsilon^2} - i\epsilon|x|)}{[2\epsilon|x|\sqrt{1+\epsilon^2} + 2i\epsilon^2 z]^{1/2}} \right], & r \gg 1, z = O(\epsilon|x|). \end{cases} \quad (55)$$

The above expressions give the leading order asymptotic behavior as $\epsilon \rightarrow 0$ in all regions of the field. We confirm the asymptotic nature of (55) by comparing it to the expansion of the exact solution in the Appendix.

In what follows, we shall be concerned with the accuracy of the approximate field (55) above for use in practical applications (i.e. for finite values of ϵ). To that end, we shall derive the far-field directivity and surface wave amplitudes from (55) and compare these to the far-field directivity and surface wave amplitude derived from the exact solution in the appendix.

5.1. Far field directivity

We shall define the far field directivity in terms of the asymptotic behavior of the pressure as $r \rightarrow \infty$. Thus we shall call $D(\theta)$ the directivity, where

$$p(r, \theta) \sim \sqrt{\epsilon/r} D(\theta) \exp(ir/\epsilon), \quad r \rightarrow \infty. \quad (56)$$

From Eq. (85) in the appendix, we see that the exact directivity is given by

$$D(\theta) = \frac{e^{-i\pi/4}}{\sqrt{2\pi}} \frac{\sin \theta}{\epsilon + i \sin \theta}. \quad (57)$$

Eq. (55), on the other hand, predicts the far-field directivity to be

$$D_{\text{outer}}(\theta) = \frac{e^{-i\pi/4}}{i\sqrt{2\pi}} \left[1 + \frac{i\epsilon}{\sin \theta} \right], \quad (58)$$

$D \sim D_{\text{outer}}$ as $\epsilon \rightarrow 0$ for values of $\theta \neq 0, \pi$. Therefore, we expect that D_{outer} in Eq. (58) will provide an approximation to D valid away from the surface. We shall refer to the result (58) as the “outer” or “non-uniform” approximation.

The form of the solution near the surface simplifies considerably in the far-field. When $r \rightarrow \infty$, we may use the large argument expansion of $\text{erfc}(z)$ [1]

$$\text{erfc}(z) \sim \pi^{1/2} z^{-1} \exp(-z^2), \quad z \rightarrow \infty, \quad |\arg z| < 3\pi/4. \quad (59)$$

Using (59) in the last of the expressions in (55) together with the identity $\text{erfc}(-z) = 2 - \text{erfc}(z)$ gives us

$$\begin{aligned} p \sim & \frac{\epsilon^{1/2} e^{-i\pi/4}}{i\sqrt{2\pi r}} \left[1 + \frac{i\epsilon}{z/|x| - i\epsilon} + O(\epsilon) \right] e^{ir/\epsilon} \\ & - i\epsilon \mathcal{H}(\epsilon|x| - z\sqrt{1+\epsilon^2}) \exp[i\sqrt{1+\epsilon^2}|x|/\epsilon - z], \quad r \rightarrow \infty, \quad z/|x| = O(\epsilon). \end{aligned} \quad (60)$$

The first term in (60) describes the near surface behavior of an expanding cylindrical wave, while the second term represents a surface wave. From the first term in (60) we see that the directivity near the surface is

$$D_{\text{inner}}(\theta) = \frac{e^{-i\pi/4}}{i\sqrt{2\pi}} \left[1 + \frac{i\epsilon}{z/|x| - i\epsilon} \right], \quad z = O(\epsilon|x|). \quad (61)$$

Here, $D \sim D_{\text{inner}}$ for angles $\theta = O(\epsilon)$ and $\theta = \pi - O(\epsilon)$. Therefore, D_{inner} provides an inner approximation to the directivity, valid at near grazing angles from the surface.

A uniformly valid composite expansion can be formed from the outer and inner expansions, equations (58) and (61), respectively. Using a multiplicative composite expansion [5] to correct for the non-uniformities at both $\theta = 0$ and $\theta = \pi$, we have

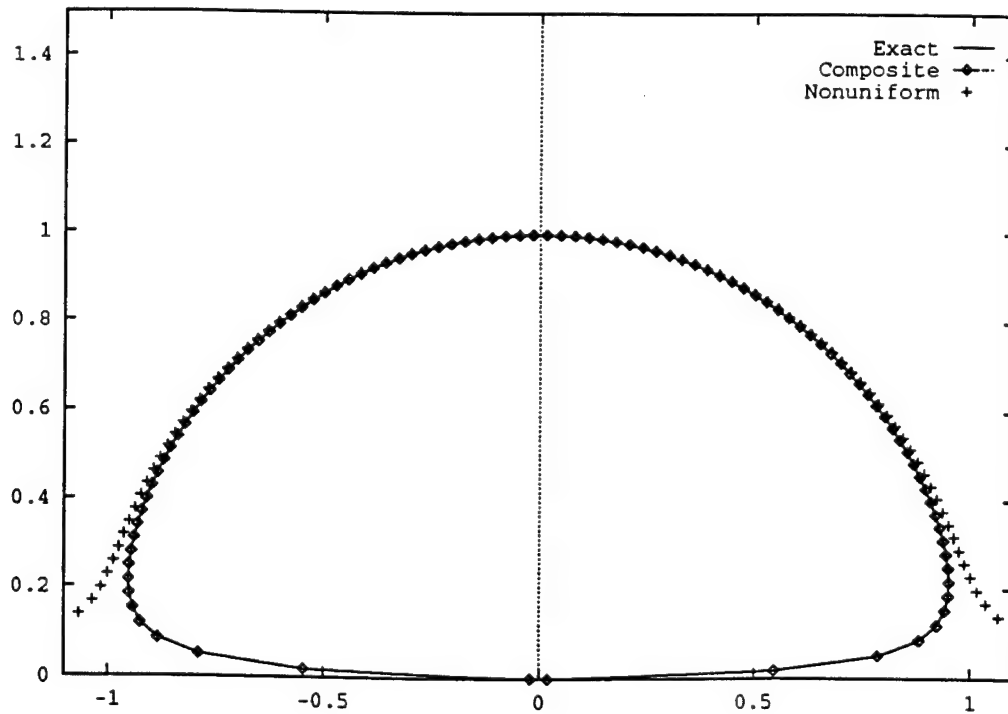


Fig. 1. Polar plot of directivities as functions of θ for $\epsilon = 0.05$. Shown are the directivities derived from the exact solution (57), the non-uniform approximation (58), and the composite uniformly valid solution (62). We note the presence of singularities in the non-uniform prediction at $\theta = 0, \pi$.

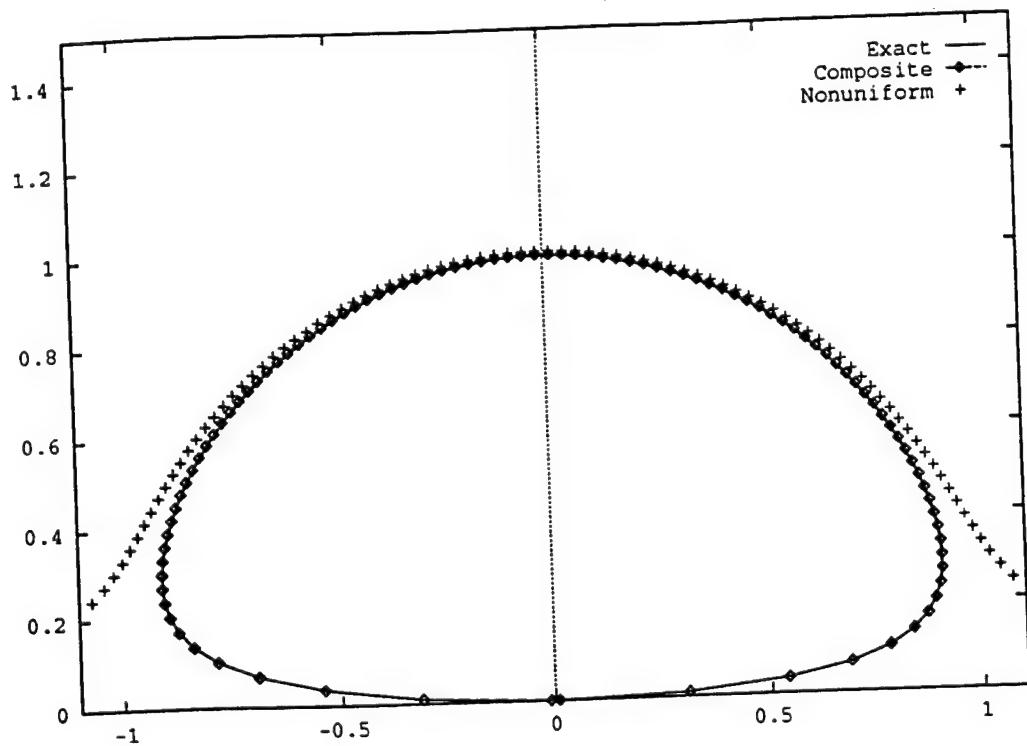


Fig. 2. Polar plot of directivities as functions of θ for $\epsilon = 0.1$.

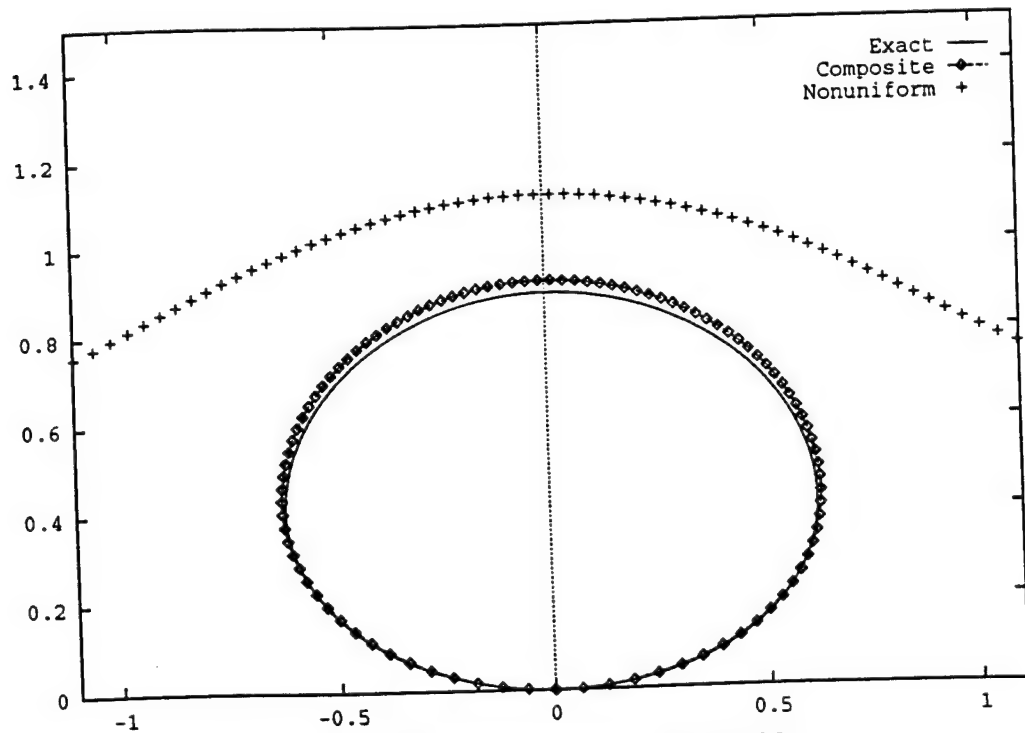
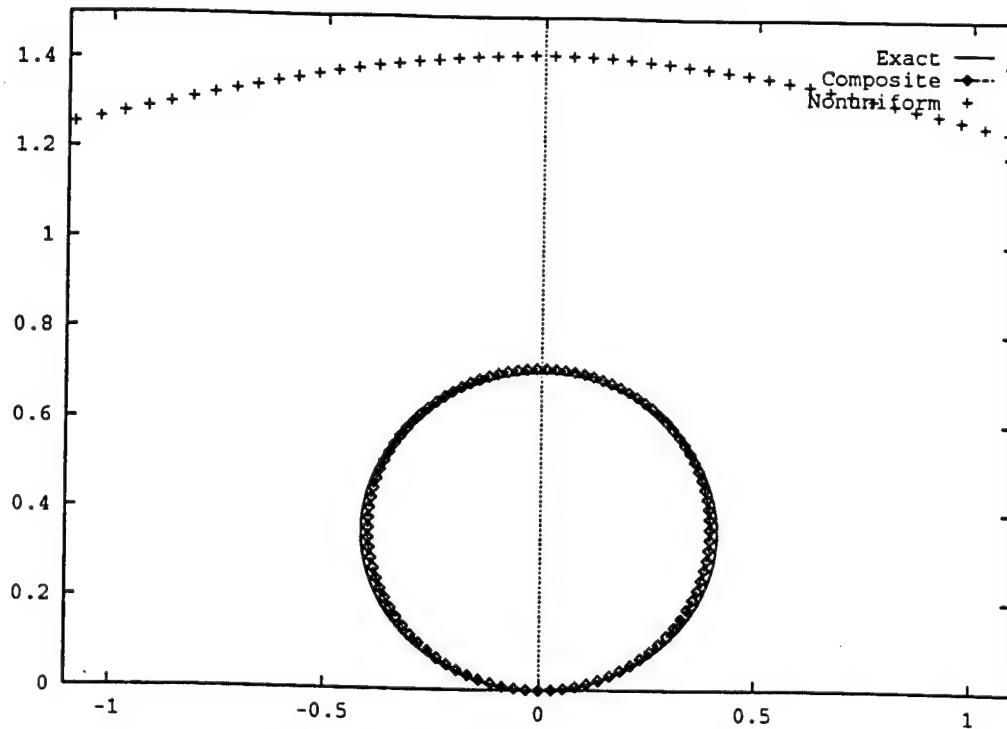


Fig. 3. Polar plot of directivities as functions of θ for $\epsilon = 0.5$.

Fig. 4. Polar plot of directivities as functions of θ for $\epsilon = 1.0$.

$$D(\theta) \sim D_{\text{composite}}(\theta) = \frac{e^{-i\pi/4}}{i\sqrt{2\pi}} \left[1 + \frac{i\epsilon}{\sin \theta} \right] \left[\frac{\theta^2}{\theta^2 + \epsilon^2} \right] \left[\frac{(\pi - \theta)^2}{(\pi - \theta)^2 + \epsilon^2} \right]. \quad (62)$$

$D_{\text{composite}} \sim D$ as $\epsilon \rightarrow 0$ for all angles θ . Therefore, we expect that $D_{\text{composite}}$ should provide a useful approximation to D . Since $D_{\text{composite}}$ has a larger range of validity than D_{outer} , it is not unreasonable to expect that $D_{\text{composite}}$ will be more accurate for larger values of ϵ than D_{outer} .

Figs. 1–4 show plots of the magnitude of $D(\theta)$, $D_{\text{outer}}(\theta)$, and $D_{\text{composite}}(\theta)$ for values of $\epsilon = 0.05, 0.1, 0.5, 1.0$, respectively. We see that the composite expansion provides a good approximation to the exact form of the directivity, even up to values of $\epsilon = 1$. The non-uniform approximation, D_{outer} is valid only at angles $\theta \gg \epsilon$, and provides an accurate approximation only for comparatively small values of ϵ . Examining the relative error of $D_{\text{composite}}$ as an approximation to D shows $D_{\text{composite}}$ to be within 10% of D for all $0 \leq \epsilon \leq 1$ and $0 \leq \theta \leq \pi$.

5.2. Surface wave excitation coefficient

The surface wave excitation coefficient is nothing other than the amplitude of the surface wave. We shall call the amplitude of the surface wave that constant A such that as $|x| \rightarrow \infty, z = 0$,

$$p \sim A \exp[i|x|\sqrt{1+\epsilon^2/\epsilon}]. \quad (63)$$

By inspection of Eqs. (34) and (54) we see that the method of matched asymptotic expansions predicts the amplitude of the surface wave to be

$$A \sim -i\epsilon, \quad \epsilon \rightarrow 0. \quad (64)$$

From Eq. (85) in the appendix, we notice that the exact amplitude of the surface wave is

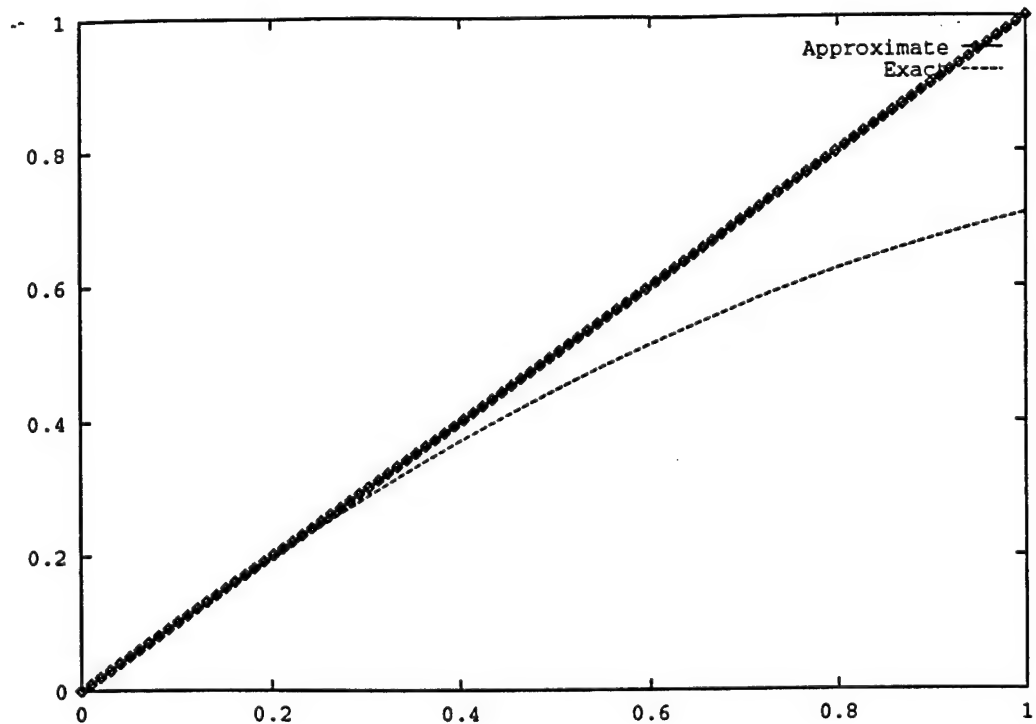


Fig. 5. Surface wave amplitude A as a function of ϵ . Shown are the exact surface wave amplitude and the approximation derived by matched asymptotics.

$$A = -i\epsilon/\sqrt{1+\epsilon^2}. \quad (65)$$

Fig. 5 shows compares the two predictions (64) and (65) on the same plot as functions of ϵ . It shows that the error of using (64) as an approximation to (65) grows with ϵ , and is approximately 40% at $\epsilon=1$.

5.3. Conclusions

We studied the acoustic field radiated by a time harmonic source placed on an infinite surface with small admittance. We derived the form of the field as a singular perturbation from the corresponding problem with a hard surface. A comparison of the expressions derived using matched asymptotic expansions to the uniformly valid expansion of the exact solution is presented in the appendix, and shows the two results to be asymptotically equivalent. A quantitative comparison of the directivities and surface wave amplitude shows the practical utility of leading order uniformly valid asymptotics.

Within the inner region, for distances $r \ll 1$, the field is well described by the hard surface field, p_0 , with a small correction of $O(\epsilon)$. At larger distances, the correction to the hard surface field is again $O(\epsilon)$ except near the surface. The near surface structure of the field was obtained by assuming the surface wave fields and matching to the outer solution. It is important to note that the outer solution exposed a non-uniformity which dictated the need for the surface wave and the associated boundary layer solution.

The method of matched asymptotic expansions has been shown to be able to determine the leading order behavior of an acoustic field scattered by a nearly hard surface. Previous results on the problem studied here are abundant, but they have been derived by determining the exact solution and then expanding for small values of the admittance.

The method of matched asymptotics, on the other hand, has the very powerful advantage of being applicable where no exact solution is available. We anticipate that singular perturbation techniques from hard surfaces shall

prove to be a powerful method in the determination of diffraction coefficients where complications due to boundary conditions or geometry preclude the possibility of finding an exact solution. For example, the application of the method described above to determine the field scattered by an impedance discontinuity is almost immediately available from the results included here. Similar statements may be made regarding diffraction from impedance wedges, elastic discontinuities under light fluid loading, and elastic wedges also under light fluid loading.

Acknowledgements

The author is grateful to Professor Allan Pierce for sharing details of the historical background of this problem, and for helpful discussions. This work is supported by ONR.

Appendix A. Comparison to exact solution

A.1. Derivation of exact solution

Here we shall derive an exact solution of the problem of a source on an impedance surface. We expand the exact solution in different regimes to illustrate how the solution derived using matched asymptotic expansions compares.

For the exact solution, the choice of variables is unimportant. We shall use the outer variables for convenience. Recalling the problem statement in Eqs. (12)–(14) shows that p satisfies

$$\frac{\partial^2 p}{\partial x^2} + \frac{\partial^2 p}{\partial z^2} + \epsilon^{-2} p = 0, \quad \text{in } z > 0, \quad (66)$$

$$\frac{\partial p}{\partial z} + p = \delta(x), \quad \text{on } z = 0, \quad (67)$$

$$p(x, z) \text{ is outgoing,} \quad \text{as } r \rightarrow \infty. \quad (68)$$

We shall explicitly extract the “hard surface” part of the field by seeking a solution of Eqs. (12)–(14) in the form

$$p = p_0 + p_s. \quad (69)$$

We define p_0 so that

$$\frac{\partial^2 p_0}{\partial x^2} + \frac{\partial^2 p_0}{\partial z^2} + \epsilon^{-2} p_0 = 0, \quad \text{in } z > 0, \quad (70)$$

$$\frac{\partial p_0}{\partial z} = \delta(x), \quad \text{on } z = 0, \quad (71)$$

$$p_0(x, z) \text{ is outgoing,} \quad \text{as } r \rightarrow \infty. \quad (72)$$

Therefore, p_0 is the solution corresponding to a source on a hard surface, while p_s is the correction to that field due to the finite surface impedance.

It is a straightforward matter to calculate p_0 and p_s . Expressing p_0 and p_s as Fourier integrals yields

$$p_0 = \frac{1}{2\pi i} \int_{-\infty}^{\infty} \mu^{-1}(\sigma) e^{i\sigma x/\epsilon + i\mu(\sigma)z/\epsilon} d\sigma, \quad (73)$$

$$p_s = \frac{-\epsilon}{2\pi i} \int_{-\infty}^{\infty} \frac{1}{\mu(i\mu + \epsilon)} e^{i\sigma x/\epsilon + i\mu(\sigma)z/\epsilon} d\sigma. \quad (74)$$

A direct comparison of (73) to (8) shows p_0 and P_0 to be identical, once the relations $x = \epsilon X$ and $z = \epsilon Z$ are used. Therefore, we expect that for small ϵ , p_s should agree with P_1 . Writing (74) in terms of inner variables yields

$$p_s = \frac{-\epsilon}{2\pi i} \int_{-\infty}^{\infty} \frac{1}{\mu(i\mu + \epsilon)} e^{i\sigma X + i\mu(\sigma)Z} d\sigma. \quad (75)$$

Thus, to leading order in ϵ , with (X, Z) fixed, (75) indeed agrees with (9). This verifies the validity of the inner expansion, or the first of the four expressions in Eq. (55).

It is more interesting to compare the exact solution (73)-(75) with the outer solution and surface wave boundary layer. For that purpose, we shall need uniformly valid expansions of p_0 and p_s .

Since p_0 is identical to P_0 , its expansion is identical to that given in Eq. (26). Thus,

$$p_0 \sim \frac{1}{2i} \sqrt{\frac{2\epsilon}{\pi r}} e^{ir/\epsilon - i\pi/4} [1 - i\epsilon/8r + O(\epsilon^2/r^2)]. \quad (76)$$

We note that a small ϵ expansion of p_0 is equivalent to a large r expansion. That is not strictly so for p_s .

A.2. Uniformly valid expansion of p_s

We shall now evaluate p_s using the method of steepest descents. To do so, we introduce a new integration variable u , defined so that

$$-\frac{1}{2}u^2 = i[\sigma \cos \theta + \mu \sin \theta - 1]. \quad (77)$$

Substituting (77) into (75) yields

$$p_s = \frac{-\epsilon}{2\pi i} e^{ir/\epsilon} \int_{-\infty}^{\infty} \frac{1}{\mu(i\mu + \epsilon)} \frac{d\sigma}{du} e^{-ru^2/2\epsilon} du - i \frac{\epsilon}{\sqrt{1+\epsilon^2}} \chi(\theta - \theta_1) e^{i|x|\sqrt{1+\epsilon^2}/\epsilon - z}. \quad (78)$$

In changing integration variables from σ to u , we have also changed integration contours from the real σ axis² to the real u axis. In moving the integration contour, there are two angles at which a residue contribution is picked up from either of the two poles in the integrand. The residue contribution is the second term in (78), in which we have implicitly assumed that $x > 0$. In what follows, we shall restrict our calculations to be applicable in the region $x > 0$. The field for $x < 0$ is obtained simply by symmetry. The angle θ_1 is the angle at which the new contour $\mathcal{I}u=0$ crosses the pole, and is defined by $\tan \theta_1 = \epsilon/\sqrt{1+\epsilon^2}$. $\chi(\theta - \theta_1)$ is unity when the pole is encircled and zero otherwise. Thus,

$$\chi(\theta - \theta_1) = \begin{cases} 1, & \text{for } \theta < \theta_1, \\ 0, & \text{otherwise.} \end{cases} \quad (79)$$

We note that the location of the pole, and thus the phase of the resulting surface wave, depends upon ϵ . For this reason, in order to develop an expansion which is uniformly valid in angle and distance along the surface, the location of the pole must be included exactly. Therefore, we will keep the factor $(i\mu + \epsilon)^{-1}$ in tact exactly, rather than expand it into a series in powers of ϵ . The result that we shall obtain in this way is equivalent to a large expansion of p_s .

In terms of the new integration variable, u , the pole in the integrand corresponding to $\sigma = \sqrt{1+\epsilon^2}$ is located at $u = u_p$, where

² Technically, the original integration contour is the real σ axis, indented below the pole and branch point on the positive real axis and indented above the pole and branch point on the negative real axis.

$$u_p = (1-i)[\sqrt{1+\epsilon^2} \cos \theta + i\epsilon \sin \theta - 1]^{1/2}. \quad (80)$$

The branch of the square root in (80) is chosen so that $\Re u_p \geq 0$. Long but simple calculations show that

$$\frac{1}{\mu(i\mu+\epsilon)} \frac{d\sigma}{du} = \frac{i}{\sqrt{1+\epsilon^2}(u-u_p)} + \frac{\sin \theta - i\epsilon - u_p \sqrt{1+\epsilon^2} e^{-i\pi/4}}{-u_p \sqrt{1+\epsilon^2}(\epsilon+i\sin \theta)} + O(u). \quad (81)$$

Substituting (81) into (78) and integrating yields

$$p_s = \frac{\sin \theta - i\epsilon - u_p \sqrt{1+\epsilon^2} e^{-i\pi/4}}{-u_p \sqrt{1+\epsilon^2}(\epsilon+i\sin \theta)} \frac{-\epsilon}{2\pi i} e^{ir/\epsilon} \int_{-\infty}^{\infty} (1+O(u)) e^{-ru^2/2\epsilon} du - \frac{\epsilon}{2\pi i} e^{ir/\epsilon} \int_{-\infty}^{\infty} \frac{i}{\sqrt{1+\epsilon^2}(u-u_p)} e^{-ru^2/2\epsilon} du - i \frac{\epsilon}{\sqrt{1+\epsilon^2}} \chi(\theta - \theta_1) e^{i|x|\sqrt{1+\epsilon^2}/\epsilon - z} \quad (82)$$

$$\sim \frac{-\epsilon \sin \theta - i\epsilon - u_p \sqrt{1+\epsilon^2} e^{-i\pi/4}}{2\pi i - u_p \sqrt{1+\epsilon^2}(\epsilon+i\sin \theta)} \sqrt{\frac{2\pi\epsilon}{r}} e^{ir/\epsilon} + \epsilon O((\epsilon/r)^{3/2}) \quad (83)$$

$$- \frac{i\epsilon}{2\sqrt{1+\epsilon^2}} \operatorname{erfc}[-iu_p \sqrt{r/2\epsilon}] \exp[ix\sqrt{1+\epsilon^2}/\epsilon - z]. \quad (83)$$

Eq. (83) is an expansion that is valid for all values of ϵ , provided $r/\epsilon \gg 1$. The first term in (83) represents part of a cylindrical wave propagation outward from the source at $r=0$. The second term represents a surface wave propagating along the boundary $z=0$ ($x>0$) with its associated “boundary layer” describing the transition between the surface wave field and the cylindrical wave field.

The argument of the complementary error function in (83) is large except where $|u_p| \ll (r/\epsilon)^{1/2}$. Away from these regions, we can use the large argument expansion of the complementary error function to simplify (83) and obtain

$$p_s \sim \frac{-\epsilon}{2\pi i} \frac{e^{-i\pi/4}}{\epsilon+i\sin \theta} \sqrt{\frac{2\pi\epsilon}{r}} e^{ir/\epsilon} - i \frac{\epsilon}{\sqrt{1+\epsilon^2}} \chi(\theta - \theta_1) e^{i|x|\sqrt{1+\epsilon^2}/\epsilon - z}. \quad (84)$$

The full expression for the pressure field is now obtained by combining (76) with (84):

$$p \sim \frac{1}{2i} \sqrt{\frac{2\epsilon}{\pi r}} e^{ir/\epsilon - i\pi/4} \left[1 - i\epsilon/8r - \frac{\epsilon}{\epsilon+i\sin \theta} \right] - i \frac{\epsilon}{\sqrt{1+\epsilon^2}} \chi(\theta - \theta_1) e^{i|x|\sqrt{1+\epsilon^2}/\epsilon - z}. \quad (85)$$

Equation (85) compares directly with the second of the expressions in Eq. (55). In addition, it also reveals the same near surface behavior of the cylindrical wave field as does Eq. (60).

The surface wave amplitude revealed in Eq. (85), however, differs from that derived previously (55) by a factor of $\sqrt{1+\epsilon^2} \sim 1 + \epsilon^2/2 + O(\epsilon^4)$. Thus, the surface wave excitation coefficient as calculated by the method of matched asymptotic expansions is wrong by $O(\epsilon^2)$, which is to be expected.

So far we have verified the form of the asymptotic solution in the inner region, the outer region away from the boundary, and near the boundary itself. It remains only to compare the exact solution to the asymptotic solution in the boundary layer region. Both solutions describe the transition in terms of a complementary error function. We shall examine the form of the argument of erfc in (83) in the vicinity of the boundary layer. We now use (80) to write

$$-iu_p \sqrt{r/2\epsilon} = -i(1-i)[\sqrt{1+\epsilon^2} r \cos \theta + i\epsilon r \sin \theta - r]^{1/2}/\sqrt{2\epsilon}. \quad (86)$$

Expressing this in terms of boundary layer coordinates, (Ξ, H) , (recall Eqs. (37) and (39)) and simplifying gives

$$-iu_p\sqrt{r/2\epsilon} = e^{-i\pi/4}[H^2/2\Xi + O(\epsilon)]^{1/2} \sim e^{-i\pi/4}\eta/\sqrt{2\xi}. \quad (87,88)$$

Thus, we see that the arguments of the complimentary error functions agree within the boundary layer.

Therefore, we conclude that the asymptotic solution constructed previously agrees to leading order with the exact solution throughout the entire domain.

References

- [1] M. Abramowitz and I.A. Stegun, *Handbook of Mathematical Functions*, Dover Publications, New York (1972).
- [2] K. Attenborough, S.I. Hayek and J.M. Lawther, "Propagation of sound above porous half-space", *J. Acoust. Soc. Am.* 68 (5) 1493–1501 (1975).
- [3] N. Bleistein and R.A. Handelsman, *Asymptotic Expansions of Integrals*, Dover, New York (1986).
- [4] C.F. Chien and W.W. Soroka, "Sound propagation along an impedance plane", *J. Sound and Vib.* 43(1) 9–20 (1975).
- [5] M. Van Dyke, *Perturbation Methods in Fluid Mechanics*, Parabolic Press, Stanford, annotated edition (1975).
- [6] U. Ingard, "On the reflection of a spherical sound wave from an infinite plane", *J. Acoust. Soc. Am.* 23(3) 329–335 (1951).
- [7] J.B. Keller and F.C. Karal, Jr., "Surface wave excitation and propagation", *J. Appl. Phys.* 31(6) (1960).
- [8] R.B. Lawhead and I. Rudnick, "Acoustic wave propagation along a constant normal impedance boundary", *J. Acoust. Soc. Am.* 23(5) 546–549 (1951).
- [9] A.R. Wenzel, "Propagation of waves along an impedance boundary", *J. Acoust. Soc. Am.* 55(5) 956–963 (1974).
- [10] Zauderer, *Partial differential Equations of Applied Mathematics*, Academic Press, New York, 2nd ed. (1989).